Local and remote sources of Arctic air pollution

Eleftherios Ioannidis

Sorbonne Université

ÉCOLE DOCTORALE
DES SCIENCES DE L'ENVIRONNEMENT D'ILE DE FRANCE

T H È S E

pour obtenir le grade de

Docteur en Sciences

de Sorbonne Université

Spécialité : Physique et chimie de l'atmosphère

Présentée et soutenue par

IOANNIDIS ELEFTHERIOS

Local and remote sources of Arctic air pollution

Thèse dirigée par Kathy S. LAW

préparée au Laboratoire ATmosphère, Milieux, Observations Spatiales (LATMOS)

Jury:

Président du Jury:	SOLENE TURQUETY
Rapporteur:	STEVE R. ARNOLD
Rapporteur:	VIRGINIE MARECAL
Directrice:	KATHY S. LAW
Examinateur:	BARBARA D'ANNA
Examinateur:	MATTHIAS BEEKMAN

SEPTEMBER 2022

Résumé

La région arctique se réchauffe plus rapidement que toute autre région de la planète en raison de l'effet des gaz à effet de serre, notamment le CO_2, et des forçeurs climatiques à courte durée de vie d'origine anthropique, comme le carbone suie (BC). Au cours des 20 à 30 dernières années, les émissions anthropiques lointain au-dessus des régions de latitude moyenne ont diminué. Les émissions anthropiques dans l'Arctique y contribuent également et pourraient augmenter à l'avenir et influencer davantage la pollution atmosphérique et le climat de l'Arctique. Les émissions naturelles, telles que les aérosols d'origine marine, pourraient également augmenter en raison du changement climatique en cours. Cependant, les processus et les sources qui influencent les aérosols et les gaz traces dans l'Arctique sont mal quantifiés, surtout en hiver. Dans cette thèse, des simulations quasi-hémisphériques et régionales sont réalisées à l'aide du modèle Weather Research Forecast, couplé à la chimie (WRF-Chem). Le modèle est utilisé pour étudier la composition atmosphérique sur la région Arctique et lors de deux campagnes de terrain, l'une au nord de l'Alaska à Barrow, Utqiaġvik en janvier et février 2014 et la seconde à Fairbanks, au centre de l'Alaska en novembre et décembre 2019 lors de la campagne française pré-ALPACA (Alaskan Layered Pollution And Chemical Analysis). Tout d'abord, les aérosols inorganiques et les aérosols de sel marin (SSA) modélisés sont évalués sur des sites arctiques pendant l'hiver. Ensuite, le modèle est amélioré en ce qui concerne les traitements des SSA, après évaluation par rapport aux données de la campagne de Barrow, et leur contribution à la charge totale d'aérosols dans la région arctique est quantifiée. Une série d'analyses de sensibilité est effectuée sur le nord de l'Alaska, révélant des incertitudes du modèle dans les processus influençant les SSA dans l'Arctique, tels que la présence de glace de mer et de chenaux ouverts. Ensuite, une analyse de sensibilité est effectuée pour étudier les processus et les sources qui influencent le BC hivernale dans l'ensemble de l'Arctique et au nord de l'Alaska, en se concentrant sur les traitements de dépôt et les émissions régionales. Des variations de la sensibilité du modèle aux dépôts humides et secs sont constatées dans tout l'Arctique et pourraient expliquer les biais du modèle. Dans le nord de l'Alaska, les émissions régionales provenant de l'extraction pétrolière contribuent de manière importante au BC observée. Les résultats du modèle sont également sensibles aux schémas de parametrisation de la couche limite. Troisièmement, la version améliorée du modèle est utilisée pour étudier la contribution des sources régionales et locales à la pollution atmosphérique dans la région de Fairbanks pendant l'hiver 2019. En utilisant des émissions actualisées, le modèle donne de meilleurs résultats pour l'hiver 2019 que pour l'hiver 2014, lorsqu'on le compare aux observations effectuées sur des sites de fond en Alaska. Les sous-estimations des aérosols modélisés de BC et de sulfate (SO_4^{2-})

s'expliquent en partie par le manque d'émissions anthropiques locales et régionales. Dans le cas du SO_4^{2-}, des mécanismes supplémentaires de formation d'aérosols secondaires dans des conditions sombres/froides doivent également être pris en compte.

Abstract

The Arctic region is warming faster than any other region on Earth due to the effect of greenhouse gases, notably CO_2, and short-lived climate forcers of anthropogenic origin, such as black carbon (BC). Over the last 20-30 years, remote anthropogenic emissions over mid-latitude regions have been decreasing. Anthropogenic emissions within the Arctic are also contributing and might increase in the future and further affect Arctic air pollution and climate. Natural emissions, such as sea-spray aerosols, also might increase due to on-going climate change. However, the processes and sources influencing Arctic aerosols and trace gases are poorly quantified, especially in wintertime. In this thesis, quasi-hemispheric and regional simulations are performed using the Weather Research Forecast model, coupled with chemistry (WRF-Chem). The model is used to investigate atmospheric composition over the wider Arctic and during two field campaigns, one in northern Alaska at Barrow, Utqiaġvik in January and February 2014 and the second in Fairbanks, central Alaska in November and December 2019 during the French pre-ALPACA (Alaskan Layered Pollution And Chemical Analysis) campaign. First, modelled inorganic and sea-spray (SSA) aerosols are evaluated at remote Arctic sites during wintertime. Then, the model is improved with respect to SSA treatments, following evaluation against Barrow field campaign data, and their contribution to the total aerosol burden within the Arctic region is quantified. A series of sensitivity runs are performed over northern Alaska, revealing model uncertainties in processes influencing SSA in the Arctic such as the presence of sea-ice and open leads. Second, a sensitivity analysis is performed to investigate processes and sources influencing wintertime BC over the wider Arctic and over northern Alaska, with a focus on removal treatments and regional emissions. Variations in model sensitivity to wet and dry deposition is found across the Arctic and could explain model biases. Over northern Alaska, regional emissions from petroleum extraction are found to make an important contribution to observed BC. Model results are also sensitive to planetary boundary layer parameterisation schemes. Third, the improved version of the model is used to investigate the contribution of regional and local sources on air pollution in the Fairbanks area in winter 2019. Using up-to-date emissions, the model performs better in winter 2019 than in winter 2014, when compared to observations at background sites across Alaska. Underestimations in modelled BC and sulphate (SO_4^{2-}) aerosols can be partly explained by lacking local and regional anthropogenic emissions. In the case of SO_4^{2-}, additional secondary aerosol formation mechanisms under dark/cold conditions also need to be considered.

Acknowledgements

I would like to take this opportunity to thank a variety of people whose help has been instrumental in accomplishing this task.

First I would like to express my deepest appreciation to thank Kathy Law, my PhD thesis supervisor, not only for accompanying and guiding me during these four years, but also for giving me the opportunity to work on this project. I am grateful for your advice, your availability and your support. I am also thankful to my thesis jury and my thesis committee, who generously provided knowledge and expertise. Finally, I would like to extend my sincere thanks to Jean-Christophe Raut, Louis Marelle and Tatsuo Onishi, for their help, valuable comments, suggestions and endless discussions about chemistry and "bugs" in the model.

This thesis would not have been been possible without the funding from MOPGA program and IPSL. Thank you for the opportunity to work at Sorbonne Université, to join LATMOS, and TROPO team, where I was warmly welcomed during this thesis, and warm thanks to all those who made these years at LATMOS enjoyable, too numerous to name them all here.

Many thanks to everyone who I collaborated with, for the interesting discussions about chemistry and valuable inputs, and for contributing to my growth as a scientist. Special thanks to Natalie Brett, Rimal Abeed, Audrey Lecouffe, Elisabeth Werner and Julia Maillard for exploring Paris with me, being there during coffee/lunch breaks and making the long nights at Jussieu enjoyable. Thank you Julia also for the fun days in Fairbanks, Alaska during the pre-campaign. I am pretty sure I am your favorite roommate. Thanks also to all the occupants of office 316 and to the other PhD students, who provided helpful coffee breaks, or there were around for a drink or a dinner.

And, last but not least, thanks to Adrien, my friends and family members for their encouragement and support throughout the PhD.

Acronyms

AAI Arctic Amplification Index

ALPACA Alaskan Layered Pollution And Chemical Analysis

AMAP Arctic Monitoring and Assessment Programme

AO Arctic Oscillation

ASTEM Adaptive Step Time-Split Euler Method

CAMS Copernicus Atmosphere Monitoring Service

CCN Cloud Condensation Nuclei

CEDS Community Emissions Data System

CESM1 Community Earth System Model

CAM-Chem Community Atmosphere Model with Chemistry

CMIP6 Coupled Model Intercomparison Project round 6

CBM-Z Carbon-Bond Mechanism version Z

DMS Dimethyl sulfide

EBAS European Monitoring and Evaluation Programme dataBASE

ECLIPSE Evaluating the Climate and Air Quality Impacts of Short-Lived Pollutants

ECMWF European Centre for Medium-Range Weather Forecasts

EDGAR Emissions Database for Global Atmospheric Research

EPA Environmental Protection Agency

EPA-ADEC EPA-Alaska Department of Environmental Conservation

ERA-Interim European Centre for Medium-Range Weather Forecasts Interim Re-Analysis

ERA5 ECMWF Reanalysis v5

ESRL Earth System Research Laboratories

FINN Fire INventory from NCAR

FNL Final

GAINS Greenhouse gas – Air pollution Interactions and Synergies

GFED Global Fire Emissions Database

GHGs greenhouse gases

GMD Global Monitoring Laboratory

DMS Dimethyl sulphide

GOCART Goddard Chemistry Aerosol Radiation and Transport

IGBP International Geosphere-Biosphere Programme

IMPROVE Interagency Monitoring of Protected Visual Environments

IPCC Intergovernmental Panel on Climate Change

ISD Integrated Surface Dataset

LSM land surface model

JRC European Joint Center

MADE Modal Aerosol Dynamics Model for Europe

MATCH Multi-scale Atmospheric Transport and Chemistry Model

MEGAN Model of Emissions of Gases and Aerosol from Nature

MERRA Modern-Era Retrospective analysis for Research and Applications

MERRA2 Modern-Era Retrospective analysis for Research and Applications

MP Multiparameterization

MODIS Moderate Resolution Imaging Spectroradiometer

MOSAIC Model for Simulating Aerosol Interactions and Chemistry

MOZART Model of Ozone and Related Chemical Tracers

MYJ Mellor-Yamada-Janjić

NAAQS National Ambient Air Quality Standard

NAO North Atlantic Oscillation

NCAR National Center for Atmospheric Research

NCEP National Centres for Environmental Prediction

NCEP-FNL National Centres for Environmental Prediction Final

NEI National Emissions Inventory

NEMO Nucleus for European Modelling of the Ocean

NMHCs non-methane hydrocarbons

NMVOCs non-methane volatile organic compounds

NOAA National Oceanic and Atmospheric Administration

NOAH National Centers for Environmental Prediction Oregon State University Air Force Hydrology Lab

NorESM Norwegian Earth System Model

NOVAC Network for Observation of Volcanic and Atmospheric Change

NPI North Pacific index

PBL Planetary Boundary layer

PNA Pacific North American

PDO Pacific Decadal Oscillation

POA Primary organic aerosol

POLARCAT POLar study using Aircraft, Remote sensing, surface measurements and modelling of Climate, chemistry, Aerosols and Transport

POLMIP POLARCAT Model Intercomparison Project

RACM Regional Atmospheric Chemistry Mechanism

RMSE Root-Mean-Square Error

RRTMG Rapid Radiative Transfer Model for GCMs

RUC Rapid Update Cycle

SAPRC-99 Statewide Air Pollution Research Center

SBIs Surface-based inversions

ScanDOAS Scanning differential optical absorption spectroscopy

SLCFs Short-Lived Climate Forcers

SMHI Swedish Meteorological and Hydrological Institute

SOA Secondary Organic Aerosols

SORGAM Secondary Organic Aerosol Model

TKE turbulent kinetic energy

USGS United States Geological Survey

VIIRS Visible Infrared Imaging Radiometer Suite

VOCs volatile organic compounds

WHO World Health Organisation

WMO World Meteorological Organization

WRF Weather Research and Forecasting

YSU Yonsei University

List of Figures

List of Tables

Contents

Introduction

Air pollution is a challenge that has affected human health from the early years of human history *(Fowler et al., 2020)*. During the industrial revolution, and due to the extensive use of coal, air quality issues started to appear, such as the Great Smog of 1952 *(Wang et al., 2016)*. Coal combustion was the main contributor to air pollution, and major pollutants, such as sulfur dioxide (SO_2) and nitrogen oxides (NO_x). Air pollution still affects millions of people, especially in urban cities, such as Beijing in China, often exceeding World Health Organisation (WHO) air quality guidelines *(Cohen et al., 2004; Institute, 2019)*. WHO estimated that 8.8 million people die annually due to indoor and outdoor air pollution.

During the decade 2011—2020 the global mean surface temperature was 1.09 °C higher than during 1850—1900, and it is now known that this global warming, which has not occurred equally everywhere, is caused by human activity *(IPCC, 2021)* due to anthropogenic emissions such as transportation, combustion of fossil fuels for heating and power generation *(Szopa et al., 2021; Wang et al., 2022)*. Increases in anthropogenic emissions led to an increase in greenhouse gases (GHGs) which warm the atmosphere, primarily CO_2, and also methane (CH_4), ozone (O_3) and nitrous oxide (N_2O) *(AMAP, 2015; Szopa et al., 2021)*. For example, according to National Oceanic and Atmospheric Administration (NOAA), Intergovernmental Panel on Climate Change (IPCC) and World Meteorological Organization (WMO) CO_2 levels in the atmosphere are 149% of the pre-industrial level, while CH_4 levels, are about 156% of the levels in 1750.

Air pollutants also act as Short-Lived Climate Forcers (SLCFs) since they contribute to warming the atmosphere. They include aerosols, in particular, black carbon (BC), and GHGs, notably CH_4 and tropospheric O_3 (e.g. *Bindoff et al. (2013)*,*Szopa et al. (2021)*). SLCFs do not act uniformly (cooling or warming) everywhere. BC causes a positive radiative forcing (warming) on a global scale *(Bond et al., 2013a)*. Other aerosols (also SLCFs), and in particular sulphate (SO_4^{2-}), have offset global warming since they reflect solar radiation and cool the climate *(Horowitz et al., 2020; Masson-Delmotte et al., 2021; Szopa et al., 2021)*.

The Arctic is warming faster than any other region on Earth, with surface temperatures rising more than twice compared the global average. In addition to CO_2, SLCFs are contributing to the Arctic warming, in particular, BC and CH_4 *(IPCC, 2021; AMAP, 2021)*. Tropospheric O_3 also contributes to Arctic warming, including that produced from CH_4 oxidation *(AMAP, 2021)*. SLCFs contribute to Arctic warming either directly in the Arctic or following warming further south followed by heat transport. BC deposited on snow in the Arctic also leads to additional warming since it accelerates snow melting by absorbing solar radiation *(AMAP, 2015)*. An increase in air pollutants might also lead to an increase in

Arctic surface warming via indirect cloud-aerosol effects *(AMAP, 2015)*. Early reports, such as *Brøgger (1881)*, and studies over the last century showed that Arctic air pollution originated primarily from mid-latitude regions transported into the Arctic during winter and spring *(Rahn and McCaffrey, 1980; Quinn et al., 2002b)*, a phenomenon called Arctic Haze. Other emissions, such as boreal fires, are also important in the summer months. However, over the last 20-30 years, mid-latitude emissions have been declining due to regulations, especially in Europe and North America (e.g. *Sharma et al. (2019)*,*Szopa et al. (2021)*). At the same time, it has become apparent that there are important local sources within the Arctic, which might increase in the future, due to future warming and increased human activity *(Schmale et al., 2018)*.

Arctic warming is largest in autumn/winter and aerosol indirect radiative warming effects are stronger in winter *(Boisvert and Stroeve, 2015; AMAP, 2015)*. However, wintertime air pollution is less studied compared to other seasons, and uncertainties remain about local sources and the extent to which they contribute to air pollution in the Arctic and their effect on Arctic warming *(AMAP, 2015; Schmale et al., 2018)*. For example, due to very cold conditions in the Arctic wintertime, the use of fossil fuels, e.g. for domestic/commercial heating and industrial activities, is extensive *(Simpson et al., 2019)*. A further increase in the Earth's population and possible population movements to higher latitudes due to ongoing climate warming could increase the demand for further industrial development in the Arctic, such as resource extraction *(AMAP, 2021; IPCC, 2021)*. It is therefore essential to improve quantification of local emissions and processes influencing Arctic atmospheric composition during winter to better communicate to policymakers what actions are needed to reduce local impacts on air quality and climate *(AMAP, 2021)*.

Models are the tools used to study air pollution and its impacts. However, models still have difficulties simulating the seasonal cycle of natural and anthropogenic trace gases and aerosols in the Arctic, and often underestimate observed aerosol composition during wintertime at remote Arctic sites *(Eckhardt et al., 2015; Whaley et al., 2022b)*. For example, models tend to lack mechanisms essential for sea-spray aerosol (SSA) production not only during summertime, but also during wintertime. Other uncertainties in the models are linked to treatments of dry and wet removal, e.g. *Mahmood et al. (2016)*, *Shen et al. (2017)*. It is important to better quantify the effect on aerosols in the Arctic in order to improve these processes in the models. Also, models may be missing important reactions and pathways for wintertime formation of secondary aerosols *(Simpson et al., 2019)*. Uncertainties in anthropogenic emissions as well as processes influencing natural emissions are also contributing to model biases and uncertainties.

Given the wider context described above the overall goal of this thesis is to improve our

understanding about local and remote Arctic air pollution in winter. These main scientific questions are addressed in this thesis:

(i) What is the contribution of natural and anthropogenic sources to aerosol composition during the Arctic winter? Can models simulate wintertime aerosol composition in the Arctic?

(ii) How sensitive are modelled aerosols to removal treatments and physical processes during wintertime?

(iii) To what extent are local Arctic anthropogenic sources contributing to wintertime atmospheric composition?

In this thesis, the regional transport model, coupled with chemistry Weather Research and Forecasting (WRF)-Chem is used *(Grell et al., 2005; Fast et al., 2006; Marelle et al., 2017)*. The model is run on quasi-hemispheric scale and evaluated against observations over the wider Arctic for winters 2014 and 2019. It was also run for shorter periods over Alaska and evaluated against data collected during field campaigns over northern Alaska in January and February 2014 *(Kirpes et al., 2018)* and central Alaska in November and December 2019 *(Simpson et al., 2019; Maillard et al., 2022)*. Model sensitivities to emissions, removal treatments and boundary layer dynamics are examined. Improvements are made to the treatment of SSA aerosols in the model.

This thesis is organised as follows. Chapter 1 introduces the scientific context and motivation for this thesis. It describes Arctic warming and atmospheric circulation linked to the main pathways for air mass transport from mid-latitudes to the Arctic, as well as remote (outside the Arctic) and local sources of air pollutants within the Arctic. The scientific context related to Alaska, the focus of this thesis, is also described. Chapter 2 introduces tropospheric aerosols, including anthropogenic and natural aerosols, their precursors and emissions, focusing on the Arctic. This chapter also describes aerosol properties and processes. Chapter 3 describes the main tools used in this thesis namely the model, including the main physics and chemistry parametrizations, emission inventories, as well as the observations and field campaigns. Chapters 4, 5 and 6 present the main results of this thesis.

Chapter 4 presents a study investigating wintertime air pollution in the wider Arctic and over northern Alaska focusing on the contribution of inorganic and, in particular, SSA aerosols to the total Arctic aerosol burden. The ability of the model to capture background anthropogenic and natural aerosols over the wider Arctic, including Alaska, is evaluated. The focus of this study is on SSA aerosols, and in particular on the physical processes

influencing their emissions over the wider Arctic and regionally over northern Alaska in winter. This chapter has been submitted as *(Ioannidis et al., 2022)*.

Chapter 5 investigates processes and sources affecting BC in the Arctic. The sensitivity to wet and dry removal is examined over the wider Arctic as well as over northern Alaska. The influence of regional and local Alaskan anthropogenic emissions, such as those related to petroleum extraction in northern Alaska, is also examined (Ioannidis et al. 2022, to be submitted).

Chapter 6 presents a study focusing on local urban pollution in Fairbanks, central Alaska, during the pre-ALPACA campaign (winter 2019). The ability of the model to capture background aerosols over Alaska, and over Fairbanks, is investigated. Uncertainties linked to removal treatments, boundary layer dynamics, and aerosol precursor emissions are investigated. The latter are used as an indicator to examine the extent to which the model maybe lacking wintertime secondary aerosol formation.

Chapter 7 summarises the main results of this study and discusses future perspectives.

Chapter 1

Arctic climate change, meteorology and air pollution

The Arctic is sensitive to on-going climate change *(IPCC, 2013)* and is warming faster than any other region on Earth, with severe effects on local ecosystems and the environment *(IPCC, 2021)*. For example, Arctic warming is leading to a decline in summer sea-ice fraction, and less and thinner sea-ice is forming during wintertime *(Stroeve et al., 2012b)*. This will impact local air pollution during summertime, for example an increase in ship cruises *(Marelle et al., 2018)* or during wintertime when new sources of SSA may contribute more to the total aerosol burden in the Arctic.

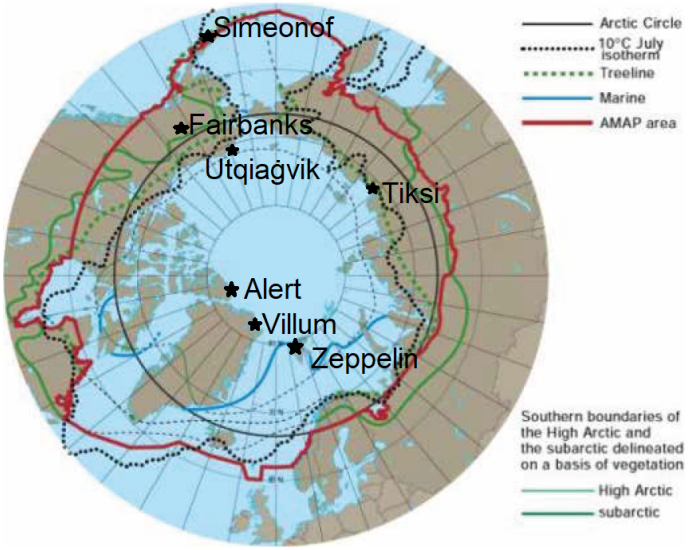

Figure 1.1: *Arctic Boundaries. Source: Arctic Monitoring and Assessment Programme Monitoring et al. (1998). This map shows also the main measurement sites used in this thesis.*

The Arctic region can be defined as the region in the northern part of the Northern

Hemisphere, in which there is at least one day without daylight in the winter and one nightless night in the summer. However, due to political, vegetation and permafrost boundaries, and important oceanographic features, there is no uniform definition of the Arctic. **Figure 1.1** shows the different boundaries of the Arctic region. For example, the Arctic Council Arctic Monitoring and Assessment Programme (AMAP), for it is scientific purposes, defines the Arctic region as the land and sea areas north of the Arctic Circle (66°32'N), north of 62°N in Asia and 60°N in North America. The Arctic region is often divided into high, low, and subarctic based on vegetation boundaries *(Linell et al., 1981)*. In this thesis, the Arctic is defined as the region north of 60°N.

This chapter first focuses on the wider Arctic and describes the main features of Arctic climate and weather during wintertime, as well as Arctic air pollution. Then, a detailed analysis is presented for Alaska, the main focus in this thesis.

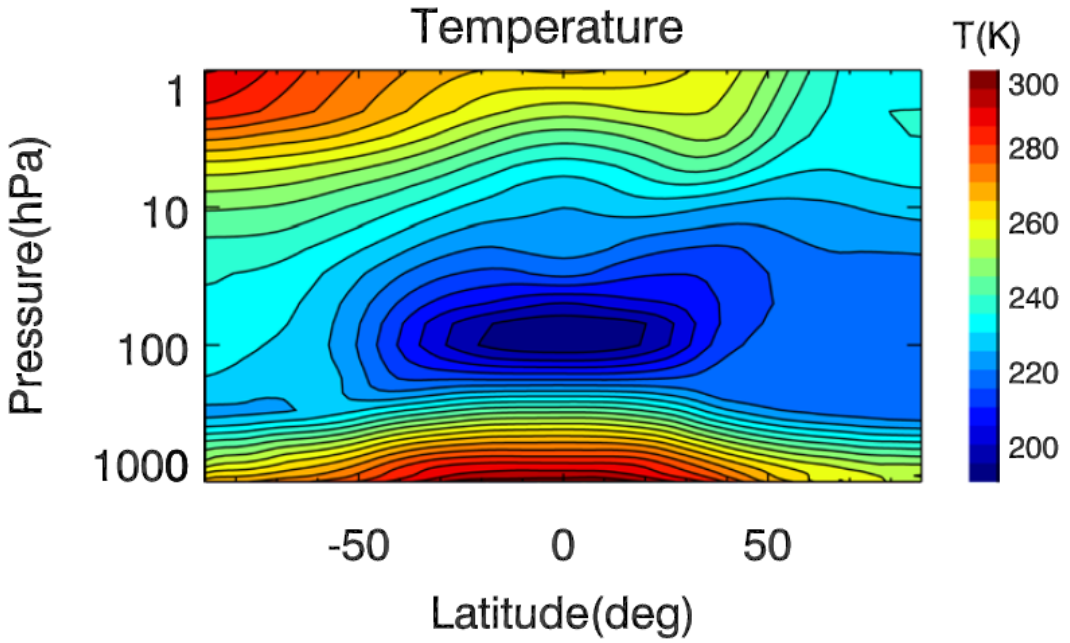

Figure 1.2: *Monthly averaged zonal-mean temperature in January 2013 from the ERA-Interim data. From (Li et al., 2021b).*

1.1 Arctic climate

Low air temperatures characterise the Arctic during wintertime compared to the mid-latitudes due to the uneven distribution of solar radiation on Earth. This drives the Arctic climate combined with the ocean and air currents that warm the Arctic. For example, this is illustrated in **Fig. 1.2**. The surface temperature (1000 hPa) in the Arctic is around -33°C,

around 60°C lower than at the Equator. In the lower atmosphere, known as the troposphere (first 10km - between 1000 and 200 hPa) the temperature changes with altitude. To quantify this change the the tropospheric lapse rate Γ is used. Γ is defined as $-dT/dz$, where T is temperature and z altitude and shows the temperature difference for a specific atmospheric layer and is given usually in K/km. *Akperov et al. (2018)*, using ERA-Interim reanalysis data, showed that Γ decreases from 5.3 K/km in sub-polar latitudes to 4.7 K/km near the pole during winter. The lapse rate is 6.5 K/km near to the Equator. The top boundary of the troposphere is called the tropopause. The tropopause height decreases in the area of the subtropical and polar front jets *(Hirschberg and Fritsch, 1991)*. The tropopause height is lowest at the poles (7–10 km above the Earth's surface), while its highest (around 17–18 km) near the Equator (e.g. *Brasseur and Jacob (2017)*).

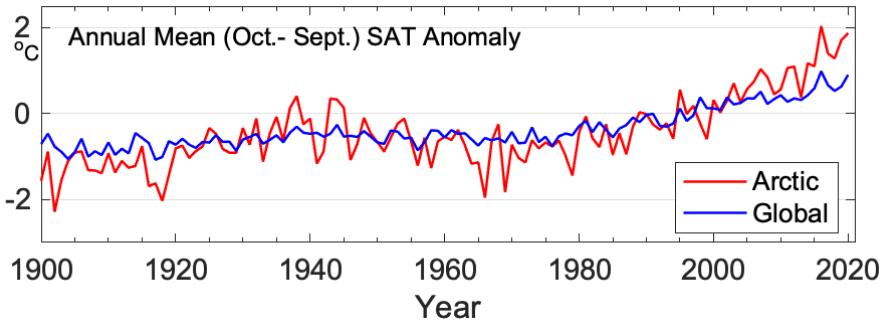

Figure 1.3: *Mean annual surface air temperatures (SAT) anomalies (in degrees C [°C]) for terrestrial weather stations located in the Arctic (60-90°N, red line) and globally (blue line) for the 1900–2020 period, relative to the 1981-2010 means. From Ballinger et al. (2020).*

1.1.1 Arctic amplification

Foote (1856) was the first to report that an increase in CO_2 will lead to an increase in air temperature; the first scientific evidence that CO_2 is responsible for global warming. *Arrhenius (1896)* also suggested that changes in the concentration of CO_2 in Earth's atmosphere could alter surface temperatures, with these changes being especially large at high latitudes. Temperatures have increased 2-3 times as fast in the Arctic compared to the rest of the world, especially since 2000, as shown in **Fig. 1.3**, a phenomenon known as "Arctic amplification" *(Ballinger et al., 2020)*. According to the summary for policy-makers AMAP report on Arctic climate change, observations show that the average increase in Arctic surface temperature between 1979 and 2019 was 3 times higher than the global average during the same period *(AMAP, 2021)*. Rapid Arctic warming is more intense during autumn and winter months *(Boisvert and Stroeve, 2015)*.

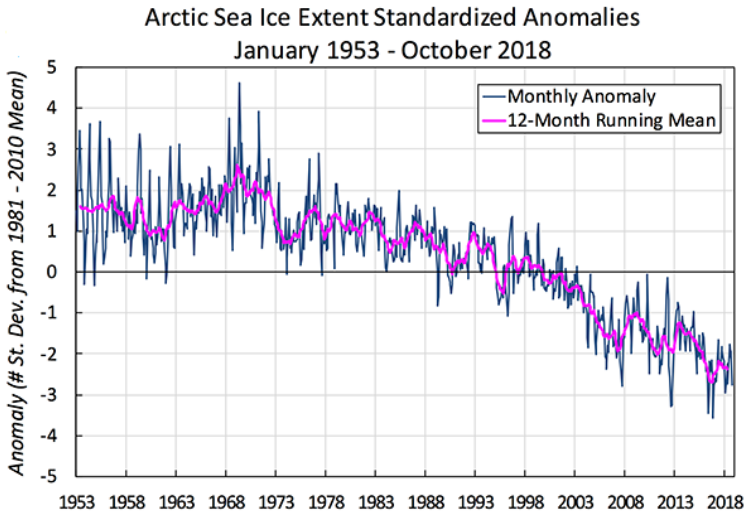

Figure 1.4: *Mean sea ice anomalies, 1953-2018. Image by Walt Meier and Julienne Stroeve: National Snow and Ice Data Center, University of Colorado, Boulder, State of the Cryosphere.* https://www.e-education.psu.edu/earth103/node/999

Arctic amplification was predicted using early climate model simulations *(Kellogg, 1975; Manabe et al., 1990)*, and more recent modelling studies *(Barnes and Polvani, 2015)* or analysis of observations *(Serreze and Francis, 2006; Cohen et al., 2014)* confirm that the Arctic is experiencing an enhanced warming. Arctic sea ice decrease has accelerated over the last years, and most models predict that the Arctic could become an ice-free region by mid-century *(Notz, 2015)*. From 2011 to 2020, the annual average Arctic sea ice area reached its lowest level since 1850 *(IPCC, 2021)*. **Figure 1.4** shows the Arctic sea ice extent anomalies, with a decrease in summertime sea ice extent since the beginning of 2000. Winter Arctic ice extent has decreased by about 3% per decade relative to the 1981-2010 average *(Cavalieri and Parkinson, 2012)*. The sea ice loss in the Arctic creates a feedback loop that accelerates global warming *(Hinzman et al., 2013)*. Ice reflects short-wave radiation back to space because it is highly reflective. As sea-ice is melting, less solar radiation is reflected, and as a result, the absorption of solar radiation by the darker ocean increases, the so-called ice-albedo feedback *(Hall, 2004; Kashiwase et al., 2017)*. Arctic amplification is stronger during autumn and winter, as the newly created open water areas generates warmer air masses over the Arctic ocean and the atmosphere also responds to warmer ocean currents (bringing heat from mid-latitudes) *(Screen and Simmonds, 2010; Cohen et al., 2014)*.

Sea-ice loss appears to be the dominant driver of Arctic amplification, but other factors also contribute to the Arctic's energy imbalance *(Stroeve and Notz, 2018)*. Global warming is caused by GHGs, notably CO_2, and warming aerosols, such as BC *(Samset et al., 2013; AMAP, 2015; Notz and Stroeve, 2016; Stjern et al., 2019)*. This is partly offset by cooling

aerosols such as SO_4^{2-} and OA. Arctic warming is due to effects of GHGs and warming aerosols in the Arctic and due to heat transport from lower latitudes. *AMAP (2015)* estimated that about half of surface temperature warming is due to Arctic effects and half is due to warming at lower latitudes followed by heat transport. Transport of heat by the oceans is also important *(Polyakov et al., 2005)*. SLCFs, such as O_3, maybe responsible for increase in air temperature by +0.12°C (AMAP, 2015). BC radiative warming within the Arctic could increase surface temperatures by +0.4°C due to BC in the air. BC on snow reduces albedo and causes extra warming, increasing in temperatures by +0.22°C (AMAP, 2015). In contrast OA and SO_4^{2-} strong radiative cooling effect maybe contributing to a decrease in Arctic air temperatures by 0.04 and 0.23°C, respectively *(AMAP, 2015)*. A recent study by *Ren et al. (2020)* estimated that 20% of the observed Arctic warming since the early 1980s is due to combined effects of BC and SO_4^{2-}. In the recent years, SO_4^{2-} might cause less cooling, due to SO_2 reductions *(Szopa et al., 2021)*. Atmospheric water vapour and cloud cover are also contributing to Arctic's energy imbalance *(Serreze et al., 2012; Jun et al., 2016)*. Cloud cover traps longwave radiation and warm the surface, but also has a cooling effect reflecting incoming solar radiation. Cloud cover in the Arctic is extensive during summer and shows a minimum during winter *(Curry et al., 1988, 1996)*. Winter clouds contain mostly ice and as result are emissive compared to summer liquid containing clouds. However, mixed-phase clouds have the same micro-physical characteristics throughout the year *(Morrison et al., 2012)*. Uncertainties are still remain to what extent Arctic cloud cover is changing due to big differences in in-situ and satellite measurements *(Chan and Comiso, 2013; Kay et al., 2016)*.

1.2 Wintertime Arctic meteorology

This section describes the location of low and high pressure systems during winter and the position of Arctic Front. This theoretical background is discussed in order to discuss the transport pathways of pollutants into the Arctic. Also, a first discussion is included on temperature inversions during wintertime focusing on the wider Arctic, with a more detailed description over Alaska in section 1.3.

1.2.1 Arctic wintertime circulation

The presence and location of low and high-pressure areas, linked to the position of the jet stream, affect the regional and local climate and weather in the Arctic. Jet streams, are regions of strong winds that blow from west to east in the upper troposphere (7 to 15 km). There are two types of jet streams: (i) the subtropical jet which forms at the poleward edge

of the Hadley cell (circulation) and (ii) the polar jet embedded in the upper troposphere polar front, located above the polar front zone *(Bluestein, 1992; Holton, 2016)*. More specifically, these two types of jet-streams form where air masses of different temperatures converge. Larger differences in the temperature leads to stronger winds. Jet streams influence surface winds and associated with high and low pressure systems.

During winter, the lower tropospheric circulation of the northern polar region is dominated by high pressure over the continents and low-pressure systems over the northern Pacific and Atlantic Oceans. There is a low-pressure system over the North Atlantic Ocean around southern Greenland and Iceland, namely the Icelandic Low, and its influence extends to the North Pole. Also, there is a low-pressure system over the Pacific Ocean, south of the Aleutians, the Aleutian Low, which is effectively blocked by the mountains of Alaska and northeast Siberia (**Fig. 1.5**) *(Serreze and Francis, 2006; Ives and Barry, 2019)*. The Aleutian and Icelandic Lows are climatological features reflecting the high frequency of lows in these areas. These Lows are separated by areas of high pressure composed of the intense Siberian High and the weaker Beaufort High.

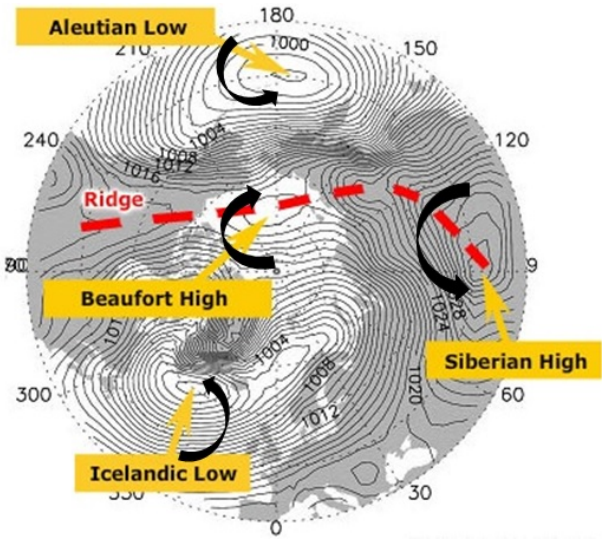

Figure 1.5: *Field of mean sea level pressure (hPa) over the period 1958-2005 for January, based on National Center for Environmental Prediction (NCEP)/ National Center for Atmospheric Research (NCAR). From Serreze and Barrett (2008). The arrows indicate the surface.*

The prevailing winds in the lower troposphere between Iceland and Scandinavia are westerly or south-westerly, transporting warm and humid air from lower latitudes toward the Arctic. Farther north, around the North Pole, the circulation is generally anticyclonic with prevailing winds from the east and northeast. Strong winds are most frequent in the Atlantic sector of the Arctic, where they follow a path from Iceland to the Barents Sea in the winter. In January, anticyclones are more frequent and stronger over Siberia and

Alaska/Yukon, with a weaker system over the central Arctic Basin and Greenland. Anticyclones are characterized by relatively low wind speeds and thus stagnant conditions. The Siberian High is an intense, shallow, cold anticyclone that forms in response to radiative cooling over eastern Siberia in winter. It is associated with frequent cold air outbreaks over East Asia *(Hordon, 2005)*. Near the surface, the relative lack of cloud cover and low incoming solar radiation during the Arctic winter can produce extended periods with surface inversions due to strong radiative cooling. These factors reduce the effectiveness of vertical mixing, and can result in the accumulation of pollution in the lower Arctic atmosphere *(Barrie, 1992; Iversen, 1996)*.

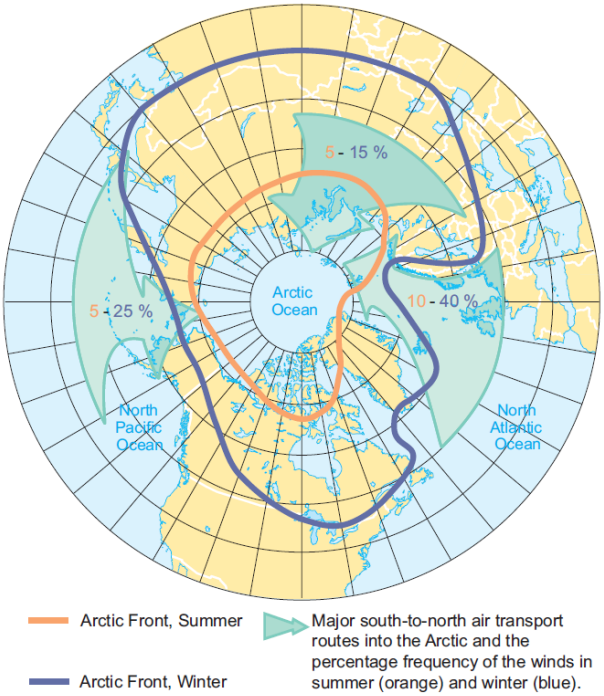

Figure 1.6: *Position of the Arctic front in winter (blue line) and summer (yellow line) (Li et al., 1993). Superimposed on the percentage frequency of major transport routes (Iversen, 1996).*

Air masses from mid-latitudes usually rise along surfaces of constant potential temperature (isentropic transport) forming the so-called polar "dome", which isolates the lower Arctic troposphere from the mid-latitudes and synoptic systems can lead to a shift of the polar dome boundary *(Stohl, 2006)*. The southern boundary of cold Arctic air masses, the Arctic front, is located much further south during winter (down to 40°N) than in summer, especially over Eurasia (*Barrie (1986)*, **Figure 1.6**). This allows emissions from high-latitude Eurasia to enter the Arctic (see discussion in the following section). The polar front, is the frontal zone separating warm mid-latitude and sub-tropical air masses from colder polar air masses. It is in general located further south compared to the Arctic front and displaced

towards the equator in summer and the poles in winter. The polar jet flow is stronger when it is located above the polar front, where there is a large difference in temperature between the equator and poles. The size of this temperature gradient influences the velocity of the jet stream, so it is also strongest in winter, when temperatures differences are larger. During winter removal processes are lower in Eurasia and in the Arctic due to strong atmospheric stability and reduced precipitation *(Garrett et al., 2011)*. On the contrary, removal processes are higher during summer, transport from Eurasia is much weaker as the Siberian high disappears, isolating the Arctic atmosphere from pollution in the mid-latitudes. The main transport pathways, which vary seasonally (**Figure 1.6**) are illustrated in **Figure 1.7** and discussed in the following section.

1.2.2 Wintertime temperature inversions

Surface-based inversions (SBIs) are a frequent feature of the atmospheric boundary layer in the Arctic during winter, where atmospheric temperature increases with the height above the surface *(Brooks, 1931)* (**Fig. 1.2**). *Wexler (1936)* was the first to point out the physical control behind the formation of Arctic inversions. There are different inversion types: radiation and elevated inversion due to advection or subsidence *(Busch et al., 1982)*.

Busch et al. (1982) and *Bradley et al. (1992)* showed that two locally-driven mechanisms dominate the formation of low-level and surface-based inversions. They may form due to radiation imbalance between outgoing (surface) longwave radiation, down-welling solar (low or zero during polar winter) and infrared radiation, and surface cooling or due to warm air advection over a cooler surface layer, depending on the synoptic situation *(Bradley et al., 1992)*. However, other processes such as turbulent mixing and surface fluxes of heat and moisture *(Curry, 1983; Serreze et al., 1992)* also affect SBIs. For example, turbulence near to the surface can destroy SBIs *(Bradley et al., 1992)*. In return, strong SBIs may influence vertical mixing of pollutants and moisture, cloud formation, surface destruction of ozone and sea-ice variability *(Andreas, 1980; Barrie et al., 1988; Mernild and Liston, 2010; Pavelsky et al., 2011)*.

Also, depending on the synoptic condition, the large-scale synoptic flow above the SBI may lead to the development of elevated inversions (EIs) *(Mayfield and Fochesatto, 2013)*. Mechanisms that affect EIs are either warm-air-advection flows or anticyclonic or subsidence inversion *(Csanady, 1974; Busch et al., 1982; Mayfield and Fochesatto, 2013)*. Inversions tend to be surface-based in winter and elevated in summer *(Kahl et al., 1992)*. SBIs mainly occur during winter and polar night (40%) than during the polar day (20%) *(Seidel et al., 2010)* and they are deeper and more intense in winter and autumn (polar night) than

spring and summer (polar day) *(Zhang et al., 2011)*. Detailed studies based on radiosondes show that in the Arctic, SBI frequency, depth, intensity, and temperature difference across the inversion layer increase from the Norwegian Sea eastward toward the East Siberian Sea probably due to gradients in turbulent mixing, cyclonic activity and cloud cover influencing down-welling longwave flux *(Serreze et al., 1992; Zhang et al., 2011)*. Strong inversions occur in Eastern Siberia also due to the influence of local topography *(Serreze et al., 1992)*.

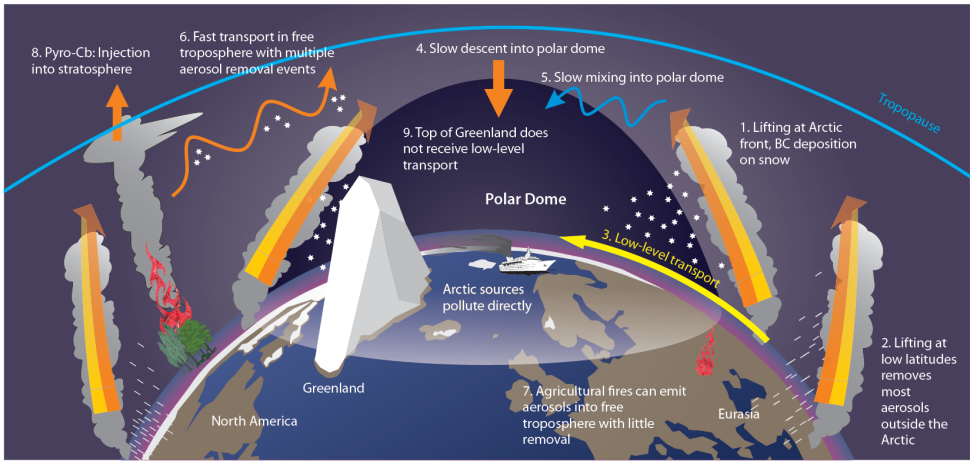

Figure 1.7: *Schematic illustration of transport pathways of pollutants into the Arctic based on the study by Stohl (2006). From (Quinn et al., 2011).*

1.3 Wintertime Arctic air pollution

Emissions of anthropogenic and natural origin from high-latitudes enter the Arctic via the low-level transport route in winter (pathway 3, **Figure 1.7**). The enhanced concentrations of air pollutants in the Arctic winter (Arctic Haze) is discussed in section 1.3.1. The northward movement of the Arctic front is one of the reasons why aerosol concentrations in the Arctic are much lower in summer than winter *(Stohl, 2006)*. Pollution emitted south of the Arctic front can reach the Arctic following the isentropic surfaces, upwards into the Arctic middle or upper troposphere (pathway 1 and 2, **Figure 1.7**) *(Carlson, 1981; Iversen, 1984; Barrie, 1986)*. Air masses can also penetrate the polar dome by slow descent from above (several weeks, pathway 4 – **Figure 1.7**) and via mixing into the polar dome (pathway 5, **Figure 1.7**). Agricultural and wildfire plumes (pathway 7 and 8, **Figure 1.7**) from various mid-latitude source regions can reach the Arctic region *(Stohl, 2006; Warneke et al., 2009; Brock et al., 2011)*, later in the spring and summer months.

During winter and spring, Eurasian (Europe and Russia) pollution is transported to the Arctic at low altitudes (low level transport) *(Rahn, 1981)*. Pollution from Asia and North

America is transported at higher altitudes (frontal transport) to the Arctic (more in the mid-troposphere). However, the emissions from mid-latitude sources have been decreasing in the last years (e.g. *Sharma et al. (2019)*). There are also local anthropogenic and natural sources within the Arctic, which are influencing local communities and adding to air pollutants transported from mid-latitudes during wintertime (e.g. *Quinn et al. (2007a)*;*Kirpes et al. (2018)*). Local sources of pollution include oil extraction, flaring, or metal smelting (see **Fig. 1.12**) affecting human health and atmospheric composition at local and regional scales *(Law and Stohl, 2007)*. However, their contribution to local air quality and impacts on climate and ecosystems are poorly quantified *(Hodson et al., 2010; Law et al., 2017; Schmale et al., 2018)*.

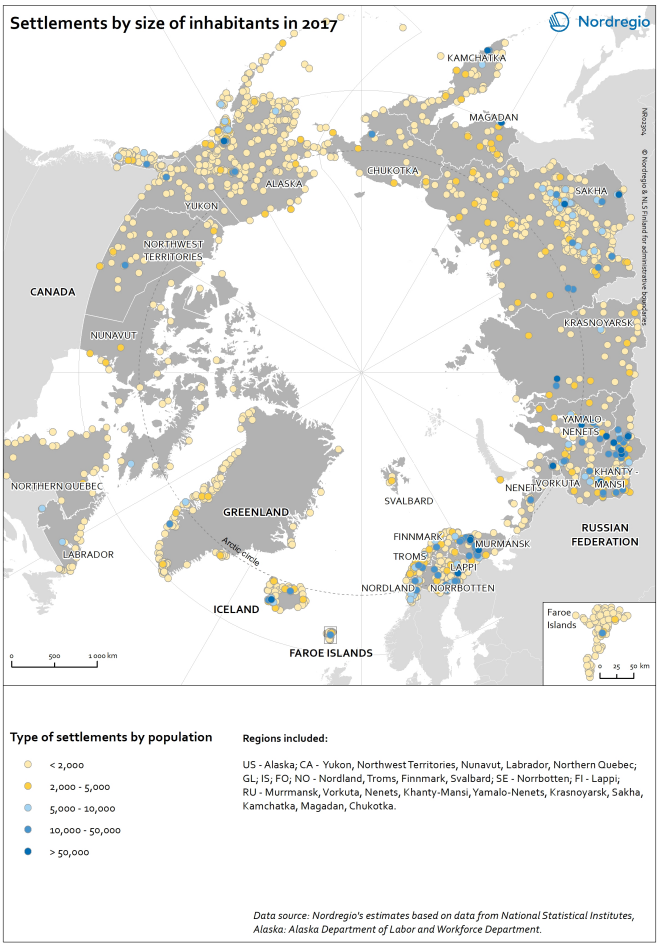

Figure 1.8: *Map showing the type of settlements by population size in the Arctic in 2017. From NORDREGIO (https://nordregio.org/maps/settlements-by-size-in-the-arctic/).*

Figure 1.8 shows the different types of settlements by population size in the Arctic. Most Arctic settlements (90.5%) are less than five thousand inhabitants. Large settlements (bigger than five thousand inhabitants) are scattered in every Arctic nation. There are large cities in, for example Alaska (e.g. Fairbanks) and in Siberia, especially south of Kara sea. These settlements are affected by air pollution, due to enhanced emissions in winter, for example heating, combined with strong wintertime temperature inversions which occur under stable conditions (see sections 1.2 and 1.4).

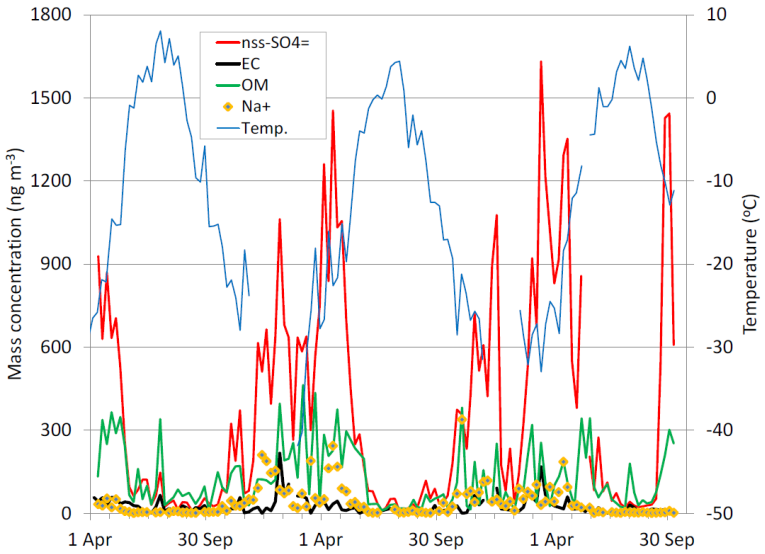

Figure 1.9: *Time series of temperature and weekly-integrated mass concentrations of OM, EC, nss-SO_4^{2-} and Na^+ for the period: 10 April 2012 to 14 October 2014. From Leaitch et al. (2018a).*

1.3.1 Arctic Haze

Greenaway (1950) and *Mitchell (1957)* first noticed that the visibility in the Arctic was not clear during springtime over Alaska. More studies followed, showing that this reduced visibility is due to enhanced air pollutants in the Arctic region, of anthropogenic origin, and observed every winter and spring *(Rahn et al., 1977; Barrie et al., 1981)*. This phenomenon is called Arctic Haze *(Mitchell, 1957)*. Arctic Haze is due to enhanced levels of SO_4^{2-}, NO_3^-, OA, BC *(Quinn et al., 2002a)*, but also CO, and volatile organic compounds (VOCs) *(Solberg et al., 1996)*.

To illustrate this, **Figure 1.9** shows the time-series of non-sea-salt (nss) SO_4^{2-} OM, elemental carbon (EC) and sodium (Na^+) mass concentrations at Alert. Each species shows similar seasonal patterns; increased concentrations of nss-SO_4^{2-} and OM during winter coexist with low temperatures, while nss-SO_4^{2-} and OM are lowest during summer. EC is higher at the end of winter (January–February) and early spring (March), coinciding

with the Arctic Haze period. Na^{+}, sea-spray origin, is higher in February and May, when winds are stronger over the northern oceans and the biological activity is lower *(Lana et al., 2011)*. Previous studies, for other sites and time periods, show maximum concentrations of nss potassium (K^{+}, indicating a combustion source), magnesium (Mg^{+2}) and calcium (Ca^{+2}) (dust) and NO_3^- during winter and spring, indicating also long-range transport to the Arctic *(Quinn et al., 2002a, 2007a; Eckhardt et al., 2015)*.

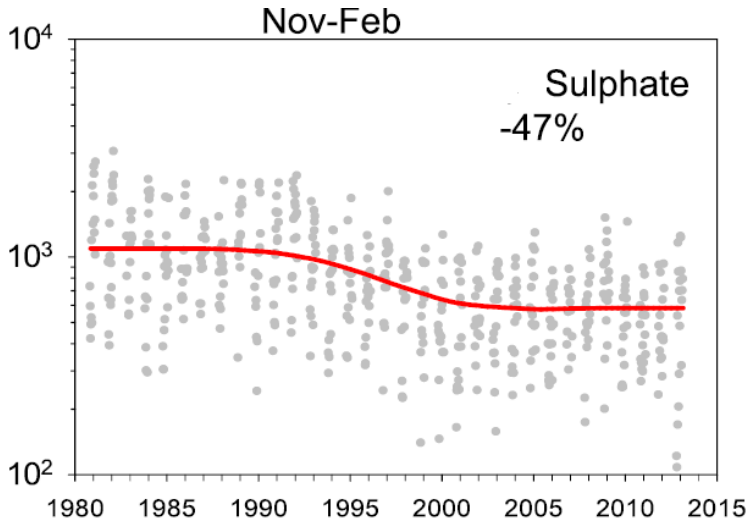

Figure 1.10: *Weekly surface-based atmospheric concentrations (ngm^{-3}) of SO_4^{2-} for the dark mid-winter months (November to February), at Alert, Canada, between 1980 and 2013. In the upper right-hand side, the percentage change between the first 5 years and the last 5 years means is shown. From Sharma et al. (2019).*

Figure 1.10 shows SO_4^{2-} mass concentrations at Alert from a recent study about Arctic aerosol trends by *Sharma et al. (2019)*. There has been a decrease in SO_4^{2-} by 47% since 1980, due to decreasing SO_2 emissions especially in Europe and North America has contributed to enhanced warming, since SO_4^{2-} aerosols cool the atmosphere. *Sharma et al. (2019)* reported that different aerosol components such as NH_4^+ and BC also decreased as emissions declined in northern Eurasia during the early 1990s. On the other hand, NO_3^- increased possibly due to a decline in aerosol acidity. These results generally agree with a more recent study by *Schmale et al. (2022)*, in which trends for BC, NH_4^+, SO_4^{2-}, are calculated for different Arctic sites, showing a decrease, and an increase for NO_3^- during the last decades (1970–2010) and wintertime.

1.3.2 Remote versus local sources of Arctic Haze

One of the main focuses of the scientific community has been to investigate the contribution of remote (outside the Arctic) anthropogenic and natural sources versus sources within

the Arctic Circle, during wintertime and springtime, since the anthropogenic emissions are decreasing over China, India, Europe, and America. In contrast, Arctic sources might increase in the future due to ongoing climate change *(Szopa et al., 2021)*.

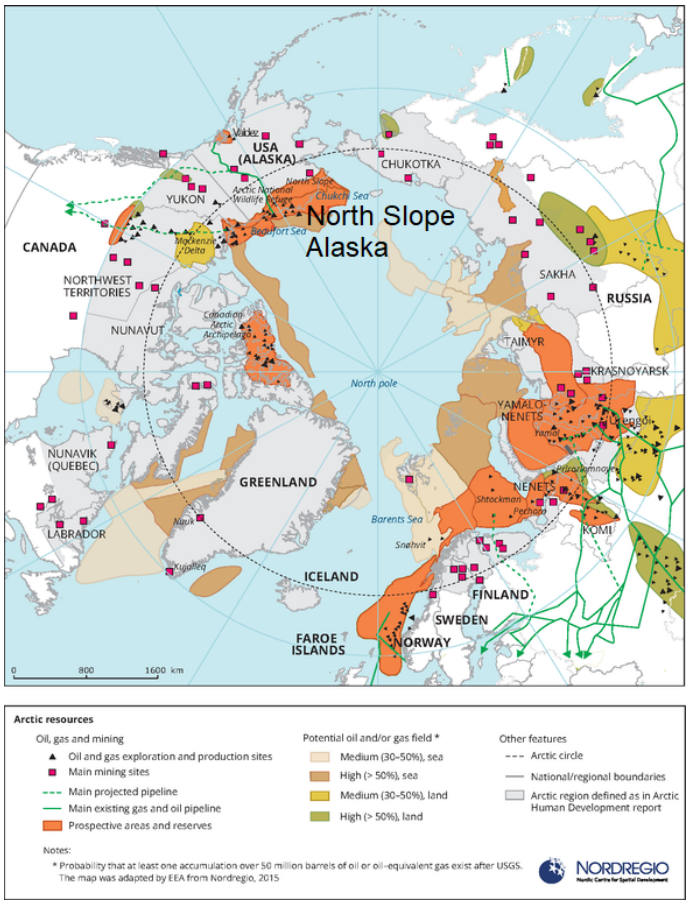

Figure 1.11: *Location of different gas, oil and mining sources in the Arctic. From NORDREGIO (https://www.eea.europa.eu/data-and-maps/figures/arctic-resources).*

Figure 1.11 shows oil, gas and mining sites within the Arctic circle, such as in northern Alaska (e.g. North Alaskan Slope (NSA) oilfields, including Prudhoe Bay), in Siberia (e.g. Nenets and Yamalo-Nenets regions) and in the Canadian Arctic Archipelago. There are also sites in the sub-Arctic region, such as Norway, central Siberia and south of Canada. These sites are located near to Arctic settlements (**Fig. 1.9**), affecting regional air pollution, for example contributing to Arctic BC, SO_4^{2-}, and as result human health (e.g. AMAP (2015);Schmale et al. (2018);Whaley et al. (2022b)). These local Arctic emissions are not well represented in global emission inventories and as result leads to uncertainties in air pollution modelling (investigated in Chapter 5). Local Alaskan sources are discussed in detail in section 1.4.3.

Oil and gas extraction in northern Russia is an important source of BC, with a contri-

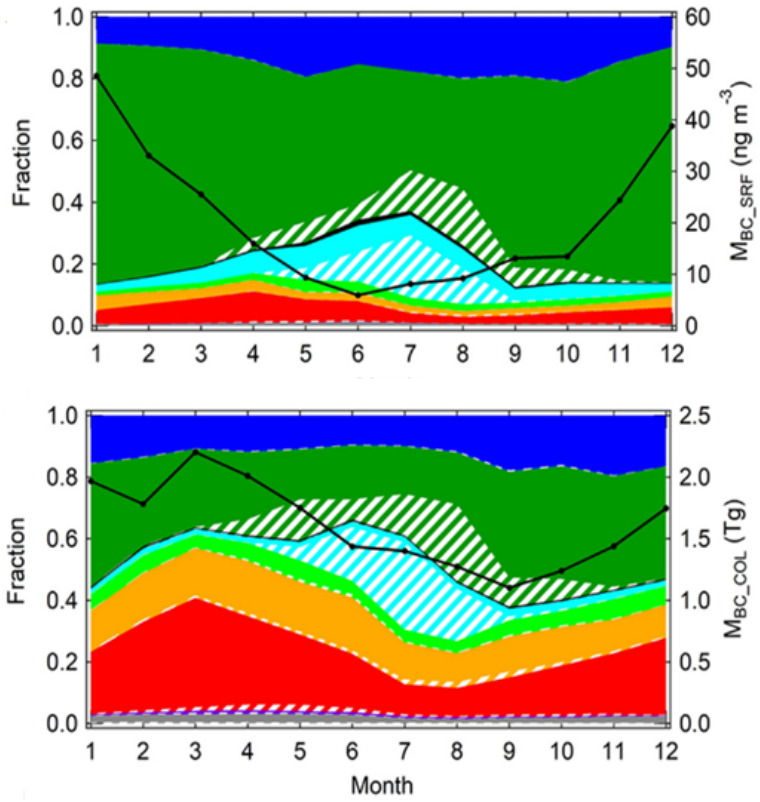

Figure 1.12: *Monthly variations of source contributions to surface BC mass concentration (M_{BC_SRF}) (upper plot) and vertically integrated BC mass concentration (M_{BC_COL}) (lower plot), in the Arctic. The filled and shaded areas indicate anthropogenic and biomass burning sources, respectively. The black lines (right axis) show total BC concentrations from all sources. Europe(blue), Siberia(green), Greenland(black), North America(light blue, north of 50^o N, light green, south of 50^o N), Central Asia(orange), East Asia(red), Southeast Asia(purple), and others(grey). From Matsui et al. (2022).*

bution of up to 66% to the total Arctic BC emissions *(Stohl et al., 2013b, 2015a)*. In contrast, emissions from transportation, domestic heating, power generation combustion (coal, oil, wood), which significantly increase during very cold Arctic winters, contribute to the atmospheric BC concentrations *(Winiger et al., 2017; Sobhani et al., 2018)*. For example, fossil fuel combustion sources are dominant at Utqiaġvik (northern Alaska) between December and February, with the air masses originating from northern Russia, the Arctic Ocean and northwest Canada *(Barrett et al., 2015)*. The contribution of anthropogenic BC from Siberia to Arctic surface BC reaches up to 75% during wintertime (December to February), while the contribution of Asia (East, Central, and Southeast Asia) is less than 15% following a recent study by *Matsui et al. (2022)* (see **Fig. 1.12**). On the other hand, the Asian emissions are contributing more to vertically integrated BC (M_{BC_COL}) during winter and spring, by 54% *(Matsui et al., 2022)*. This is linked to differences in transport pathways, as discussed earlier. Overall, anthropogenic emissions from Russia account for 61% to 76% of total BC in

the Arctic from October to May, based on this analysis. The largest part of these emissions is coming from gas flaring (28%–57%) and secondary from residential burning (13%–25%), based on another study *(Zhu et al., 2020)*.

A modelling study by *Yang et al. (2018)* examined SO_4^{2-} source attribution in the Arctic considering 14 anthropogenic geographical source regions: East Asia, Europe, North America, Russia/Belarus/Ukraine, South Asia, the Middle East, Pacific/Australia/New Zealand, North Africa, Central America, Central Asia, Southern Africa, South America, Southeast Asia, and the rest of the world, including oceans, polar continents and Arctic local emissions. This study showed that the relative contributions to Arctic surface SO_4^{2-} are mainly from within the Arctic. Secondary source regions were Russia/Belarus/Ukraine, followed by central Asia, Europe and East Asia during wintertime. At higher altitudes, this study found that the main source regions contributing to Arctic SO_4^{2-} were East and South Asia, followed by the Arctic itself, Russia/Belarus/Ukraine, volcanic SO_2 and Europe.

During wintertime OA in the Arctic are dominated by anthropogenic emissions mainly from Eurasia *(Moschos et al., 2022a)*. A detailed positive matrix factorization analysis by *Moschos et al. (2022a)* showed that during wintertime the dominant factor influencing OA at Alert (Canada) and Zeppelin (Norway) (up to 46% and 49% respectively) is due to Arctic Haze with a secondary contribution (up to 31% and 36%) from primary-anthropogenic organic aerosol (POA). At other Arctic sites, such as Pallas, Finland, Baranova, Siberia, Utqiaġvik, Alaska, Villum Research Station, Greenland the Arctic Haze factor ranges between 13% and 37%, while the POA factor ranges between 30% and 40%. POA is mainly related to gas flaring and a major source region for POA during wintertime is West Siberia. Other factors contributing to the total OA are oxygenated organic aerosol (OOA), primary biological organic aerosol (PBOA) and biogenic secondary organic aerosol (BSOA). The total OA concentration at the discussed sites ranged between 0.05 and 0.48 μgm^{-3}. Chapter 4 investigates the possible contributions of marine organics to OA in northern Alaska during winter 2014.

Natural sources are also an important component of sub-micron aerosols with diameters (r_d) less than 1.0 µm ($r_d \leq 1.0$) and super-micron aerosols (1.0 µm $< r_d <$ 10.0 µm) in the Arctic including dust and volcanic emissions *(Huang et al., 2015; Stone et al., 2014; Zwaaftink et al., 2016; Dagsson-Waldhauserova et al., 2019)* during winter and spring. A recent study by *Moschos et al. (2022b)* showed that coarse-mode ($r_d \leq 10.0$) SSA are an important contributor to PM_{10} at remote Arctic coastal sites, such as Alert (56%), Utqiaġvik (66%), Baranova (Russia) (41%), Villum (Greenland) (32%), during wintertime. Chapter 4 examines the contribution of modelled and observed SSA to wintertime Arctic aerosol composition, including marinɛ organics.

1.4 Alaska

This thesis focuses on northern and central Alaska. Detailed observations and field campaigns have taken place recently in Alaska, which can help to better constrain regional models and understand processes influencing wintertime aerosols *(Kirpes et al., 2018; Simpson et al., 2019)*. Alaskan sites can represent the wider Arctic, such as Siberia where field campaign and continuous monitoring sites are less available. This section discusses briefly Alaskan warming and focuses on the connection between the large-scale oscillations and synoptic conditions with wintertime Alaskan weather patterns. It builds on the necessary theoretical background to understand wintertime temperature inversions over Alaska, an important feature which affects local air pollution.

1.4.1 Alaska warming

Over the last 60 years, the average air temperature during wintertime has increased by 6°C in Alaska *(Agency, 2016)*. A recent study by *Sulikowska et al. (2019)* showed that minimum and maximum temperatures at Utqiaġvik, Fairbanks, Bethel (southwest of Alaska) and Juneau (southeast of Alaska) increased by up to 6°C between 1950 and 2010, based on observations.

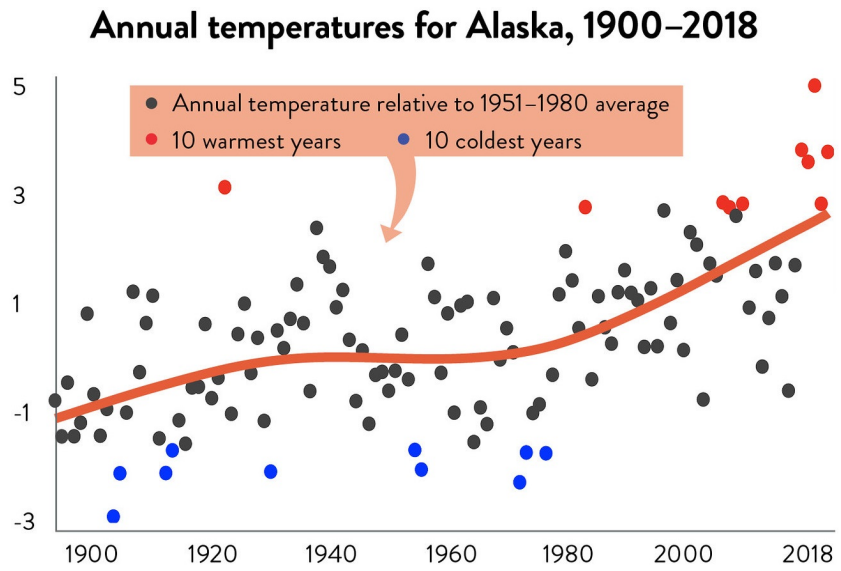

Figure 1.13: *Annual average temperatures for Alaska between 1900 and 2018 relative to 1951–1980 average. From Thoman and Walsh (2019).*

In northern Alaska, the temperature at Utqiaġvik increased by 1.6°C, between 1949 and 1998 *(Stafford et al., 2000)*, in agreement with *Curtis et al. (2003)* showing that Utqiaġvik

warmed by 2°C, between 1990 and 2000. **Figure 1.13** shows that the temperature in Alaska has been rising since 1970, with the ten warmest years reported mostly after 2010. In Fairbanks, a city located in continental Alaska, in the central Tanana Valley, with a sub-Arctic climate, the air temperature increased by 1.4°C, compared to 0.8°C worldwide *(Wendler and Shulski, 2009)*. Around 45% of the observed changes in air temperature have been explained by the increased concentration of CO_2 and also circulation changes such as the Pacific Decadal Oscillation (PDO) (see below). If the temperatures continue to rise, this will lead to severe effects on Alaskan permafrost, ecosystems and local communities *(Chapin et al., 2014)*. *Thoman and Walsh (2019)* also showed that there had been fewer cold days (temperature -35°C) in Alaska in the last years, including interior Alaska locations, such as Fairbanks.

1.4.2 Wintertime meteorology

1.4.2.1 Role of large-scale oscillations on Alaskan wintertime weather patterns

Temperature anomalies over Alaska are influenced by synoptic-scale flow influenced by large-scale climate oscillations *(Papineau, 2001)*. PDO and North Pacific index (NPI) reflect two types of large-scale climate variability that influence the low-frequency variability of lower troposphere inversion parameters in Alaska *(Bourne et al., 2010)* (see next section for details about wintertime temperature inversions). A shift from the negative to positive mode of the PDO, could mean a deepening and eastward movement of the Aleutian Low, establishing a steadier pressure gradient with the semi-permanent Beaufort Sea anticyclone, causing more frequent easterly winds *(Papineau, 2001)*. The PDO is correlated with wintertime Fairbanks inversion depth *(Bourne et al., 2010)*. More specifically, positive PDOs are better correlated with weaker inversions, while negative PDO with stronger inversions. On the other hand, the North Atlantic Oscillation (NAO) and Alaska surface inversion parameters are correlated on decadal and longer time scales. Moreover, synoptic-scale patterns cause warm temperature anomalies in central Alaska. In contrast, cold temperature anomalies result from local conditions, such as radiative cooling at the surface and orographic blocking by the Alaska and Brooks mountain Ranges *(Bourne et al., 2010)*.

1.4.2.2 Wintertime synoptic conditions over Alaska

A study by *Cassano et al. (2016)*, using surface-level pressure from the ERA-Interim, showed that a low-pressure system to the south of Alaska and an eastward extension of the Siberian High is responsible for low wintertime temperatures in southern Alaska. This pattern was

also found in a recent data analysis study by *Maillard et al. (2022)* focusing on Fairbanks in December 2019, during which winds were low and there were clear skies. *Maillard et al. (2022)* also reported that later in December, the surface temperature increased by 15 K due to the presence of several low-pressure systems moving northeast into Alaska, bringing southerly winds and clouds. Similar patterns were also reported by *Cassano et al. (2016)*.

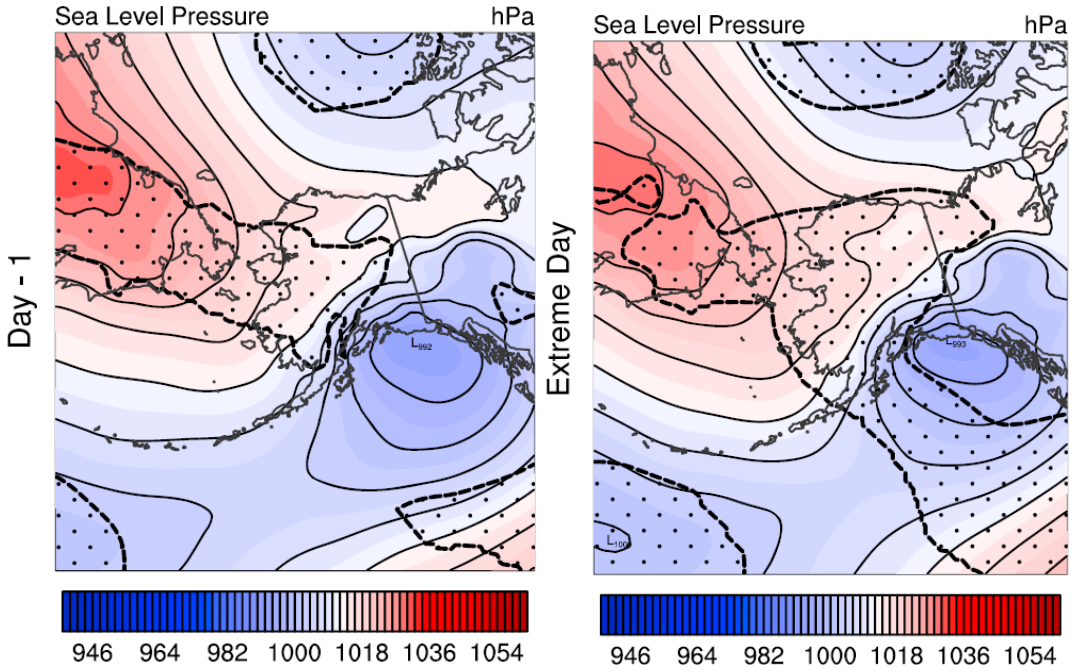

Figure 1.14: *Composite for all widespread cold extreme days. The figure on the left shows the sea level pressure, in hPa, one day before the extreme cold event, while the figure on the right shows the sea level pressure during the extreme day. This example shows the Gulf of Alaska low, in which the center of the low is east of Kenai Peninsula. From Cassano et al. (2016).*

Figure 1.14 shows an example of the Alaskan Λow prior to and during an extreme cold episode during wintertime over Alaska. Before and during the cold episode, there was a low-pressure system in the Gulf of Alaska and over the northern Beaufort Sea and a high-pressure system over eastern Siberia, extending across northern Alaska. The surface winds over Alaska weaken over time, allowing strong surface-based inversions to develop towards the coldest day. During winter synoptic activity in the Alaskan Arctic basin is dominated by anticyclones (Beaufort High) *(Kahl, 1990)*. The skies are typically clear, with low precipitation and increased stability slowing dispersion of air pollutants (stagnate episodes) (e.g. *Thishan Dharshana et al. (2010)*). The influence of synoptic-scale meteorology is investigated further in Chapter 6.

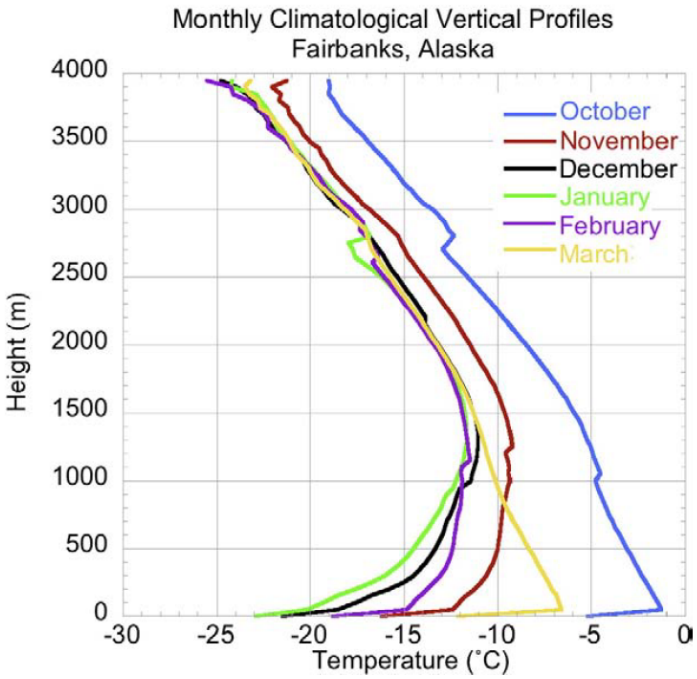

Figure 1.15: *Monthly average (1957–2008) vertical temperature profiles in °C for Fairbanks, Alaska from October to March. From Bourne et al. (2010).*

1.4.2.3 Wintertime Alaskan temperature inversions

Inversions are mostly surface-based along the Alaskan Arctic coast, e.g. at Utqiaġvik and are more frequent during winter *(Busch et al., 1982; Zhang et al., 2011)*. However, even during winter months, EIs can occur above the surface as discussed earlier *(Kahl, 1990)*. Along the Alaskan Arctic coast the inversion depth follows the annual cycle of clear-sky percentages, showing that the development and maintenance of an inversion is the result of complex interactions between radiative forcing, synoptic activity and sea-ice dynamics *(Kahl, 1990; Zhang et al., 2011)*.

Detailed analysis of SBIs have been performed in the Fairbanks area *(Wendler and Nicpon, 1975; Bourne et al., 2010; Zhang et al., 2011)*. Wintertime (December) inversions, which develop in Fairbanks, are the strongest, with a temperature difference of 20°C in the lowest 200 m (Wexler, 1941; Ohtake, 1967; Wendler, 1969). More specifically, strong inversions have been observed between October and March in Fairbanks (**Fig. 1.15**). During the cooler months (November to February, **Fig. 1.15**), inversions have a more complicated structure, with shallow SBIs and a deeper elevated inversion aloft *(Bourne et al., 2010; Zhang et al., 2011)*. When the surface air temperature is cold (warm), the inversion depths are deep (shallow), and inversion temperature differences are large (small). Throughout wintertime (Dec-Feb), SBIs are very common in Fairbanks, Alaska, occurring 77% of the time, while

23% are elevated *(Hartmann and Wendler, 2005)*. The strength of the inversions increases with negative net radiation, decreasing cloud cover and wind speed *(Wendler and Nicpon, 1975; Hartmann and Wendler, 2005)*. Also, during wintertime, northerly winds, up to 1.5 ms^{-1}, are associated with stronger inversions *(Wendler and Nicpon, 1975)*. In general, during wintertime, winds are less than 0.5 ms^{-1} *(Kankanala, 2007)*. During wintertime, these strong inversions trap pollution near the ground and lead to air quality problems *(Benson, 1970; Bowling, 1986; Mölders et al., 2011)*.

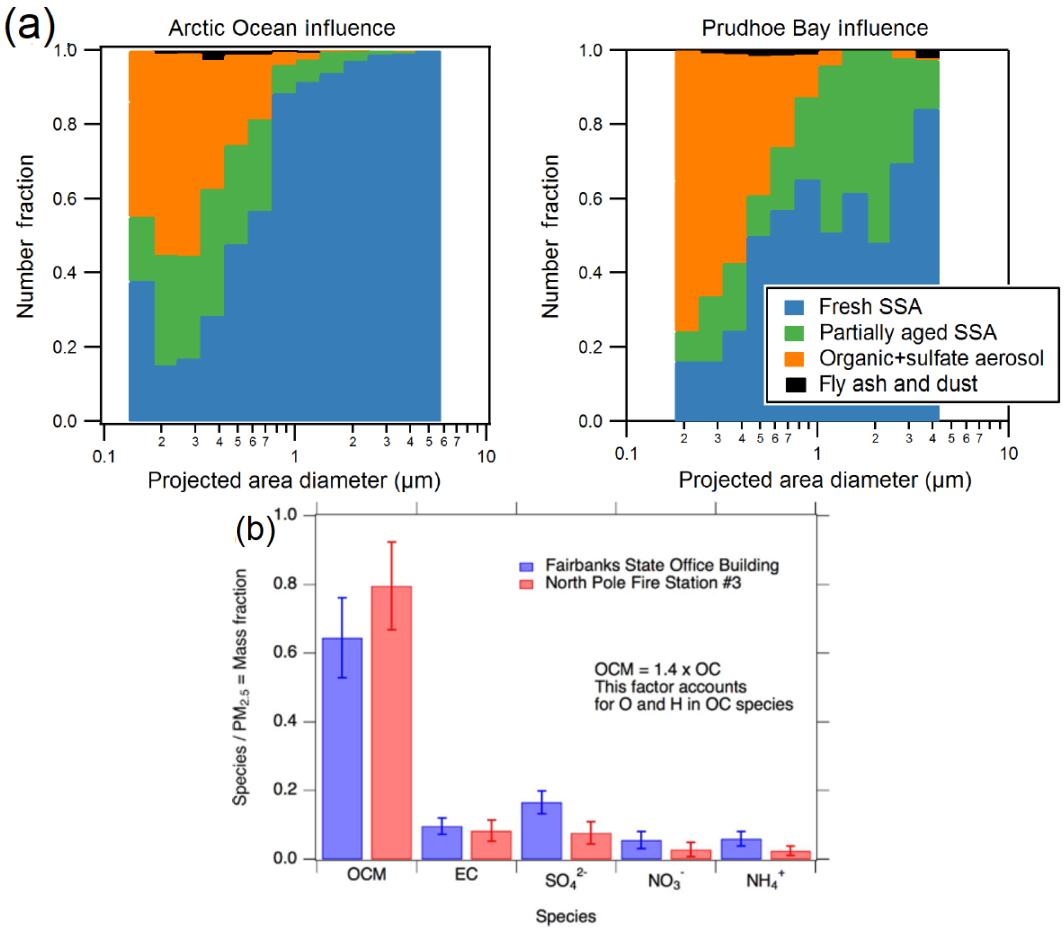

Figure 1.16: *(a) Size-resolved number fractions of observed particulate matter ($PM_{1.0}$), when samples were influenced by the Arctic Ocean (left panel) or Prudhoe Bay (right panel). From Kirpes et al. (2018), (b) Fractional mass composition of $PM_{2.5}$ in Fairbanks and North Pole, Alaska during wintertime. The species shown here are: OCM – organic carbonaceous materials (1.4 x OC), EC, SO_4^{2-}, NO_3^- NH_4^+. Data used for this plot cover three winters, from November 2011 to February 2014. From Simpson et al. (2019)*

1.4.3 Alaskan sources of air pollution

Previous studies showed that oil/gas emissions from Russia industrial source areas from Eurasia and fossil fuel combustion sources (northern Russia, Arctic Ocean and northwest Canada) contribute to BC burden at Utqiaġvik, northern Alaska during winter (October – February) *(Polissar et al., 1999, 2001; Barrett et al., 2015; Winiger et al., 2019)*. Pollution from mid-latitudes, such as that due to combustion affects Utqiaġvik during winter and winter-spring transition *(Quinn et al., 2009)*. However, there are important local sources that maybe affecting air pollution during wintertime over Alaska, such as are oil/gas extraction on the NSA (e.g. at Utqiaġvik, Alaska *Kirpes et al. (2018)*) or combustion sources and power plants at Fairbanks *(Simpson et al., 2019)*.

As an example, **Figure 1.16a** shows the size-resolved number fractions of sub-micron particles sampled at Utqiaġvik during days where air masses were influenced more by the Arctic Ocean (left panel) and by Prudhoe Bay (NSA) (right panel). Aerosol samples were collected during field campaigns in January and February 2014 *(Kirpes et al., 2018)*. SSA were always internally mixed with secondary SO_4^{2-}, or with both SO_4^{2-} and NO_3^-. The samples were influenced by air masses originating from the Arctic Ocean to the north and Prudhoe Bay oilfields to the east. This suggests, aerosols were influenced by Arctic Haze and regional oil fields. **Figure 1.16a** also highlights the significant contribution of SSA to total sub-micron particles (see Chapter 4). An example of a city with a severe wintertime air pollution, under cold/dark conditions, combined with calm winds, is Fairbanks, Alaska (e.g. *Tran and Mölders (2011)*). In Fairbanks, during wintertime, $PM_{2.5}$ concentrations exceed the limit of 35 μgm^{-3} (e.g. *Cesler-Maloney et al. (2022)*), implemented by the United States (US) Environmental Protection Agency (EPA).

Figure 1.16b shows an example of the fractional composition of wintertime $PM_{2.5}$ in Fairbanks and North Pole, a residential community southeast of Fairbanks *(Simpson et al., 2019)*. Organic carbonaceous material (OCM) species are the majority of $PM_{2.5}$ mass fraction, more than 60% and 80%, at the North Pole site and Fairbanks, respectively, due to high domestic heating emissions *(Ward et al., 2012)*. The contribution of inorganic ions (SO_4^{2-}, NO_3^-, NH_4^+) and EC is smaller. SO_4^{2-} in Fairbanks could be due to higher sulphur emissions from combustion for residential and commercial heating *(Ward et al., 2012)*, however there are uncertainties in SO_4^{2-} due to missing sources of SO_2 *(Shakya and Peltier, 2013)*. Between 2013 and 2019, SO_4^{2-} and NO_3^- contributions to $PM_{2.5}$ increased compared to 2005–2012 period, while wood smoke and diesel contributions decreased, probably due to emission control measures *(Ye and Wang, 2020)*. In addition, it is still unclear how secondary aerosols are produced under cold/dark winter conditions in Arctic polluted environments and in Arctic

Haze *(Simpson et al., 2019)*. This is discussed further in Chapter 6.

1.5 Modelling wintertime Arctic air pollution: Uncertainties and limitations

Different climate and regional models can be used to simulate atmospheric transport, meteorological conditions, atmospheric chemistry and aerosol dynamics and deposition losses during transport to and within the Arctic. One of the motivation for this thesis is to evaluate and improve the simulation of Arctic aerosols. However, models have difficulties representing wintertime temperature inversions and aerosols in the Arctic during winter and spring. A detailed analysis by *Mölders and Kramm (2010)* showed that the WRF model had difficulties capturing surface temperature and elevated dew-points inversions during cold episodes. They tested two different combinations of physical packages, and regardless of the combinations, the model was biased compared to the observations in the Fairbanks region. These biases in the meteorology (temperature, relative humidity) can have an impact on chemistry and be partly responsible for model underestimates of air pollutants under cold/dark conditions in the presence of strong temperature inversions *(Mölders et al., 2011)*. Models also underestimate SO_4^{2-} and BC at remote Arctic sites *(Shindell et al., 2008; Lee et al., 2013; Whaley et al., 2022b)*. This can be due to a variety of reasons including wet or dry removal *(Browse et al., 2012; Wang et al., 2013; Whaley et al., 2022b)* or due to underestimation of anthropogenic sources in emissions inventories *(Eckhardt et al., 2015)*. A multi-model inter-comparison study by *AMAP (2015)* showed that models also underestimate CO (a good tracer of anthropogenic emissions) in the Arctic during winter and spring due to emission deficiencies, modelled oxidants and chemical processing. A more recent multi inter-comparison study indicated that a combination of model difficulties could explain the uncertainties of aerosols in the Arctic *(Whaley et al., 2022b)*. Such uncertainties could be due to, for example excessive BC deposition in mid-latitudes, transport or emissions uncertainties (e.g. for SO_4^{2-}), missing reactions (e.g. aqueous phase reactions for SO_4^{2-} in WRF-Chem), problems simulating the boundary layer. **Figure 1.17** shows an example of monthly observed BC at Arctic sites evaluated against different models, including WRF-Chem *(Whaley et al., 2022b)*. During wintertime, most models still underestimate BC at Utqiaġvik or Alert, while mixed patterns occurred at the other sites.

In addition, local anthropogenic sources in the Arctic are poorly quantified *(Schmale et al., 2018)*. Missing sources, formation mechanisms and pathways during wintertime, under dark conditions, are likely contributing to poor model performance during wintertime

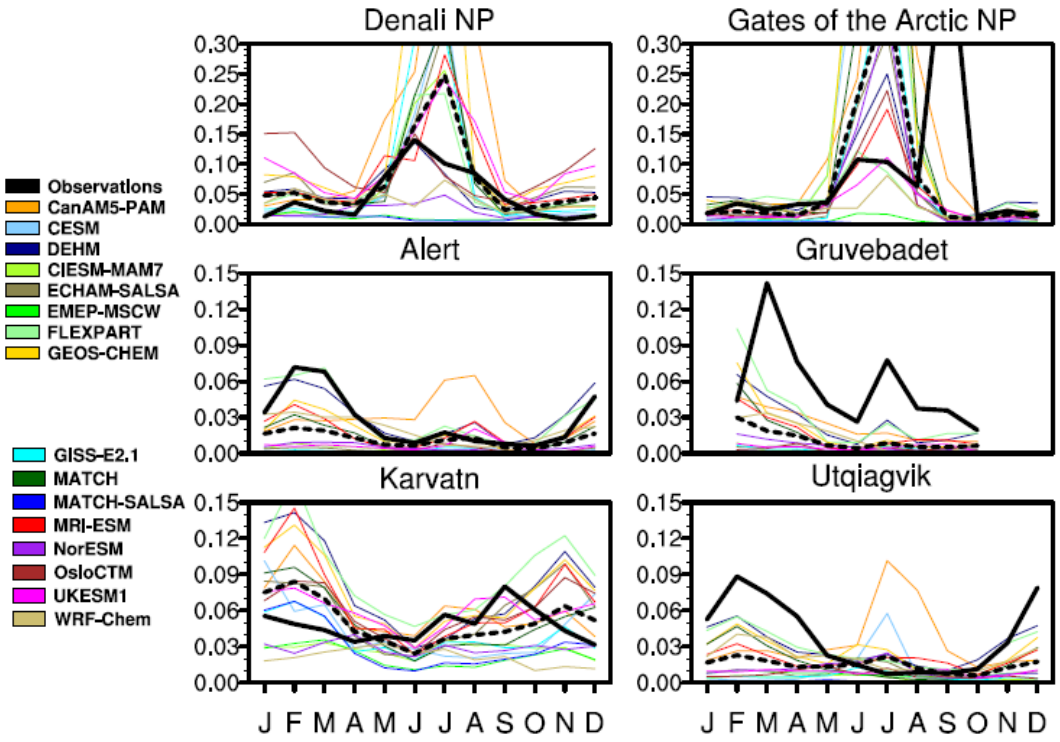

Figure 1.17: *Modelled (thin colored lines) and measured (thick black line) monthly mean BC concentrations (in μg m^{-3}) at surface Arctic measurement sites in 2014–15. The dashed line shows the multi–model mean. From Whaley et al. (2022b).*

(Schmale et al., 2018; Simpson et al., 2019). Chapter 4 focuses on the model missing natural sources, in particular marine organics and the formation and physical processes influencing SSA in the Arctic and northern Alaska. Chapter 5 addresses the model uncertainties linked to removal treatments, representation of boundary layer dynamics and regional sources on BC in the Arctic and northern Alaska. Chapter 6 also examines the role of wintertime meteorological conditions and removal treatments on regional air pollution over the Fairbanks area and investigates the extent to which limitations in emission inventories can explain discrepancies in modelled aerosols and precursor gases.

Chapter 2

Tropospheric aerosols in the Arctic

Aerosols are short-lived climate forcers that affect air quality and, as a result, human health. It is critical to identify sources, formation pathways and processes governing aerosols globally, including in the Arctic and during wintertime, and to understand their impacts on climate change. This chapter presents anthropogenic and natural sources of primary and secondary aerosols and their precursors, their formation pathways (Section 2.1), and their properties and physical processes (Section 2.2, 2.3 and 2.4, respectively).

2.1 Aerosol formation and sources

Tropospheric aerosols derive from anthropogenic and natural sources. They are liquid, solid or mixed particles with highly variable chemical composition and size distributions. There are two types of aerosols: (i) primary aerosols, which are emitted directly, and (ii) secondary aerosols, formed by nucleation from precursor gases. Nucleation is the formation of aerosols from precursor gases. The chemical reactions taking part in the formation of secondary aerosols can be classified as homogeneous or heterogeneous. Homogeneous reactions involve reactants in the same phase, and heterogeneous reactions involve reactants in two or more phases. Nucleation processes can be homomolecular (involving a single species) or heteromolecular (involving two or more species). Four types of nucleation processes can be identified: (i) homogeneous–homomolecular, (ii) homogeneous–heteromolecular, (iii) heterogeneous–homomolecular and (iv) heterogeneous–heteromolecular *(Seinfeld and Pandis, 2006)*. New particle formation involves binary (by sulphuric acid-water vapour) or ternary (sulphuric acid-ammonia-water vapour) nucleation. Further details are provided in the following sections.

Aerosol composition can be categorised into the following categories: carbonaceous

Table 2.1: *Emissions of global anthropogenic and natural primary aerosol, secondary aerosol production and their precursor emissions, in Tg year^{-1} (1: Boucher et al. (2013), 2: Granier et al. (2011), 3:Seinfeld and Pandis (2013). 4:Tsigaridis et al. (2006), 5:Delmas et al. (2005), 6: Andreae and Rosenfeld (2008), 7: Liao et al. (2003), 8: Steinfeld (1998), 9: Adams et al. (1999), 10:Spracklen et al. (2011))*

Source	Emissions (Tg year^{-1})
Anthropogenic	
Primary aerosols	
BC	3.6-6.0$^{(1)}$
Primary Organic Matter (POM)	6.3-15.3$^{(1)}$
Aerosol precursors	
SO_2	43.3-77.9$^{(1)}$
NO_x	70$^{(2)}$
NH_3	34.5-49.6$^{(1)}$
Non-methane volatile organic compounds (NMVOCs)	98.2-157.9$^{(1)}$
Secondary aerosols	
Nitrate from NO_x	21.3$^{(3)}$
Sulphate from SO_2	120$^{(5)}$
Ammonium from NH_3	20.2$^{(9)}$
Secondary organic aerosols (SOA) from VOC	100$^{(10)}$
Natural	
Primary aerosols	
Sea-spray	1400-6800$^{(1)}$
Marine POM	2-20$^{(1)}$
Mineral dust	1000-4000$^{(1)}$
Volcanic dust (coarse mode)	30$^{(8)}$
Biogenic POM	15-70$^{(6)}$
Aerosol precursors	
Volcanic SO_2	9.2$^{(4)}$
Volatile organic compounds (VOCs)	265.2$^{(4)}$
Dimethyl sulphide (DMS)	10-40$^{(1)}$
Secondary aerosols	
Sulphate from DMS	12.0$^{(7)}$-18.5$^{(4)}$
Sulphate from volcanic SO_2	21$^{(8)}$
Ammonium from NH_3	13.4$^{(9)}$
Nitrate from NO_x	4$^{(5)}$
SOA from biogenic VOC	20-380$^{(1)}$
Biomass burning organic aerosols	26-70$^{(6)}$

(e.g. BC, OC), and inorganic secondary aerosols, such as SO_4^{2-}, NO_3^-, NH_4^+, SSA (Na^+, chloride (Cl^-)), which are hydrophilic, and other aerosols, including dust, ash. Anthropogenic emissions originate primarily from (a) fuel combustion, (b) industrial processes, (c) non-industrial fugitive sources and (d) on and non-road transportation. **Table 2.1** shows the global anthropogenic and natural emissions of primary and secondary aerosols and their precursors. Secondary aerosols with high emissions anthropogenic origin are SO_4^{2-}, NO_3^- and NH_4^+. Natural emissions are higher than anthropogenic emissions, mainly due to SSA and mineral dust emissions. Other significant natural sources of primary aerosols are biogenic and volcanic emissions. Natural secondary aerosols are composed mostly of sulphates and nitrates formed through condensation of sulphur and nitrogen and may condense onto existing particles or form new particles with sizes smaller than 0.01 µm *(Steinfeld, 1998)*. Details about anthropogenic and natural emissions of each aerosol species and their precursors are discussed in the following sections.

2.1.1 Carbonaceous aerosols

The incomplete combustion of carbon-containing particles leads to the formation of elemental carbon (EC) particles (mostly $r_b \leq 2.5$ µm). EC is defined as a "substance" containing only carbon, and examples of EC are soot, diamond and graphite. BC is mostly made of EC atoms, but it also includes other light-absorbing compounds *(Petzold et al., 2013)*. The terms EC and BC refer to materials with different optical and physical properties *(Petzold et al., 2013)*. The term Equivalent black carbon (EBC) is also used in many studies (e.g. *Sharma et al. (2013)*, *Popovicheva et al. (2022)*). It refers to observations obtained from optical absorption methods in which a specific mass absorption cross-section factor (MAC) is applied to convert absorption coefficient into mass concentration. Primary organic matter (POM), or organic matter (OM) as defined in Chapter 4, is a mixture of many compounds, either emitted directly or produced through atmospheric reactions involving gaseous organic precursors. OC refers to the carbon fraction in numerous organic compounds that contain hydrogen and, usually, oxygen and are emitted to the air as particles *(Bond et al., 2013a)*. To obtain OM mass concentrations, OC is often multiplied by a fraction that depends on the mix of compounds emitted and varies between emission sources. OM to OC fraction for primary emissions varies between 1.3 and 2.1 *(Tissari et al., 2007; Aiken et al., 2008)*.

Secondary Organic Aerosols (SOA) originate in the atmosphere via the mass transfer of low-pressure products. Organic and carbonaceous aerosols are produced by gas to particle (g-to-p) conversion of volatile organic compounds (VOCs). Three major chemical species

families are involved in g-to-p conversion processes and contain sulphur or nitrogen or organic and carbonaceous substances. The organic gases are oxidized in the gas phase by species such as the hydroxyl radical (OH), O_3, and the nitrate radical (NO_3). Currently, global carbonaceous aerosol emissions originate primarily from Asia and Africa, representing about 80% of total global emissions (*IPCC (2021)* and references therein). Important sources of BC are flaring emissions linked to oil and gas extraction, such as in Russia or Alaska *(Stohl et al., 2013b, 2015a; Böttcher et al., 2021)*, surface transportation *(AMAP, 2015)*, domestic heating *(Stohl et al., 2013b; Winiger et al., 2017)*, industry (e.g. mining industry, *Evans et al. (2015)*), shipping emissions *(Marelle et al., 2016)*, biomass burning, liquid fossil fuel and coal combustion *(Winiger et al., 2016)*. The BC lifetime ranges between 4 and 11 days *(Sharma et al., 2013; Samset et al., 2014; Ikeda et al., 2017b; Lund et al., 2018; Liu and Matsui, 2021)*. OC can be emitted directly into the atmosphere from vehicular emissions *(He et al., 2008)*, incomplete or uncontrolled combustion in residential and commercial settings *(Bond et al., 2013a)*, residential, such as woodsmoke sources at Fairbanks, Alaska *(Ward et al., 2012)*, waste, energy and industrial activities *(McDuffie et al., 2020)*, biomass burning *(Xu et al., 2018)*. There are anthropogenic sources of VOCs, such as energy and industrial activities, residential, road transportation, and solvents *(McDuffie et al., 2020)*. Oil production distribution, especially in North America, and transport are the dominant anthropogenic VOC emissions. On the other hand, anthropogenic VOCs emissions in China are due to solvent use and the industrial sector. Half of the anthropogenic VOCs emissions in many European cities are due to wood-burning *(Szopa et al., 2021)*. There are also indications that chemical products (i.e. household chemicals, personal care products, solvents) contribute to anthropogenic VOCs emissions in the US *(McDonald et al., 2018)*. There are also two sub-groups: (i) semi-volatile organic compounds (SVOCs) and (ii) intermediate-volatile organic compounds (IVOCs). SVOCs (e.g. pesticides) are less volatile compared to VOCs *(Quality, 1989)*. There are also anthropogenic emissions of SVOCs, from mobile sources *(Gordon et al., 2013; Zhao et al., 2016)* and aircraft engines *(Cross et al., 2013, 2015)*. IVOCs are important SOA precursors *(Ma et al., 2017; Lu et al., 2020)*. IVOCs are emitted from anthropogenic and biogenic sources, such as mobile emissions *(Lu et al., 2018; Drozd et al., 2018; Qi et al., 2019)*, coal combustion *(Cai et al., 2019)*, biomass burning *(Hatch et al., 2018)* and volatile chemical products *(McDonald et al., 2018)*.

2.1.2 Inorganic aerosols

This section summarises the main formation pathways of inorganic aerosols, including SSA, as well as their precursors and their emissions.

Sulphate aerosols: SO_4^{2-} aerosols are emitted directly or are formed from the gas-phase oxidation of SO_2 by OH radicals to form sulphuric acid (H_2SO_4) which can condense onto pre-existing aerosols. OH can be produced in the atmosphere by photo-chemical reactions involving photolysis of O_3 and water vapour (H_2O) (R1–R5). SO_4^{2-} can also be formed from the heterogeneous aqueous-phase oxidation of SO_2. Under sunlight conditions, aqueous oxidation in-clouds by hydrogen peroxide (H_2O_2) or O_3 is a major pathway for SO_4^{2-} formation from SO_2 (R6-R8) and it is dominated by oxidation by H_2O_2 *(Alexander et al., 2012)*. In the reactions below M is a third body, $O(^1D)$ is the oxygen atom in its single excited state, HSO_3 is hydroxysulphonyl radical, and SO_3 is sulphur trioxide (in the gas phase).

$$O_3 + hv \xrightarrow{\lambda<320nm} O_2 + O(^1D) \tag{R1}$$

$$O(^1D) + H_2O \longrightarrow 2\,OH \tag{R2}$$

$$SO_2(g) + OH + M \longrightarrow HSO_3 + M \tag{R3}$$

$$HSO_3 + O_2 + M \longrightarrow SO_3 + HO_2 \tag{R4}$$

$$SO_3 + H_2O + M \longrightarrow H_2SO_4(g) + M \tag{R5}$$

During wintertime, in the absence of sunlight, SO_4^{2-} could be produced from metal catalysed O_2 oxidation of S(IV) *(McCabe et al., 2006; Alexander et al., 2009)*. S(IV) stands for total dissolved SO_2 ($\equiv SO_2 \cdot H_2O + HSO_3^- + SO_3^{2-}$). S(IV) can also be oxidized in the aqueous-phase by other oxidants including O_3, O_2 catalysed by transition metal ions (Fe(III), which refers to the element iron in its third oxidation state and Mn(II), Manganese(II) oxide) *(Hoffmann et al., 1991)*, NO_2 *(Lee and Thiemens, 2001)*, or peroxynitric acid (HNO_4) *(Dentener et al., 2002)*. Other wintertime oxidation pathways could include in-cloud/fog formation of hydroxy methane sulphonate ($HOCH_2SO_3^-$ or HMS) *(Kok et al., 1986; Kovacs et al., 2005; Moch et al., 2018)*. Wintertime SO_4^{2-} formation is addressed further in Chapter 6.

$$SO_2(g) \longleftrightarrow SO_2 \cdot H_2O \tag{R6}$$

$$SO_2 \cdot H_2O + H2O \longrightarrow HSO_3^- + H^+ \quad \text{(R7)}$$

$$HSO_3^-(aq) + H_2O_2(aq) + H^+ \longrightarrow SO_4^{2-}(aq) + 2\,H^+ + H_2O \quad \text{(R8)}$$

The primary anthropogenic sources of SO_2, the main SO_4^{2-} precursor, are the burning of high-sulphur coals and heating oils in power plants, industrial boilers and metal smelting. Additional smaller sources of SO_2 are released from the burning of fuels with a high sulphur content by locomotives, large ships and non-road equipment. In the Arctic, important anthropogenic sources of SO_2 are in Siberia and linked to copper (e.g. Karabash, Russia, *Kalabin and Moiseenko (2011)*) and nickel (e.g. Ufaleynikel, Norilsk, Kola Peninsula Russia, *Baklanov et al. (2013); Stohl et al. (2013b)*) smelting. Iron refining activities are another source of SO_2 (e.g. iron mine and ore dressing mill in Kostomuksha, Russia, *Fioletov et al. (2016)*). Also, oil refineries are a source of SO_2 emissions (e.g. Alaska - Prudhoe Bay, *Administration (2015)*), Canada, Russia, North of Europe). For example, in 2014, over 80% of anthropogenic SO_2 emissions originated from power plants and industry, with Asian sources contributing more than 50% to the total emissions *(Szopa et al., 2021)*. The global lifetime of SO_4^{2-} is about 5 days *(Langner and Rodhe, 1991)*. The lifetime of SO_4^{2-} formed by gas-phase oxidation is 6.1 days. Estimates of modelled and in-situ observations SO_2 lifetimes differ. Modelled SO_2 lifetime estimated to by 48h and observed 58h, a difference by 10h during wintertime *(Lee et al., 2011)*, while SO_2 lifetime is shorter in summer *(Lee et al., 2011)*.

Nitrate aerosols: NO_3^- is formed in the atmosphere from the main precursor species (i) NH_3 and (ii) nitric acid (HNO_3). HNO_3 during daytime is formed through the gas phase reaction (R9) and can then form NO_3^- aerosols in the aqueous-phase (R10):

$$NO_2 + OH \longrightarrow HNO_3 + M \quad \text{(R9)}$$

$$HNO_3(g) \longrightarrow H^+(aq) + NO_3^-(aq) \quad \text{(R10)}$$

Reactions involving NO_x and O_3 also contribute to NO_3^- aerosols. Tropospheric O_3 is produced from the photo-chemical reactions of anthropogenic and natural precursor emissions of NO_x, CO, CH_4, and other VOCs. The main chemical reaction producing O_3 in the troposphere involves the photolysis of NO_2 (R11,R12). O_3 can also react with NO to produce NO_2. In the reactions below $O(^3P)$ is the oxygen atom in its triplet state.

$$NO_2 + hv \xrightarrow{\lambda<424nm} NO + O(^3P) \quad \text{(R11)}$$

$$O_2 + O(^3P) + M \longrightarrow O_3 + M \quad \text{(R12)}$$

During nighttime HNO_3 can be formed from reactions involving NO_3 radicals and O_3 to form dinitrogen pentoxide (N_2O_5) (R13–R15), followed by heterogeneous hydrolysis, on an aerosol surface to from HNO_3 (R16). N_2O_5 has short lifetime (6 minutes) during night-time and winter in the Arctic *(Apodaca et al., 2008)*. N_2O_5 can also react with Cl^-, to form nitryl chloride ($ClNO_2$) and NO_3^- aerosols (R17):

$$NO + O_3 \longrightarrow NO_2 + O_2 \quad \text{(R13)}$$

$$NO_2 + O_3 \longrightarrow NO_3 + O_2 \quad \text{(R14)}$$

$$NO_2 + NO_3 \rightleftharpoons N_2O_5 \quad \text{(R15)}$$

$$N_2O_5 + H_2O \xrightarrow{\text{surface}} 2\,HNO_3 \quad \text{(R16)}$$

$$N_2O_5 + Cl^- \xrightarrow{\text{surface}} ClNO_2 + NO_3^- \quad \text{(R17)}$$

Previous studies have measured NO_3 and N_2O_5 during night-time *(Ayers and Simpson, 2006; Chang et al., 2011; Riedel et al., 2012; Wagner et al., 2013)*. Dark NO_x oxidation requires O_3, which is typically absent at the surface in urban areas and during night-time, due to the efficient titration of O_3 by NO and the absence of NO_2 photolysis during night-time *(Simpson et al., 2019)*.

NO_x is emitted primarily as NO from combustion-related emissions sources, such as fossil fuel combustion (coal- and gas- power plants) and the operation of motor vehicles. Fuel-burning appliances, like home heaters and gas stoves, produce substantial amounts of NO_x in indoor settings. Important sources of NO_x in the Arctic are oil production *(Peters et al., 2011; Böttcher et al., 2021)*, surface transportation (AMAP, 2015), and power generation *(Roiger et al., 2015)*. Furthermore, nitrate photochemistry in the snow can be a significant source of NO_x at the Arctic surface *(Grannas et al., 2007)*. NO_x has a long lifetime in the Arctic, 29h during daytime and 6.3h during night-time due to lower dry deposition caused by snow and ice and the lack of vegetation *(Kenagy et al., 2018)*. Overall, global emissions of

NO_x have been increasing in the last years, even though in regions such as North America, Europe, Japan and Korea, the emissions from vehicles are reduced *(Szopa et al., 2021)*.

Ammonium nitrate (NH_4NO_3) is formed in areas with high NH_3 emissions and HNO_3 concentrations in the presence of low SO_4^{2-} concentrations. Depending on the ambient relative humidity, NH_4NO_3 may exist as a solid or aqueous solution of NH_4^+ and NO_3^-. NH_4^+ (R18–R19) and NO_3^- (R20) can be formed in the aqueous phase.

$$NH_3(g) \longleftrightarrow NH_3(aq) \tag{R18}$$

$$H_2O(aq) + NH_3(aq) \longrightarrow OH^-(aq) + NH_4^+(aq) \tag{R19}$$

$$HNO_3(g) \longrightarrow H^+(aq) + NO_3^-(aq) \tag{R20}$$

Ammonium bisulfate ($(NH_4)HSO_4$) is formed in areas characterized by low NH_3 to neutralize the available SO_4^{2-}. Thus, the aerosol phase will be acidic.

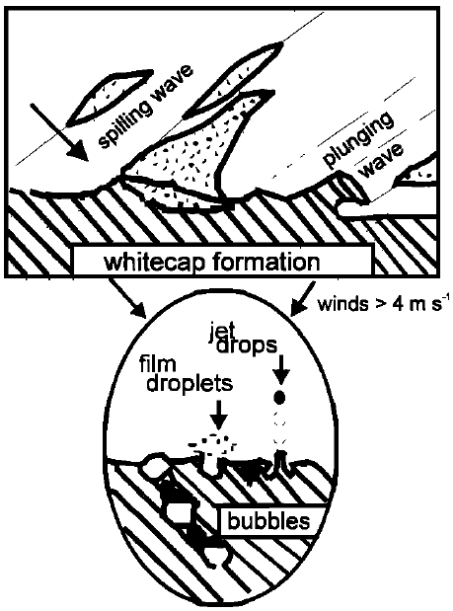

Figure 2.1: *Mechanism for sea-salt aerosol generation by bubbles (indirect production). From Gong et al. (1997).*

There are sources of NH_3 from industrial processes and fossil fuels *(Bouwman et al., 1997)*, waste and commercial and residential fuel combustion *(Roe et al., 2004; McDuffie et al., 2020)*. Other anthropogenic sources of NH_3 include animal livestock, synthetic fertilizers, energy and transport sectors *(Riddick et al., 2012; Behera et al., 2013)*. High NH_3 emissions

also are present within the Arctic and sub-Arctic region, such as in Russia, Canada, Europe, India, China *(Behera et al., 2013; Whaley et al., 2018; Lutsch et al., 2019)*.

Sea-spray aerosols: SSA are produced from the ocean into the air through the bubble bursting (jet-drop and film-drop formations) mechanism during whitecap formation (**Fig. 2.1**) *(Monahan et al., 1986b)*. Whitecaps are generated by wave breaking, but other processes contribute to wave breaking, such as current–wave interactions *(Massel, 2007)*. The production of SSA due to winds is proportional to the whitecap coverage (W). SSA are mainly constituted of Na^+, Cl^-, but other chemical ions can be found such as magnesium (Mg^{2+}), potassium (K^+), calcium (Ca^{2+}), sodium nitrate ($NaNO_3$), sodium sulphate (Na_2SO_4) and silicates. In the Arctic aged SSA is found to be internally mixed with secondary SO_4^{2-}, or with SO_4^{2-} and NO_3^- and reduced Cl^-, due to a background (Arctic Haze) or regional (oil-field emissions) anthropogenic influence as mentioned earlier *(Song and Carmichael, 1999; Kirpes et al., 2019)*. The presence of SSA may favour the formation of coarse NO_3^- aerosol, for example sodium nitrate ($NaNO_3$) (R21) instead of fine NH_4NO_3 or ammonium chloride (NH_4Cl) *(Campbell et al., 2002)*. Other reactions on SSA to form NO_3^- are the heterogeneous R22 and R23 *(Mamane and Gottlieb, 1990; Abbatt and Waschewsky, 1998; Dasgupta et al., 2007)*. SO_4^{2-} can also form on SSA via aqueous phase reactions *(Sievering et al., 1991; Zhuang et al., 1999)* following the uptake and oxidation of sulphur compounds (R.24). SO_4^{2-} formed on SSA has short lifetime, around 0.5-1.7 days *(Alexander et al., 2005)*.

$$NaCl(s) + HNO_3(g) \longrightarrow NaNO_3(s) + HCl(g)\uparrow \quad \text{(R21)}$$

$$2\,NO_2(g) + NaCl(s) \longrightarrow NaNO_3(s) + ClNO(g) \quad \text{(R22)}$$

$$HNO_3(g) + Cl^-(aq) \rightleftharpoons NO_3^-(aq) + HCl(g) \quad \text{(R23)}$$

$$H_2SO_4(aq) + 2\,NaCl(aq,s) \longrightarrow Na_2SO_4(aq,s) + 2\,HCl(g) \quad \text{(R24)}$$

Other sources of SSA are blowing snow and frost flowers *(Shaw et al., 2010; Frey et al., 2020)*. Super-micron SSA lifetime is less than 12h (Williams et al., 2002). Sub-micron SSA in the Arctic originating from the open ocean have a shorter lifetime (3.5 days) than those originating from blowing snow (6.6 days) and frost flowers (7.0 days) *(Huang and Jaeglé, 2017)*. Marine organics can also emitted with SSA *(Hoffman and Duce, 1976; Frossard et al., 2014; Kirpes et al., 2018)*.

2.1.3 Dust

Industrial dust is mainly emitted from (i) vehicles, (ii) cement manufacturing, (iii) coal and fuel combustion in industrial processes, (iv) metallurgy and (v) waste incineration. Industrial activities, such as mining generate local dust emissions in the Arctic *(Groot Zwaaftink et al., 2016)*. Mineral dust originates from desert regions (e.g. Sahara, Africa) and semiarid land surfaces (Gobi Desert). In addition, dry lakes are sources of atmospheric dust *(Prospero, 1999)*. Mineral particles can be internally mixed with SSA components *(Trochkine et al., 2003)* or sulphur and organic matter *(Falkovich et al., 2001; Gao et al., 2007)*. Mineral dust in the Arctic originates from Asia (38%) and Africa (32%) *(Takemura et al., 2009; Zwaaftink et al., 2016)*. However, there are also local sources of dust within the Arctic (Bowen and Vincent, 2021). Arctic sources of dust are mostly from retreating glaciers *(Crusius et al., 2011)*. Lakes in Canada, dunes in Denmark and glaciers in Greenland and Iceland are important sources of dust in the Arctic *(Meinander et al., 2021)*. There are high dust emissions in Siberia, including Apatity and Tiksi, originating from mining, dumps and tailing pits *(Amosov and Baklanov, 2015; Meinander et al., 2021)*. The main Alaskan dust sources are glaciers, re-suspension of ash from past volcanic eruptions and glacial sediments carried by major rivers *(Meinander et al., 2021)*.

2.1.4 Other natural aerosols

Primary biogenic aerosols are released into the atmosphere from plants and animals. They consist of plant debris (leaf fragments), microbial particles (fungi, algae, seeds), marine colloids and humic matter. Their shape and size (0.1 to 250 µm) vary due to different origins. Biogenic aerosol particles are 1% of the total aerosols in remote oceanic regions and around 2-3% in continental areas *(Pósfai et al., 2003; Winiwarter et al., 2009)*. OC also has a natural origin. This includes sources such as plant debris, fungal spore *(Liang et al., 2017; Li et al., 2018b)*.

Biomass burning originates from fires in forests, Savannah grass, and other vegetation types. Emissions from fires include EC, OC, CO_2, CO, NO_x, CH_4, and VOCs. Open biomass burning represent about 30%, 10%, 15% and 40% of present-day global emissions of CO, NO_x, BC, and OC, respectively *(Van Marle et al., 2017; Hoesly et al., 2018)*. Boreal forest fires emit large amounts of VOCs which can produce OA *(Akagi et al., 2011)*.

Volcanoes emit particles and gases into the atmosphere during their eruptions. Volcanoes contribute significantly to the main SO_4^{2-} precursor, SO_2 in the upper troposphere *(Graf et al., 1997; Pattantyus et al., 2018)*. There are active volcanoes in the Arctic, especially in Iceland. Fore example, the Holuhraun volcanic eruption between September

2014 and February 2015 emitted large amounts of SO_2, which quickly spread over Iceland *(Ilyinskaya et al., 2017)*, and affected Greenland *(McCoy and Hartmann, 2015)* and Western Europe (*Boichu et al. (2016)* and references therein). There are also active volcanoes in Alaska. For example, three volcanoes, located in the Aleutians islands, south of Alaska, erupted simultaneously in Alaska in 2021 (source Alaska volcano observatory, https://avo.alaska.edu/), possibly affecting background SO_4^{2-}.

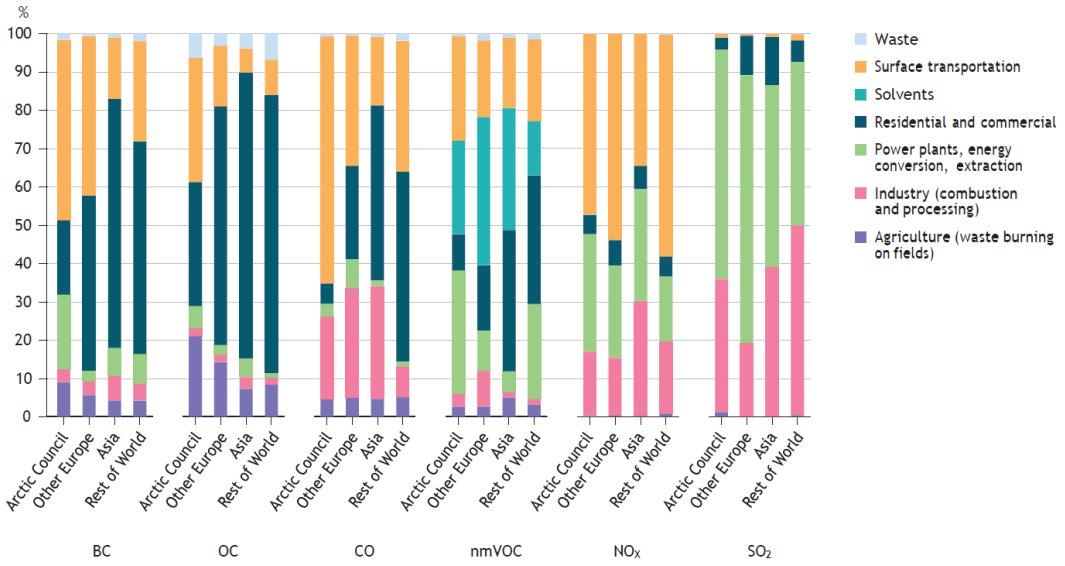

Figure 2.2: *SLCFs emissions by major economic sectors in 2010, derived from ECLIPSE v5. The Arctic Council nations are: Canada, Denmark, Finland, Iceland, Norway, Russia, Sweden, and United States. From AMAP (2015).*

Secondary biogenic aerosols: Organic and carbonaceous aerosols are formed from naturally VOCs. For example, the primary natural sources of carbonaceous aerosols are atmospheric oxidation of biogenic VOCs (BVOCs), such as isoprene *(Claeys et al., 2004)*. A wide range of BVOCs are emitted from vegetation, and the dominant compounds are isoprene and monoterpenes, sesquiterpenes, alkenes, alcohols, aldehydes and ketones. NO_x emitted from soil (biogenic/microbial nitrification and denitrification processes, *Ciais et al. (2014)*) and lightning (around 10% of the total NO_x emissions, *Murray (2016)*), can also lead to the formation of HNO_3 and then NO_3^- aerosols.

Chemical reactions which produce SO_4^{2-} aerosols in the atmosphere involve gaseous precursors (e.g. hydrogen sulphide – H_2S, carbonyl sulphide – COS, carbon disulphide – CS_2). SO_4^{2-} aerosols are formed from SO_2 produced by volcanoes and dimethyl sulphide (DMS), emitted by biogenic sources. DMS is produced from dimethylsulphoniopropionate (DMSP) and is linked to marine algae *(Ishida, 1996; Ackman et al., 1966)*.

Recent studies show that there are natural emissions of NH_3 in the Arctic region, origi-

nating from seabirds *(Riddick et al., 2012; Croft et al., 2016)* and chicken farming *(Jiang et al., 2021)*.

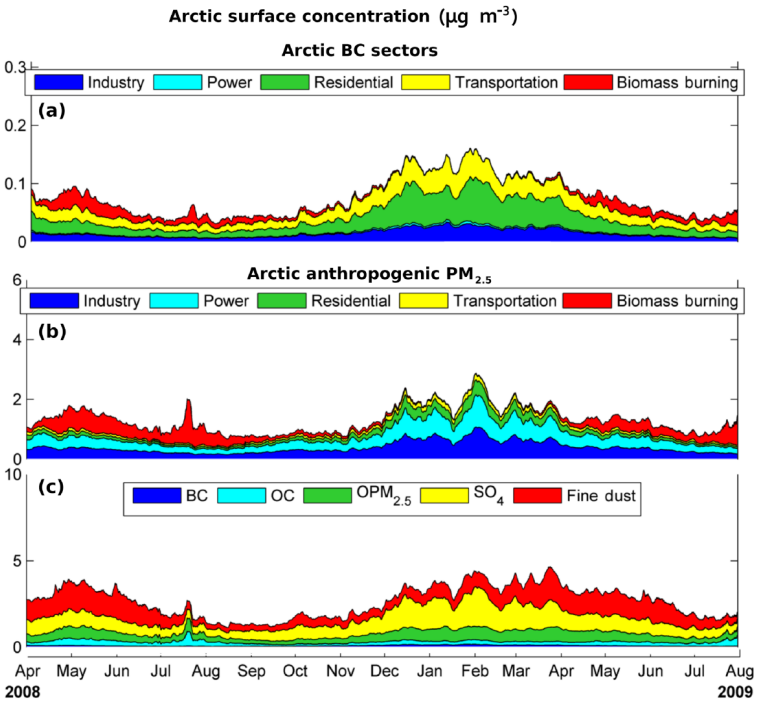

Figure 2.3: *Time series concentration and contribution of different sectors to (a)BC concentration, (b) $PM_{2.5}$ concentration, (c) and different $PM_{2.5}$ species. $OPM_{2.5}$ is the acronym for other PM2:5 and refers to other primary emitted non-carbonaceous particles with aerodynamic diameters less than 2.5 µm such as fly ash, road dust, and cement. SSA were not included in this analysis. From Sobhani et al. (2018).*

2.1.5 Aerosol emissions influencing the Arctic

The Arctic is influenced by aerosols emitted or produced from precursor emissions, outside or withing the Arctic. For example, the primary anthropogenic sources and the emissions of SLCFs produced globally and regionally, per economic sector, and geographical area are shown in **Figure 2.2**. The most important sources of BC and OC in the Arctic Council nations are residential, commercial and surface transportation, with secondary sources being power plants, agriculture and industries. The industry and power sectors are the most important contributors to SO_2 emissions in every region. For NO_x emissions the most important contributors are the surface transportation, industry and power sectors. Total oil production increased rapidly in the Arctic west Russia from 1970s and until the collapse of Soviet Union in the early 1990s *(AMAP, 2015)*. Oil production in Alaska also started to increase from late 1970s. Primarily west Russia, followed by Alaska were the two regions with the highest Arctic oil and gas production from 1990 to 2004 *(Peters et al., 2011)*. Arctic

oil and gas activities, including oil refineries, are also another important source of BC and SO_2 *(Stohl et al., 2013a; AMAP, 2015)*. These sectors are expected to keep affecting local air quality in the future, however their current emissions remain uncertain *(Peters et al., 2011; AMAP, 2015)*. Further discussion is provided in Chapters 4 and 5.

Figure 2.3 shows results from a source attribution model study investigating the emission sectors contributing to different aerosols in the Arctic. The contribution to BC from the residential sector significantly increases during wintertime since the burning of biofuels and coal is the main heating source at higher latitudes. Power, industry, and transportation sectors are the largest contributors to $PM_{2.5}$ (particulate matter, rd $\leq$ 2.5 µm) during wintertime, reflecting the increased energy consumption for domestic and industrial heating (**Fig. 2.3b**). Also, during wintertime SO_4^{2-} and fine dust are the main contributors to $PM_{2.5}$ (**Fig. 2.3c**). SO_4^{2-} peaks during the wintertime due to a large contribution from European emissions, resulting in higher use of fossil fuel and coal burning and SO_2 emissions for industry, power, and residential purposes. More details about the emission inventories used in this thesis are presented in Chapter 3.2.

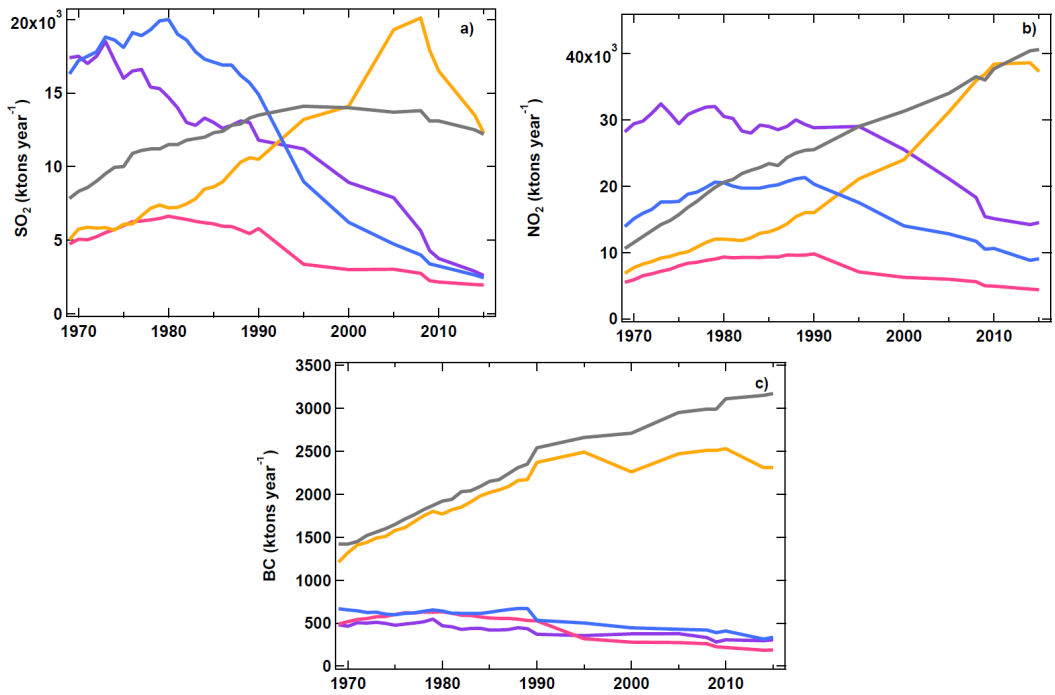

Figure 2.4: *Anthropogenic emissions of (a) SO_2, (b) NO_2, and (c) BC. Anthropogenic emissions are based on ECLIPSE v6b (Höglund-Isaksson et al., 2020). Data before 1990 are based on CMIP6 (Van Marle et al., 2017; Hoesly et al., 2018). The Western Arctic (purple) region refers to the following countries: USA and Canada; Eastern Arctic (pink) region: Kingdom of Denmark, Finland, Iceland, Norway, the Russian Federation, and Sweden. The plots also include Asia (yellow), the rest of the world (grey) and Europe (blue). From Schmale et al. (2022).*

Figure 2.4 shows a more recent example of anthropogenic emissions for SO_2, NO_2 and BC for different regions *(Schmale et al., 2022)*. SO_2 and NO_2 emissions are rapidly decreasing in the Western (USA and Canada) and Eastern Arctic (Kingdom of Denmark, Finland, Iceland, Norway, the Russian Federation, and Sweden), with Asia being an important contributor to NO_2. On the other hand, there was a large increase in BC due to emissions from Asia and the rest of the world, while in the Arctic and Europe, BC emissions are steadily decreasing.

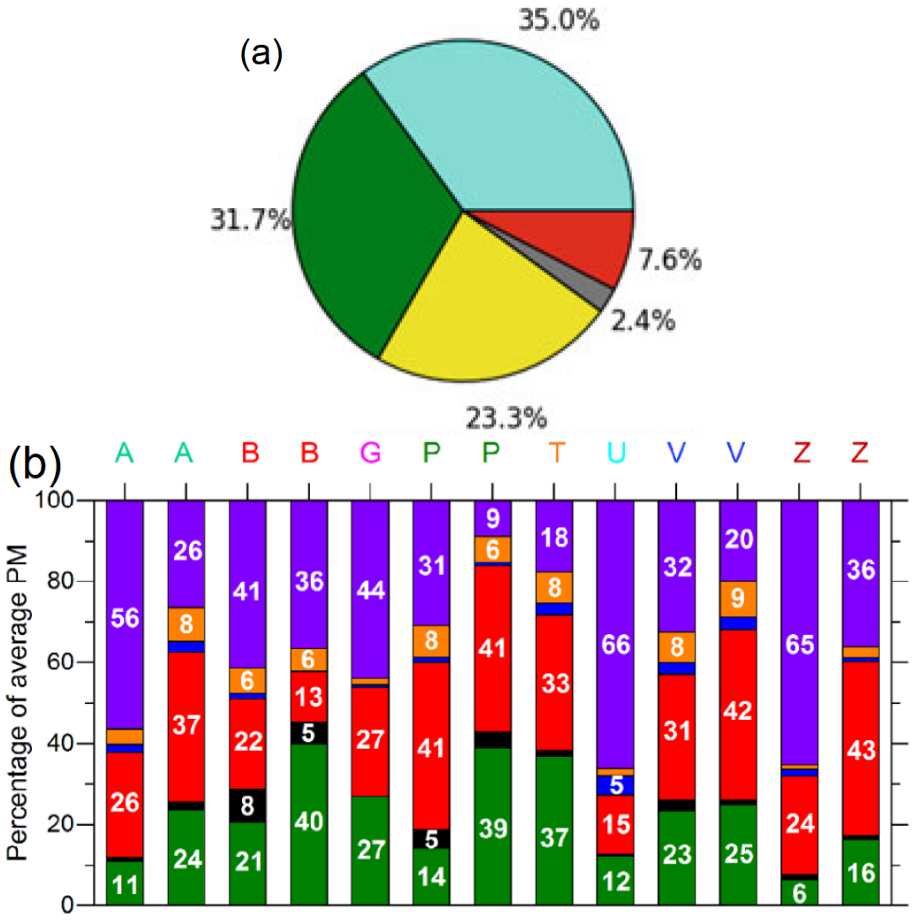

Figure 2.5: *(a) Chemical composition (average) of sub-micron ($PM_{1.0}$) at ground level at Utqiaġvik during winter months (October-May). Green: non-sea-salt sulfate and nitrate, blue: sea salt, yellow: mineral dust, grey: black carbon, and red: water-soluble organic matter. Figure from Udisti et al. (2020), (b) Percent contributions of sea salt (purple), ammonium (orange), nitrate (blue), non-sea-salt (nss) sulphate (red), EC (black), and OA (green) to the average PM_{10} at eight Arctic stations. A: Alert, Canada, B: Baranova, Russia, G: Gruvebadet, Norway, P: Pallas, Finland, T: Tiksi, Russia, U: Utqiagvik, United States of America (USA), V: Villum, Greenland and Z: Zeppelin, Norway. First column of each letter corresponds to wintertime, while second column to summertime. G is only for summertime. T is only for wintertime. From Moschos et al. (2022b).*

2.2 Aerosol properties

Aerosol particles vary in size, source and chemical composition. This section describes the main aerosol properties and provides examples for sites within the Arctic.

2.2.1 Chemical composition

Table 2.1, presented in the beginning of this Chapter, illustrates the chemical variety of anthropogenic and natural aerosols. Aerosol composition varies not only between seasons and aerosols size, but also depends on the location of the site, reflecting the different sources and formation mechanisms *(Frossard et al., 2011; Schmale et al., 2011; Frossard et al., 2014; Kirpes et al., 2019)*. To illustrate this, the most important components of sub-micron particles in an Arctic remote site, such as Utqiaġvik, during wintertime, is SSA (35%), followed by nss-SO_4^{2-} and NO_3^- (31.7%) and mineral dust (23.3%) (**Fig. 2.4a**), while BC is almost 15 times less (2.4%). **Fig. 2.4b** shows that at all coastal sites in the Arctic, SSA are the major component of PM_{10}, following by SO_4^{2-} and then OA. The only exceptions are Pallas (P) and Tiksi (T) sites, where during wintertime, SO_4^{2-} is the main contributor to PM_{10}, followed by SSA and OA, respectively. A significant component of sub-micron SSA is organic matter of marine origin *(Frossard et al., 2014; Kirpes et al., 2019)*.

2.2.2 Size distribution

Atmospheric aerosol particles exhibit a wide range of sizes, ranging between 0.002 and 100 μm (**Fig. 2.6**). Aerosols are often non-spherical, and an equivalent diameter is introduced, such as the aerodynamic diameter or the Stokes diameter.

Aerosol distributions are typically characterised by two modes: (i) fine mode when the diameter is smaller than 2.5 μm and (ii) coarse mode when the diameter is bigger than 2.5 μm. Fine mode is divided into three categories: (i) nucleation mode (about 0.0001 μm < r_d < 0.01 μm), (ii) Aitken mode (0.01 μm < r_d < 0.1 μm) and (iii) accumulation mode (0.1 μm < r_d < 2.5 μm). For example, dust and SSA are mostly bigger than 1 μm, while BC and OA are often fine mode (**Fig. 2.6**).

Aerosols are defined as Particulate Matter (PM) mass for air quality and health studies. $PM_{1.0}$ (sub-micron) is any particulate matter or aerosol in the air with an aerodynamic diameter less than 1.0 μm. Sources of $PM_{1.0}$ could be combustion activities (motor vehicles, power plants, wood burning) and industrial processes. $PM_{2.5}$ and PM_{10} are also used and defined as any particulate matter in the air with an aerodynamic diameter less than 2.5 and 10 μm, respectively. Sources of larger particles include crushing or grinding operations, dust

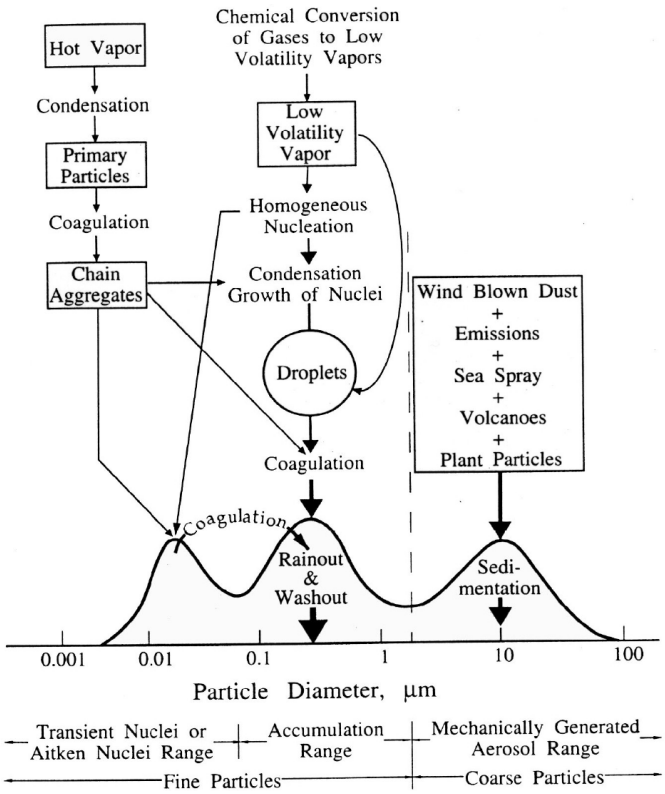

Figure 2.6: *Size distribution of surface area of aerosols. The graph also shows the different aerosol processes occurring at different particle sizes. From Whitby (1978).*

from paved or unpaved roads or deserts, and bubbles bursting from the ocean producing SSA particles.

Number size distribution is used to describe the number of particles (population) which exist in a specific volume of air at different diameters. To illustrate the number size distribution it is common to plot $dN/dlogD_p$ in cm^{-3}, as a function of D_p in nm, where dN is the number of particles, $dlogD_p$ is the diameter difference between the upper and lower limit in log and D_p is the particle diameter, usually aerodynamic, given in nm.

Figure 2.7 shows an example of monthly average number size distributions at Zeppelin, Norway and Villum Research Station, Station Nord, during wintertime *(Dall'Osto et al., 2019)*. During January and February (**Fig. 2.7a,b**), particle number concentrations are low and mostly in accumulation mode (250 nm for Zeppelin and 180 nm for Villum). Also, low particle number concentrations are observed during November and December, with Villum experiencing less new particle events than Zeppelin. Statistical analysis revealed that the accumulation mode is dominant during the winter months at Zeppelin and peaks during February and April (not shown here) associated with enhanced aerosol concentrations at both stations (Arctic Haze, see Chapter 1, section 1.3.1).

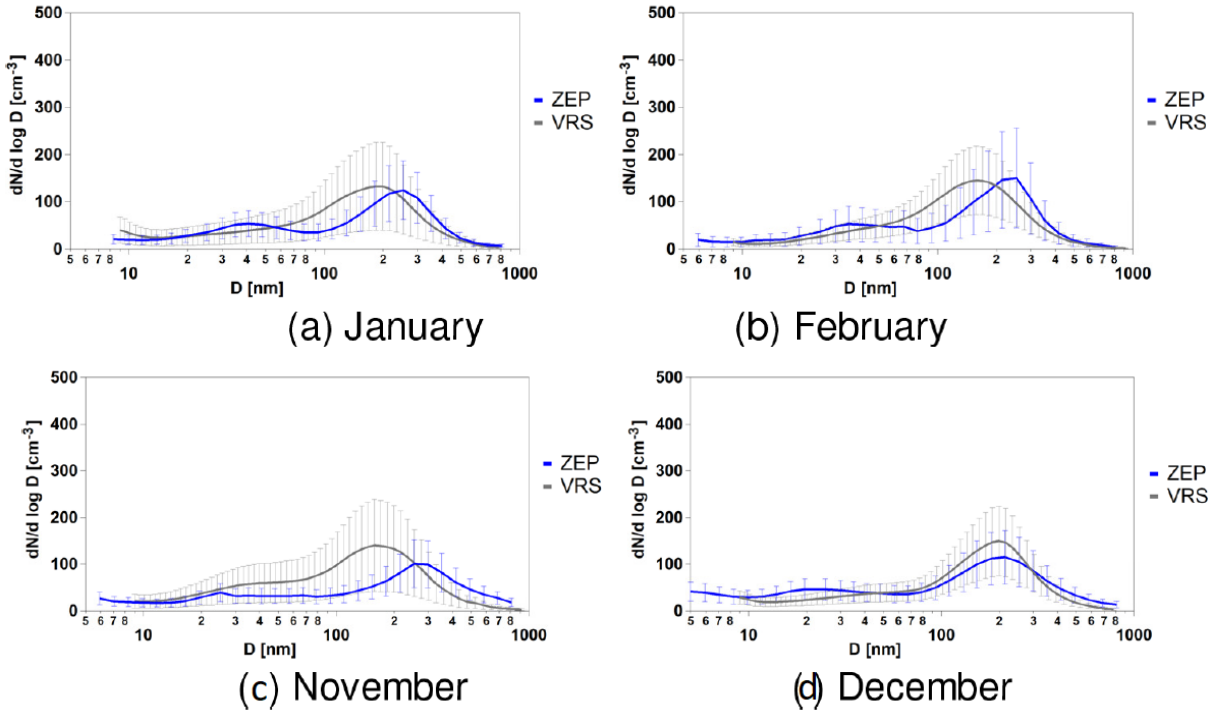

Figure 2.7: *Monthly (2013-2015) average number size distributions at Zeppelin and Villum Research station (VRS), during wintertime. From Dall'Osto et al. (2019).*

2.2.3 Mixing state

Aerosol mixing state shows spatial and temporal variations consistent with aerosol characteristics and aerosol type over different locations *(Ramachandran and Srivastava, 2016)*. There are different mixing states, such as external, internal, core-shell and random spherical inclusions. External mixing occurs when each particle size is associated with a single composition, while internal mixing assumes that aerosols of a given size have the same (mixed) composition. In polluted regions in the Arctic during wintertime, such as the Alaskan Arctic, analysis of single particles has shown that SO_4^{2-}, NO_3^- are internally mixed with OC or SSA and soot with organic and SO_4^{2-} compounds *(Kirpes et al., 2018, 2019)*.

2.3 Aerosol processing and removal

Once formed aerosols can undergo coagulation, condensation as shown in Fig. 2.6 and loss by dry deposition and wet removal. These processes are presented shortly in this section.

2.3.1 Aerosol growth and ageing

Once formed, small aerosols can grow by coagulation or condensation (**Fig. 2.6**). Coagulation is caused by particle collisions and coalescence, primarily by Brownian motion *(Fuchs et al., 1965)*. Larger particles can also coagulate due to differences in updraft speed during sedimentation or turbulent motion. Aerosols can also grow by water uptake if they are hydrophilic. Coagulation and condensation are more efficient for small particles and explain the growth of aerosols up to the accumulation mode. Chemical ageing refers to oxidation reactions occurring at the surface or in the interior of primary organic aerosol and could affect hydrophobic-to-hydrophilic conversion *(Rudich, 2003; Kanakidou et al., 2005)*. For example, the ageing rate affects global BC concentrations and distributions *(Petters et al., 2006)*. Aged BC particles can act as cloud condensation nuclei (CCN) and be removed by in-cloud scavenging. The time-scale of BC ageing is different during daytime and night-time under pollution conditions. *Riemer et al. (2004)* found that the time scale is less than 2 hours during daytime in polluted regions, while during night-time, it is longer, from 10 to 40 hours. Other aerosols can act also as CCN. For example, SSA contribution to CCN is less than 30%, while the CCN population between 70°S and 80°S is mainly composed of non-sea-salt (nss) SO_4^{2-} aerosols *(Quinn et al., 2017)*.

An example of condensation on pre-existing particles, includes gaseous NH_3, HNO_3, H_2SO_4. More specifically, H_2SO_4 is non-volatile in the atmosphere and its condensation on particles is irreversible, but other gases (HNO_3, HCl, organic gases, e.g. R24) are semi-volatile and could evaporate *(Zaveri et al., 2008)*.

2.3.2 Aerosol dry and wet removal

Aerosols can be removed from the atmosphere through two different processes: dry and wet deposition. Dry deposition is a process that removes particles from the atmosphere and deposits them on a surface through sedimentation, interception, and Brownian motion. Dry deposition includes the settling or falling-out of particles due to the influence of gravity. An aerosol compound can be transported by turbulence close to the surface and then by molecular diffusion through the laminar boundary layer *(Wesely, 1989)*. Thus, dry deposition is driven by turbulence and thus friction velocity and surface roughness, and strongly depends on particle size *(Mariraj Mohan, 2016)*. Aerosol precursor gases, such as SO_2, can also be removed by dry deposition. Dry deposition is highly affected by the type of land surface. It is typically faster over vegetation due to uptake in plants *(Erisman et al., 1994)*. During the Arctic Ocean Expedition in 1996 dry deposition was measured over open ocean, ice and open leads *(Nilsson and Rannik, 2001a)*. Dry deposition was larger over open

ocean than the other surfaces. A data analysis study by *Macdonald et al. (2017b)* showed that dry deposition might be the dominant aerosol removal mechanism during wintertime at Alert, Canada.

Wet deposition can be split into two scavenging mechanisms: in-cloud scavenging, which removes aerosols from the cloud layer during precipitation formation and cloud and ice droplets grow, and below-cloud scavenging, which removes aerosols by impaction. Gaseous precursor gases also undergo similar scavenging processes. Most of wet deposition occurs along the North Atlantic or North Pacific storm tracks (polar front - pathway 2, see Chapter 1) *(Iversen, 1984)*. During unstable atmospheric conditions, below-cloud scavenging is may be less important compared to in-cloud scavenging *(Schumann et al., 1988)*. Under stable conditions, when aerosols are trapped within the boundary layer, below-cloud scavenging may contribute significantly to wet deposition *(Zinder et al., 1988)*. A data analysis study by *Mori et al. (2020)* showed that during wintertime wet removal is stronger at Zeppelin, Norway than at Utqiaġvik, Alaska. Lower wet and dry removal in winter/spring compared to summer, leads to longer aerosol lifetime *(Barrie, 1986; Quinn et al., 2007a; Garrett et al., 2011)*.

2.4 Aerosol optical properties and radiative effects

The optical properties describing the interaction between aerosol and solar radiation are the extinction and scattering coefficients, the single-scattering phase function, and the vertical optical depth *(Levoni et al., 1997)*. Aerosols interact with solar radiation by absorbing (e.g. BC, mineral dust) and scattering (e.g. SO_4^{2-}, NO_3^-, SSA) solar radiation. This interaction is defined as the direct radiative effect of aerosols on Earth's radiation budget and is low during Arctic wintertime due to a lack of incoming solar radiation *(Haywood and Shine, 1995)*. Aerosol direct radiative effects depend on their size distribution, structure, and chemical composition. For example, SO_4^{2-} particles are more diffusive, while soot particles are strong light absorbers. BC contributes to local warming in the Arctic, as it absorbs solar radiation in the atmosphere (Wang et al., 2011). BC is also deposited onto the snow and ice, which also contributes to local warming *(Warren and Wiscombe, 1980; Quinn et al., 2008)*. As a result, surface albedo may decrease, but BC can also affect the snow grain size, which may increase *(Flanner et al., 2007)*. BC deposition can trigger then snow albedo feedback with snow melting faster, leading to a further warming *(Flanner et al., 2009)*.

Aerosols also affect cloud droplet/particle number, effective radius, and cloud water content, interactions called the aerosol indirect effect. An increase in aerosol concentration leads to an increase in droplet/particle concentration (cloud albedo effect), while the

reduction in cloud droplet/particle size results in changes in precipitation efficiency (cloud lifetime effect) *(Penner et al., 2001)*. The indirect effect is notable in the Arctic during wintertime due to cloud-aerosol interactions and can cause warming (e.g. *Zhao and Garrett (2015)*). One study showed that cloud-aerosol interactions caused warming at Utqiaġvik, Alaska between October and May and cooling between June and September *(Zhao and Garrett, 2015)*.

Chapter 3

Tools: Models, emission inventories and observations

In order to quantify and examine the contribution and impacts of remote, regional and local sources of air pollution on Arctic aerosols during wintertime it is necessary to use models combined with data analysis. Regional 3-D models consider meteorological, physical and chemical interactions in the atmosphere, using emission inventories for aerosols and trace gases as input data. Detailed representation of meteorological (e.g. wind speed and direction, temperature) and chemical fields, as well as removal processes are included in 3D models, which affect the transport of aerosols in the atmosphere and drive pollutant composition. Also, a detailed representation of chemistry (gas-phase and aqueous-phase reactions) is included in 3D models. To simulate Arctic air pollution and focus on specific periods and regions, for example Alaska, it is preferable to use a regional than a global model. An essential advantage of using regional instead of global models is linked to horizontal resolution, as regional models allow the user to define a domain, using higher grid resolution combined with detailed aerosols and gas mechanisms. Regional simulations can focus on specific regions/events at high resolution and with a representation of physics and chemistry interactions, such as aerosol-clouds interactions.

This chapter describes the atmospheric models used in this thesis, the input data used as initial conditions and to constrain boundary conditions, the emission inventories used as input for the simulations, the Arctic measurements of aerosols and meteorological parameters used to validate the model and finally, the field campaigns for which the model is used to investigate case studies of wintertime Arctic meteorological conditions and air pollution.

3.1 Regional model: WRF coupled with chemistry (WRF-Chem)

For the purposes of this thesis the regional WRF-Chem model is used *(Grell et al., 2005; Fast et al., 2006)*. More specifically, quasi-hemispheric and regional simulations are performed using v.3.9.1.1, with updates discussed in *Marelle et al. (2017)*. Details of the numerical schemes used in WRF-ARW (Advanced Research WRF) can be found in the technical description by *Skamarock et al. (2008a,b)*. Briefly, the equations are prepared in Cartesian (horizontal) coordinates and in a pressure-based terrain adjusted to "eta" (vertical) coordinates *(Laprise, 1992)*. A 5th-order scheme is used for horizontal scalar and momentum advection, and a 3rd-order scheme for vertical advection. Advection schemes conserve mass, and use a monotonic flux limiter (*Wang et al. (2009)* and references within). Sub-grid-scale horizontal turbulent mixing is calculated using a 2nd-order scheme, and vertical mixing is accounted for in the chosen Planetary Boundary layer (PBL) scheme (see section 3.1.1).

The WRF-Chem model has been used for large-scale simulations *(Eckhardt et al., 2015; Whaley et al., 2022b,a)*, and also for regional modelling over the Arctic, e.g. during wintertime *(Mölders and Kramm, 2010; Mölders et al., 2011)* or during spring and summer *(Raut et al., 2017; Marelle et al., 2018, 2021)*, to investigate regional and local air pollution. WRF/WRF-Chem is used by many international groups for simulations over different regions, such as Europe *(Chen et al., 2016)*, Africa *(Adefisan and Oghaego, 2018)*, North America *(Bucaram and Bowman, 2021)*, the Arctic region *(Whaley et al., 2022b,a)*, Alaska *(Mölders et al., 2011; Monaghan et al., 2018b; Marelle et al., 2021)*, Siberia *(Raut et al., 2017)*, Asia *(Zeng et al., 2020; Li et al., 2021a)*. As a result different physical parametrisations, such as land surface models, e.g., National Centers for Environmental Prediction Oregon State University Air Force Hydrology Lab (NOAH) land surface model (LSM)/ Multiparameterization (MP), Rapid Update Cycle (RUC) and boundary layer schemes, e.g., Mellor-Yamada-Janjić (MYJ), Yonsei University (YSU) have been developed and adapted to WRF. The above parametrisations can be combined with aerosols/chemistry modules, such as Regional Atmospheric Chemistry Mechanism (RACM)-Modal Aerosol Dynamics Model for Europe (MADE)/ Secondary Organic Aerosol Model (SORGAM), Model for Simulating Aerosol Interactions and Chemistry (MOSAIC)-4 bin/8-bin and gas mechanisms, e.g. Carbon-Bond Mechanism version Z (CBM-Z), Statewide Air Pollution Research Center (SAPRC-99) to simulate meteorological conditions and aerosol patterns in different regions of the world. Further details are provided in the following sections.

3.1.1 WRF setup: Meteorological parametrisations

Part of this thesis examines the role of boundary layer dynamics on aerosols over the Arctic, focusing on Alaska during wintertime. Different schemes within WRF are tested to understand in particular how the Arctic boundary layer is simulated and influences mixing of aerosols under cold/dark conditions. It is essential to simulate the stable conditions, with strong temperature inversions, which occur during winter in the Arctic, as they are responsible for trapping pollution near to the surface.

The PBL is the part of the lower troposphere affected by the Earth's surface via troposphere–surface exchanges of heat, moisture, and momentum on sub-hourly time scales *(Stull, 1988)*. **Figure 3.1** shows the boundary layer in high-pressure regions over land, consisting of three major parts: a very turbulent mixed layer, a less-turbulent residual layer containing former mixed-layer air, and a nocturnal stable boundary layer of sporadic turbulence. The mixed layer can be divided into cloud and sub-cloud layers. The evolution of the stable boundary layer is mostly driven by turbulent mixing, interactions between the atmosphere and the surface, and radiative effects. At mid-latitude regions the boundary layer is usually up to 1 km deep, while in the Arctic it is much more shallow, typically a few hundred meters or less. The stable atmospheric boundary layer is common in the Arctic during winter, where the absence of incoming solar radiation causes a negative net radiation at the surface (Chapter 1). If conditions are anticyclonic for several days, then stable stratification may develop. In this case, the residual layer may be completely eroded, leaving the stable layer in direct contact with the free atmosphere. Dry deposition (and local wet deposition) also depend on correct representation of the PBL structure. First the schemes used in this thesis are presented, including a few examples showing the effect of different schemes used throughout the different studies over Alaska and during winter.

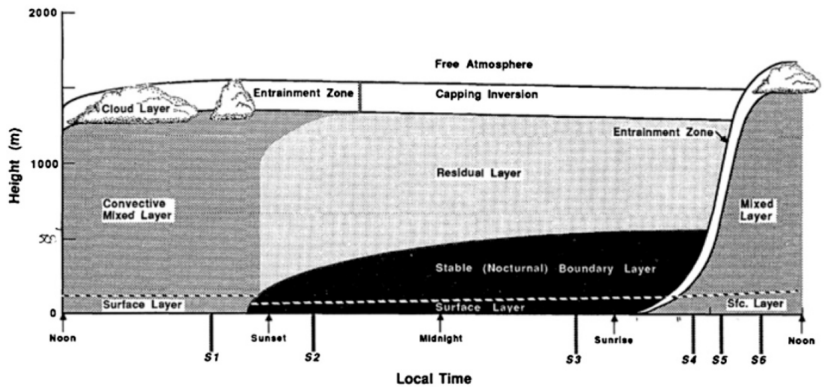

Figure 3.1: *Diurnal evolution of a boundary layer land surfaces in high pressure regions. From Stull (1988).*

Land surface models: Two land surface models are tested as part of this thesis: NOAH LSM and NOAH MP. A detailed explanation about the differences between the two versions of the land surface model (LSM and MP) can be found on *Niu et al. (2011a); Chen and Dudhia (2001)* and references within. Briefly, NOAH LSM calculates sensible and latent heat fluxes, as well as ground heat flux, considering parameters such as snow cover and soil, which influences the temperature and moisture of the land *(Skamarock et al., 2008a)*. The snowpack is considered as a single layer, while the soil is divided into four layers for which the heat diffusion equation is solved. NOAH MP requires its own namelist with options for different physics parametrisations, such as turbulence exchange coefficients, radiation. The NOAH MP namelist used throughout this thesis is shown in APPENDIX A. NOAH MP is considered an evolution of NOAH LSM, including more detailed soil and snow parametrisations, combined with improved canopy representation. More specifically, NOAH MP simulates more accurate snow skin temperature diurnal variations and improves modelled runoff *(Niu et al., 2011b; Yang et al., 2011)*.

Surface-layer schemes: The surface-layer scheme determines friction velocities and turbulent exchange coefficients. In WRF, the surface-layer scheme is linked to a specific boundary layer scheme. That being said, YSU is linked to Model Version 5 similarity (MM5) surface-layer revised scheme *(Grell et al., 1994; Jiménez et al., 2012)*, while MYJ is linked to Eta "similarity theory" *(Janjic, 1996; Janić, 2001)* surface-layer scheme. In the MM5 scheme, Monin-Obukhov similarity theory is applied *(Monin and Obukhov, 1954)*.

Boundary layer schemes: WRF includes many different boundary layer schemes and a few are tested during this thesis for the analysis over central and northern Alaska. In this thesis results from two commonly used schemes are presented: YSU, a first-order closure model *(Hong et al., 2006; Hong, 2010; Skamarock et al., 2008a)* and MYJ, a 1.5 order closure model *(Mellor and Yamada, 1982; Janjic et al., 2001)*. Briefly, the boundary layer schemes parametrise turbulent mixing and can be categorized as local (e.g. MYJ) and non-local (e.g. YSU). In local schemes, the thermodynamic properties of a layer interact only with the neighbouring layers.

The MYJ scheme determines eddy diffusion coefficients from prognostically calculated turbulent kinetic energy (TKE), and determines the PBL height using the TKE profile. TKE is the kinetic energy per unit mass and its associated with eddies in turbulent flow. The TKE is largest within the PBL. MYJ defines the top of the PBL as the height where TKE decreases to a prescribed low value *(Janjic et al., 2001)*. MYJ generates less turbulent mixing than non-local schemes, which may lead to cold biases in more convective situations *(Hu et al., 2010)*. On the other hand, in non-local schemes, such as YSU, the effect of mixing by larger eddies is considered by applying a counter-gradient (for unstable conditions only) flux contribution

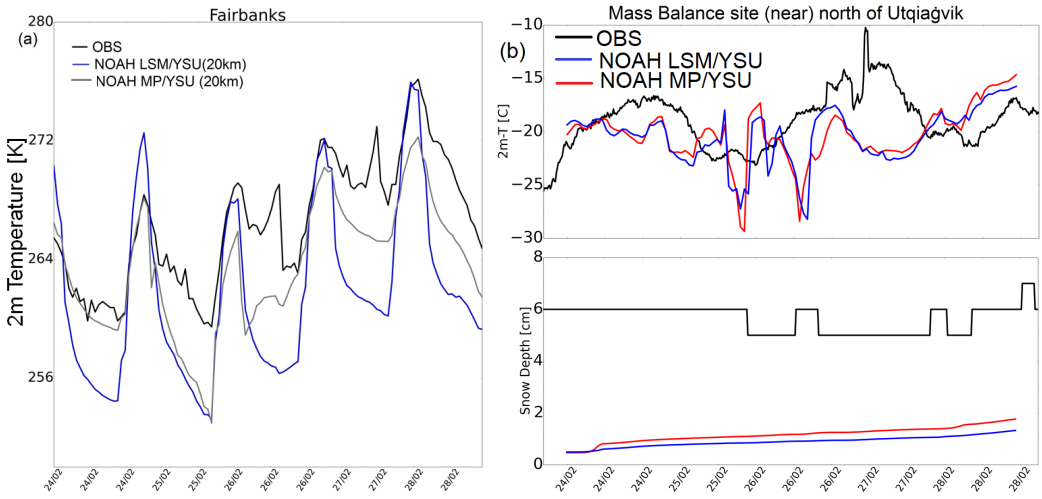

Figure 3.2: *(a) Model comparison between NOAH MP and LSM, against observed 2m temperatures, in Kelvin, in Fairbanks during a simulation at 20km over northern Alaska during February 2014. Observations: US Environmental Protection Agency (EPA). (b) Model comparison between NOAH MP and LSM, against 2m temperatures (upper plot), in °C, and snow depth, in cm, (lower plot) at a site located north of Utqiaġvik during a regional simulation at 20km over northern Alaska in February 2014. Observations: Joshua Jones, Research Professional Geophysical Institute, University of Alaska Fairbanks. For both comparisons NOAH MP and LSM are coupled to YSU boundary layer scheme.*

for theta and momentum, so the properties of one layer may mix with those layers further away, not just the adjacent layers. The YSU scheme was modified in WRF version 3 using the formulation by *Hong et al. (2006)* and increasing the critical bulk Richardson number, which is the ratio of the density gradient to the velocity gradient and is used as a turbulence indicator and an index of stability, from zero to 0.25 over land, thereby enhancing mixing in the stable boundary layer *(Hong and Kim, 2008)*. The YSU scheme uses the bulk Richardson number for defining the top of the PBL and it is calculated starting from the surface *(Hong et al., 2006)*. Further details are given in *Cohen et al. (2015)* and references within.

Figure 3.2 shows an example of NOAH MP and LSM validation coupled with YSU at regional scale (20km) over Alaska during February 2014. Over central Alaska (Fairbanks) NOAH MP is warmer during the cold periods compared to NOAH LSM and in better agreement with the observations, whereas, NOAH LSM is slightly warmer than MP when observations are closer to zero (273 K) (**Fig. 3.2a**). At a site north of Utqiaġvik in northern Alaska the differences in 2m temperatures between NOAH MP and LSM are smaller compared to Fairbanks (**Fig. 3.2b**). During this comparison there are also cases where either NOAH MP or LSM performed slightly better. In terms of other physical parameters, such as snow depth, both versions of land surface model have difficulties reproducing observed patterns, however NOAH MP simulates more snow. Both NOAH MP and LSM, combined with different boundary layer schemes, were validated against detailed in-situ observations over

Alaska for the different studies. This analysis is not included in this thesis, however the results revealed that NOAH MP coupled with different boundary layer schemes captures better than NOAH LSM wintertime meteorological conditions over Alaska. The results presented in Chapter 4–6 of this thesis used the NOAH-MP scheme. Prior to this, comparisons and evaluations of different set ups were performed, notably for winter 2014. These parametrisation schemes can be used with the MOSAIC aerosol 8-bin scheme (see chapter 3.1.2 for more information) *(Marelle et al., 2017)*.

Remaining physics parametrisations: For micro-physics parametrisation, the Morrison 2-moment scheme is used, in which cloud formation, cloud properties, and precipitation at the grid-scale are calculated *(Morrison, 2009)*. For horizontal resolutions coarser than 10 km, an additional parametrisation for sub-grid cumulus clouds, the Modified Kain-Fritsch scheme, an evolution of the initial Kain–Fritsch cumulus parametrisation is used *(Berg et al., 2013, 2015)*. The long-wave (LW) and the short wave (SW) radiation calculations are performed using the Rapid Radiative Transfer Model for GCMs (RRTMG), and it is coupled with the aerosol optical properties calculated by the Mie code *(Iacono et al., 2008; Iacono and Nehrkorn, 2010)*. Mie calculations are performed assuming spherical aerosols and an average refractive index within each bin.

Initial and boundary conditions: For meteorology they are derived from the National Centres for Environmental Prediction Final (NCEP-FNL) meteorological reanalysis data (0.1°x0.1°, `http://rda.ucar.edu/datasets/ds083.2/`) and the European Centre for Medium-Range Weather Forecasts (ECMWF) Reanalysis v5 (ERA5, *Hersbach and Dee (2016)*), with a horizon/tal resolution of 0.25°x.25° and updated every 6 h. Briefly, FNL fields are used in the models runs presented in Chapters 4 and 5 for winter 2014. They are produced from the Global Data Assimilation System (GDAS), which uses the same data assimilation and forecast system as the NCEP Global Forecast System (GFS). FNL provides the geopotential height, temperature, relative humidity, and other parameters at 26 and more pressure levels from 1.000 to 10 hPa. ERA5 data are used in the model runs presented in Chapter 6 for winter 2019. ERA5 is the latest generation European reanalyses produced by the ECMWF. Compared to ERA-Interim former reanalysis data, ERA5 includes a higher spatial and temporal resolution as well as a more recent model and data assimilation system. Parameters such as precipitation, for example, are represented better at ERA5 than ERA-Interim *(Albergel et al., 2018)*. A recent detailed study by *Chen et al. (2021)*, showed that ERA5 performs better than FNL, on a global scale, for parameters such as weighted mean temperatures. Overall ERA5 performs better than other reanalysis data (such as ERA-I, Modern Era Retrospective analysis for Research and Applications-version 2 (MERRA-2)) for temperature, wind speed,

and specific humidity compared to observations in the high Arctic (79° N) *(Graham et al., 2019)*. However, it is known that perform less well over Arctic sea ice *(Kayser et al., 2017; Naakka et al., 2018)*. In this thesis, 50 pressure levels are used, with 10 levels in the PBL. It would be advisable to use more pressure levels for simulations in the Arctic, however for chemistry and aerosol simulations this is more computationally expensive.

Land use categories: Two different databases of land use categories are provided with the WRF version used in this study (https://www2.mmm.ucar.edu/wrf/users/docs/user_guide_V3/). The default choice is Moderate Resolution Imaging Spectroradiometer (MODIS) – International Geosphere-Biosphere Programme (IGBP) 20 category data, which is based on data from January to December 2001 *(Friedl et al., 2002)*. An alternative set of land use categories data is provided based on 24 United States Geological Survey (USGS) categories, which contains global imagery from April 1992 to March 1993 *(Esteve and Sistach)*. The data are provided in different resolutions, such as 30", 2',5'and 10', where " stands for arc seconds and 'arc minutes. MODIS land use categories are used in this thesis. USGS data are tested regionally for simulations over central Alaska and the results are briefly discussed here.

Table 3.1 shows the different land use categories in MODIS and USGS. In a simulation for winter 2019 and at 33km over central Alaska, the model, using MODIS data, 'sees' the Fairbanks area as Evergreen Broadleaf Forest. On the other hand, when USGS data are used, the model 'sees' also Evergreen Broadleaf for Fairbanks, but mixed forest (#15 - USGS, **Table 3.1**) to the north. At this coarse resolution, the model does not see urban areas, however at higher resolutions (e.g. 1 km), the model distinguishes better urban, forests and tundra (Maillard et al. in prep. for GMD). The differences in temperatures due to using different land use categories databases are small in Fairbanks, with USGS leading to higher winds in the model (not shown here). Further investigation is needed to determine the reasons for these discrepancies in model meteorology due to land use categories. Both databases were generated a long time ago and since then land-use patterns have changed *(Jiang et al., 2008; Nguyen et al., 2020)* and more recent studies have updated land use categories, using remote sensing data, leading to improved simulated air temperature, winds and precipitation *(Chang et al., 2014; De Meij et al., 2014; Schicker et al., 2016; Li et al., 2020)*. Land-use categories are used as input to calculate dry deposition velocities of aerosols and trace gases for specific parametrisations in WRF-Chem (see section 3.1.2.1).

Nudging methods: Two different nudging methods are applied: grid and spectral nudging. In this thesis, the WRF temperatures and winds are nudged at each dynamical step to the reanalysis above the atmospheric boundary layer. See Chapters 4, 5, 6 for further discussion. A series of studies investigated the role of grid and spectral nudging, above

Table 3.1: *Land-use mapping using the 20-category MODIS–IGBP and 24-category USGS schemes.*

MODIS	USGS	MODIS	USGS
Evergreen Needeleleaf Forest	Evergreen Needleleaf	1	14
Evergreen Broadleaf Forest	Evergreen Broadleaf	2	13
Deciduous Needleleaf Forest	Deciduous Needleleaf Forest	3	12
Deciduous broadleaf Forest	Deciduous Broadleaf Forest	4	11
Mixed Forest	Mixed Forest	5	15
Closed Shrubland	Shrubland	6	8
Open Shrubland	Mixed Shrubland/Grassland	7	9
Woody Savanna	Savanna	8	10
Savanna	Savanna	9	10
Grassland	Grassland	10	7
Permanents Wetland	Herbaceous Wetland	11	17
Cropland	Irrigated Cropland and Pasture	12	3
Urban and Built-up	Urban and Built-up Land	13	1
Cropland/Natural Mosaic	Cropland/Grassland Mosaic	14	5
Snow and Ice	Snow and Ice	15	24
Barren or Sparsely Vegetated	Barren or Sparsely Vegetated	16	19
Water	Water Bodies	17	16
Wooded Tundra	Wooded Tundra	18	21
Mixed Tundra	Mixed Tundra	19	22
Barren Tundra	Bare Ground Tundra	20	23

the planetary boundary layer, on regional simulations *(Miguez-Macho et al., 2004; Pohl and Crétat, 2014; Omrani et al., 2015; Mai et al., 2017)*. Briefly, for spectral nudging, proposed by *Waldron et al. (1996)* and later improved by *von Storch et al. (2000)*, a fast-Fourier transform is used to transform the input analysis data for spectral analysis and then to nudge WRF fields. This technique ensures consistency between the simulated large-scale circulation and the analysis fields and allows small-scale details in the model to evolve without nudging. On the other hand, an artificial tendency term is used for grid nudging in the prognostic equations to relax each grid point toward the difference between a value that is interpolated in time from the analyses and the model values *(Stauffer and Seaman, 1990)*. Spectral nudging is applied in zonal and meridional directions, while grid nudging is conducted in every grid cell *(Liu et al., 2012)*. In a spring-summer study over China, *Ma et al. (2016)*, using WRF, reported that, compared to observations, spectral nudging improved simulated precipitation, while grid nudging improved simulated air humidity and wind speeds. However, *Liu et al. (2012)*, also using WRF, reported that spectral nudging outperformed grid nudging at large and small scales. It is an open research issue and further investigation is needed to determine which method is more suitable for large/regional scale simulations.

3.1.2 WRF-Chem: Aerosol and chemistry schemes

MOSAIC aerosol scheme: There are different aerosol modules implemented in WRF-Chem. In this thesis, the MOSAIC aerosol model is used *(Zaveri et al., 2008)*. There are eight discrete size bins between 39 nm and 10 μm in MOSAIC, representing the aerosol size distribution. In the version used here, MOSAIC includes 176 aerosol species: 8 bins × 11 species (mass concentrations for 8 chemical species + 2 species for aerosol water + 1 bulk number concentration) × 2 (activated or interstitial aerosol). As a result, MOSAIC is one of the most computationally costly aerosol mechanisms available in WRF-Chem. In the current form, MOSAIC cannot be used to perform high resolution simulations over long periods and large domains. Aerosols are internally mixed within each bin. Within each size bin and each grid cell, MOSAIC calculates aerosol number concentrations, as well as mass concentrations of SO_4^{2-}, NO_3^-, NH_4^+, BC, OA, Na^+, Cl^-, and "other inorganic" (OIN, including silica, other minerals, and trace metals). Inorganic species such as potassium (K) and magnesium (Mg) are not explicitly modelled in MOSAIC as they are usually present in smaller amounts compared to other cations in aerosols. Coagulation is calculated following the approach of *Jacobson et al. (1994)*. Nucleation is based on the homogeneous H_2SO_4-H_2O scheme of *Wexler et al. (1994)*, and new particles grow (as SO_4^{2-} and NH_4^+) to the lower bin of the MOSAIC 8-bin scheme (39 nm). Aqueous chemistry in clouds follows *Fahey and Pandis (2001)* and includes oxidation of S(IV) by H_2O_2, O_3 and other radicals, as well as uptake of NH_3, HNO_3 and HCl. MOSAIC includes 18 irreversible heterogeneous reactions, including reactions of solids and liquids with gases such as H_2SO_4 (nonvolatile), methanesulphonic acid (CH_3SO_3H), HNO_3, HCl and NH_3 *(Zaveri et al., 2008)* (see discussion in Chapter 2). Gas-particle partitioning in MOSAIC uses module called Adaptive Step Time-Split Euler Method (ASTEM), described in detail in *Zaveri et al. (2008)*. Further discussion is provided about available and possible missing reactions on SSA in Chapter 4 and for secondary formation of NO_3^- and SO_4^{2-} aerosols in Chapter 6.

Gas-phase chemistry schemes: MOSAIC 8-bin is coupled to three different gas-phase chemistry schemes available in WRF-Chem: CBM-Z (73 species, 237 reactions, *Zaveri and Peters (1999)*), SAPRC-99 (79 species, 235 reactions, *Carter (2000)*) and Model of Ozone and Related Chemical Tracers (MOZART) (85 species and 196 reactions, *Emmons et al. (2010)*). In this thesis, SAPRC-99 scheme is used, as it is coupled to MOSAIC and SOA formation *(Shrivastava et al., 2011a; Marelle et al., 2017; Whaley et al., 2022b)*. MOSAIC is coupled with a SOA formation mechanism, Volatility Basis Set with 2 volatility species (VBS-2) and uses the "volatility basis set" approach *(Robinson et al., 2007; Shrivastava et al., 2011a)*. The VBS-2 mechanism represents POA by two volatility species: (i) aerosol-phase POA and gas-phase

POA species. The latter reacts with OH to produce SI-SOA(a) and SI-SOA(g). SI-SOA is a component of SOA formed due to photochemical oxidation of all S/IVOC precursors. The VBS-2 mechanism also includes 1-species treatment of traditional SOA (V-SOA), produced by oxidation of biogenic and traditional anthropogenic VOCs. It also includes SOA formation from the oxidation of S/IVOCs. In total, there are 40 POA species (8 gas, 32 aerosols), 20 SI-SOA species (4 gas, 16 aerosols) and 10 V-SOA species (2 gas, 8 aerosols), which are up to 5 times less than the species included in VBS-9 scheme, also implemented in MOSAIC, but not used due to huge computational burden. SOA formation from S/IVOC is not included in this version of the MOSAIC/VBS-2 mechanism. There are uncertainties on the way S/IVOC emissions are estimated, as POA or VOC emissions are multiplied by a factor of 6.5, based on case studies in Mexico city *(Hodzic et al., 2010)*, and cannot be used for global studies *(Shrivastava et al., 2015)*. Also, the current treatment of S/IVOC formation in the model was found to be extremely computationally expensive for quasi-hemispheric simulations *(Marelle et al., 2017)*. Gas-phase chemistry equations in SAPRC-99 are solved by a Runge-Kutta-Rosenbrock-type code (Rodas3 solver, *Sandu et al. (1997)*).

Initial and boundary conditions of trace gases and aerosols are derived from the global chemical-transport model MOZART-4 *(Emmons et al., 2010)* and from the Community Atmosphere Model with Chemistry (CAM-Chem) *(Buchholz et al., 2019; Emmons et al., 2020)*. Briefly, MOZART-4 is a global chemical transport model for the troposphere and requires meteorological fields from either climate models or reanalysis data. MOZART-4 fields are used in the model runs presented in Chapters 4 and 5 for winter 2014. The standard MOZART-4 mechanism includes 85 gas-phase species, 12 bulk aerosol compounds, 39 photolysis and 157 gas-phase reactions and the calculation of SO_4^{2-}, BC, POA, SOA, NH_4NO_3, and SSA. MOZART-4 simulations are run using fixed lower boundary conditions constrained by observations, instead of direct emissions for CH_4, H_2 and N_2O and mixing ratios of several species (O_3, NO_x, HNO_3, N_2O_5, CO, CH_4) are constrained in the stratosphere since MOZART-4 does not have complete stratospheric chemistry (*Emmons et al. (2010)* and references within). CAM-Chem output based on simulations at 0.9 x 1.25 horizontal resolution simulation with 56 vertical levels, the meteorology is driven by specified dynamics, by nudging to Modern-Era Retrospective analysis for Research and Applications (MERRA2) reanalysis and the anthropogenic emissions are from Coupled Model Intercomparison Project round 6 (CMIP6). CAM-Chem fields are used as input and boundary conditions in the model runs presented in Chapter 6 for winter 2019. The MOZART-tropospheric chemistry scheme (T1) mechanism is used, which includes 46 gas-phase species, 28 photolysis, 112 kinetic reactions and it is considered an improvement compared to previous versions (*Emmons et al. (2020)* and references within). CH_4 and CO_2 in WRF-Chem are set to a single global value:

1.7 parts per billion (ppb) CH_4, 390 parts per million (ppm) CO_2.

3.1.2.1 Removal treatments

In WRF-Chem, wet and dry removal treatments are included for gases and aerosols. Wet removal of aerosols by grid-resolved clouds includes in-cloud and below-cloud removal by rain, snow, and graupel by Brownian diffusion, interception, and impaction mechanisms *(Easter et al., 2004; Chapman et al., 2009)*. Wet-removal due to subgrid-scale convective clouds *(Berg et al., 2015)* is also included in this MOSAIC version and described on previous studies *(Marelle et al., 2017; Raut et al., 2017)*. In-cloud wet removal occurs when cloud droplets including aerosols are converted to precipitation. Modelled precipitation can also remove a fraction of below-cloud aerosols by impaction. Also, wet removal in cumulus parameterization is included, considering the effect of cumuli on aerosols and trace gases in the model *(Berg et al., 2015)*.

Dry deposition of aerosols and trace gases are also included in the model. For the different gas-phase schemes in WRF-Chem (e.g. SAPRC-99, MOZART), the dry deposition is calculated following the resistance scheme of *Wesely (1989)* for different seasonal categories in the WRF-Chem. This version of WRF-Chem includes a modified version of *Wesely (1989)* to improve dry deposition on snow *(Marelle et al., 2016)*. In this thesis, two different aerosol dry deposition schemes are used. Initially, the model is run using *Zhang et al. (2001)* dry deposition scheme, calculating aerosol dry deposition velocities over different land categories. The MOSAIC dry deposition scheme is also tested, which is based on *Binkowski and Shankar (1995)*. In both cases, factors for aerodynamic resistance, Brownian diffusion, impaction process, interception collection efficiency are calculated, either taking into account the different land categories *(Zhang et al., 2001)* or by using uniform factors, e.g., for the calculation of Stokes number in MOSAIC dry deposition scheme and applying an empirical correction for convective velocity scale obtained from *Wesely (1989)*. Aerosol sedimentation in MOSAIC is calculated throughout the atmospheric column based on the Stokes velocity scheme, as described in *(Marelle et al., 2017)*. As mentioned earlier, land-use categories are important for calculating dry deposition velocities. From version WRF-Chem 3.8 the default choice to produce land use categories has changed, from USGS to MODIS data. However, parts of WRC-Chem code were not adapted to this changes. To calculate the dry deposition velocities using *Zhang et al. (2001)* parametrisation it is necessary first to map model land-use categories with the categories used by *Zhang et al. (2001)*. This mapping was based on the assumption that USGS land use data are used in the model. As a result the calculated dry deposition velocities were wrong, as the parameters applying to the calculations were

based on the wrong land use category. In the version used here this bug is corrected and the module now checks first which database is used before the mapping with the *Zhang et al. (2001)* land categories. Further details for the dry deposition schemes are presented in Chapter 4.

3.2 Anthropogenic emissions

In order to simulate Arctic Haze and investigate the contribution of regional and local sources on aerosol composition in the Arctic region, it is essential to provide the model with the necessary input emission data. These emissions are derived from two different emission inventories, and they are described in the following sub-sections.

3.2.1 ECLIPSE emission inventory

In the first half part of this thesis (Chapters 4 and 5) global anthropogenic emissions of NO_x, CO, BC, SO_2, NH_3, OC, OM, VOCs derived from Evaluating the Climate and Air Quality Impacts of Short-Lived Pollutants (ECLIPSE) version 6b, with initial resolution of 50×50 km are used (**Fig. 3.3**) *(Klimont et al., 2017; Höglund-Isaksson et al., 2020)*. These emissions were developed and used for the AMAP SLCF assessment report and evaluated in *Whaley et al. (2022b)*, including WRF-Chem. WRF-Chem, among other models, performed well on simulating mid-latitude O_3, NO_2 and SO_4^{2-} to within 10%–20% *(Whaley et al., 2022b)*. Briefly, the ECLIPSE emission inventory was created with the Greenhouse gas – Air pollution Interactions and Synergies (GAINS) (`http://gains.iiasa.ac.at`) model *(Amann et al., 2011; Klimont et al., 2017)*, which provides emissions of long-lived greenhouse gases and shorter-lived species, including information about key sources of emissions, environmental policies, and mitigation scenarios. For more information, see *Stohl et al. (2015b)* and references within.

Emissions from the energy, industrial, residential, transportation, agriculture, shipping, waste processing, flaring and solvent sectors are included in ECLIPSE v6b. ECLIPSE v6b, compared to previous versions, has improved regional resolution (e.g. Africa), updated legislation and historical data, includes a new sector (waste) and soil emissions for NO_x, gridding patterns updated for several sectors, including power plants, flaring, transport, industry, and significant sulphur emission reductions *(Grennfelt et al., 2020)*. **Figure 3.3 (a-g)** shows total annual emission fluxes for all mentioned species, and **Figure 3.3 (h1,h2)** shows BC emissions from energy and industry and flaring sectors for 2014 (results presented for winter 2014 in **Chapter 5**). Agricultural waste burning emissions from ECLIPSE v6b are

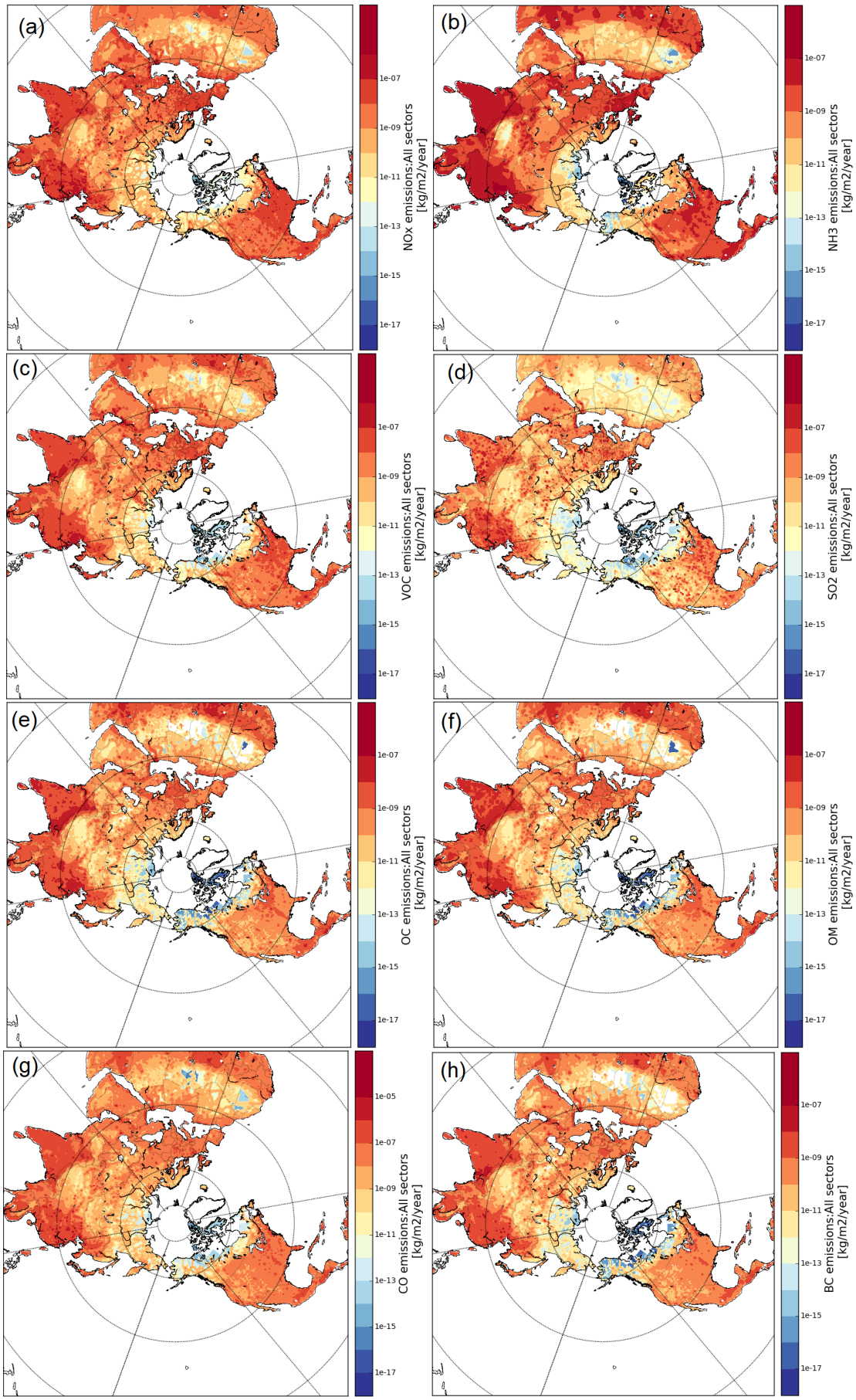
(a)
NOx emissions:All sectors [kg/m2/year]
(b)
NH3 emissions:All sectors [kg/m2/year]
(c)
VOC emissions:All sectors [kg/m2/year]
(d)
SO2 emissions:All sectors [kg/m2/year]
(e)
OC emissions:All sectors [kg/m2/year]
(f)
OM emissions:All sectors [kg/m2/year]
(g)
CO emissions:All sectors [kg/m2/year]
(h)
BC emissions:All sectors [kg/m2/year]

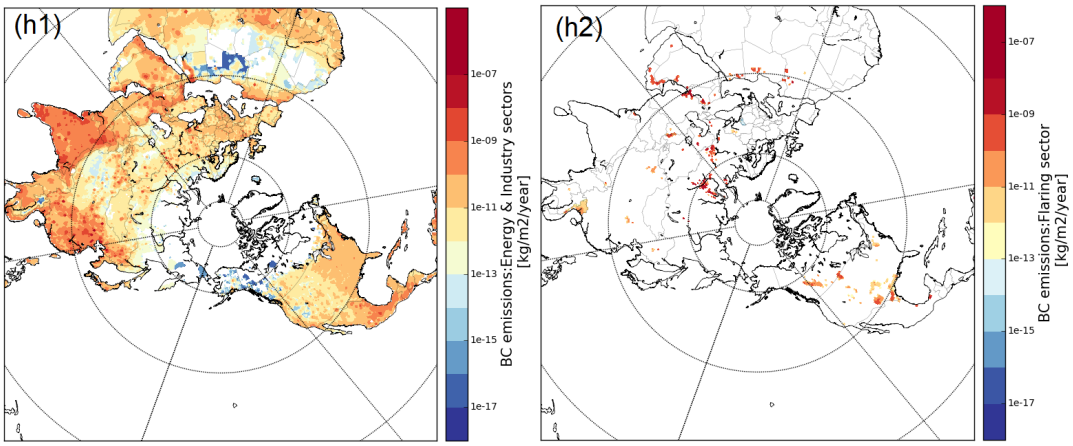

Figure 3.3: *Yearly ECLIPSE v6b anthropogenic emission fluxes in the Northern Hemisphere for (a) NO_x, (b) NH_3, (c) VOCs, (d) SO_2, (e) OC, (f) OM, (g) CO and (h) BC in $kgm^{-2}year^{-1}$, including all the sectors, as described in section 3.2.1. (h1) and (h2) show BC emissions only for energy, industry and flaring sectors, respectively.*

excluded to avoid double counting with biomass burning emissions which are discussed in Section 3.3.

3.2.2 CAMS emission inventory

Copernicus Atmosphere Monitoring Service (CAMS) emission inventory, version 5.3, is used also in this thesis, with initial resolution of 10×10 km ((*Soulie, 2022*)). Results presented for winter 2019 in **Chapter 6**) and sensitivity analysis comparing to ECLISPE v6b in **Chapter 5**. Briefly, CAMS anthropogenic emissions are based on Community Emissions Data System (CEDS) version 2 and the different sectors need to correspond to Emissions Database for Global Atmospheric Research (EDGAR) version 5 emissions *(McDuffie et al., 2020)*. Anthropogenic emissions from energy plants, oil refineries, industry, fugitives, road and non-road transportation, residential, solvents, manure management, soil, and water waste sectors are included in CAMS inventory. Agricultural waste burning emissions from CAMS are also excluded. **Figure 3.4 (a-g)** also shows total emissions for all mentioned species, and **Figure 3.4 (g1,g3)** shows BC emissions from energy (energy plants) and industry, fugitive and oil refineries sectors for 2019 (see in **Chapter 6** for further discussion).

3.2.3 ECLIPSE vs. CAMS anthropogenic emissions

Table 3.2 shows the sum of total emissions, in $Mtyear^{-1}$, of NO_x, NH_3, CO, SO_2, OC, OM, VOCs, NMVOC, BC for 2014 and 2019, for ECLIPSE v6b and CAMS v5.3 emission inventories. Also, the sum calculated for BC for specific only sectors, e.g., industry and energy

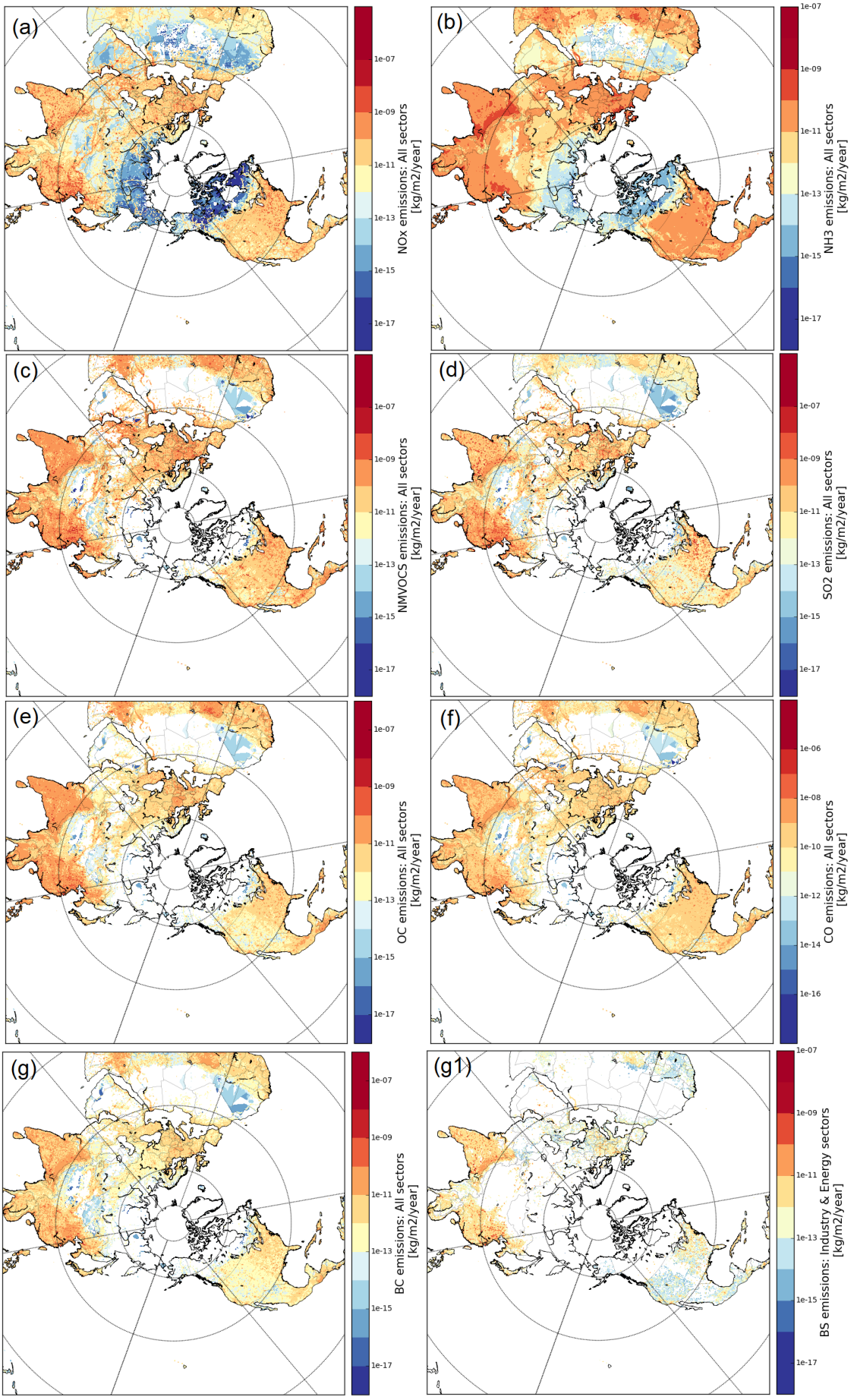
(a)
NOx emissions: All sectors [kg/m2/year]
(b)
NH3 emissions: All sectors [kg/m2/year]
(c)
NMVOCS emissions: All sectors [kg/m2/year]
(d)
SO2 emissions: All sectors [kg/m2/year]
(e)
OC emissions: All sectors [kg/m2/year]
(f)
CO emissions: All sectors [kg/m2/year]
(g)
BC emissions: All sectors [kg/m2/year]
(g1)
BS emissions: Industry & Energy sectors [kg/m2/year]

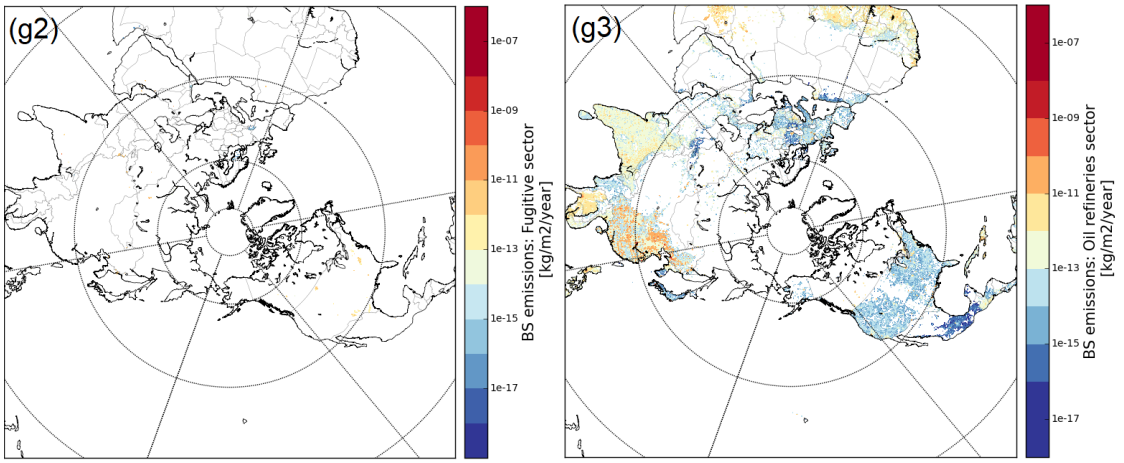

Figure 3.4: *Yearly CAMS 4.2 anthropogenic emissions in the Northern Hemisphere for (a) NO_x, (b) NH_3, (c) NMVOC, (d) SO_2, (e) OC, (f) CO and (g) BC in $kgm^{-2}year^{-1}$, including all the sectors, as described in sub-section 3.2.1. (g1), (g2) and (g3) show BC emissions only for energy (energy plants) and industry, fugitive and oil refineries sectors, respectively.*

Table 3.2: *Total global emissions of NO_x, NH_3, CO, SO_2, OC, OM, BC and BC flaring and industry and energy emissions for 2014 (ECLIPSE v6b and CAMS v5.3 (in parenthesis) inventories) and 2019 (CAMS inventory) in Mt $year^{-1}$.*

	ECLIPSE v6b (CAMS) 2014	CAMS 2019
NO_x	125.8 (77.9)	75.4
NH_3	60.5 (48.4)	49.8
CO	540.2 (581)	558
SO_2	78.2 (104)	90.6
OC	13.5 (11.8)	11.6
OM	21.8 (N/A)	N/A
VOCs	110 (166)	163.3
NMVOCs	N/A (144)	144
BC	6.3 (4.39)	4.15
BC-flaring (oil refineries)	0.15 (0.834)	0.729
BC-fugitive	N/A (0.0157)	0.0180
BC-industry-energy	0.64 (1.366)	1.256

sectors, flaring (ECLIPSE v6b) and fugitive (CAMS v5.3) sector. During 2014 ECLIPSE and CAMS emissions report similar magnitude for NH_3, CO, OC, BC, however ECLIPSE includes almost double NO_x emissions compare to CAMS. CAMS inventory includes more SO_2 and BC due to industry and energy sectors, compared to ECLIPSE for 2014.

3.3 Biomass burning emissions

Biomass burning emissions are an important source of air pollution in the Arctic, during spring (transported from low altitudes – *(Warneke et al., 2010)*) and summer or early autumn (local fires in Alaska and Siberia – *(Haque et al., 2021; Johnson et al., 2021)*). While this thesis focuses on the wider Arctic region and most specifically over Alaska during wintertime, biomass burning emissions are included in the simulations since the model is run either from early or mid–autumn at a quasi-hemispheric scale. WRF-Chem includes a fire plume rise model *(Freitas et al., 2007; Sessions et al., 2011)*. Global Fire Emissions Database (GFED) emissions are used in Chapters 4 and 5. FINN emissions are used in Chapter 6 and both and are described here.

GFED emission inventory (version 4.1), with a spatial resolution of 0.25 degrees, is used in this thesis and specifically for the two out of three projects (Chapter 4 and 5) *(RANDERSON et al., 2017)*. GFED provides global estimates of monthly burned area, emissions and fractional contributions of different fire types and daily/3-hourly fields to scale the monthly emissions to higher temporal resolutions. It was used in the recent AMAP runs for 2014/2015, including WRF-Chem *(Whaley et al., 2022b)*.

3.3.1 FINN

FINN v2.4 emission inventory (Wiedinmyer et al. 2022 in prep.), with a spatial resolution of 1 km, is also used in this thesis as part of the third project (Chapter 6). FINN emissions are based on fire detections by Moderate Resolution Imaging Spectroradiometer (MODIS) and Visible Infrared Imaging Radiometer Suite (VIIRS) space-born instruments.

3.4 Natural emissions

Natural emissions, such as SSA , have been identified as an essential component of fine and coarse mode aerosols at remote Arctic sites, contributing to the total aerosol burden in the Arctic region *(Kirpes et al., 2019; Moschos et al., 2022b)*. This is investigated further in Chapter 4. Dust and volcanic emissions also contribute to Arctic Haze and thus it is important to include those emissions on our simulations *(Huang et al., 2015; Stone et al., 2014; Zwaaftink et al., 2016)*. The subsections below describe the natural emissions used in this thesis.

3.4.1 Sea-spray emissions

SSA emissions are calculated online in the model. The primary mechanism leading to the formation of SSA is bubble bursting (jet-drop and film-drop formations) on the sea surface due to wind stress during whitecap formation *(Monahan et al., 1986a)*. SSA are calculated for the available schemes in WRF-Chem, for example GOCART or MOSAIC. Briefly, in the base version of WRF-Chem for MOSAIC, SSA emissions are calculated using the source function from *Gong et al. (1997)*, which depends on the whitecap formation, by *Monahan et al. (1986a)*, and thus depends on modelled 10 m wind speed. The emission flux scales linearly with the fraction of ocean area covered by whitecaps. There are a variety of ways to determine whitecap fraction, such as by using photos, videos from cruises, laboratory experiments and using satellite data *(De Leeuw et al., 2011)*. Also, a source function for small particles, coupled to *Gong et al. (1997)* scheme, based on *Fuentes et al. (2010, 2011)* is to include a source of marine organics. The whitecap fraction used in MOSAIC is based on laboratory results by *Monahan and Muircheartaigh (1980)*.

Results presented in Chapter 4 of this thesis show the importance of taking into account different mechanisms affecting SSA productivity, following more up-to-date studies. The updates include a more realistic whitecap fraction based on satellite data *(Salisbury et al., 2014)*, a SST dependence of SSA emissions *(Jaeglé et al., 2011)*, considering emissions from open leads, by calculating SSA emissions from a grid which is not fully sea-ice covered, including a local source of marine organics for simulations focusing on northern Alaska *(Kirpes et al., 2019)* and a higher wind speed dependence for sub-micron SSA based on results from an Arctic cruise *(Russell et al., 2010)*.

3.4.2 Biogenic emissions

Biogenic emissions derived from the online Model of Emissions of Gases and Aerosols from Nature (MEGAN, *Guenther et al. (2006)*), with a resolution of 1 km are used for simulations in all Chapters. MEGAN estimates the net emission of gases and aerosols from terrestrial ecosystems into the atmosphere. Moreover, WRF-Chem includes input land cover data, derived either from U.S. Geological Survey (USGS) or MODIS and then parameters such as green vegetation fraction and leaf area index are estimated (*Li et al. (2014)* and references within).

Also, soil daily NO_x emissions, 1.0° x 1.0°, are used in the model runs presented in this thesis, which derived from POLar study using Aircraft, Remote sensing, surface measurements and modelling of Climate, Chemistry, Aerosols, and Transport (POLARCAT) model inter-comparison (POLMIP, Emmons et al. (2015)) project.

3.4.3 Volcanic emissions

Daily volcanic daily SO_2 emissions, 1.0° x 1.0°, are implemented in the model for simulations presented in Chapters 4 and 5, and derived from POLar study using Aircraft, Remote sensing, surface measurements and modelling of Climate, chemistry, Aerosols, and Transport (POLARCAT) model inter-comparison (POLMIP, *Emmons et al. (2015)*) project.

Volcanic daily emissions, 1.0° x 1.0°, from CAMS are used in the 2019 runs (Chapter 6). The volcanic gas emission data are obtained from the Network for Observation of Volcanic and Atmospheric Change (NOVAC) network, and for each volcano, data are combined with meteorological information to derive daily statistics of total SO_2 emission for each volcano. The gas emission is calculated using the Scanning differential optical absorption spectroscopy (ScanDOAS) technique described in *Galle et al. (2010)*.

3.4.4 DMS emissions

Dimethyl sulphide (DMS) emissions are also used in the runs presented in Chapters 4,5 6, which is an important source of SO_2 and SO_4^{2-}. Monthly oceanic DMS emissions derived from *Lana et al. (2011)* and the implementation in the model is described in Marelle et al. (2017).

3.4.5 Dust and lighting NO_x emissions

Dust emissions are also calculated online in the model, and they are based on the Goddard Chemistry Aerosol Radiation and Transport (GOCART) emission scheme *(Chin et al., 2002)*, considering modelled 10 m wind speed and soil water content.

Online lightning NO_x emissions are based on a scheme by *Barth et al. (2014)*. However, these are not essential emissions for regional simulations over Alaska and the broader Arctic region due to a lack of lightning activity (lack of local thunderstorms) during wintertime.

3.5 Observations: Routine monitoring sites and campaign data

Different in-situ databases are used at Arctic-wide or regional scale, providing detailed observations of meteorological and aerosol composition data to evaluate the different simulations performed with WRF-Chem. All the different databases used in this thesis are described in detail in Chapters 4, 5 and 6.

Briefly, aerosol concentrations, such as total PM2.5 or speciated measurements such as NO_3^-, SO_4^{2-}, Na^+, Cl^-, NH_4^+, OC, EBC, and meteorological, such as temperature, wind speed and direction, either at the surface or different altitudes are used. This includes observations from Environmental Protection Agency (EPA), European Monitoring and Evaluation Programme dataBASE (EBAS, http://ebas.nilu.no), Interagency Monitoring of Protected Visual Environments (IMPROVE, (http://views.cira.colostate.edu/fed/QueryWizard/Default.aspx), NOAA / Earth System Research Laboratories (ESRL) / Global Monitoring Laboratory (GMD), University of Wyoming.

Case studies are also presented in Chapters 4, 5 and 6, focusing on particular periods when field campaigns took place:

Field campaign at Utqiaġvik: This campaign focused on improving our understanding about aerosol chemical composition and heterogeneous processing during wintertime in the Arctic due to changes on marine emissions coupled with transported anthropogenic pollution. During the field campaign (January – February 2014) at Utqiaġvik atmospheric particles were collected northeast of Utqiaġvik town *(Kirpes et al., 2018, 2019)*. The analysed samples were collected either during daytime or nighttime, and only when wind directions were between 75 and 225 degrees, to exclude local pollution. See Chapter 1 for the location of Utqiaġvik.

pre-ALPACA campaign: Detailed observations of aerosols, trace gases and aerosol distribution (e.g. BC, O_3, NO_2, CO, NO) were collected during the French pre-ALPACA campaign (November – December 2019) at Fairbanks downtown and led by researchers from six French laboratories and the University of Alaska Fairbanks (UAF) *(Simpson et al., 2019; Maillard et al., 2022; Cesler-Maloney et al.)*. It took place before the main ALPACA campaign, in January–February 2022 as part of the PACES/IGAC (Pollution in the Arctic: Climate, Environment and Societies/ International Global Atmospheric Chemistry) initiative *(Simpson et al., 2019)*. The aim of ALPACA is to provide insights on wintertime Arctic air pollution in urban areas. Detailed observations will help us to better understand how secondary aerosols are formed under dark/cold conditions and the influence of wintertime meteorological conditions. This knowledge can be applied in the wider Arctic where detailed observations are less available to address air pollution impacts due to increasing local sources because of the rapid economic development in the Arctic. See Chapter 1 for location of Fairbanks. Further information about the observations collected during and the aim of the pre-ALPACA campaign are given in Chapter 6.

Statistical tools, such as bias and Root-Mean-Square Error (RMSE) are used through out the thesis to evaluate the model performance with regard to observed meteorological parameters and aerosols. Model output files are every 3h, due to limited storage space. The

model output parameters, such as temperatures, winds, aerosols are not averaged over the 3h, but the output model parameters are the value at the specific moment. Note that in the model parameters such as precipitation or deposition are accumulated.

Observations are usually every 5 or 30 minutes, hourly or daily averages, but not always available during all simulation days. For example, to compare the model results with daily averaged observations, the corresponding model daily averages are calculated. In both cases, only the model results which correspond to same observed date/period are used. In case the observations are at higher resolution then the hourly averages are calculated and observations and model output corresponding to the same period are used. Here, two methods are used to calculate biases (Equations 3.1 and 3.2).

$$\text{bias} = \text{model\_average} - \text{observations\_average} \tag{3.1}$$

$$\text{bias}_\text{i} = \text{model}_\text{i} - \text{observations}_\text{i} \tag{3.2}$$

In the first method (Eq. 3.1) first the average value of the model outputs and observations are calculated and then the differences. Note that the observations and model include the same number of data points (i), which correspond to the same time and date periods. For the second method (Eq. 3.2), first the differences (biases) between the model and observations are calculated point by point (for each i) and then the average of these differences are calculated separately. These two methods generally lead to similar results, with only very small differences between the two (less than 1%).

To calculate RMSE the following expression is used:

$$\text{RMSE} = \sqrt{\frac{1}{n}\sum_{i=1}^{n}(x_{\text{mod,i}} - x_{\text{obs,i}})^2} \tag{3.3}$$

where x_{mod} and x_{obs} are the modelled and observed parameter and n the total number of points.

Chapter 4

Wintertime Arctic Haze and sea-spray aerosols

The Arctic is influenced by enhanced concentrations of air pollutants from mid-latitudes source regions, during winter and spring *(Rahn and McCaffrey, 1980; Quinn et al., 2002a)*. However, there are also local anthropogenic and natural sources within Arctic, which are contributing to Arctic Haze during winter and the winter-spring transition *(Schmale et al., 2018; Kirpes et al., 2019)*. Regional and global models tend to underestimate wintertime Arctic Haze composition, such as SO_4^{2-} *(Whaley et al., 2022b)*. SSA are an important contributor to total aerosol burden at coastal Arctic sites, but their contribution to Arctic Haze has not been examined in detail *(Kirpes et al., 2019)*.

This study first investigates the ability of the model to simulate Arctic Haze at remote Arctic sites during wintertime. A particular focus of is on SSA, to improve our understanding about processes affecting modelled SSA and their contribution to Arctic Haze over the wider Arctic. A more detailed regional study over northern Alaska, following a field campaign which took place at Utqiaġvik during winter 2014 *(Kirpes et al., 2018, 2019)*. The role of processes, such as dry deposition and sea-ice fraction, on SSA are also examined, as well as production of marine organics associated with SSA. It is discussed whether other sources of SSA, such as blowing snow and frost flowers, might be important for sub-micron SSA at coastal Arctic sites during wintertime.

This study is submitted as: Ioannidis, E., Law, K. S., Raut, J.-C., Marelle, L., Onishi, T., Kirpes, R. M., Upchurch, L., Massling, A., Skov, H., Quinn, P. K., and Pratt, K. A.: Modelling wintertime Arctic Haze and sea-spray aerosols, EGUsphere [preprint], https://doi.org/10.5194/egusphere-2022-310, 2022. The paper is presented in the following sections. The Supplementary Material is given in Appendix A.

4.1 Modelling wintertime Arctic Haze and sea-spray aerosols

4.1.1 Abstract

Anthropogenic and natural emissions contribute to enhanced concentrations of aerosols, so-called Arctic Haze in the Arctic winter and early spring. Models still have difficulties reproducing available observations. Whilst most attention has focused on the contribution of anthropogenic aerosols, there has been less focus on natural components such as sea-spray aerosols (SSA), including sea-salt sulphate and marine organics, which can make an important contribution to fine and coarse mode aerosols, particularly in coastal areas. Models tend to underestimate sub-micron and overestimate super-micron SSA in polar regions, including in the Arctic region. Quasi-hemispheric runs of the Weather Research Forecast model, coupled with chemistry model (WRF-Chem) are compared to aerosol composition data at remote Arctic sites to evaluate the model performance simulating wintertime Arctic Haze. Results show that the model overestimates sea-salt (sodium and chloride) and nitrate and underestimates sulphate aerosols. Inclusion of more recent wind-speed and sea-surface temperature dependencies for sea-salt emissions, as well as inclusion of marine organic and sea-salt sulphate aerosol emissions leads to better agreement with the observations during wintertime. The model captures better the contribution of SSA to total mass for different aerosol modes, ranging from 20-93% in the observations. The sensitivity of modelled SSA to processes influencing SSA production are examined in regional runs over northern Alaska (United States) where the model underestimates episodes of high SSA, particularly in the sub-micron, that were observed in winter 2014 during field campaigns at the Barrow Observatory, Utqiaġvik. A local source of marine organics is also included following previous studies showing evidence for an important contribution from marine emissions. Model results show relatively small sensitivity to aerosol dry removal with more sensitivity (improved biases) to using a higher wind speed dependence based on sub-micron data reported from an Arctic cruise. Sea-ice fraction, including sources from open leads, is shown to be a more important factor controlling modelled super-micron SSA than sub-micron SSA. The findings of this study support analysis of the field campaign data pointing out that open leads are the primary source of SSA, including marine organic aerosols during wintertime at the Barrow Observatory, Utqiaġvik. Nevertheless, episodes of high observed SSA are still underestimated by the model at this site, possibly due to missing sources such as SSA production from breaking waves. An analysis of the observations and model results does not suggest an influence from blowing snow and frost flowers to SSA during the period of interest. Reasons for the high concentrations of sub-micron SSA observed at this site,

higher than other Arctic sites, require further investigation.

4.1.2 Introduction

The Arctic region is warming faster than any other region on Earth *(IPCC, 2021)*. Greenhouse gases, in particular carbon dioxide, and short-lived climate forcers like methane, ozone and, aerosols have a significant impact on the environment, with a particularly strong warming effect in the Arctic region *(AMAP, 2015; IPCC, 2021)*. This region is influenced by enhanced concentrations of aerosols (including sulphate (SO_4^{2-}), nitrate (NO_3^-), black carbon (BC) and organic aerosols (OA)) during winter and spring, a phenomenon called Arctic Haze *(Rahn and McCaffrey, 1980; Barrie et al., 1994; Quinn et al., 2002b)*. Transport of aerosols and their precursors from mid-latitudes anthropogenic emissions contribute to Arctic Haze *(Heidam et al., 2004; Quinn et al., 2007b; Law et al., 2014)*. Local within and near-Arctic anthropogenic and natural sources also contribute to Arctic Haze during wintertime and the winter-spring transition *(Law et al., 2017; Schmale et al., 2018; Kirpes et al., 2019)*. During wintertime 14% of organic mass at Alert originated from gas flaring in northern Russia *(Leaitch et al., 2018a)*. For example, gas flaring from Russia contributes to black carbon at Alert (northern Canada) and Utqiaġvik (northern Alaska) *(Stohl et al., 2013b; Qi et al., 2017; Xu et al., 2017; Marelle et al., 2018)*. Metal industry and combustion sources, such as power generation, from Siberia (e.g. Kola peninsula) were identified as sources of pollution at Villum station, Greenland during winter and spring *(Nguyen et al., 2013)*. Metal smelting from Siberia also contributes to SO_4^{2-} at Zeppelin during wintertime *(Hirdman et al., 2010)*. A more recent study by *Winiger et al. (2019)* showed that during wintertime Arctic sites, such as Utqiaġvik, Alert, Zeppelin, are influenced by fossil fuel combustion emissions. Petroleum extraction on the North Slope of Alaska, including Prudhoe Bay, was found to influence aerosol distributions, composition, and particle growth at Utqiaġvik, with enhanced growth of ultrafine particles *(Kolesar et al., 2017; Kirpes et al., 2018)*.

Natural aerosol sources also contribute to Arctic Haze such as dust, volcanic emissions and and sea-spray aerosols (SSA) *(Rahn et al., 1977; Barrie and Barrie, 1990; Quinn et al., 2002b; Stone et al., 2014; Huang et al., 2015; Zwaaftink et al., 2016; Kirpes et al., 2018)*. Dust is not only transported from mid-latitudes sources (Asia, Africa), but it is also produced within the Arctic, with local dust contributing up to 85% to total dust burden in the Arctic *(Zwaaftink et al., 2016)*. During wintertime, fresh SSA (including sodium ions (Na^+), chloride ions (Cl^-), sea-salt (ss)-SO_4^{2-} and marine organics) can be a significant fraction of particulate matter, 40% of super-micron (1 to 10 µm particle diameter) and 25% of sub-micron (up to 1 µm particle diameter) *(Quinn et al., 2002b)*. While studies have largely focused on

anthropogenic sources of Arctic Haze influencing, in particular BC and SO_4^{2-}, there have been fewer studies on the contribution of SSA, the focus of this study. The primary mechanism leading to the formation of SSA is bubble bursting (jet-drop and film-drop formations) on the sea surface due to wind stress during whitecap formation *(Monahan et al., 1986a)*. For this reason, wind speed is a significant parameter affecting SSA productivity *(Russell et al., 2010; Saliba et al., 2019)*. Arctic warming is leading to a decrease of sea-ice during summertime and, as a result, less and thinner sea-ice is forming during wintertime *(Stroeve et al., 2012a)*. Thus, new SSA sources, such as open ocean and leads, may contribute more in the future to the total aerosol burden over Arctic coastal regions, impacting CCN concentrations and radiative forcing *(Ma et al., 2008)*.

A detailed analysis of in-situ aerosol composition in Utqiaġvik revealed that, due to long-range transport from the North Pacific (due to strong winds in source regions, such as in the Pacific Ocean), sub-micron SSA peaks in winter and early spring, while super-micron SSA peaks in summer, due to sea-ice retreat *(Quinn et al., 2002b)*. However in winter, super-micron SSA mass concentrations increase in the presence of open leads, while sub-micron SSA appear to be more influenced by long-range transport *(May et al., 2016; Kirpes et al., 2019)*. *Kirpes et al. (2018)* analysed atmospheric particle samples collected in winter 2014 in Utqiaġvik. They found that the samples were influenced by air masses from the Arctic Ocean to the north and Prudhoe Bay oilfields to the east. Aged SSA were always internally mixed with secondary SO_4^{2-}, or with both SO_4^{2-} and NO_3^- and reduced chlorine, suggesting anthropogenic influence from background Arctic Haze or Alaskan oil field emissions.
Kirpes et al. (2019) concluded that fresh SSA, based on the presence of Na^+ and Cl^- in ratios similar to seawater, including marine organic aerosols, were produced locally from open leads, with indications of secretions from sea ice algae and bacteria based on observed enrichments in carbon/sodium ($C:Na^+$) ratios. Previous studies of the Arctic and North Atlantic during wintertime and the winter-spring transition also showed that the majority of sub-micron organic mass (OM) is highly correlated with Na^+ concentrations *(Russell et al., 2010; Shaw et al., 2010; Frossard et al., 2011; Leaitch et al., 2018a)*. Frost flowers with organic-salt coatings have also been proposed as a possible source of wintertime SSA *(Xu et al., 2013)*, although *Kirpes et al. (2019)* found no evidence of frost flowers or blowing snow as a potential source, supporting the findings of older studies *(Roscoe et al., 2011)*.

Regional and global models have difficulties capturing wintertime Arctic Haze composition and often underestimate SO_4^{2-} and BC *(Bond et al., 2013b; Eckhardt et al., 2015; Sato et al., 2016; Schwarz et al., 2017; Whaley et al., 2022b)*, while the contribution of SSA to Arctic Haze remains poorly evaluated *(Kirpes et al., 2019)*. Representation of SSA concentrations

in models has been improved over recent years, but with less focus on the Arctic winter. For example, SSA source functions with updated dependencies on wind speeds, sea surface temperatures (SSTs) or salinity *(Revell et al., 2019; Jaeglé et al., 2011; Sofiev et al., 2011)* have led to improve simulation of super-micron SSA. However, sub-micron SSA is often still underestimated *(Sofiev et al., 2011; Huang and Jaeglé, 2017)* and sub-micron emissions of SSA from frost flowers and blowing snow have been included in models *(Xu et al., 2013, 2016; Huang and Jaeglé, 2017; Rhodes et al., 2017)*. Modelled SSA including a source of frost flowers captures better monthly SSA concentrations at Alert during wintertime, while a source of blowing snow overestimates observations *(Huang and Jaeglé, 2017; Marelle et al., 2021)*. At Utqiaġvik during January and February a source of blowing snow improves modelled SSA; however it still cannot explain the high observed SSA, while the blowing snow explains high observed SSA in the Antarctic *(Huang and Jaeglé, 2017)*.

In this study, the performance of the Weather Research Forecast model, coupled with chemistry (WRF-Chem), is examined with regard to its ability to simulate Arctic Haze composition as well as SSA components, including ss-SO_4^{2-} and marine organics. The model is first evaluated against available data over the wider Arctic, and the sensitivity to more recent treatments of SSA wind speed and SST dependencies, is investigated. Inclusion of a marine organic source is also examined *(Fuentes et al., 2010, 2011)*. The findings of *Kirpes et al. (2019)* are used as a basis for a more focused regional study to evaluate modelled Arctic wintertime aerosol composition in northern Alaska. The sensitivity of model results to processes influencing SSA production and concentrations are investigated including aerosol dry deposition, wind speed dependence and sea-ice fraction. Missing local sources of marine organics are also examined based on the findings of *Kirpes et al. (2019)*.
A companion paper, *Ioannidis et al., (2022)* (in prep.), examines the contribution of remote and regional anthropogenic emissions to Arctic BC in northern Alaska and northern Russia during wintertime.

The model setup, including the emissions are described in Section 4.2.3. The observed aerosol composition used to evaluate the model performance are introduced in Section 4.2.4. The model runs, including sensitivity simulations, together with results are presented in Sections 4.2.5 and 4.2.6. First, in Section 4.2.5, simulated Arctic Haze, focusing on SSA, is evaluated at remote Arctic sites. Second, in Section 4.2.6, the results from the regional study over northern Alaska during wintertime and sensitivity of results to processes influencing SSA production in the model are presented. The implications of our findings for the simulation of Arctic Haze aerosols and conclusions are presented in Section 6.

4.1.3 WRF-Chem

4.1.3.1 Model Setup

WRF-Chem chemical transport model version 3.9.1.1 is used to simulate quasi-hemispheric and regional Arctic Haze aerosols and to examine local SSA sources over northern Alaska. WRF-Chem is a fully coupled, online meteorological and chemical transport mesoscale model *(Grell et al., 2005; Fast et al., 2006)*. Recent improvements in the WRF-Chem model over the Arctic are included in the version used in this study *(Marelle et al., 2017)*. The model setup, including meteorological and chemical schemes, is shown in **Table 4.1**. Briefly, Yonsei University (YSU - boundary layer), Model Version 5 similarity (MM5 - surface layer) and Noah-Multiparameterization Land Surface Model (NOAH MP, land surface model) are used. More details about the NOAH MP scheme are given in APPENDIX A.1.

All the various processes for aerosols in the atmosphere, like nucleation, evaporation, coagulation, condensation, dry deposition, aerosol/cloud interactions and aqueous chemistry, are included in the Model for Simulating Aerosol Interactions and Chemistry (MOSAIC, *Zaveri et al. (2008)*) scheme. MOSAIC treats all the major aerosol species, such as SO_4^{2-}, NO_3^-, Cl^-, ammonium (NH_4^+), Na^+, BC, and OA. The size distribution of each aerosol species is represented by eight bins, from 39 nm to 10 µm. Each bin is assumed to be internally mixed, and both mass and number are simulated. The applied MOSAIC version includes secondary organic aerosol formation (SOA) from the oxidation of anthropogenic and biogenic species *(Shrivastava et al., 2011b; Marelle et al., 2017)* and is combined with SAPRC-99 gas-phase chemistry. In the base model, OA is the sum of SOA and anthropogenic emissions of organic matter (OM). Aerosol sedimentation in MOSAIC is calculated throughout the atmospheric column based on the Stokes velocity scheme, as described in *Marelle et al. (2017)*.

4.1.3.2 Emissions

This section provides details about the emissions that are used in the simulations. More details are provided about SSA emissions since this is the focus of this study.

Anthropogenic and natural emissions

Anthropogenic emissions are from the Evaluating the Climate and Air Quality Impacts of Short-Lived Pollutants version 6 (ECLIPSE v6b) inventory, with a resolution of 0.5° x 0.5° *(Whaley et al., 2022b)*, including emissions of OM. Emissions of dimethyl sulfide (DMS),

Table 4.1: *WRF-Chem model setup.*

parametrisation scheme	Options
Physics (WRF)	
Planetary boundary layer	Yonsei University (YSU) - *(Hong et al., 2006)*
Surface layer	Pennsylvania State / NCAR Mesoscale Model Version 5 (MM5) similarity *(Grell et al., 1994; Jiménez et al., 2012)*
Land surface	NOAH MP *(Niu et al., 2011a)*
Microphysics	Morrison *(Morrison, 2009)*
SW & LW radiation	Rapid Radiative Transfer Model (RRTMG - *Iacono and D. (2008)*)
Cumulus parameterization	Kain-Fritsch with cumulus potential (KF-CuP) *(Berg et al., 2013)*
Chemistry (WRF-Chem)	
Aerosol model	MOSAIC 8-bins *(Zaveri et al., 2008)*
Gas-phase chemistry	Statewide Air Pollution Research Center SAPRC-99 modified with added dimethyl sulphide chemistry *(Carter, 2000; Marelle et al., 2017)*
Photolysis	Fast-J *(Wild et al., 2000)*
Sea-spray emissions	*Gong et al. (1997)*

mineral dust, and lightning NO_x are calculated online in the model (see *Marelle et al. (2017)* and references therein). Biogenic emissions for 2014 are calculated online using Model of Emissions of Gases and Aerosol from Nature (MEGAN) model *(Guenther et al., 2012)*.

Sea-spray emissions

In the control simulation, sea-salt emissions of Na^+ and Cl^- are included. They are calculated per particle radius, with 1000 sub-bins per MOSAIC bin, using the density function dF/dr (in particles m^{-2} s^{-1} µ m^{-1}) from *(Gong et al., 1997)* (G97 from now on) which represents the rate of seawater droplets form per unit area (sea surface) and per increase of particle radius and its derived from the source function based on laboratory experiments described in *Monahan et al. (1986a)* (MO86 from now on):

$$\frac{dF}{dr} = 1.373 \times U_{10}{}^{3.41} \times r^{-3}(1 + 0.057 \times r^{1.05}) \times 10^{1.19e^{-B^2}} \tag{4.1}$$

where F is a function of U and r, r is the particle radius at relative humidity (RH) equal to 80%, U the 10m-elevation wind speed and $B = \frac{(0.380 - logr)}{0.650}$. The source function is applied for particles with dry diameters of 0.45 µm or more. For particles with dry diameters less

than 0.45 µm, a correction is applied to the formula based on *O'Dowd et al. (1997)*. This approach is based on the whitecap method, where the emission flux scales linearly with the fraction of ocean area covered by whitecaps. Over open ocean, the whitecap fraction, W(U), is determined as a function of wind speed (*Monahan and Muircheartaigh (1980)*; MO80 from now on):

$$W(U) = 3.84 \times 10^{-6} \times U_{10}{}^{3.41} \tag{4.2}$$

This expression for W(U) is included implicitly in Equation (4.1) following details provided in MO80. In the base version of WRF-Chem SSA emissions are calculated for every grid cell, which is open ocean or salt-water lakes. In this study, the grid cell which is covered by sea-ice is considered and then the fraction of that ice-free grid is used. In this way, SSA emissions from open leads are taken into account.

Figure 4.1: *WRF-Chem simulation domains: d1 is the 100km domain and d2 is the 20km domain.*

4.1.3.3 Simulations

Two simulation domains on a polar stereo-graphic projection are used in this study, as shown in **Figure 4.1**. The first (parent) domain (d1) covers a large part of the Northern Hemisphere with 100 × 100 km horizontal resolution. The boundary and initial conditions, are derived from National Centres for Environmental Prediction Final meteorological re-

analysis data (NCEP FNL 1°x1°), (*National Centers for Environmental Prediction, National Weather Service, NOAA, U.S. Department of Commerce (2000)* and Model for OZone And Related chemical Tracers (MOZART, *Emmons et al. (2010)*) for atmospheric trace gases and aerosols. The nested domain (d2), run at horizontal resolution of 20 × 20 km, covers continental Alaska, a small area of northwest Canada, and the Chukchi and Beaufort Seas (see Figure 1). 50 vertical levels and grid nudging are used for the 100 km resolution domain, while calculating spectral nudging parameters as in *Hodnebrog et al. (2019)*, is implemented in the nested domain. WRF-Chem temperatures and winds are nudged at each dynamical step to the reanalysis, which are updated every 6 hours, above the atmospheric boundary layer.

The simulations performed in this study are discussed in sections 4.2.5 and 4.2.6. Simulations at 100 km are run for 4 months from November 2013 until the end of February 2014, with the first two months considered as spin-up. The model is run at 20 km for two different periods (23–28 January 2014 and 24–28 February 2014) corresponding to the campaign which took place in Utqiaġvik, and described earlier (*Kirpes et al. (2018, 2019)*, KRP18 and KRP19 from now on, respectively, see also sub-section 4.2.4.2). For these simulations, the initial, and boundary conditions are derived from the quasi-hemispheric simulation. A series of sensitivity runs are performed to examine processes affecting SSA emissions over northern Alaska. They are summarized in **Table 4.3** and discussed in detail in Section 4.2.6. At 20 km for all the simulations, 4 days prior to the beginning of the campaign considered spin up. In all runs, the model results are output every 3h.

4.1.4 Aerosols

4.1.4.1 Routine monitoring sites

Surface mass concentration data (for aerodynamic diameters (defined as d_a) $\leq$ 2.5 µm and d_a < 10 µm), from EMEP (European Monitoring and Evaluation Programme) dataBASe (EBAS - http://ebas.nilu.no) for Zeppelin, Ny-Ålesund, Norway (78.9N, 11.88W) and Alert, Canada (82.5N, -63.3W), are used to evaluate the quasi-hemispheric model simulations together with data from Villum Research Station, Station Nord, Greenland (81.6N, -16.7W), referred to as Villum from now on (reporting total suspended particulates). The data are collected on a daily (Zeppelin) and weekly (Villum, Alert) basis. At Alert, and Zeppelin *(Aas et al., 2021)*, observations for Na^+, Cl^-, NH_4^+, NO_3^- and SO_4^{2-} measured with ion chromatography are used *(Sharma et al., 2019)*. At Villum, the same observations are collected using a filter-pack over a week and analysed using by ion-chromatography (Cl^-, SO_4^{2-}), cat-ion ionchromatograph (Na^+) and segmented flow analysis (NH_4^+). For all the EBAS stations,

the units of inorganic aerosols (NH_4^+, SO_4^{2-}, NO_3^-) are converted to model units (μgm^{-3}), using the ratio of molar weights of NH_4^+, NO_3^-, SO_4^{2-} to molar weights of nitrogen or sulphur, respectively. With regard to measurement uncertainties, EBAS documentation notes, in the case of Alert only, that there are uncertainties of around 33% and 36% in Na^+, SO_4^{2-}, NO_3^- and Cl^-, respectively, and higher uncertainties (43%) for NH_4^+.

Surface mass concentration data, diameter less than 2.5 μm ($r_d \leq 2.5$ μm), from the Interagency Monitoring for Protected Visual Environments (IMPROVE) database is also used for model evaluation for Simeonof (55.3N, -160.5W), a sub-Arctic site on the Aleutians islands, south of Alaska and an inland site, Gates of the Arctic (66.9N, -151.5W) which is located south-east of Utqiaġvik. The samples are collected on-site (e.g. Simeonof site) over 24 hours every three days (http://views.cira.colostate.edu/fed/QueryWizard/Default.aspx, *Malm et al. (1994)*). At these two sites observations of Na^+, Cl^-, OC, NO_3^- and SO_4^{2-} are used. To compare with the OC observations at the two Alaskan sites modelled OA is divided by 1.8, the reported ratio of OM/OC in the documentation for these two stations *(Malm et al., 1994)*. In this study, mass concentration data with diameter ≤ 2.5 μm are defined as fine mode aerosols, while diameter < 10 μm then are defined as coarse mode aerosols.

Sub-micron ($d_a < 1.0$μm) and super-micron ($1.0 < d_a < 10$ μm) surface mass concentration data from the National Oceanic and Atmospheric Administration (NOAA) Barrow observatory (71.3N, -156.8W), near Utqiaġvik town, is also used in this study, with daily and weekly temporal coverage, respectively. The sampling site is located 8 km northeast of Utqiaġvik, 20 m above mean sea level (msl), with a prevailing, east-northeast wind off the Beaufort Sea. Concentration data (Na^+, Cl^-, NH_4^+, NO_3^- and SO_4^{2-}) are determined by ion chromatography *(Quinn et al., 1998)* and are sampled only for wind directions between 0 and 130 degrees (with 0 degrees indicating north). According to *Quinn et al. (2002b)* measurement uncertainties of SSA components and SO_4^{2-} are below 1%, while for NH_4^+ they are 7.8%. Observed ss-SO_4^{2-} is calculated from observed Na^+ concentrations and the mass ratio of SO_4^{2-} to Na^+ in seawater of 0.252 *(Bowen et al., 1979; Calhoun et al., 1991)*.

The model Stokes diameter (r_d) is converted to aerodynamic diameter using the *Seinfeld and Pandis (1998)* formula. Thus, the diameter of modelled sub-micron particles is up to 0.73 μm (including the first four MOSAIC bins and a fraction of the 5th bin), and super-micron particle diameters are between 0.73 to 7.3 μm (fraction 5th bin, 6th and 7th bins and fraction 8th bin). Seven MOSAIC bins and a fraction of the 8th bin are used (modelled stokes $r_d \leq$ 7.3 μm) to compare with Alert and Zeppelin observations (aerodynamic $d_a < 10$ μm, coarse mode). All model aerosol bins are used to compare with observations at Villum, where the observations are reported as total suspended particulates (TSP), i.e. there is no cutoff. For

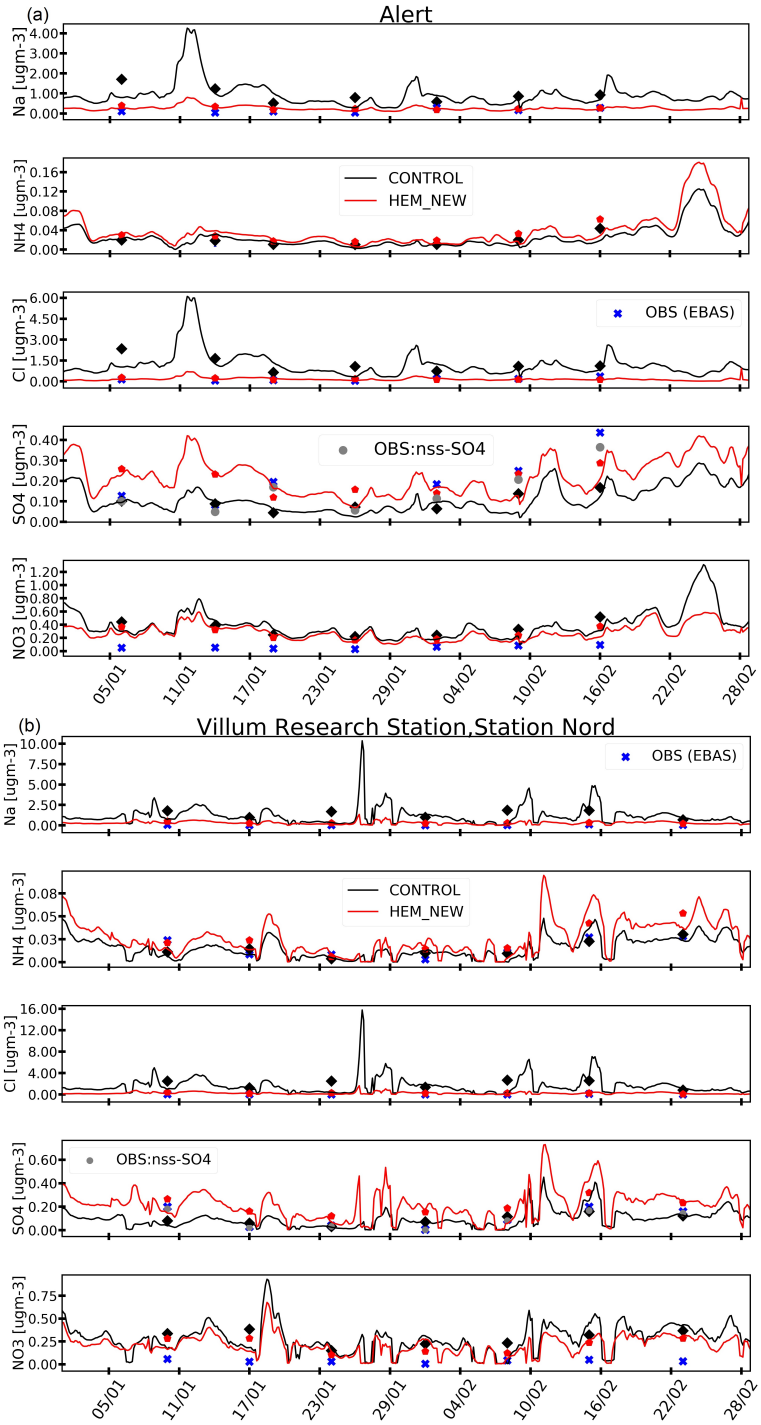
(a)
Alert
Na [ugm-3]
NH4 [ugm-3]
Cl [ugm-3]
SO4 [ugm-3]
NO3 [ugm-3]
CONTROL
HEM_NEW
OBS (EBAS)
OBS:nss-SO4
05/01
11/01
17/01
23/01
29/01
04/02
10/02
16/02
22/02
28/02
(b)
Villum Research Station,Station Nord

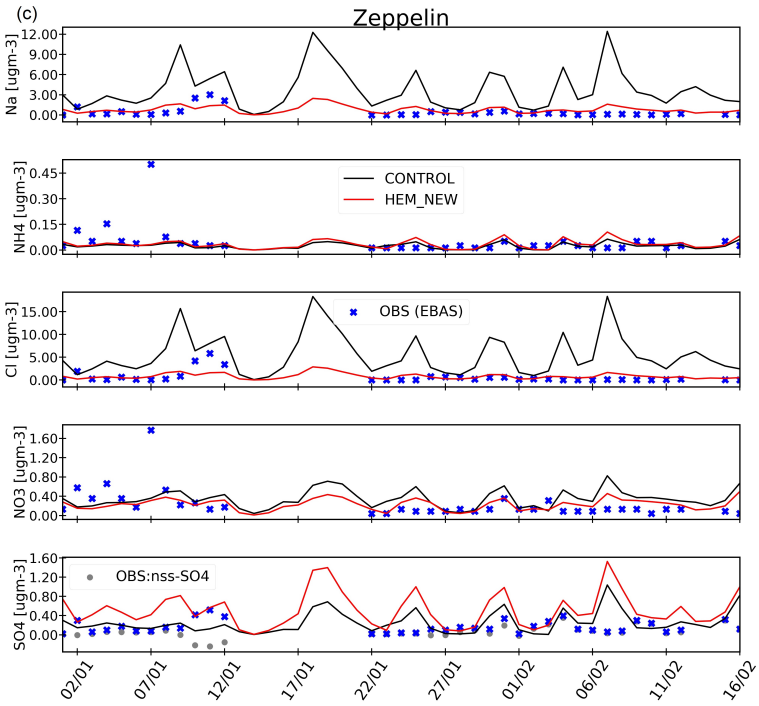

Figure 4.2: *Evaluation of modelled aerosol composition (runs CONTROL and HEM_NEW) against in-situ observations of (a) coarse mode aerosols ($d_a < 10$ μm) at Alert, Canada (standard temperature pressure (STP) conditions), (b) TSP aerosols ($d_a \leq 10$ μm) at Villum, Greenland and (c) coarse mode aerosols ($d_a < 10$ μm) at Zeppelin, Norway in UTC. The black line shows model results from the CONTROL run; the red line shows the HEM_NEW run, while observations are shown as blue crosses. Villum and Alert observations are weekly averages, and the corresponding model weekly averages are shown as black diamonds for CONTROL and red pentagons for HEM_NEW. Zeppelin observations are daily 24h averages. Observations are shown only when they are available. See the text for details about the observations and model runs.*

each site, modelled aerosols are estimated at the same conditions (temperature, pressure) as the reported observations. Overall, particles at different size ranges (up to 1.0 μm, 2.5 μm, and 10 μm) are used to validate the model performance in each domain.

4.1.4.2 Campaign data

Details about the field campaign (January 23–27 and February 24–28, 2014) measurements near Utqiaġvik, Alaska can be found in KRP18 and KRP19. Briefly, atmospheric particles were collected using a rotating micro-orifice uniform deposition impactor located 2 m above the snow surface at a site located 5 km across the tundra from the NOAA Barrow Observatory and inland from the Arctic Ocean. The sampled particles were analysed by computer-controlled scanning electron microscopy with energy scattering X-ray spectroscopy (CCSEM-EDX) to determine the individual particle morphology and elemental composition. The analysed samples were collected either during daytime or nighttime and

only when wind directions were between 75 and 225 degrees, corresponding to minimise local pollution influence. Data analysis provided information about the different chemical components as a fraction of the total number of particles sampled.

4.1.5 Processes influencing SSA over the wider Arctic and their contribution to wintertime Arctic aerosols

This section focuses on evaluating the capability of the model to simulate Arctic Haze aerosols during wintertime and improving model treatments of SSA. Briefly, in the base simulation (CONTROL), sea-salt emissions are calculated using the G97 parametrisation scheme, including the MO80 whitecap method. All the updates described below are included in a new quasi-hemispheric simulation (HEM_NEW) with the aim to improve the model. This includes addition of marine organics *(Fuentes et al., 2010)*, using a more recent whitecap method *(Salisbury et al., 2014)*, including the dependence of SSA emissions on SST *(Jaeglé et al., 2011)*, and the addition of a ss-SO_4^{2-} component, based on *Kelly et al. (2010)*. HEM_NEW simulation is then evaluated (sub-section 4.2.5.6) compared to CONTROL and the observations at the different sites followed by a discussion of the new results.

4.1.5.1 Anthropogenic and natural aerosols in the Arctic

First considering the observations, at remote sites such as Alert (**Fig 4.2a**), observed Na^+, Cl^- and NO_3^- coarse mode mass concentrations do not exceed 0.3, 0.5 and 0.09 μ g m^{-3}, respectively, during the study period. Total SO_4^{2-} (sum of ss-SO_4^{2-} and nss-SO_4^{2-}) reach 0.44 μ g m^{-3}, which is mostly nss-SO_4^{2-}, as ss-SO_4^{2-} does not exceed 0.09 μgm^{-3}, likely to be due to long-rage transport from sources in north-central, western, northwest Russia and Europe *(Leaitch et al., 2018a)*. Similar magnitudes have been reported in previous studies during winter months *(Leaitch et al., 2018a)*. NH_4^+ peaks at 0.06 μgm^{-3} and originates from Russia and Europe during winter *(Leaitch et al., 2018a)*. At Villum (**Fig 4.2b**), observed TSP Na^+, Cl^- and NO_3^- reach up to 0.12, 0.13 and 0.06 μ g m^{-3}, respectively. These concentrations are lower than at Alert which could be explained by the fact that during winter the sea surrounding Villum station is frozen *(Nguyen et al., 2013)*. Total SO_4^{2-} does not exceed 0.2 μ g m^{-3} and is mostly nss-SO_4^{2-} (up to 0.18 μ g m^{-3}), while ss-SO_4^{2-} does not exceed 0.03 μ g m^{-3}. At Villum, SO_4^{2-} peaks during wintertime *(Massling et al., 2015)* and is the dominant component of Arctic Haze at this site *(Lange et al., 2018)*. NH_4^+ concentrations at Villum are up to 0.1 μ g m^{-3}. In the high Arctic, Na^+ could potentially also originate from anthropogenic sources which could account for up to 35% of total Na^+ *(Barrie and Barrie, 1990)*. Note that this source is not included in the model, or in models generally. Higher

Na^+, Cl^- and NO_3^- concentrations are observed at Zeppelin (coarse mode) reaching up to 3.0, 5.9 and 1.8 μ g m^{-3}, respectively (**Fig. 4.2c**). Total SO_4^{2-} does not exceed 0.8 μ g m^{-3} and might originate from metal smelting in Siberia *(Hirdman et al., 2010)*. ss-SO_4^{2-} contributes up to 0.8 μ g m^{-3} of the total SO_4^{2-}. Note that, in some cases, nss-SO_4^{2-} has small negative concentrations, due to depletion of ss-SO_4^{2-} through fractionation processes *(Quinn et al., 2002b)*. Observed NH_4^+ does not exceed 0.5 μ g m^{-3} during the study period.

At Simeonof, an ice-free sub-Arctic island in south western Alaska, high concentrations of fine mode Na^+ and Cl^- are observed of up to 2.1 and 1.0 μ g m^{-3}, respectively (**Fig. 4.3a**), especially at the beginning of January 2014, with low values of NO_3^- (peaking at 0.25 μ g m^{-3}). Total SO_4^{2-} reaches 1.0 μ g m^{-3} and is mostly nss-SO_4^{2-} (0.9 μ g m^{-3}), while the contribution of ss-SO_4^{2-} is smaller (up to 0.3 μ g m^{-3}). Lower concentrations of fine mode Na^+ and Cl^- (up to 0.35 μ g m^{-3}) are observed at Gates of the Arctic (**Fig. 4.3b**), a non-coastal site located 404 km south-east of Utqiaġvik in the Brooks Range Mountains, while NO_3^- peaks at 0.45 μ g m^{-3}. Total SO_4^{2-} peaks at 0.64 μ g m^{-3} and 0.56 μgm^{-3} is nss-SO_4^{2-} possibly due to local anthropogenic emissions originating from the North Slope of Alaska oilfields which may affect the measurements although this site is located inland (391 km) south of the oilfields. The contribution of ss-SO_4^{2-} is insignificant (no more than 0.08 μ g m^{-3}) at this site.

At Utqiaġvik, observed super-micron ($1.0 < d_a < 10.0$ μm) Na^+ and Cl^- concentrations reach 1.2 μ g m^{-3} (**Fig. 4.4b**), while NO_3^- peaks at 0.2 μ g m^{-3}. Super-micron SO_4^{2-} and NH_4^+ do not exceed 0.16 and 0.009 μ g m^{-3}, respectively. Super-micron NH_4^+ concentrations are insignificant *(Quinn et al., 2002b)*. However, there is more ss-SO_4^{2-} (up to 0.18 μgm^{-3}) than nss-SO_4^{2-}. On the other hand, observed sub-micron Na^+, Cl^- and NO_3^- at Utqiaġvik peak at 2.0, 2.2, and 0.9 μ g m^{-3} respectively (**Fig. 4.4a**). Note that based on the findings of KRP18, only 1%, by number, of the particles across the 0.15-1.0 μm size range corresponded to fly ash and dust, as compared to 50-90% from SSA across the same size range. This supports the assumption of Na^+ being primarily from SSA during this study. High sub-micron observed total SO_4^{2-} (mostly nss-SO_4^{2-}) concentrations were measured at Utqiaġvik and peak at 2.4 μ g m^{-3}, possibly due to local influence from Prudhoe Bay oil fields to the east (KRP18, KRP19), a magnitude much higher than super-micron SO_4^{2-}, also reported for Utqiaġvik by *Quinn et al. (2002b)*. Enhanced nss-SO_4^{2-} during this period at Utqiaġvik could also be due to transport from mid-latitude sources, as well as due to transport and oxidation of SO_2 to SO_4^{2-} near and within the Arctic region *(Barrie and Hoff, 1984)*. Sub-micron ss-SO_4^{2-} peaks at 0.5 μ g m^{-3}. Observed NH_4^+ is higher compared to the other remote Arctic sites (up to 0.34 μ g m^{-3}). NH_4^+ temporal variation during January and February follows that of nss-SO_4^{2-} due to NH_3 reaction with acidic SO_4^{2-} aerosol near source regions outside of the

Arctic *(Quinn et al., 2002b)* or due to regional sources of NH_3, e.g. combustion of fossil fuels *(Whaley et al., 2018)*.

Finally, only two sites provide total organic carbon (tOC) observations. Here, observed total organic carbon is assumed to include secondary organic aerosols, anthropogenic organic carbon emissions and marine organics. Thus, from now on it will be referred as tOC, to distinguish from OA and OM defined earlier. tOC ranges between 0.15 and 0.3 μ g m^{-3} at Simeonof and 0.15 and 0.5 μgm^{-3} at Gates of the Arctic during January and February 2014.

Evaluation of the CONTROL simulation shows that the model overestimates observed fine/coarse mode, super-micron and TSP Na^+ and Cl^- at most sites, and especially at Simeonof (by up to 15 μ g m^{-3}), Zeppelin (**Fig. 4.2c**) (by up to 5.0 μ g m^{-3}), Utqiaġvik (by up to 0.3 μ g m^{-3}) and Gates of the Arctic (**Fig. 4.3b**) (by up to 4.0 μ g m^{-3}) site. The CONTROL simulation also overestimates NO_3^- by up to 0.5 μgm^{-3} at each site. On the other hand, this simulation captures NH_4^+ variability quite well at Alert, Villum and Utqiaġvik (super-micron) (see also biases and RMSEs (Root Mean Square Error) in APPENDIX A3 and Tables A2, A3 and A7 respectively), whilst it overestimates NH_4^+ at Zeppelin by up to 0.4 μ g m^{-3}. CONTROL includes only the nss-SO_4^{2-} component, however it captures observed variability of total SO_4^{2-} at Zeppelin (coarse mode), Villum (TSP) and Utqiaġvik (super-micron), but underestimates total SO_4^{2-} at Gates of the Arctic (fine mode) and Alert (coarse mode) by 0.5 and 0.2 μ g m^{-3}, respectively. In addition, the model underestimates sub-micron Na^+, Cl^-, SO_4^{2-} and NH_4^+ at Utqiaġvik. It also underestimates OA at the two sites compared to the measurements. In the following sections, model improvements are described. Biases and RMSEs in μgm^{-3}, are given in APPENDIX A3 for all sites and available aerosol species at each location.

4.1.5.2 Marine organics

Recent data-analysis studies *(Saliba et al., 2019; Kirpes et al., 2019)*, have suggested that marine organics contribute significantly to natural aerosol composition as ocean biomass can influence SSA number concentrations and diameter. In the CONTROL run, marine organics are not activated; however a source code is included in the model by *Archer-Nicholls et al. (2014)*. For this reason, the parameterization, based on *Fuentes et al. (2010, 2011)* (F10 and F11 from now on, respectively) is activated in the MOSAIC scheme to include a source flux for marine organics with dry diameters up to 0.45 μm. The scheme is based on an analysis of data from a cruise in mid-latitudes investigating the influence of dissolved organic matter on the production of sub-micron SSA. The F10 SSA source function also depends on MO80 whitecap coverage. In this study, organic fractions equal to 0.2 for the first and second MO-

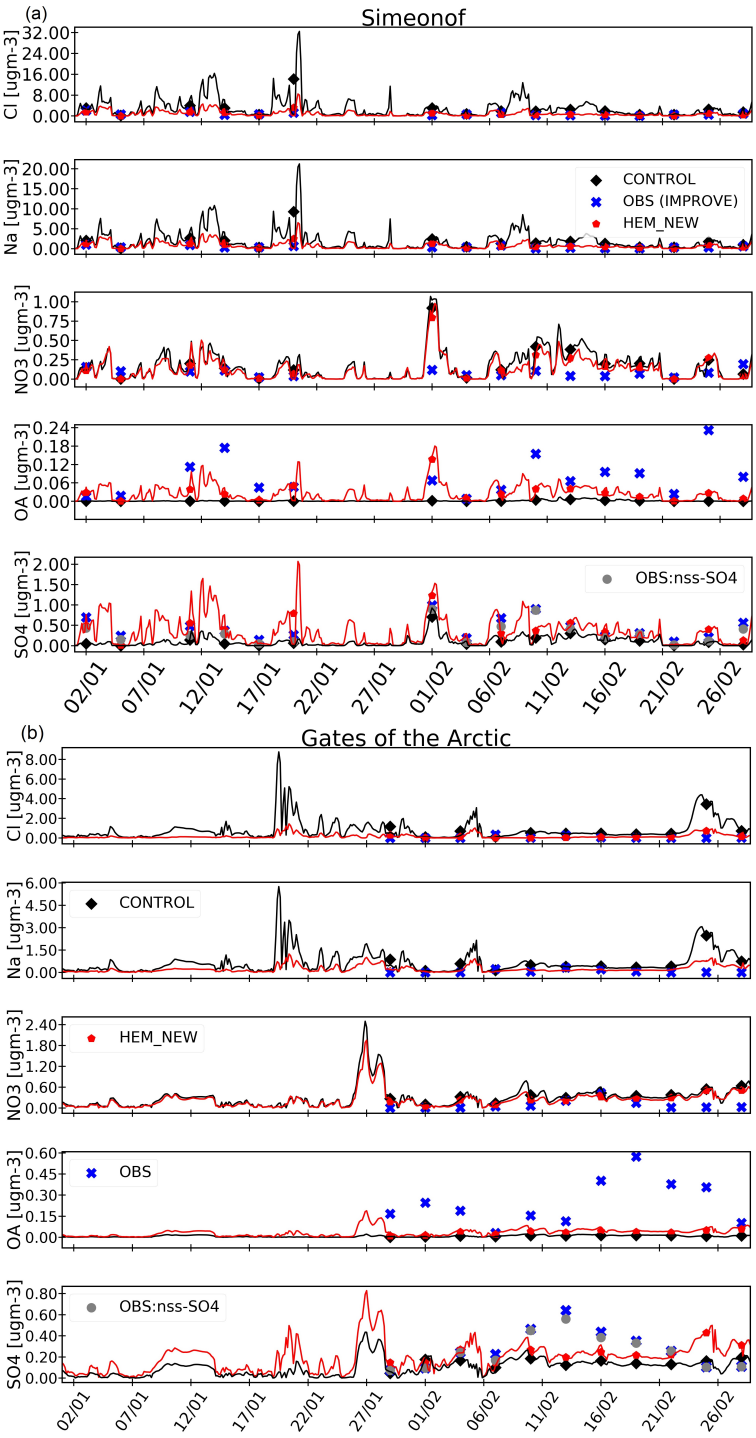

Figure 4.3: *Evaluation of modelled aerosol composition (runs CONTROL and HEM_NEW) against in-situ aerosol observations of fine mode ($r_d \leq 2.5$ μm) (both sites) at (a) Simeonof, Aleutians Islands, Alaska and (b) Gates of the Arctic, north of Alaska in local Alaskan time (AKST). The black line shows model results from the CONTROL run; the red line shows the HEM_NEW run, while observations are shown as blue crosses. Simeonof and Gates of the Arctic observations are 24h averages every three days and the corresponding model daily averages are shown as black diamonds for CONTROL and red pentagons for HEM_NEW. Observations are shown only when they are available. See the text for details about the observations and model runs.*

SAIC bins, 0.1 for the third bin and 0.01 for the remaining bins are used following the high biogenic activity scenario which assumes high C:Chlorophyll-a (Chl-a) ratios. F11 found that higher particle organic fractions are expected in algal bloom regions with high C:Chl-a ratios and Chl-a varying between 0.4-10 µg/L. The use of the F11 high biogenic activity option in our simulations is justified since MODIS-Aqua satellite data (https://neo.sci.gsfc.nasa.gov/view.php?datasetId=MY1DMW_CHLORA&date=2014-12-01) for January-February 2014 show that Chl-a south of Alaska and along the west coast of the United States varied between 0.3 and 3.0 µg/L. *Fujiki et al. (2009)* also found that Chl-a varied between 0.4 and 1.0 µg/L at six stations south of the Aleutian Islands, Alaska, during a sub-Arctic cruise in autumn 2005. Details about the F10 SSA source function are given in APPENDIX A2. In the case of the model uses a source for marine organics, then OA is the sum of SOA, anthropogenic emissions of OM and marine organics. A more detailed analysis of marine organics, focusing on northern Alaska, is presented in 4.2.6.2.

4.1.5.3 Whitecap method

In agreement with previous modelling studies, e.g. *(Jaeglé et al., 2011)*, JA11 from now on and *(Spada et al., 2013; Revell et al., 2019; Hartery et al., 2020)* the CONTROL simulation produces too much coarse mode and TSP Na^+ and Cl^-. The G97 parametrisation, which depends on the whitecap method and thus has a high wind speed dependence (see Eq. 4.1), has been widely adopted to simulate SSA emissions in global and regional models, e.g. JA11 and *Barthel et al. (2019)*. Several studies tried to improve upon the whitecap method ($W(U_{10})$), especially for super-micron SSA. *Callaghan et al. (2008)* used an automated whitecap extraction technique to derive two whitecap expressions that differ from MO80, which are based on cubed relationships for U_{10}). Other factors, such as the wave field *(Salisbury et al., 2013)*, surfactant (amphiphilic organic material) activity *(Callaghan, 2013)* and fetch-dependent threshold for breaking waves *(Revell et al., 2019; Hartery et al., 2020)*, have also been shown to affect whitecap lifetime, with implications for SSA production. *Goddijn-Murphy et al. (2011)* analysed Marine Aerosol Production (MAP) whitecap data, in combination with analysis of in-situ and satellite data (from Quick Scatterometer, QuikSCAT) for winds and waves. The satellite data were used to derive an expression with a lower wind speed dependence compared to MO80 (*Salisbury et al. (2014)*, SALI14 from now on). Here, the SALI14 parametrisation is implemented instead of the MO80 whitecap fraction expression:

$$W(U) = 4.60 \times 10^{-5} \times {U_{10}}^{2.26} \tag{4.3}$$

Based on Figure 2 in SALI14, the seasonal mean of $W(U_{10})$ using Eq. 4.3 is lower at high

latitudes compared to MO80 during autumn and winter. By using this more recent whitecap fraction expression in the quasi-hemispheric simulation, super-micron SSA concentrations decrease overall within the Arctic (not shown here). More specifically, super-micron Cl^- and Na^+ decrease more south of Alaska, by up to 20 μ g m^{-3} (Aleutians Islands) and less north of Alaska, by up to 0.5 μ g m^{-3}. NO_3^- also decreases slightly over continental Alaska, by up to 0.5 μ g m^{-3}, due to increased heterogeneous formation on SSA.

4.1.5.4 SST dependence

Recent data-analysis studies *(Saliba et al., 2019; Liu et al., 2021)* pointed out that wind speed alone cannot predict SSA variability, and it is important also to include a dependence on SSTs for SSA prediction. Recent modelling studies *(Jaeglé et al., 2011; Sofiev et al., 2011; Spada et al., 2013; Barthel et al., 2019)* showed that the application of SST dependence improves simulated SSA concentrations compared to observations. More specifically, previous studies *(Spada et al., 2013; Grythe et al., 2014; Barthel et al., 2019)* tested different SSA source functions, with and without SST dependence, and reported that including such a dependence improves model results, regardless of the SSA source function employed. However, uncertainties still remain about the role of SSTs on SSA production *(Revell et al., 2019)*, including the role of other factors, such as seawater composition *(Callaghan et al., 2014)* or wave characteristics (e.g. wave speed and breaking wave type, *Callaghan et al. (2012)*), which might be more important than SSTs alone. In this study, the JA11 SST correction factor is applied when SSTs are between -2°C and 30°C to evaluate the effect of SST on sub- and super-micron SSA emissions in the Arctic. In our simulations, SSTs are provided by reanalyses data, in this case, FNL, and in the presence of sea-ice, SST is set equal to -1.75°C.

4.1.5.5 Sea-salt sulphate

Standard versions of the WRF-Chem model do not include ss-SO_4^{2-}. The Community Multiscale Air Quality (CMAQ) model includes a ss-SO_4^{2-} component estimating it to be 7% of the total SSA emissions. The mass fraction of ss-SO_4^{2-} can be estimated to be 0.25 of the Na^+ mass fraction *(Kelly et al., 2010; Neumann et al., 2016)* and applied in WRF-Chem to calculate ss-SO_4^{2-}. Note that the total fraction of Na^+, Cl^-, marine organics and ss-SO_4^{2-} is equal to 1.0, and additional mass is not added. The mass fraction of ss-SO_4^{2-} is estimated to be 9.9% of the total SSA emissions in our simulations.

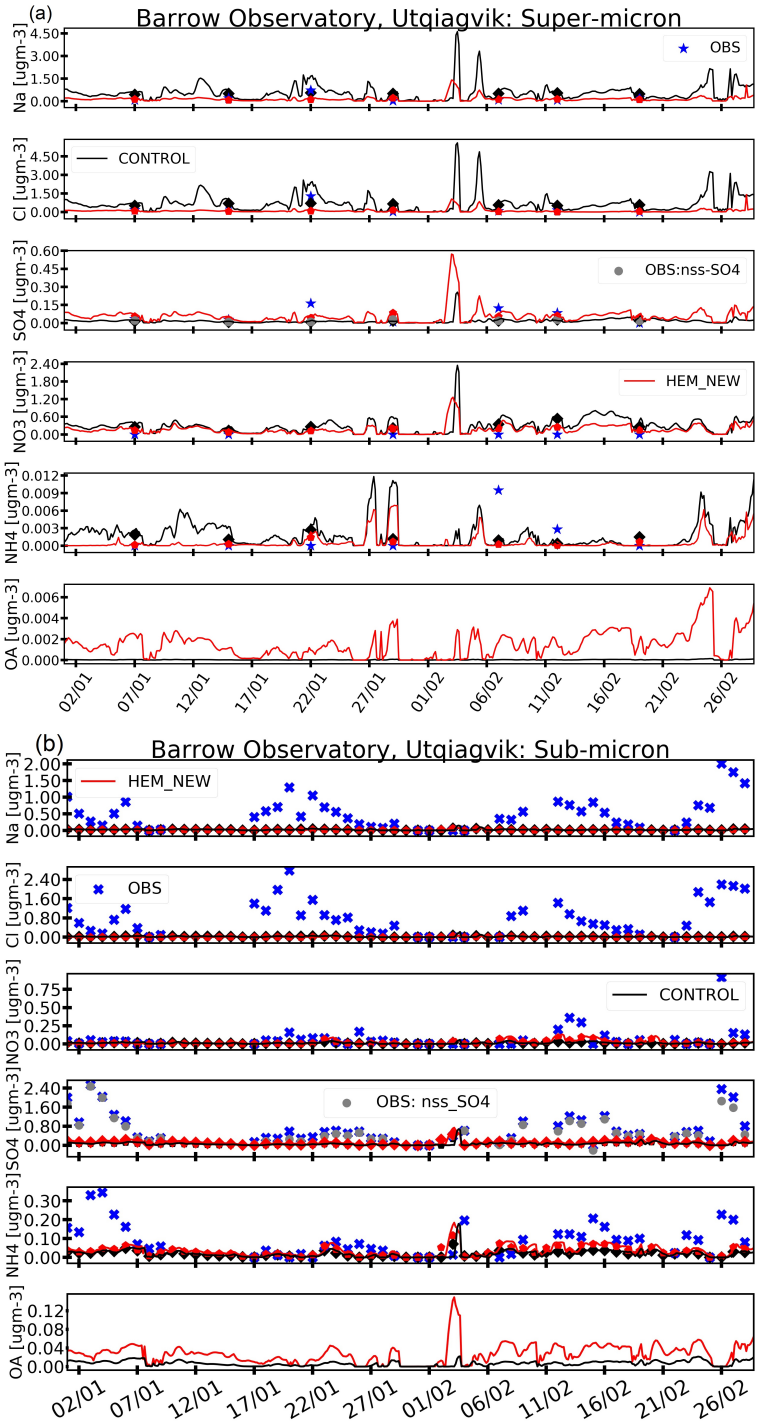

Figure 4.4: *Evaluation of modelled aerosol composition (runs CONTROL and HEM_NEW) against in-situ observations at Barrow Observatory, near Utqiaġvik, Alaska for (a) super-micron and (b) sub-micron in UTC and in STP conditions. The black line shows model results from the CONTROL run; the red line shows the HEM_NEW run, while observations are shown as blue crosses. Sub-micron observations are daily averaged and super-micron observations are weekly averages. The corresponding model daily/weekly averages are shown as black diamonds for the CONTROL simulation and as red pentagons for the HEM_NEW. Observations are shown only when there are available. See the text for details about the observations and model runs.*

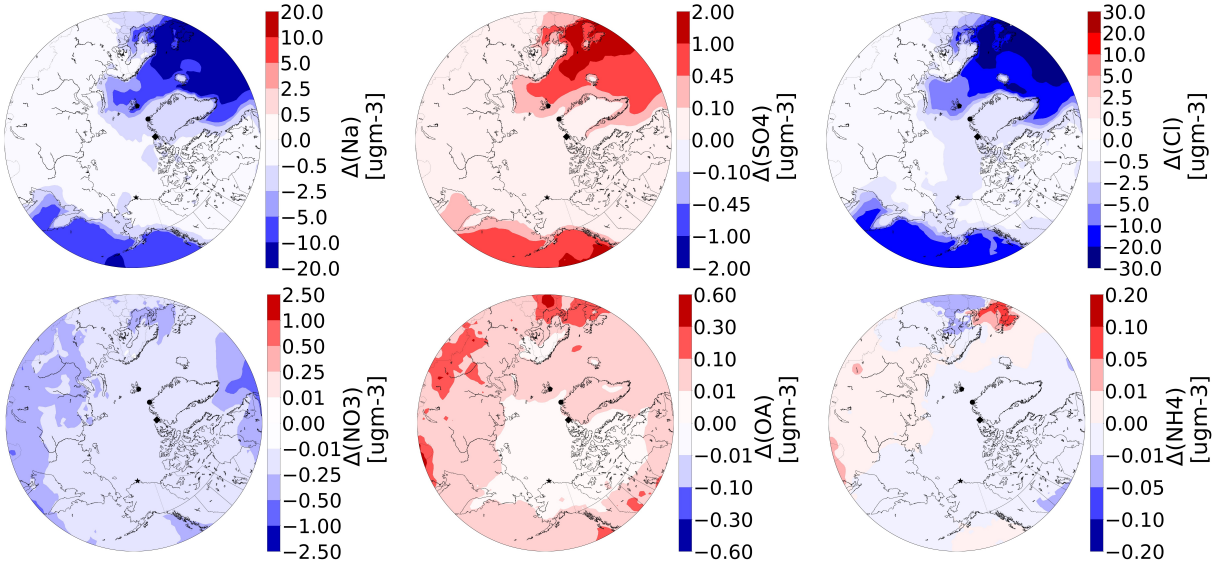

Figure 4.5: *Average differences in super-micron aerosol mass concentrations (μ g m^{-3}) at the surface between HEM_NEW and CONTROL during January and February 2014. The black star in northern Alaska shows where Utqiaġvik is located. The black circle shows Alert, Canada, the black diamond shows Villum in Greenland, while the black pentagon shows Zeppelin, Svalbard.*

4.1.5.6 Discussion

Average differences in aerosol concentrations between the HEM_NEW and CONTROL simulations are shown in **Figures 5 and 6** for January and February 2014 super-micron and sub-micron aerosols, respectively. The updated model simulates less super-micron Na^+ by up to 20 μ g m^{-3}, and Cl^- by up to 30 μ g m^{-3}, especially south of Alaska and north of the Atlantic Ocean (**Fig. 4.5**). These decreases lead to an overall decrease (up to 2.5 μ g m^{-3}) in super-micron NO_3^-, over continental and coastal regions and the North Atlantic. This is in agreement with *Chen et al. (2016)* who examined the influence of SSA on NO_3^- and reported that overestimation of SSA can lead to an overestimation of super-micron NO_3^-, due to formation of NO_3^- via heterogeneous uptake of nitric acid (HNO_3) on SSA. Furthermore, due to the addition of ss-SO_4^{2-} component in the model, there is more super-micron SO_4^{2-}, of up to 2 μ g m^{-3}, over marine regions. Super-micron NH_4^+ also increases (by up to 0.2 μgm^{-3}) in regions, such as Siberia and North of Europe, coinciding with decreases and increases in NO_3^- and SO_4^{2-}, respectively. Super-micron OA increases by up to 0.6 μ g m^{-3} due to the inclusion of marine organics. During winter, the Beaufort Sea, located north of Alaska is covered by sea-ice. Here, the implemented changes lead to smaller decreases in super-micron Na^+ and Cl^- compared to ice-free regions such as the Aleutians islands, e.g., Simeonof site (**Fig. 4.2a**) further south. The local effect of sea-ice fraction and open leads on SSA production is examined further in 4.2.6.4.

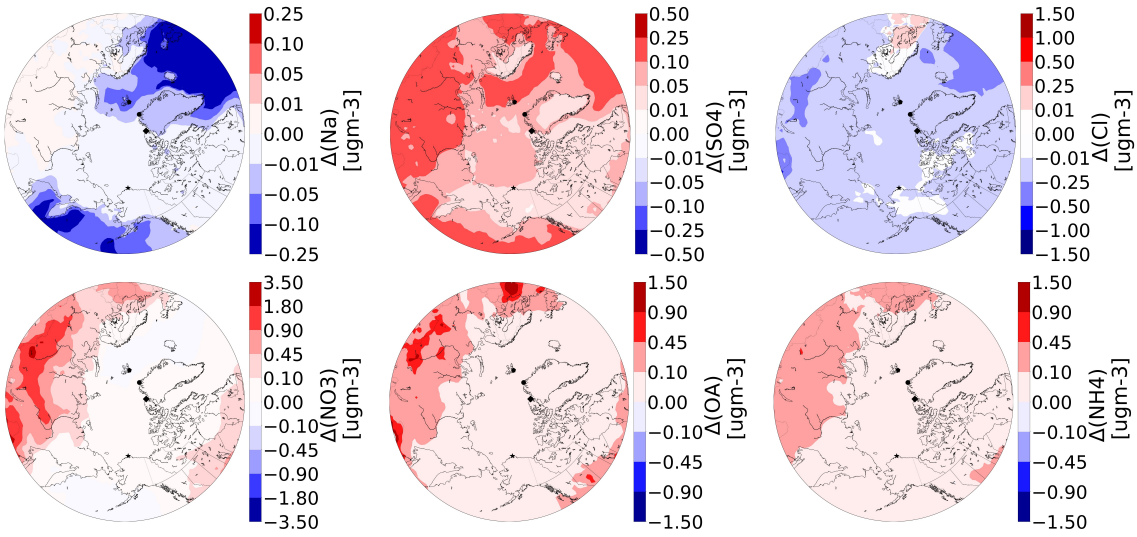

Figure 4.6: *Average differences in sub-micron aerosol mass concentrations (μ g m^{-3}) and at the surface between HEM_NEW and CONTROL during January and February 2014. The black star in northern Alaska shows where Utqiaġvik is located. The black circle shows Alert, Canada, the black diamond shows Villum in Greenland, while the black pentagon shows Zeppelin, Svalbard.*

On the other hand, the effect of model updates on sub-micron Na^+ is smaller, with decreases of up to 0.25 μ g m^{-3} south of Alaska and the North Atlantic (**Fig. 4.6**) due to use of lower wind speed dependence (SALI14 instead of MO80). The lifetime of SSA, estimated to be between 1 to 4 days over open ocean, in the Arctic and during wintertime *(Rhodes et al., 2017; Xu et al., 2016; Huang and Jaeglé, 2017; Hoppel et al., 2002)*, could explain the small decrease of sub-micron Cl^- over continental coastal areas (e.g. south of Alaska) in HEM_NEW. This could also affect long range transport of sub-micron SSA from oceanic regions leading to decreases over continental regions, such as northeast United States of America (USA) and Siberia. Sub-micron OA increases by up to 1.5 μ g m^{-3} due to inclusion of the F10 parametrisation. Note that including ss-SO_4^{2-} leads to a decrease in Na^+ and Cl^- fractions per bin since no additional mass is added. In contrast to super-micron NO_3^-, sub-micron NO_3^- increases by 3.5 μgm^{-3} over sources regions and total SO_4^{2-} increases due to ss-SO_4^{2-} component. Also, sub-micron NH_4^+ slightly increases, showing similar patterns to sub-micron NO_3^- and SO_4^{2-}, probably due to a potential shift in the balance between $(NH_4)_2SO_4$ and NH_4NO_3.

To investigate the variations in modelled NO_3^-, SO_4^{2-} and NH_4^+, the mean neutralized factor (f) is calculated (not shown here) as the ratio of NH_4^+ to the sum of ($2SO_4^{2-}$ + NO_3^-), in molar concentrations, following, for example *Fisher et al. (2011)*, for sites in the Arctic with available observations of these aerosols. When f is equal to 1 aerosols are more neutralized, while when $f < 1$ then aerosols are acidic, and more acidic when f is closer to 0 *(Fisher*

et al., 2011). At all sites, except Zeppelin, higher molar concentrations were observed for SO_4^{2-} compared to NO_3^- and NH_4^+. At Utqiaġvik, the average observed value of f is equal to 0.15 for super-micron aerosols, whilst in the model f decreases from 0.7 to 0.66. This implies that observed super-micron aerosols are more acidic while in the model they are more neutralized *(Fisher et al., 2011)*, probably because modelled NH_4^+ decreased more than SO_4^{2-} and NO_3^- (**Fig. 4.4a**) between the two simulations. There is less super-micron NH_4^+ in the model than the sum $2SO_4^{2-}$ + NO_3^-, as in observations, however observed $2SO_4^{2-}$ + NO_3^- is much higher than modelled. Observed super-micron aerosols at Utqiaġvik are more acidic compared to sub-micron aerosols for which f equals 0.34. For sub-micron aerosols, HEM_NEW has an average f value of 0.08 compared to 0.01 in the CONTROL run. The increase in modelled sub-micron f could be due to the bigger increase in modelled NH_4^+ between the two simulations (**Fig. 4.4b**). However, in the observations, the higher sub-micron f is because the sum $2SO_4^{2-}$ + NO_3^- is much higher than NH_4^+. At Alert (coarse mode), model f increases from 0.14 (CONTROL) to 0.19 (HEM_NEW), with observed f equal to 0.21, implying that model and observations are acidic, in contrast to Utqiaġvik modelled super-micron aerosols. Similar values of f are found for Zeppelin (coarse mode) and Villum (TSP) (0.12 for CONTROL, 0.13 and 0.18 for HEM_NEW, respectively) with observed aerosols (0.34 and 0.36 respectively) being less acidic at these sites. Overall the model inorganic aerosols are mostly too acidic compared to the observations. This could be due to underestimation of anthropogenic sources of NH_3 on the above sites, originating from mid-latitudes. It can be noted that in the model is assumed that all of the aerosol species are internally mixed. However, in reality some of the NO_3^- and SO_4^{2-} are observed to be mixed with SSA (KRP18). Based on that, the calculated f for observations would be biased (too acidic), as some of the NO_3^- and SO_4^{2-} are present as Na_2SO_4 and $NaNO_3$.

Figures 4.2 and **4.3** show the effect of all the modifications (HEM_NEW) compared to CONTROL and the observations at four Arctic and one sub-Arctic sites. At the two remote high-Arctic sites surrounded by sea-ice (Alert and Villum, **Figure 4.2a,b**), HEM_NEW captures better Na^+ and Cl^- variability, with a small overestimation at Villum (maximum 0.2 μ g m^{-3}). Biases, in μ g m^{-3}, at Alert for Na^+ and Cl^- decrease from 0.81 to 0.12 and from 1.05 to -0.03, respectively. Model results also improve at Villum for Na^+ and Cl^- with biases reduced from 1.3 to 0.25 and from 1.9 to 0.22 μ g m^{-3}, respectively. The high variability in SSA at Villum at the end of January and the middle of February is likely to be due to fluctuations in sea-ice fraction around the site, as seen in the FNL sea-ice reanalysis product (varies between 0.93 and 1.0-fully covered, in January and February). Also, HEM_NEW captures better NO_3^- and NH_4^+ at Alert while slightly overestimates total SO_4^{2-} (see APPENDIX A3, Table A2). At Villum, HEM_NEW captures better SO_4^{2-} compared to CONTROL run,

slightly underestimates NH_4^+ end of February, but still overestimates NO_3^- (see APPENDIX A3, Table A3). Similar results are found for Zeppelin where HEM_NEW simulates better Na^+, Cl^-, NO_3^- and NH_4^+, but overestimates SO_4^{2-}. More specifically, HEM_NEW slightly underestimates observed Na^+, Cl^- and NH_4^+, but the model results improve in this site. SSA updates also improve modelled NO_3^- (see APPENDIX A3, Table A4).

At Simeonof, HEM_NEW captures better Na^+, Cl^- and NO_3^- variability during winter 2014 and, due to the inclusion of marine organics, the model simulates more tOC, although it still underestimates observed variability. Calculated biases decrease from 1.4 to 0.3, 2.0 to 0.1, 0.12 to 0.08, -0.08 to -0.05 μ g m^{-3} for Na^+, Cl^-, NO_3^- and tOC, respectively. Also, the addition of ss-SO_4^{2-} in HEM_NEW leads to improvements (biases, RMSEs) in simulated SO_4^{2-} even if the model occasionally underestimates by up to 0.6 μ g m^{-3}. Similar patterns are found for the Gates of the Arctic in northern Alaska. Na^+ and Cl^- are lower in HEM_NEW while modelled NO_3^- and tOC also improve, with biases decreasing for all the four species (0.56 to 0.16, 0.70 to 0.09, 0.26 to 0.18 and -0.24 to -0.21 μ g m^{-3} for Na^+, Cl^-, NO_3^- and tOC, respectively, see also APPENDIX C for RMSEs). HEM_NEW simulates more total SO_4^{2-} at this site but still underestimates the observations, in particular nss-SO_4^{2-}. Here, the contribution of ss-SO_4^{2-} is minimal, as shown in Fig. 3b. Thus, the model underestimation could be due to issues related to long-range transport of nss-SO_4^{2-}, such as wet deposition, or to missing local anthropogenic sources (e.g. Prudhoe Bay oilfields). Additional wintertime production of SO_4^{2-} via mechanisms not requiring sunlight may also contribute. For example, *McCabe et al. (2006)* suggested that there is secondary SO_4^{2-} at Alert during wintertime from metal catalyzed O_2 oxidation of S(IV) (10–18%). Results from HEM_NEW also underestimate tOC at Gates of the Arctic, possibly due to underestimation of marine organics (see discussion in next section) or missing regional or remote sources.

Figure 4.4 compares results from CONTROL and HEM_NEW with observations for super-micron (weekly averages) and sub-micron (daily averages) aerosols at Utqiaġvik. While CONTROL overestimates SSA and NO_3^- and underestimates SO_4^{2-} (only non-ss-SO_4^{2-}), in general, HEM_NEW captures better observed super-micron Na^+, Cl^-, NO_3^- and NH_4^+ aerosols during the simulation period (**Fig. 4.4a**) (see also Appendix A3). The Na^+ bias decreases from 0.3 to -0.07 μ g m^{-3} but Cl^- is now underestimated (bias decreases from 0.27 to -0.26 μ g m^{-3}), due to the introduction of the SST dependence (not shown). Also, there is more super-micron SO_4^{2-} in HEM_NEW and the model slightly underestimates observed SO_4^{2-} by about 0.1 μ g m^{-3}. Super-micron OA is smaller in magnitude compared to the other aerosol components. However, super-micron OA mass concentration measurements are not available in winter 2014 to evaluate the model. Overall, modelled super-micron SSA concentrations decrease in HEM_NEW, as at other remote sites (**Fig. 4.2** and **4.3**) in better

Table 4.2: *Calculated fractions of observed and modelled (HEM_NEW) SSA to total aerosol mass concentrations (summed from available observations at each site). For each site SSA are defined as the sum of Na^+, Cl^- and ss-SO_4^{2-}. Total is defined as the sum of SSA and inorganic aerosols. Inorganic is the sum of nss-SO_4^{2-}, NH_4^+ and NO_3^- for each station except for Simeonof and Gates of the Arctic where inorganic is the sum of nss-SO_4^{2-} and NO_3^-. Note that NH_4^+ is rarely internally mixed within SSA aerosol, because most NO_3^- and SO_4^{2-} forms via Cl^- (e.g. $NaCl + HNO_3 \rightarrow NaNO_3 + HCl$). Total_all below is defined as the sum of SSA, nss-SO_4^{2-}, NH_4^+, NO_3^-, BC, OA and dust (model only). The aerosol size for SSA, Total and Total_all varies per station and corresponds to observed aerosol sizes as described in Section 3.*

Sites	SSA/Total [OBS]	SSA/Total [HEM_NEW]	SSA/Total_all [HEM_NEW]
Simeonof (fine mode)	0.73	0.84	0.74
Gates of the Arctic (fine mode)	0.20	0.44	0.33
Utqiaġvik-sub-micron	0.60	0.22	0.13
Utqiaġvik-super-micron	0.93	0.57	0.54
Alert (coarse mode)	0.59	0.54	0.45
Villum (TSP)	0.32	0.63	0.52
Zeppelin (coarse mode)	0.56	0.75	0.62

agreement with the observations compared to the CONTROL run.

On the other hand, while HEM_NEW (**ig. 4.4b**) represents better periods with low concentrations of sub-micron Na^+ and Cl^- at Utqiaġvik in January and February 2014 (up to 0.3 μ g m^{-3}), it still underestimates episodes with very high observed Na^+ and Cl^-, especially at the end of February 2014. The model simulates better NO_3^- but underestimates NH_4^+ and SO_4^{2-}, especially at the beginning of January and end of February 2014. Sub-micron OA at 100 km ranges between 0.01 and 0.15 μ g m^{-3}. However, observations of OA at Utqiaġvik during this period are not available with which to validate the model. *Barrett et al. (2015)* and *Barrett and Sheesley (2017)* showed that OC at Utqiaġvik is influenced by primary and secondary biogenic carbon and fossil fuel carbon, with air masses originating from the Arctic Ocean, Russian and Canadian Arctic. More specifically, *Barrett and Sheesley (2017)* made measurements of OC (diameter less than 10 μm) collected during winter 2012-2013 northeast of Utqiaġvik and reported average OC of 0.22 μ g m^{-3}. To compare directly with the model results we divide the modelled value by 1.4 (**Fig. 4.5**). In that case, modelled super-micron tOC at Utqiaġvik is three times less than the observed OC, showing that the model lack sources of OC. *Shaw et al. (2010)* reported sub-micron OM equal to 0.43 μ g m^{-3} during winter 2008 (November to February) at Utqiaġvik, almost double the simulated OA at Utqiaġvik. Their analysis showed that OM was correlated with organic and inorganic seawater components with the air masses originating along the coastal regions of the Northwest Territories of Canada. Also, the model results can be compared with

weekly average sub-micron OM data collected at Alert (*Leaitch et al. (2018a)* and **Fig. 2**). At Alert, OM reaches up to 0.25 μ g m^{-3} in February 2014, which is almost double compared to the model results for Utqiaġvik, North Slope of Alaska and Alert (**Fig. 4.6**). At Villum, a recent study by *Nielsen et al. (2019)* showed that OA peaks at 2.2 μ g m^{-3} at the beginning (21 to 28 February 2015) of their study period. Their study shows that the majority of OA is mostly due to Arctic Haze influence (up to 1.1 μ g m^{-3}) with secondary influence, due to hydrocarbon-like organics (up to 1.0 μ g m^{-3}) and a marine influence (up to 0.2 μ g m^{-3}). Reasons for these differences on modelled and observed OA are investigated in the next section focusing on regional processes affecting SSA near northern Alaska.

Previous studies *(Quinn et al., 2002b; Quinn and Bates, 2005; May et al., 2016; Kirpes et al., 2018, 2019)*, pointed out that SSA are an important contributor in the total sub-micron and super-micron mass fraction in the Arctic during wintertime. A recent study by *Moschos et al. (2022b)* showed that during wintertime SSA dominates PM_{10} (particulate matter with diameter $\leq$ 10 μm) mass concentrations at remote Arctic sites, including Alert (56%), Baranova (41%) (Russia), Utqiaġvik (66%), Villum (32%), and Zeppelin (65%). In contrast, at sites such as Tiksi (Russia) and Pallas (Finland), SO_4^{2-} and OA dominate (70% and 55%, respectively). To investigate the contribution of SSA to total mass concentrations during the period of this study, the observed and modelled fraction of SSA to "total" (SSA plus inorganic) aerosols are estimated (see **Table 4.2**). However, it should be noted that this fraction varies between sites since not all components were measured.

Overall, taking into account the observations available at each site, the fraction of SSA to total SSA+inorganics is higher at all the coastal sites (Utqiaġvik, Alert, Simeonof, Villum) and Zeppelin ranging from 54 to 93%. Only at the Gates of the Arctic and Villum stations the fraction of SSA is smaller (20% and 32%). The modelled HEM_NEW SSA fraction shows similar patterns (fraction ranges between 44% and 84%) compared to the observations. An exception is sub-micron modelled SSA at Utqiaġvik due to low modelled concentrations. When taking into account all aerosol components in the model, including OA, BC and dust, SSA is dominant at Simeonof, Utqiaġvik (super-micron), Zeppelin and Villum (more than 54%), whereas at Alert, SSA contributes about 45%. This analysis shows that SSA is an important fraction of total fine mode, super-micron, coarse mode and TSP aerosols in the most Arctic coastal sites during wintertime.

4.1.6 Regional processes influencing SSA over northern Alaska

In this section, processes which could affect SSA emissions on a regional scale over northern Alaska are examined. In general, the improved model simulates better observed super-

Table 4.3: *WRF-Chem model simulations including details about SSA treatments in the regional runs.*

Simulation Name	Description
Regional simulations [20km]	
ALASKA_CONTROL_FEB	Control run for February 2014
DRYDEP_FEB	+ Updated dry deposition velocities over snow-ice and open water on *(Zhang et al., 2001)* based on *(Nilsson et al., 2001)*
LOC_ORG_FEB	+ Local source marine organics *(Kirpes et al., 2019)*
SSA_WS_DEP_FEB	+ Sub-micron SSA wind-speed dependence *(Russell et al., 2010)*
NEW_ALASKA_FEB	DRYDEP_FEB + LOC_ORG_FEB + SSA_TEST_FEB + ERA5 sea-ice fraction
ALASKA_CONTROL_JAN	Control run for January 2014 (same setup as ALASKA_CONTROL_FEB)
NEW_ALASKA_JAN	including all updates in NEW_ALASKA_FEB

micron, TSP, fine and coarse mode SSA, NO_3^- and SO_4^{2-} aerosols at different sites in the Arctic but the model has difficulties capturing sub-micron SSA during wintertime at at Utqiaġvik. Possible reasons for these discrepancies are investigated in model runs at 20 km resolution during the campaign periods in January and February 2014 with boundary and initial conditions from HEM_NEW. The sensitivity of modelled SSA to various processes is examined including aerosol dry deposition over snow/ice, inclusion of local marine organic aerosols, higher wind speed dependence for sub-micron SSA and representation of sea-ice fraction. The possible role of blowing snow and frost flowers is also discussed. Details about the simulations are provided in **Table 4.3**.

4.1.6.1 Aerosol dry deposition

Previous studies have shown the importance of including wet and dry removal treatments in models *(Witek et al., 2007; Eckhardt et al., 2015; Whaley et al., 2022a)*. *Sofiev et al. (2011)* estimated that dry deposition, including sedimentation, could contribute more than 50% to SSA removal, especially for super-micron SSA. JA11, using model treatments for dry deposition from *Zhang et al. (2001)* over land and *Slinn (1982)* over ocean, reported that the loss of super-micron SSA is dominated by dry deposition. In the quasi-hemispheric simulations, dry deposition velocities are calculated in MOSAIC based on the *Binkowski and Shankar (1995)* parametrisation. Here, the *Zhang et al. (2001)* scheme is applied over Alaska, in which the dry deposition velocities are calculated taking into account the different land categories, in contrast to MOSAIC scheme, which uses universal values for processes such as Brownian diffusion and Schmidt number *(?Slinn, 1982)*. *Zhang et al. (2001)* has been used in previous studies, for example, by *Fisher et al. (2011)* and *Huang and Jaeglé (2017)*. These

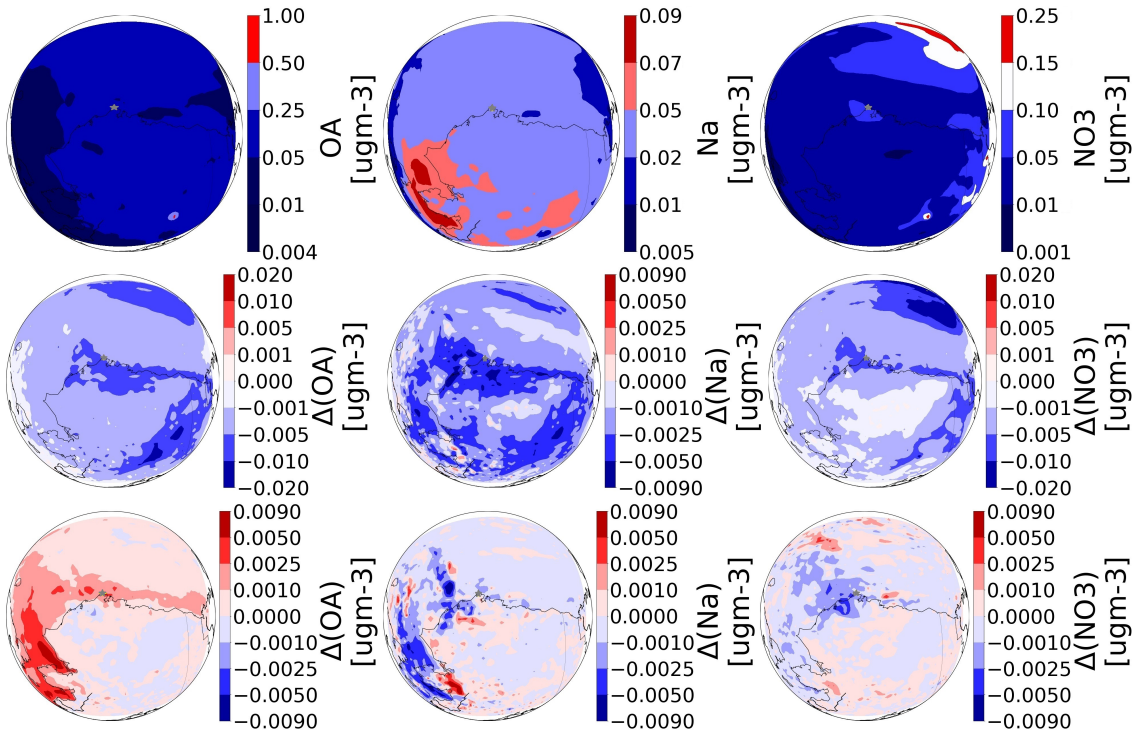

Figure 4.7: *First row shows the average values of aerosol mass concentrations for sub-micron during February campaign. Average differences at the surface between DRY_DEP_FEB and ALASKA_CONTROL_FEB (second row), and between LOC_ORG_FEB and DRY_DEP_FEB (third row) during February campaign for sub-micron Na^+, OA, NO_3^- (μ g m^{-3}). See text and Table 2 for detailed description of the model runs.*

studies applied aerosol dry deposition velocities of 3.0×10^{-4} m s^{-1} over snow and ice surfaces for all aerosol diameters and the dry deposition velocity is calculated as a function of aerosol diameter. *Zhang et al. (2001)* includes detailed treatments of deposition processes, such as Brownian diffusion, impaction, interception, gravitational settling and particle rebound, which highly vary depending on land surface type. Certain parameters link to interception, such as collection efficiency by interception, or impaction processes (e.g. Stokes number) over specific land use categories (such as ice/snow and open ocean), are calculated without considering the radius of surface collectors *(Giorgi, 1988)*, but using kinematic viscosity of air, gravitational settling velocity of particle, friction velocity *(Slinn, 1982; Seinfeld, 1986)*. Thus, dry deposition velocities over ice/snow and open ocean are set equal to 3.0×10^{-4} and 1.9×10^{-3} m s^{-1}, respectively, for both sub- and super-micron aerosols, following *Nilsson and Rannik (2001b)*, who reported dry deposition velocity measurements from an Arctic Ocean expedition in 1999. In that way, the influence of more realistic dry deposition velocities on SSA aerosols is examined during wintertime.

Figures 4.7 and 4.8 show the effect of this modification for sub- and super-micron SSA

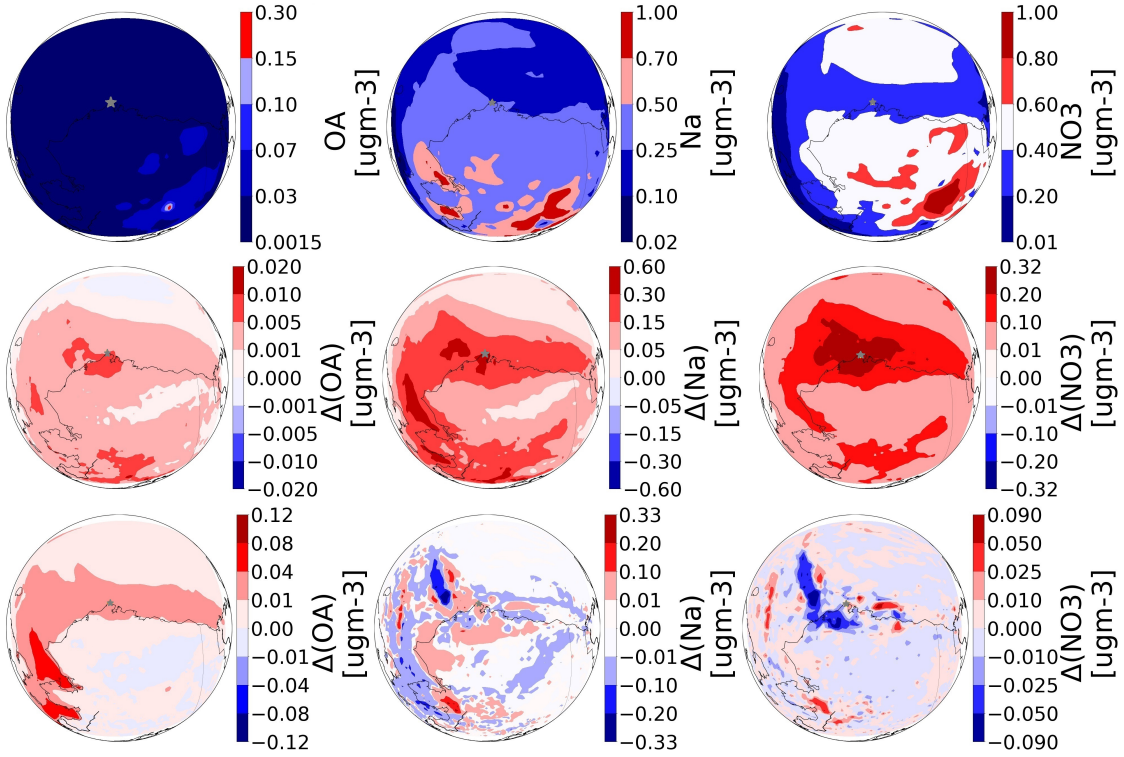

Figure 4.8: *First row shows the average values of aerosol mass concentrations of super-micron during February campaign. Average differences at the surface between DRY_DEP_FEB and ALASKA_CONTROL_FEB (second row), and between LOC_ORG_FEB and DRY_DEP_FEB (third row) in super-micron Na^+, OA, NO_3^- (μ g m^{-3})during February campaign. See text and Table 2 for detailed description of the model runs.*

and NO_3^-, respectively (differences between DRYDEP_FEB and ALASKA_CONTROL_FEB runs). Sub-micron Na^+, OA and NO_3^- decrease very slightly, whereas super-micron Na^+, OA and NO_3^- increase by up to 0.6, 0.02 and 0.3 µ g m^{-3}, respectively, with the largest increase over sea-ice areas or regions with snow cover. These changes in modelled sub- and super- micron aerosols are due to differences between the dry deposition velocities in the two schemes. Over model grids covered with snow or ice and open ocean MOSAIC dry deposition velocities are smaller (larger) for sub-micron (super-micron) in magnitude compared to reported velocities by *Nilsson and Rannik (2001b)*. During wintertime over northern (in-land) Alaska, all the grid cells during the simulations are snow covered. Based on these results, and the fact that super-micron Na^+ and Cl^- are slightly underestimated at 100 km and Utqiaġvik (see section 4.2.5.6), the following simulations use the observed dry deposition velocities reported by *Nilsson and Rannik (2001b)*.

These results show that sub- and super-micron (mostly) SSA are sensitive to different dry deposition parametrisation in WRF-Chem. To address potential uncertainties in dry removal treatments and their influence on SSA regionally, a series of sensitivity tests are also

performed. Firstly, correct modelling of aerosol dry deposition depends on the ability of the model to capture the structure of the Arctic boundary layer including vertical temperatures and winds. Model results at 20 km and 100 km horizontal resolution are compared against hourly in-situ 2 m, 10 m temperatures and 10 m wind speeds or temperature and wind speed profiles up to 4 km for January and February 2014 (see figures in APPENDIX A4 with calculated bias and RMSE for the two periods). Observed wind speeds during January ranged between 4.7 and 14.1 ms^{-1} and wind directions were mostly easterly (77 to 135 degrees). During February, wind speeds ranged between 0.4 and 13.3 m s^{-1} and wind directions were mostly easterly, except from 22 UTC 25 February to 11 UTC 26 February when the winds were westerly. In general, the model performs well at 20 km, and better than at 100 km, in terms of temperature and winds, although it slightly underestimates observations at the surface. On the other hand, there are small discrepancies, of up to 10 degrees, between modelled (at 20 km) and observed wind direction at the Barrow site, near Utqiaġvik town, except at 26 February when these discrepancies are up to 70 degrees.

To examine further causes of variability in modelled dry removal of SSA, a sensitivity test is carried out where aerosol dry deposition and gravitational settling are switched off during a windy day, 28 February 2014. On this day, 10 m wind speeds at Utqiaġvik varied between 7 and 13.5 m s^{-1} and were easterly (104 to 130 degrees). This corresponds to a period when observed sub-micron Na^{+} and Cl^{-} concentrations were high, around 1.4 and 2.0 μ g m^{-3}, respectively (see **Figure 4.10b**). During this day the model captures quite well observed wind speeds and directions, with small differences of up to 2 m s^{-1} and up to 10 degrees differences in wind direction (not shown here). In this sensitivity run, the model simulates more super-micron SSA (an increase up to 0.8 μ g m^{-3}), which is expected due to the influence of gravitational settling on super-micron particles. The increase on sub-micron SSA is smaller. However, observations of dry deposition of different aerosols are needed to better constrain the model in the Arctic.

4.1.6.2 Local source of marine organics

For the simulations at 100 km, the F10 parametrisation is used based on C:Chl-a from a cruise at mid-latitudes. Whilst phytoplankton blooms may not expected in the high Arctic winter, previous studies have shown evidence of sea ice biological activity under low light conditions in the Arctic *(Krembs et al., 2002; Lovejoy C., 2007; Hancke et al., 2018)*. In addition, *Russell et al. (2010)* (from now on RUS10) analysed samples from the International Chemistry Experiment in the Arctic Lower Troposphere (ICEALOT) cruise and found that most organic mass in clean regions of the North Atlantic and the Arctic is com-

posed of carbohydrate-like compounds containing organic hydroxyl groups from primary ocean emissions. *Frossard et al. (2014)* (FRSS14 from now on) investigated the sources and composition of atmospheric marine aerosol particles based on the analysis of samples, including those from ICEALOT, reporting that ocean-derived organic particles include primary marine organic aerosols. In particular, they calculated the ratio of OC:Na^+ as a metric for comparing the composition of model-generated primary marine aerosol and seawater, previously used by *Hoffman and Duce (1976)*, and reported OC:Na^+ ratios of 0.45 for atmospheric marine aerosol particles. KRP19 also reported that during their campaigns in 2014 almost all the individual SSAs had thick organic coatings (average C:Na mole ratios of 0.5 and 0.3 for sub-micron and super-micron SSA, respectively) made up of marine saccharides. They also identified open sea ice leads enriched with exopolymeric substances as contributing to organics in winter SSA.

Here, elemental fractions for sub- and super-micron aerosols sampled during the KRP19 campaigns are used to better constrain modelled organic marine emissions (mOC). More specifically, the ratio of sub- and super-micron OC:Na^+ is calculated, following FRSS14 and using the elemental fractions from KRP19, as an indicator of the presence of a local source of marine organics. The organic fraction of the total SSA for the high organic activity scenario in WRF-Chem is increased to 0.4 for sub-micron (1st to 5th MOSAIC 8-bins) and to 0.11 for super-micron (6th to 8th MOSAIC 8-bins). Note again that no additional SSA mass is added. **Figures 4.7 and 4.8** show the sensitivity of the model results to including a larger marine organic fraction. Sub- and super-micron OA concentrations increase on average by up to 0.009 and 0.12 μ g m^{-3}, respectively, especially south-west of Alaska and along coastal areas, including Utqiaġvik. Sub-micron Na^+ and NO_3^- slightly decrease (0.005 μ g m^{-3}) around Utqiaġvik region, and super-micron Na^+ and NO_3^- decrease north-west of Utqiaġvik.

KRP19 reported measured sub-micron organic carbon volume fractions based on analysis of 150 SSA particles between 0.3 μm and 0.6 μm comparable to organic carbon volume fractions observed in SSA produced in mid-latitude algal bloom regions. This suggests the presence of significant organic carbon associated with locally produced SSA on the coast of northern Alaska. There are two available daily observations at Gates of the Arctic during the February campaign. The model captures better observed tOC at the end of February in the run LOC_ORG_FEB with higher organic fraction. However, it underestimates tOC on 25 February when the observed tOC reached 0.33 μ g m^{-3} (see APPENDIX F). As mentioned previously, this discrepancy could also be due to missing local anthropogenic sources related to North Slope oil field emissions *(?)*. In the following runs, marine organics based on the calculated ratio of OC:Na^+ are included instead of F10 considering the importance of

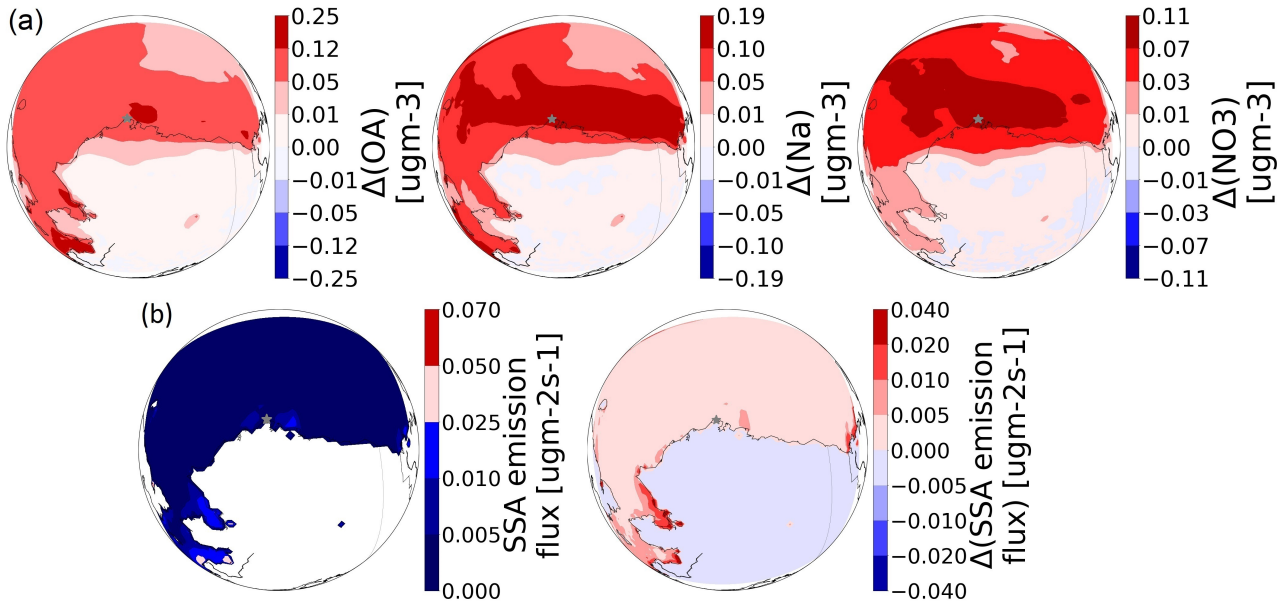

Figure 4.9: *Average differences in mass concentrations of (a) sub- micron Na^+, OA, NO_3^-,in μgm^{-3}, at the surface between SSA_WS_DEP_FEB and LOC_ORG_FEB. Grey star indicates the location of Utqiaġvik. (b) The map on the left shows the average value of SSA emission fluxes in $\mu gm^{-2}s^{-1}$ during February campaign and the map on the right shows average differences between SSA_WS_DEP_FEB and LOC_ORG_FEB in $\mu gm^{-2}s^{-1}$.*

local SSA marine sources at Utqiaġvik (KRP19). By including a local source of marine organics in the model, this leads to a better agreement with the findings of the previous studies discussed in section 4.2.5.6. It can be noted that there are only sporadic measurements of OA/OC at remote Arctic sites and detailed long-term observations are not available which might help to better constrain model simulations.

4.1.6.3 Wind-speed sensitivity to sub-micron SSA emissions

In the regional runs presented so far, the lower wind speed dependence based on satellite data is used (SALI14) since it improves modelled SSA compared to observations in the 100 km runs (see in section 4.2.5.3). However, RUS10 found evidence for higher wind speed dependence during the ICEALOT cruise in the Arctic. They found that wind speed is a good predictor of a marine factor, calculated using positive matrix factorization, for sub-micron organic mass ($OM1_{sea}$). Their analysis showed a high correlation between $OM1_{sea}$, sub-micron sodium (Na^+1) concentration and wind speed at 18 m (correlation r equal to 0.90 for the North Atlantic and Arctic region, see Table S3 Supplementary Material in RUS10). Average $OM1_{sea}$ concentrations (0.2 µ g m^{-3}) reported by RUS10 for the eastern Arctic Ocean are about half those reported at Utqiaġvik by *Shaw et al. (2010)* during wintertime.

In a sensitivity simulation, the results from RUS10 are used to include a higher wind

speed dependence for sub-micron SSA. Equations (5) and (6) from the RUS10 analysis for the Arctic legs of their cruise are applied to the model as a correction factor:

$$Na^{+}1 = 0.022 \times U_{18} - 0.012 \tag{4.4}$$

$$OM1_{sea} = 0.025 \times U_{18} - 0.049 \tag{4.5}$$

where U_{18} is wind speed at 18 m in ms^{-1}, ranging between 2 and 14 m s^{-1} (Figure 2, RUS10). RUS10 used $Na^{+}1$ as a proxy for sub-micron NaCl, and subsequently SSA, because $Na^{+}1$ equalled sub-micron $Cl^{-}1$ on a molar basis for the North Atlantic and Arctic sampling regions. Thus, Equation (5) is also used to estimate a correction factor for Cl^{-}. Here, wind speeds in the first model layer are used, i.e. around 26 m. Differences in U_{18m} and U_{26m} reach a maximum of 1 m s^{-1} (see Fig.A1 in APPENDIX A4). Following RUS10, correction factors are only applied in the model to the number and mass of the SSA emissions when modelled wind speeds are between 2 and 14 ms^{-1}, and when RUS10-calculated sub-micron SSA concentrations are greater than model calculated SSA. In this way, SSA emissions are enhanced during periods of higher wind speeds.

To illustrate the sensitivity of the results to applying this correction, **Fig. 4.9** shows sub-micron aerosol concentrations and SSA emission fluxes, the latter being the sum of dry mass emissions calculated in the model. Overall, this leads to an increase of 0.25, 0.19 and 0.11 μ g m^{-3} in sub-micron Na^{+}, NO_3^{-} and OA, respectively, over the Utqiaġvik region and southwest Alaska during the February campaign. The SSA emission flux is influenced directly by the area in the model grid which is ice-free. This leads to SSA production east and west of Utqiaġvik while the highest values are southwest of Alaska. By adding the RUS10 correction, SSA emission fluxes increase slightly by up to 0.035 μ g m^{-2} s^{-1} along the southwest Alaskan coast, and by up to 0.015 μ g m^{-2} s^{-1} around Utqiaġvik. RUS10 showed that sub-micron SSA and wind speed are well correlated over open ocean. Thus, a correction factor to sub-micron SSA, based on is-situ data, improves sub-micron model SSA and could be included in future simulations for studies focusing on the Arctic region.

4.1.6.4 Sea-ice fraction

The sensitivity of modelled SSA to prescribed sea-ice fractions during wintertime and the role of leads, is investigated since KRP19 already pointed out the importance of using realistic sea-ice to simulate marine aerosols. High spatial resolution images of sea-ice cover are available, including during the Polar Night, from a marine radar operating on top of a building in downtown Utqiaġvik (7117'13" N, 15647'17" W), 22.5 m above sea level, with a range of up to 11 km to the northwest (http://seaice.alaska.edu/gi/data/

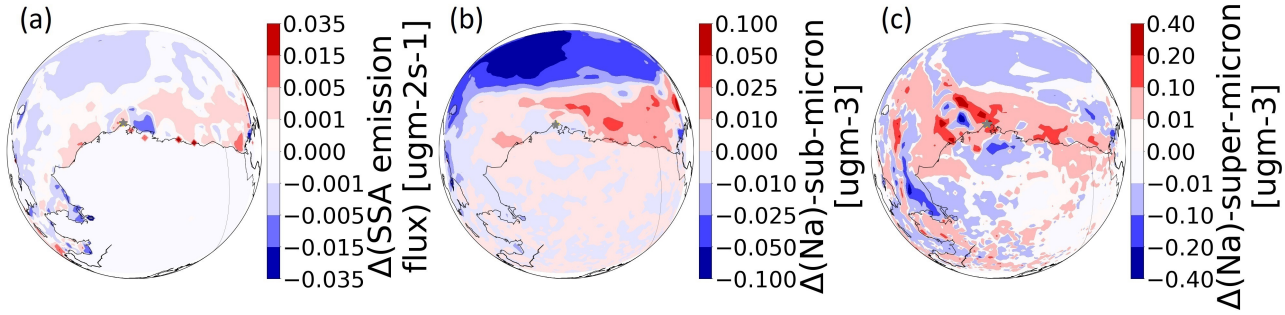

Figure 4.10: *Average differences between ALASKA_NEW_FEB and SSA_WS_DEP_FEB showing the effect of switching from FNL to ERA5 sea-ice fractions during February for (a) SSA emission fluxes (μ g m^{-3}), (b) sub-micron mass concentration of Na^+ and (c) super-micron mass concentration of Na^+ in μ g m^{-2} s^{-1}. The grey star shows the location of Utqiaġvik.*

barrow_radar) (*Druckenmiller et al., 2009*; *Eicken et al., 2011*). *May et al. (2016)* showed increased super-micron Na^+ mass concentrations during periods of elevated wind speeds and lead presence, in a multiyear study using the sea ice radar data at Utqiaġvik. Between 23-28 January 2014, when the winds at Barrow observatory were easterly, the radar showed that the coastal area east of Utqiaġvik featured leads (KRP19). From 24-28 February 2014, the west coastal area also featured leads as shown by Moderate Resolution Imaging Spectroradiometer (MODIS) satellite images (KRP19). To examine the sensitivity of SSA emissions to sea-ice cover, ERA5 sea-ice fractions with a resolution of 0.25° x 0.25° are used instead of FNL fraction at 1.0° x 1.0° resolution. Note that only sea-ice fraction field is different, while the rest of the meteorological fields are from FNL.

Results for February are shown in **Fig. 4.10**. The SSA emission flux (**Fig. 4.10a**) increases over a small region around Utqiaġvik and across the North Slope of Alaska due to decreased sea-ice fraction but decreases east of Utqiaġvik and southwest of Alaska (e.g. Selawik Lake and Norton Bay) due to increased sea-ice fraction. Sub-micron Na^+ slightly increases along the north coast of Alaska by up to 0.1 μgm^{-3} and around Utqiaġvik (see **Fig. 4.10b**) and super-micron Na^+ increases by up to 0.4 μ g m^{-3} around Utqiaġvik and decreases by up to 0.4 μ g m^{-3} southwest of Alaska (**Fig. 4.10c**). The model results for January indicate that there is less sea-ice in the region around Utqiaġvik and south west of Alaska. Therefore, higher SSA emission fluxes were simulated for February (0.035 μ g m^{-2} s^{-1}) compared to January (0.015 μ g m^{-2} s^{-1}) (maps not shown here).

Two further simulations are performed to examine model sensitivity to sea-ice fraction. First, ERA5 sea-ice fractions are set equal to 0 (ice-free conditions) to the north, west, and east of Utqiaġvik to examine the effect of having ice-free conditions and the presence of open leads locally (as seen by the radar). Second, ERA5 sea-ice fractions are set equal to 0.75 north, west, east of Utqiaġvik and northwest of Alaska. In both cases, the model is

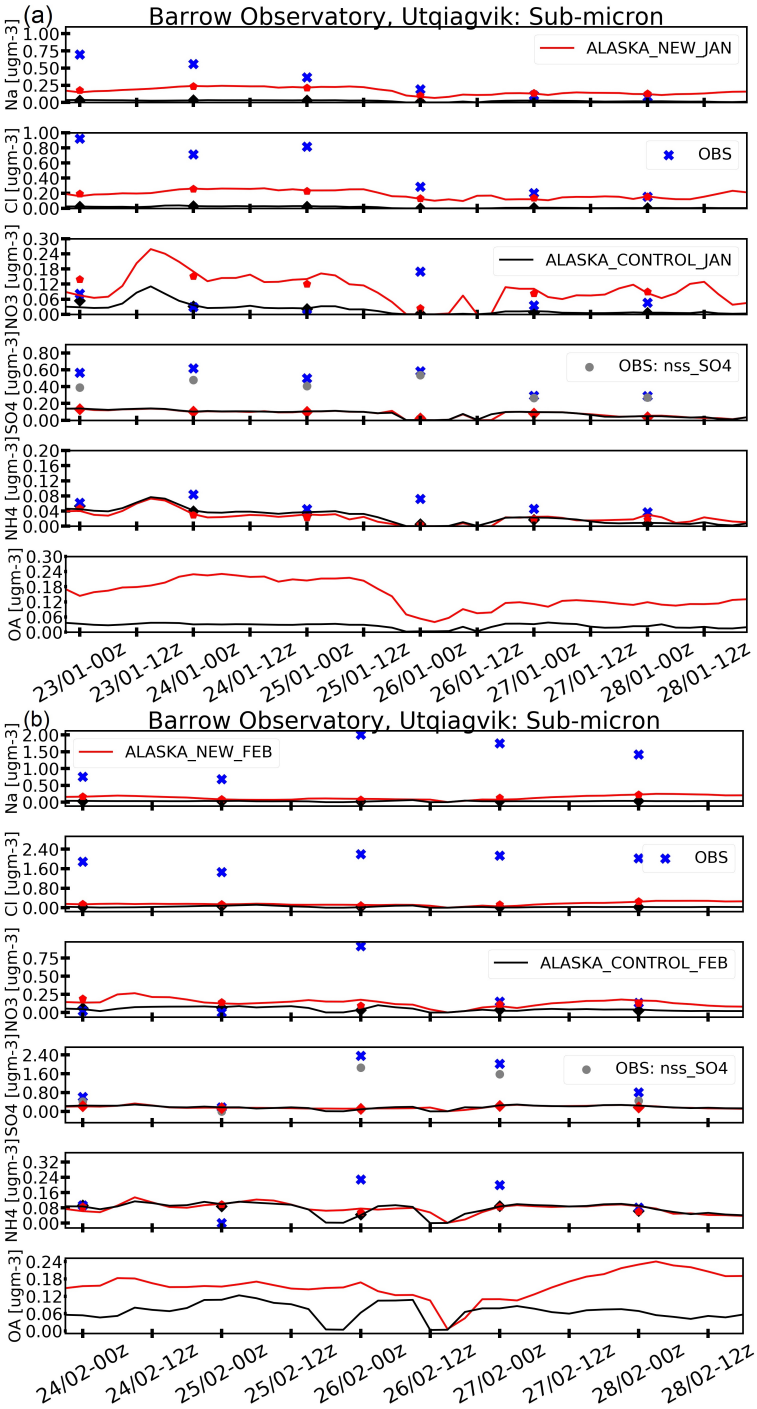

Figure 4.11: *Time-series during a) January and b) February 2014 of sub-micron mass concentrations of* Na^+, Cl^-, NO_3^-, NH_4^+, SO_4^{2-}, *in* $\mu g\ m^{-3}$, *simulation period. Model simulations are validated against in-situ sub-micron aerosols at Utqiaġvik, Alaska, in UTC (every 12h; 00z,12z). The black line shows model results from the CONTROL run; the red line shows the ALASKA_NEW run, while the daily observations are shown in blue crosses. The corresponding model daily averages are shown as black diamonds for the control simulation and as red pentagons for the ALASKA_NEW runs. See the text for details about the observations and model runs.*

run on a windy day (28 February 2014). The first sensitivity test leads to an increase in SSA emission fluxes by up to 0.2 μ g m^{-2} s^{-1} where sea-ice fraction equals zero (not shown) and to an increase of up to 1.2 μ g m^{-3} and 0.05 μ g m^{-3} in super-micron and sub-micron Na^{+} respectively. The second sensitivity test yields similar results. This is because ERA5 sea-ice fractions are higher than the test case (0.75) leading to an overall increase in the SSA emission flux of up to 0.02 μ g m^{-2} s^{-1}, especially east of Utqiaġvik, affecting primarily super-micron SSA (increases of up to 1.5 μ g m^{-3}) rather than sub-micron SSA, probably due to the short simulation period.

These results illustrate the sensitivity of super-micron SSA, in particular, to the prescribed sea-ice fraction and point out the need of improving this in models. Regarding sub-micron SSA, which is less sensitive to local sea-ice in these model simulations, there is the possibility that missing mechanisms influencing sub-micron SSA emissions need to be included such as SSA production from breaking waves in the surf zone for particles with diameters between 1.6 and 20 μm *(De Leeuw et al., 2000)* or diameters ranging between 0.01-0.132 (ultrafine), 0.132-1.2 and 1.2-8.0 μm *(Clarke et al., 2006)*, which would be important and in the ice free ocean.

4.1.6.5 Evaluation against observations in northern Alaska

The model is also run for January 2014 including all the updates described above (see **Table 4.2** and section 4.2.3.3). **Fig. 4.11** shows the comparison between runs with and without all these updates compared to sub-micron aerosol observations at Utqiaġvik during the January and February campaigns. Note that the focus of this section is on sub-micron SSA, as there are not detailed super-micron observations during the periods of the simulations due to their weekly temporal variation and due to the fact that the model still underestimates observed sub-micron SSA at Utqiaġvik.

There are differences in the observations between the two periods. While sub-micron observed Na^{+} and Cl^{-} did not exceed 1 μ g m^{-3} during January, observed sub-micron Na^{+} and Cl^{-} concentrations reached up to 2.5 μgm^{-3} in February. As noted earlier such high concentrations of Na^{+} and Cl^{-} were not observed at Alert and Villum during January and February 2014. This could be explained by the fact that these two sites are entirely surrounded by more sea-ice in winter. Overall, the model simulates better observed sub-micron Na^{+} and Cl^{-} in January but still underestimates concentrations by up to 0.3 and 0.6 μ g m^{-3}, respectively, while sub-micron NO_3^{-} is slightly overestimated. Biases in January decrease from -0.31 to -0.16, -0.50 to -0.33 and -0.04 to 0.039 μ g m^{-3}, respectively. On the other hand, sub-micron Na^{+}, Cl^{-} are still underestimated in the run including all the updates

(ALASKA_NEW_FEB) by up to 2.0 μ g m^{-3} in February indicating that there are missing processes in the model linked to sub-micron SSA emissions, as discussed earlier. However, overall the results at Utqiaġvik in February, including all the updates (ALASKA_NEW_FEB), are better compared to the control simulation (ALASKA_CONTROL_FEB). Biases for Na^+, Cl^- and NO_3^- decrease from -1.29 to -1.18, -1.90 to -1.78 and -0.20 to -0.11 μ g m^{-3}, respectively. During both months, the model lacks SO_4^{2-} due to missing local anthropogenic sources, as discussed in section 4.2.5.6 and due to small contribution from ss-SO_4^{2-} as is shown also in section 4.2.5.1 for different Arctic sites. Missing aqueous phase reactions, such as the oxidation of SO_2 by ozone in alkaline SSA aerosols *(Alexander et al., 2005)* and SO_4^{2-} production from metal catalyzed O_2 oxidation *(McCabe et al., 2006)* are missing from the model and might explain these high discrepancies compared to sub-micron observations at Utqiaġvik. Also, the variations in modelled NH_4^+ between the ALASKA_CONTROL_JAN and ALASKA_NEW_JAN for January and February simulations are small. The model underestimates observed NH_4^+, which peaks at 0.2 μ g m^{-3} during February. Calculated biases and RMSEs for all aerosol species and for January and February campaigns are given in APPENDIX A5.

Comparison with data from Gates of the Arctic (see APPENDIX A6) shows that there are not significant differences between the control run and including all the updates in February 2014. The model still underestimates observed tOC due to missing local anthropogenic sources and overestimates SO_4^{2-}, NO_3^-, Na^+ and Cl^-. However, due to short period of the simulation only two observations are available, thus more detailed observations are needed to examine further the reason why the model differs from the observations at this site.

4.1.6.6 Are blowing snow and/or frost flowers a source of sub-micron SSA during wintertime at Utqiaġvik?

Lastly, we consider whether enhanced SSA at Utqiaġvik could be due to blowing snow or frost flower sources. We noted earlier that KRP19 found no evidence of blowing snow or frost flowers at this site but that SSA originated from open leads during wintertime. The findings of KRP19 are supported by the earlier laboratory study of *Roscoe et al. (2011)* who reported that frost flowers are not an efficient source of SSA. However, an older study by *Shaw et al. (2010)* found that during winter at Utqiaġvik surface frost flowers formed on the sea and lake ice are a source of ocean derived OM. Modelling studies that have included a source of blowing snow and frost flowers suggest that they are contributing to SSA at this time of year at Utqiaġvik, Alert and Zeppelin *(Xu et al., 2013, 2016; Huang and Jaeglé, 2017; Rhodes et al., 2017)*.

Table 4.4: *Average sub-micron modelled and observed depletion factors, following* Frey et al. (2020)*, during the January and February campaigns 2014 in Utqiaġvik. Model results for ALASKA_NEW_JAN and ALASKA_NEW_FEB simulations are shown here, respectively. Observations refer to sub-micron data from NOAA. See text for details.*

Depletion Factors	Model	Observations
January campaign		
$DF_{SO_4^{2-}}$	-0.77	-7.56
DF_{Na^+}	-1.05	-0.09
February campaign		
$DF_{SO_4^{2-}}$	-4.8	-2.15
DF_{Na^+}	-1.1	-0.19
DF_{Br^-}	-	0.063

To investigate whether blowing snow or frost flowers could also be a source of SSA during the campaigns at Utqiaġvik, depletion factors are estimated following *Frey et al. (2020)*. *Frey et al. (2020)* reported that blowing snow was the main source of SSA rather than frost flowers and open-leads in Antarctic wintertime, based on SO_4^{2-} and Br^- depletion in SSA being indicative of blowing snow origin, and not sea water. Here, depletion factors are calculated using modelled and observed sub-micron aerosol concentrations, during the campaign periods. More specifically, SO_4^{2-} depletion relative to Na^+ ($DF_{SO_4^{2-}}$), Na^+ depletion relative to Cl^- (DF_{Na^+}) and Br^- depletion relative to Na^+ (DF_{Br^-} only for observations in this case) are calculated using the following equation:

$$DF_x = 1 - \frac{R_{smpl}}{R_{RSW}} \tag{4.6}$$

where, R is the mass ratio (x:y) in the model or in the sample (smpl) and in reference seawater (RSW) *(Millero et al., 2008)*. A depletion factor (DF_x) between 0 (small) and 1 (strong) indicates 0–100% depletion, whereas DF_x smaller than 0 indicates enrichment. *Frey et al. (2020)* suggested, based on depletion of SO_4^{2-} relative to Na^+, that most SSA originates from blowing snow on sea-ice with minor contributions from frost flowers, and not from open leads.

Average values of modelled and observed DFs are shown in **Table 4.4**. In January, observed SO_4^{2-} concentrations are 8.56 times more than in reference seawater, possibly due to internal mixing with anthropogenic SO_4^{2-} from NSA oilfield emissions (KRP18), whilst in the model, SO_4^{2-} concentrations are 1.77 times higher than in reference seawater, showing enrichment in both cases (**Table 4**). Modelled and observed depletion factors also show enrichment in February. This is in contrast with results from *Frey et al. (2020)* who reported substantial depletion. They also reported a case of enrichment due to possible contamina-

Table 4.5: *Average modelled and observed molar ratios for sub-micron SSA, following* Kirpes et al. (2019)*, during January and February campaign 2014 in Utqiaġvik. Model results from ALASKA_NEW_JAN and ALASKA_NEW_FEB simulations are used. Observations refer to sub-micron data from NOAA.*

Molar ratios	Model	Observations
January campaign		
SO_4^{2-}:Na^+	0.11	0.55
Cl^-:Na^+	0.74	1.1
February campaign		
SO_4^{2-}:Na^+	0.37	0.2
Cl^-:Na^+	0.8	1.08

tion from the ship, an anthropogenic source. Our modelling results and the observations at Utqiaġvik indicate enrichment of SO_4^{2-} relative to Na^+, suggesting that blowing snow and frost flowers are not a source of SSA, at least during these campaigns. Previous studies *(Douglas et al., 2012; Jacobi et al., 2012)* suggested that blowing snow and frost flowers near Utqiaġvik are characterised by SO_4^{2-} depletion compared to seawater. Na^+ depletion relative to Cl^- during both campaigns also shows enrichment, albeit more negligible in the observations than in the model. Observed Na^+ depletion relative to Cl^- is 1.09 or 1.19 times more than in reference seawater, during January and February, respectively.

SSA can also play an important role in polar tropospheric ozone and halogen chemistry through the release of active bromine during spring *(Fan and Jacob, 1992; Simpson et al., 2007; Peterson et al., 2017)*. Reactions involving bromine are an important sink of ozone (O_3) *(Barrie, 1986; Barrie et al., 1988; Wang et al., 2019a; Marelle et al., 2021)* and also cause mercury oxidation *(Schroeder et al., 1998)*. Br^- depletion relative to Na^+ is calculated only during February, since observed Br^- was zero during the period of January campaign, and indicates a small depletion in reference seawater. The calculated observed mass ratio of Br^- to Na^+, based on the available observations of Br^- during February, indicates a seawater origin. The observed mass ratio of Br^- to Na^+ ranges between 0.0057 and 0.0059, while the mass ratio of Br^- to Na^+ in reference seawater is equal to 0.006. On the other hand, *Frey et al. (2020)* reported no or little Br^- depletion relative to Na^+ due to Br^- loss at the surface and small depletion further aloft. For a more comprehensive analysis, observations are required at different locations and altitudes across coastal northern Alaska.

We note that the version of WRF-Chem used in this study does not include halogen chemistry. It has since been implemented in a later version by *Marelle et al. (2021)* to examine ozone depletion events during March-April 2012 at Utqiaġvik. Heterogeneous reactions on sea salt aerosols emitted from the sublimation of lofted blowing snow were included.

Their results suggested that blowing snow could be a source of SSA during spring although it should be noted that this version of the model overestimated SSA at remote Arctic sites, such as Alert and Villum, when blowing snow was included as a source of SSA. Also, they did not examine wintertime conditions.

Finally, following KRP19, modelled and observed molar ratios of sub-micron Cl^-:Na^+ and SO_4^{2-}:Na^+ are estimated to further examine the origins of SSA and to compare our findings with KPR19 (see **Table 4.5**). Observed molar ratios of Cl^-:Na^+ and SO_4^{2-}:Na^+ for January and February campaign periods agree with KRP19 (Cl^-:Na^+ equal to 1.08, see KRP19 supplement - Table S3 and text). This indicates a seawater origin (following *Pilson (2012)*), and confirms the findings of KRP19 that there was no evidence for blowing snow and frost flowers as a source of SSA during the campaigns. Model averaged molar ratios are smaller in magnitude than the observations. Observed and modelled ratios differences in magnitude could be altered by the fact that the model underestimates sub-micron SSA and SO_4^{2-}, due to missing mechanisms for sub-micron SSA emissions and local/regional anthropogenic sources of SO_4^{2-}. Differences between observed and modelled Cl^-:Na^+ ratios could also be due related to issues with modelled SSA lifetime and chemical processing during long range transport. Previous studies found that sub-micron SSA have larger chloride depletion than super-micron SSA *(Barrie et al., 1994; Hara et al., 2002; Leck et al., 2002)*. *May et al. (2016)* used molar ratio enrichment factors of Cl^-:Na^+ as an indicator of long-range transport influence on SSA at Utqiaġvik. They reported that Cl^- depletion was larger for sub- than super-micron SSA due to a longer lifetime. On average during the simulation periods in January and February 2014, the results indicate that modelled Cl^- has undergone significant atmospheric processing. This is consistent with KRP18 observing the presence of both nascent (locally-produced) SSA and aged (partially chloride-depleted) SSA. Based on this analysis of depletion factors and molar ratios, little evidence suggest a blowing snow influence on SSA during the campaigns at Utqiaġvik is found. Rather, the presence of predominantly easterly winds (s.s. 4.2.6.3) and the presence of leads east of Utqiaġvik (especially during February), suggests that the primary source of SSA was marine from open-leads, in agreement with the findings of KRP19.

4.1.7 Conclusions

In this study WRF-Chem is used to investigate Arctic Haze composition at remote Arctic sites during wintertime with a particular focus on SSA, processes influencing SSA emissions and the contribution of SSA to Arctic Haze. Model performance is evaluated first in terms of reproducing aerosol composition in the Arctic before focusing on processes influencing

SSA at regional scales over northern Alaska during winter 2014.

The control version of WRF-Chem overestimates super-micron, coarse mode and TSP SSA due to missing and out of date SSA emission treatments in the model. In particular, the addition of a more realistic wind speed dependence for SSA, based on satellite data, and inclusion of a dependence of SSA emissions on SSTs leads to improved results for super-micron, coarse mode and TSP SSA and NO_3^- over the Arctic. The latter has already been included in certain modelling studies. Also, recent data analysis studies in the Arctic have pointed out that wind speed alone cannot predict SSA production and that other mechanisms, such as SST dependence, are needed. However, there are still uncertainties regarding the role of SSTs in SSA production. Other factors such as seawater composition, wave characteristics, fetch model and salinity need to be considered in future versions of WRF-Chem. In this study, marine organic aerosol emissions are also activated in the model since they are an important component of SSA in the Arctic and globally. Inclusion of all these updates leads to improved representation of SSA over the wider Arctic. Modelled super-micron, coarse mode and TSP SSA are reduced at all Arctic sites in better agreement with the observations. Results for NO_3^- are also improved overall due to less formation via heterogeneous uptake of HNO_3. Inclusion of the SST dependence only has a small effect on sub-micron SSA in the Arctic. In the future, other SST dependencies could be considered such as that proposed by *Sofiev et al. (2011)* which could increase sub-micron SSA at low temperatures *(Salter et al., 2014, 2015; Barthel et al., 2019)*. However, further field data studies are needed to confirm such dependencies in the Arctic.

A source of ss-SO_4^{2-} is also added to the model leading to improved modelled SO_4^{2-} in the high Arctic (e.g. Alert) and Alaskan (e.g. Gates of the Arctic, Simeonof) sites. However, at sites such as Utqiaġvik, which may be influenced by the Prudhoe Bay oilfields, the model still underestimates sub-micron SO_4^{2-} possibly due to missing anthropogenic emissions. Missing aqueous chemical formation of SO_4^{2-} in dark conditions may also explain these discrepancies (e.g. SO_4^{2-} production from metal catalyzed O_2 oxidation of S(IV), *McCabe et al. (2006)*). Results from the improved quasi-hemispheric run indicate a shift in the balance between $(NH_4)_2SO_4$ and NH_4NO_3, with aerosols being less acidic than the base version of the model.

Overall, super-micron, coarse mode and TSP SSA, OA, SO_4^{2-}, NH_4^+ and NO_3^- are improved in the HEM_NEW quasi-hemispheric simulation compared to observations at Arctic sites, based on biases and RMSEs. However, the model underestimates sub-micron SSA at Utqiaġvik where there are episodes with significantly higher SSA compared to other Arctic sites.

Model sensitivity to different processes affecting SSA over northern Alaska during win-

ter is explored. KRP19 pointed out that there is sea ice biology influence at Utqiaġvik during wintertime and that marine emissions are an important source of organic aerosols at this location. In order to include local sources of marine organics, the ratio of OC:Na^+ is used leading to higher modelled OA, in better agreement with previous measurements at this site (and at Alert) and its advised to be included in future WRF-Chem simulations in the Arctic region. To further explore the uncertainties on sub-micron SSA, ERA5 sea-ice fraction is tested in the model. The results, in combination with different sensitivities changing sea-ice fraction, show that super-micron SSA are more sensitive to sea-ice treatments than sub-micron SSA in the model. The use of satellite sea-ice data, combined with higher resolution simulations over Utqiaġvik and coastal Arctic sites, will help to gain more detailed insights into the influence of open-leads on SSA production during wintertime. The results of this study also highlight that SSA dry removal is less important than the role of open leads in the Arctic during wintertime. The role of wet deposition on SSA is also examined. In that case, the precipitation flux is doubled and as result super-micron SSA decreased, but the sensitivity did not affect sub-micron SSA. Wet deposition is not addressed further in this study, because according to NOAA climate data recorded precipitation and snowfall was the lowest during February 2014. Wet deposition is addressed in details in the companion paper for BC. Our results suggest that further investigation is needed to determine more realistic dry deposition velocities over snow, ice and ocean in the Arctic and to derive more realistic sea-ice fractions, including the presence of open leads, which can vary over periods of days. The sensitivity of model results to using a higher wind speed dependence, based on data from *Russell et al. (2010)*, is investigated for sub-micron SSA. This leads to small improvements in the model sub-micron SSA, with the model performing better during January than February period of the campaign.

Further analysis is required to understand the origins of, in particular sub-micron SSA in northern Alaska, and to improve their representation in the WRF-Chem model. For example, missing sources of sub-micron SSA, such as a source function for ultrafine SSA particles due to breaking waves *(Clarke et al., 2006)* could be included. Also, anthropogenic sources of Cl^- may need to be considered, such as road salt in urban areas *(McNamara et al., 2020; Denby et al., 2016)* or coal combustion, waste incineration, and industrial activities *(Wang et al., 2019b)* which are not included in current global inventories. The model also lacks anthropogenic emissions of Na^+. Anthropogenic sources of Na^+ could be wastewater and sewage treatment systems, contamination from landfills and salt storage areas (e.g. *Panno et al. (2006)*). However, detailed analysis of depletion factors and molar ratios at Utqiaġvik, Alaska showed that during the simulation period the main source of SSA are from marine emissions including open ocean or leads and there is no evidence of frost flowers or blowing

snow as a source of SSA, at least during the periods considered in this study, in agreement with the findings of KRP19. Further observations from field measurements are needed to better understand SSA emissions and their dependencies.

This model study supports recent findings based on observations that SSA make an important contribution to super-micron (coarse mode, TSP) mass concentrations during wintertime at remote Arctic sites. Future work has to consider carefully possible sources of sub-micron SSA and their inclusion in models, in order to explain elevated observed SSA during wintertime. Processes linked to the open ocean are likely to become more important with decreasing sea-ice cover in the Arctic due to climate warming. Observations of SSA components including organic aerosols (often missing) are needed to improve understanding about processes and their treatments in models, and in order to reduce uncertainties in estimation of aerosol radiative effects.

Chapter 5

Processes and sources affecting modelled wintertime BC over the Arctic and north of Alaska: a sensitivity study

Air pollution transported from mid-latitude source regions during winter and early spring leads to elevated concentrations of aerosols in the Arctic, including BC, the so-called Arctic Haze phenomenon. BC, an important SLCF, absorbs incoming solar radiation and leads to warming in the Arctic *(AMAP, 2015)*. Observation based studies report elevated EBC measurements during winter and early spring at remote Arctic sites *(Schmale et al., 2022)*. Local sources within the Arctic also contribute to the observed EBC burden, with significant sources, for example in Siberia and Alaska. Regional transport models are needed to better quantify the contribution of remote and local sources to Arctic BC, coupled with up to date global emission inventories. Detailed multi-model studies have pointed out that models underestimate BC concentrations during wintertime and are not capable capturing episodes with elevated EBC *(Eckhardt et al., 2015; Mahmood et al., 2016; Whaley et al., 2022b)*. These discrepancies could be due to model uncertainties, such as removal processes or missing regional and local sources in global emission inventories. WRF-Chem is used in this study to investigate the model's ability to simulate Arctic BC. Simulations at quasi-hemispheric and regional scales over northern Alaska are used to gain insights into processes and sources affecting Arctic BC. This work will help to better understand and quantify the contribution of already existing regional and local BC emissions in the Arctic, which might increase due to climate warming and associated industrial development.

This Chapter is being prepared for submission as: Ioannidis, E., Law, K.S., Raut, J.-C., Marelle, L., Onishi, T., Andrews, E., Ohata S., Mori T., Morris, S., Kondo, Y., Soulie A.,

Darras, S., Granier, C., Quinn, P.K., Pratt, K.A.: Processes and sources affecting modelled wintertime BC over the Arctic and northern Alaska: a sensitivity study
The paper is presented in the following sections. The Supplementary Material is given in Appendix B.

5.1 Introduction

Anthropogenic sources from mid-latitudes (Europe, Asia, North America) are the main source of air pollution transported to the Arctic during wintertime and the winter-spring transition *(Barrie et al., 1981; Quinn et al., 2002b; Stohl, 2006; AMAP, 2015)*. Enhanced concentrations of aerosols (such as sulfate (SO_4^{2-}), nitrate (NO_3^-), black carbon (BC), organic aerosols (OA)) during winter and early spring are reported by early studies (Rahn and McCaffrey, 1980; Barrie et al., 1994; Quinn et al., 2002b), a phenomenon called Arctic Haze. BC is a short-lived climate forcer and absorbs incoming solar radiation *(AMAP, 2015)*. It causes warming in the Arctic by *AMAP (2015)*. BC also affects aerosol-cloud interactions and when deposited on snow or ice results in a sea-ice feedback, accelerating sea-ice melting *(Quinn et al., 2008; Flanner, 2013; Yun et al., 2013; AMAP, 2015)*. Local anthropogenic and natural emissions within the Arctic region contribute to Arctic Haze *(Schmale et al., 2018; Kirpes et al., 2018)*. For example, gas flaring and combustion sources, including domestic, transportation, industries and power plants, in Siberia *(Stohl et al., 2013b; Winiger et al., 2017, 2019; Zhu et al., 2020; Matsui et al., 2022; Popovicheva et al., 2022)*, oil fields on the north Alaskan slope (NSA), including Prudhoe Bay *(Kirpes et al., 2018; Kolesar et al., 2017)* are contributing to Arctic aerosols. Residential emissions and power generation combustion (coal, oil, wood), which significantly increase during very cold Arctic winters, are also contributing to BC burden in the Arctic (Sobhani et al., 2018). Metal industry and combustion sources, such as power generation, from Siberia (e.g. Kola peninsula) identified as sources of pollution at Villum station, Greenland during winter and spring *(Nguyen et al., 2013)*. However, the magnitude and contribution of different sources is still highly uncertain. This is especially true for within Arctic BC sources over northern Alaska which have received less attention than other regions such as Siberia.

A study by *Leaitch et al. (2018a)* estimated that 28% of BC at Alert, Canada during wintertime is associated with gas flaring emissions from northern Russia and Eurasia. A modelling study by *Zhu et al. (2020)* showed that 64% of Arctic BC in January is from Russian anthropogenic emissions, with gas flaring emissions, from regions in Russia such as Komi Republic and Yamalo-Nenets Autonomous Okrug, contributing up to 33%, while the contribution of residential combustion is up to 18%. Early studies showed that emissions from oil/gas

production in Russia (e.g. Norilsk), industrial source areas in Eurasia (e.g. Norilsk) and combustion sources (e.g. Tyumen, Russia) contribute to BC burdens at Utqiaġvik, Alaska (formerly known as Barrow) during winter (October – February) *(Polissar et al., 1999, 2001)*. A source apportionment study by *Barrett et al. (2015)* showed that fossil fuel combustion sources are dominant at Utqiaġvik between December and February, with the air masses originating from northern Russia, the Arctic Ocean and northwest Canada.

Data analysis studies show that elevated BC concentrations observed during late winter and early spring at remote Arctic sites *(Sharma et al., 2006; Winiger et al., 2017; Schmale et al., 2022)*. However, models tend to underestimate Arctic BC during wintertime regardless of the model or the emission inventory *(Shen et al., 2017; Mori et al., 2020; Liu and Matsui, 2021; Whaley et al., 2022b)*. Model underestimations could be due to missing regional and local Arctic sources in global emissions inventories *(Stohl et al., 2013b; Klimont et al., 2017; Winiger et al., 2017)*, representation of BC lifetime in the models *(Liu and Matsui, 2021)*, treatments of BC ageing *(Liu et al., 2011; Ikeda et al., 2017a)*, limited model resolution *(Ma et al., 2013)* or uncertainties in simulated dry and wet removal *(Liu et al., 2011; Sharma et al., 2013; Mahmood et al., 2016; Shen et al., 2017; Xu et al., 2019)*.

Dry deposition occurs locally, especially over regions with high emissions, whereas wet deposition occurs during the transport of air masses into the Arctic at different altitudes. Dry and wet removal is shown to have seasonal variations, which also drives BC seasonality *(Shen et al., 2017; Matsui et al., 2022)*. However, earlier studies do not clearly indicate which removal process affects Arctic BC more during wintertime. Dry deposition, which mainly affects surface concentrations, maybe is weaker during wintertime *(Quinn et al., 2007a)*. *Sharma et al. (2013)* also estimated that dry deposition is the dominant removal for Arctic BC north of 70°N and wet removal is dominant south of 70°N during wintertime, showing that BC is removed en route to the Arctic. In contrast, a more recent multi-model study by *Mahmood et al. (2016)* showed that dry and wet deposition are equally important during wintertime. Wet deposition is more important during summer and autumn *(Sharma et al., 2006; Mahmood et al., 2016)*. In the latest Arctic Monitoring and Assessment Programme (AMAP) evaluation, the models, including the Weather Forecast model, coupled with chemistry (WRF-Chem), overestimate total deposition (wet and dry) in Greenland and the European Arctic *(Whaley et al., 2022b)*, which may help to explain why the models underestimate wintertime BC. Thus, it is important to quantify better and improve our understanding of the contribution of removal processes to model deficiencies.

In this study the ability of the WRF-Chem model to simulate wintertime Arctic BC is examined. First model performance is evaluated against observed BC in the high Arctic during wintertime. Then, to better understand the cause of modelled BC discrepancies

compared to the observations, the sensitivity to processes affecting modelled BC in the Arctic is investigated. This includes the contribution of wet and dry deposition (remote and within the Arctic) over source regions and during transport affecting the Arctic. A second focus is on the sensitivity to processes, including boundary layer dynamics, and the contribution of regional (local) sources over northern Alaska, in particular the NSA oilfields, to BC at Utqiaġvik on the north coast of Alaska. For this study, WRF-Chem is run on a quasi-hemispheric and regional scale over northern Alaska for shorter periods in January (and February) 2014, coinciding with the measurement campaign reported by *Kirpes et al. (2018, 2019)*. *Kirpes et al. (2018)* analysed atmospheric particle samples collected in winter 2014 in Utqiaġvik and showed that their measurements were influenced by air masses from the Arctic Ocean to the north and NSA oilfields, including Prudhoe Bay, to the east. Soot was internally mixed with organic and SO_4^{2-} aerosols, suggesting an anthropogenic influence from background Arctic Haze and Alaskan oil field emissions. This study builds on the study presented in *Ioannidis et al. (2022)* (Chapter 4) which focused on improving sea-spray aerosols (SSA) emissions and adding missing sources of marine organics in the model during winter 2014 over the wider Arctic and northern Alaska also following the findings of *Kirpes et al. (2018)*. The scope of the previous study was not to investigate the contribution of anthropogenic emissions from the NSA oilfields to aerosols burden at Utqiaġvik. The possible influence of these emissions to SO_4^{2-} at Utqiaġvik was briefly discussed. This study aims to fill in this gap by investigating the influence of NSA oilfields on BC at Utqiaġvik.

The WRF-Chem model, emission inventories and model sensitivity simulations are described in Section 5.2. The BC observations used to validate the model in this study are introduced in section 5.3. The results are presented in Sections 5.4 and 5.5. In section 5.4, model BC is evaluated at remote Arctic sites, and the contribution of removal processes to BC is examined. The results from the regional study focusing on Utqiaġvik, Alaska are presented in section 5.5. Processes which affect BC at a regional scale, such as removal treatments and boundary layer dynamics are investigated. The sensitivity to regional and local sources of BC at Utqiaġvik during wintertime is also investigated. The implications of our findings for the simulation of Arctic BC and conclusions are presented in Section 5.6.

5.2 Methodology

5.2.1 WRF-Chem model setup

The WRF-Chem (Weather Research and Forecasting coupled with Chemistry) chemical transport model version 3.9.1.1 is used to perform quasi-hemispheric and regional simu-

lations to investigate Arctic BC. WRF-Chem is a fully coupled, online meteorological and chemical transport mesoscale model *Grell et al. (2005)*. In this study, a modified version by *Marelle et al. (2017)* and *Ioannidis et al. (2022)* is used, including the updates on SSA. The model setup is the same as the one described in detail in Chapter 4. MOSAIC scheme and model removal treatments are described in Chapters 3 and 4.

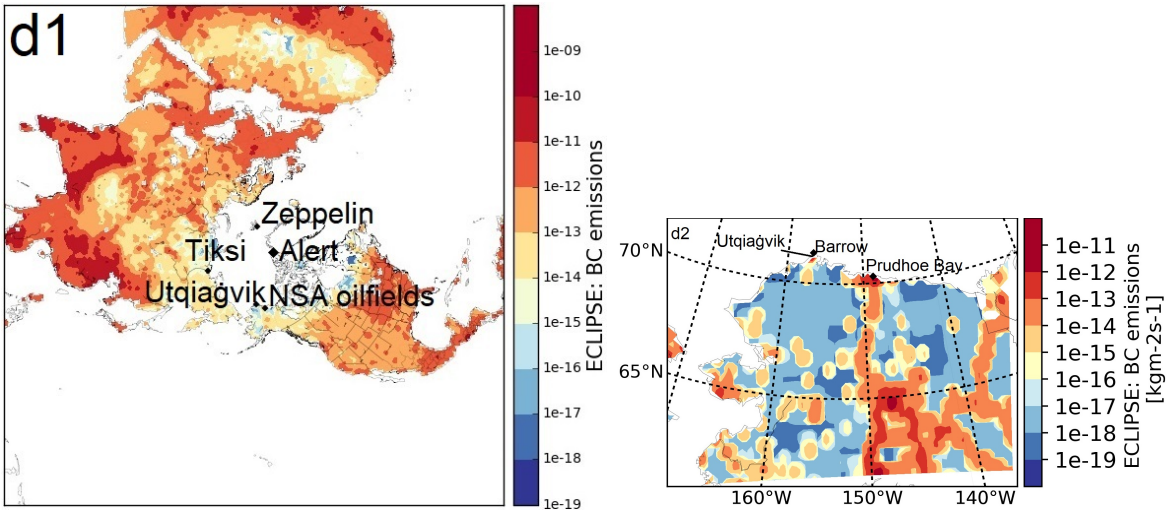

Figure 5.1: *Average BC emissions (ECLIPSE v6b), in $kgm^{-2}s^{-1}$, during January and February 2014, interpolated on the WRF-Chem grid at 100km (d1: left map) and during January 2014 at 20km (d2: right map). The map on the left shows the locations of four remote Arctic sites used in this study and the location of North Alaskan Oilfields (NSA). The map on the right shows the location of Prudhoe Bay oilfields and the Barrow Observatory near Utqiaġvik town.*

5.2.2 WRF-Chem simulations

Two simulation domains (polar stereo-graphic projection) are used in this study, as shown in Figure 5.1. The first (parent) domain (d1) covers a large part of the Northern Hemisphere with 100 × 100 km horizontal resolution. Boundary and initial conditions and nudging methods are the same as in Chapter 4.

As a reminder, the model is run at 100 km from November 2013 to February 2014 and the first two months are considered spin up. The model is run at 20 km from 23 to 28 January 2014 corresponding to one the campaigns which took place in Utqiaġvik *(Kirpes et al., 2018, 2019)*. The model is run also for the campaign in February 2014 (from 24 to 28 February). Here the results are only discussed in section 5. For all these simulations, 4 days prior to the beginning of the campaign is considered spin up and the model output is every 3h. The simulations at the quasi-hemispheric and regional scales are summarized in Table 5.2 and discussed in detail in Sections 4 and 5, respectively.

Table 5.1: *List of WRF-Chem simulations.*

Simulation Name	Description
Quasi- hemispheric simulations (100km)	
CONTROL	Base simulation
WET_DEP_OFF	Total wet deposition OFF
DRY_DEP_OFF	Dry deposition OFF
Regional simulations over Alaska (20km)	
ALASKA_CONTROL	Base simulation
DRY_DEP_OFF_20km	Dry deposition OFF
WET_DEP_OFF_20km	Total wet deposition OFF
METEO	Sensitivity to boundary layer dynamics
ANTHR_OFF	Local Alaskan anthropogenic emissions off
CAMS_ANTHR	CAMS anthropogenic emissions
ANTHR_5x	5x Alaskan anthropogenic emissions (ECLIPSE v6b)

5.2.3 Emissions

5.2.3.1 Anthropogenic emissions

ECLIPSE inventory: Anthropogenic emissions from the Evaluating the Climate and Air Quality Impacts of Short-Lived Pollutants version 6 (ECLIPSE v6b) inventory, with a resolution of 50 x 50 km are applied in all simulations at quasi-hemispheric and regional scale for winter 2013–2014 *(Amann et al., 2011; Klimont et al., 2017; Höglund-Isaksson et al., 2020; Whaley et al., 2022b)*. Nine sectors are included in the ECLIPSE v6b inventory: agriculture (livestock), residential, energy, industry, gas flaring and venting, international shipping, transportation, waste, and solvent use. **Figure 5.1** shows BC average emissions at quasi-hemispheric scale during January and February 2014.

CAMS inventory: Anthropogenic emissions from Copernicus Atmosphere Monitoring Service (CAMS) emissions are applied at a regional scale over northern Alaska for a sensitivity simulation during January 2014. More specifically, CAMS version 5.3, at a resolution of 10 x 10 km are used *(Soulie, 2022)*. Eight sectors are included in the CAMS v5.3 inventory: agriculture (livestock and soils), power plants, fugitives, industry, oil refineries and transformation industry, residential and commercial combustion, shipping, solid waste and waste water, road and off-road transportation. Shipping emissions in this version are derived from the Finnish Meteorological Office (FMI), based on the exact location of the ships, using AIS (Automatic Identification System) *(Johansson et al., 2017)*.

5.2.3.2 Natural emissions

Emissions of Dimethyl Sulphide (DMS), mineral dust, and lightning NO_x are calculated online (see in *Marelle et al. (2017)* and references within). Biogenic emissions for 2014 are calculated online from Model of Emissions of Gases and Aerosol from Nature (MEGAN) inventory *(Guenther et al., 2012)*. SSA emissions are described in section 2.1 and *Ioannidis et al. (2022)*.

5.3 Observations

Different sites within the Arctic region are used to evaluate model BC during January and February 2014 using a variety of different measurement techniques depending on location (see **Figure 5.1**).

5.3.1 Filter-based absorption photometer: Aethalometer data

Aerosol absorption coefficient data (b_{abs}), in 1/Mega-meters [Mm^{-1}], is obtained from European Monitoring and Evaluation Programme (EMEP) dataBASe (EBAS - http://ebas.nilu.no) for Zeppelin, Svalbard, Norway and Alert, Canada. Tiksi, Russia data are derived from National Oceanic and Atmospheric Administration (NOAA). The Aethalometer (Magee AE-31) measures the attenuation of light transmitted through particles accumulating on a quartz fiber filter at seven wavelengths (370, 470, 520, 590, 660, 880, and 950 nm). More information about AE-31 Aethalometer can be found in different studies, such as *Sharma et al. (2017)*, *Backman et al. (2017)*, *Ohata et al. (2020)* and references therein. The equivalent black carbon (EBC) measurements used in this study are based on absorption at 880 nm to minimize potential interference from other absorbing factors (e.g. brown carbon) *(Sharma et al., 2017, 2019)*. *Backman et al. (2017)* estimated 36% relative uncertainty for this instrument, due to particle loading and scattering that cannot be determined. For each site a constant mass absorption coefficient (MAC), in m^2g^{-1}, is applied to the b_{abs} data to give EBC in ngm^{-3}, as described below. In this study, EBC observations with diameter smaller than 1.0 µm ($r_d \leq 1.0$ µm) are defined as sub-micron, EBC $r_d \leq 2.5$ µm are defined as fine mode EBC. In the case of $r_d < 10$ µm then EBC is defined as total EBC. All the observations are given in UTC.

Zeppelin, Norway: This station is located near to Ny-Alesund, on Svalbard (78.9N, 11.9W). b_{abs} at 880 nm wavelength is used to estimate EBC (sub-micron), by applying MAC, which relates the optical attenuation through the filter to the BC concentration. The MAC

value for this aethalometer at Zeppelin station and 880 nm wavelength is equal to 15.9 m^2g^{-1}. More information about this data can be found in *Eleftheriadis et al. (2009)*.

Tiksi Observatory, Russia: This site is located in northern Siberia, Russia on the coast of the Laptev Sea and is surrounded by tundra (71.6N, 128.9E). To determine EBC (total EBC), b_{abs} at 880 nm is used with a MAC equal to 16.6 m^2g^{-1}. The observatory is located south of Tiksi city. Wind direction and wind speed criteria are applied to sampling at this site to remove local pollution, mainly related to activities in Tiksi city. More specifically, data are removed when wind directions are between 315° and 45° and when wind speeds are less than 1 ms^{-1} *(Asmi et al., 2016)*.

Alert, Canada: The observatory is located on the edge of the Lincoln Sea at the north-eastern tip of Ellesmere Island, Nunavut in the Canadian Arctic (82.5N, -63.3W). A MAC equal to 16.6 m^2g^{-1} is used to estimate EBC (fine mode). From now on will refer to Tiksi Observatory as Tiksi.

5.3.2 Barrow Observatory, Utqiaġvik, Alaska

Observations of b_{abs} from two different instruments at Barrow Observatory are used in this study to estimate observed EBC.

5.3.2.1 Aethalometer and nephelometer measurements

Barrow Observatory at Utqiaġvik is located on the north coast of Alaska (71.3N, -156.6W). All air masses originating from the wind sector 130° to 360° are removed to exclude local pollution from Utqiaġvik town. The data are obtained from National Oceanic and Atmospheric Administration (NOAA) and can be downloaded from the following link: https://gml.noaa.gov/dv/data/. Two types of instruments measure absorption coefficient data at the Barrow Observatory (refer to it as Barrow). A seven wavelength Magee Aethalometer (AE31) has been operating at Barrow, measuring b_{abs}, with a cut-off size at 10μm (*Backman et al. (2017)* and references within). Also, b_{abs} measured with a particle soot absorption photometer (PSAP) are used in this study *(Lack et al., 2008)*. PSAP uncertainties depend on the uncertainty of the flowmeter calibration (1.5 %) and measurement of spot size (2 %) *(Sharma et al., 2017)*. The PSAP instrument has two cut-off sizes, at 1.0 μm and 10 μm and data at wavelength 530 nm is used in this study. PSAP b_{abs} is corrected for instrument non-idealities using the *Bond et al. (1999)* correction with the *Ogren (2010)* adjustment for multiple wavelengths. All observations provided in UTC.

5.3.2.2 Continuous soot monitoring system

A continuous soot monitoring system (COSMOS) has been developed to measure mass concentration of BC *(Miyazaki et al., 2008; Kondo et al., 2009, 2011; Ohata et al., 2020)*. COSMOS derives light absorption coefficients at a wavelength of 565 nm from the change in transmission through a quartz-fiber filter after loading with BC particles *(Kondo et al., 2009; Ohata et al., 2019)*. COSMOS measures BC with $r_d \leq 1.0$ μm, the data are hourly and no wind direction criteria are applied. The COSMOS instrument is located at Barrow, 11 m above sea level (masl). *Ohata et al. (2019)* estimated the accuracy of BC measurements comparing COSMOS measurements with a single-particle soot photometer at different sites and reported it to be 10%.

5.3.2.3 Absorption coefficients

To calculate EBC from the AE31 and PSAP instruments at Barrow, the MAC is calculated as in *Ohata et al. (2020)*. MAC is equal to the slope of the correction between b_{abs} and COSMOS-BC. More specifically, during January and February 2014, hourly b_{abs}-AE31 and COSMOS-BC are highly correlated (coefficient of determination - r^2 = 0.90 (not shown here)). The MAC for AE31 is equal to 24.5 m^2g^{-1}. Also, b_{abs}-PSAP for particles with diameters less than 1 μm and less than 10 μm, and COSMOS-BC are highly correlated (r^2 = 0.92 and r^2 = 0.90, respectively (not shown here)). Similarly, MAC for PSAP is equal to 12.61 m^2g^{-1} ($r_d \leq 1.0$ μm) and 11.33 m^2g^{-1} ($r_d \leq 10.0$ μm).

5.4 Sensitivity of Arctic BC to removal processes

First the capability of the model to simulate Arctic BC during wintertime over the wider Arctic is evaluated. More specifically, four Arctic sites are used to assess modelled BC (CONTROL), located close to or downwind of Russian emissions (Tiksi), or European emissions (Zeppelin) or Alaskan emissions (Barrow) or in the high Arctic (Alert). Then the results of two sensitivity simulations are presented. First dry and then wet deposition are switched off, to examine the effect of removal on modelled Arctic BC over the Arctic and at the different measurement sites.

5.4.1 Evaluation of modelled Arctic BC

First considering the observations, at Alert (**Fig. 5.2a**) during the study period observed EBC reaches higher concentrations, up to 200 ngm^{-3}, at the end of February 2014, probably

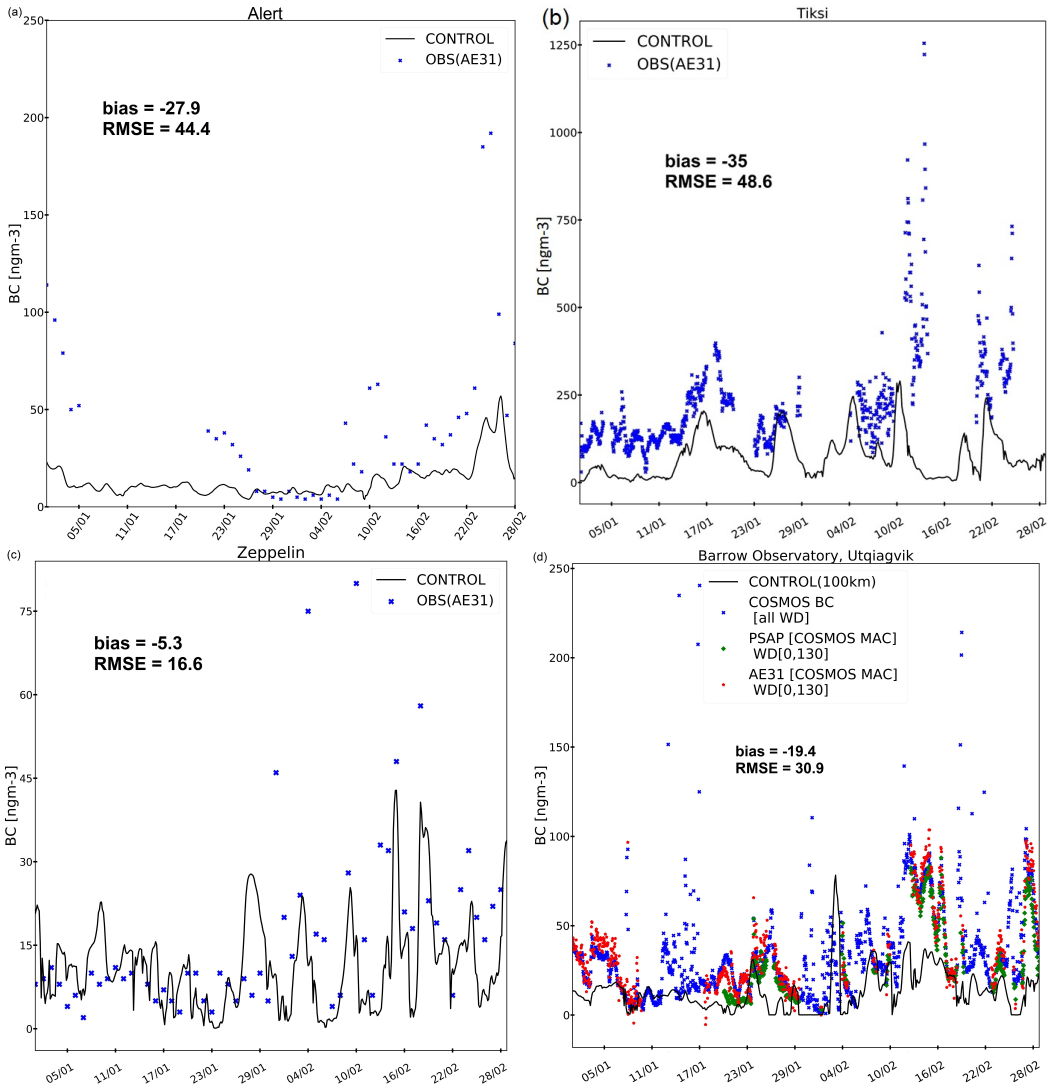

Figure 5.2: *Model validation of BC, in ngm^{-3}, against in-situ observations of (a) fine mode EBC at Alert, Canada, (b) total EBC at Tiksi, Russia, (c) sub-micron EBC at Zeppelin, Svalbard, Norway and (d) sub-micron EBC at Barrow, near Utqiaġvik town, Alaska, in UTC during January and February 2014. The black line shows model results from CONTROL. Blue crosses show observations from AE31 and COSMOS (Barrow). Green triangles show PSAP EBC, while red pentagons show AE31 (Barrow) obtained EBC. Note that the scales are different between the four sites. The scales are the same only for Alert and Barrow. See text for details.*

due to the transport of air masses from mid-latitude source regions, such as Siberia and Europe (Sharma et al., 2006). At Tiksi, observed EBC has periods with elevated concentrations, up to 1250 ngm^{-3} (**Fig. 5.2b**). Elevated BC observations at Tiksi during winter and spring are due to long-range transport from mid-latitudes, dryer winter months (less wet scavenging), and local sources (surface transportation, domestic and power plants) trapped on the ground due to stable conditions (Asmi et al., 2016; Winiger et al., 2017, 2019; Popovicheva

et al., 2019). At Zeppelin, EBC ranges between 5 and 75 ngm^{-3}, with higher EBC observed in February (**Fig. 5.2c**). EBC at Barrow varies between 1 and 250 ngm^{-3} during January and February 2014 (**Fig. 5.2d**). The highest concentrations are observed when EBC is measured using the COSMOS instrument, sampling all wind directions. PSAP and AE31 EBC do now show the same elevated concentrations, since wind direction criteria are applied and include only regional or large scale influences. EBC at Barrow and Alert are of similar magnitude during the study period, with more frequent elevated EBC at Barrow, possibly due to local influence. Barrow is also further south and closer to the Asian emissions compared to Alert. However, previous studies showed that both Alert and Barrow can be influenced by Russian anthropogenic emissions (Polissar et al., 1999, 2001; Sharma et al., 2006; Barrett et al., 2015; Leaitch et al., 2018b). The highest EBC concentrations are reported at Tiksi during winter 2014, while the lowest are at Zeppelin. Previous studies have reported lower EBC concentrations at Zeppelin compared to other Arctic sites, possibly due to higher precipitation during wintertime *(Freud et al., 2017; Schmale et al., 2022)*. **Figure 5.3a** shows average modelled surface BC during January and February 2014, over the whole domain from the base CONTROL quasi-hemispheric run. The highest values are over source regions in China and India, reaching up to 22000 ngm^{-3} on average. Lower BC is simulated over the Arctic (**Fig. B1**, APPENDIX B.1). Over Siberia, BC reaches up to 2300 ngm^{-3}, likely due to Russian gas flaring, industry and energy emissions. Modelled BC over coastal northern Alaska and Canada is up to 20 ngm^{-3}. The base simulation (CONTROL) underestimates BC at all sites as shown in **Fig. 5.2** and based also on the calculated biases and RMSEs (see Chapter 3 for details). At Alert, the model simulates BC up to 55 ngm^{-3} and underestimates observed EBC by up to 150 ngm^{-3} (bias = -27.9 and RMSE = 44.4). During wintertime BC at Alert is mainly due to long-range transport as noted earlier. At Tiksi, the model simulates more BC than at Alert, by up to 250 ngm^{-3}, since Tiksi is located closer to Russian emissions, as noted above. However, the model underestimates (bias = -35, RMSE = 48.6) observed EBC. Pollution episodes at Tiksi are also underestimated by up to 1000 ngm^{-3}. The measurements may still be influenced by local emissions even if a filter has been applied. At Zeppelin, the model simulates less BC, by up to 45 ngm^{-3}, compared to Alert and Tiksi, but in better agreement with the observations (bias = -5.3 and RMSE = 16.6). At Barrow, model BC does not exceed 80 ngm^{-3} and underestimates (bias = -19.4, RMSE = 30.9) observed EBC. Pollution episodes at Barrow are also underestimated by up to 220 ngm^{-3}. The measurements may still be influenced by local emissions even if a filter has been applied. Overall the model captures EBC variability, for example at Zeppelin, but it underestimates EBC, for example at Tiksi and Barrow. The influence of wet and dry removal on modelled BC is investigated in the next section.

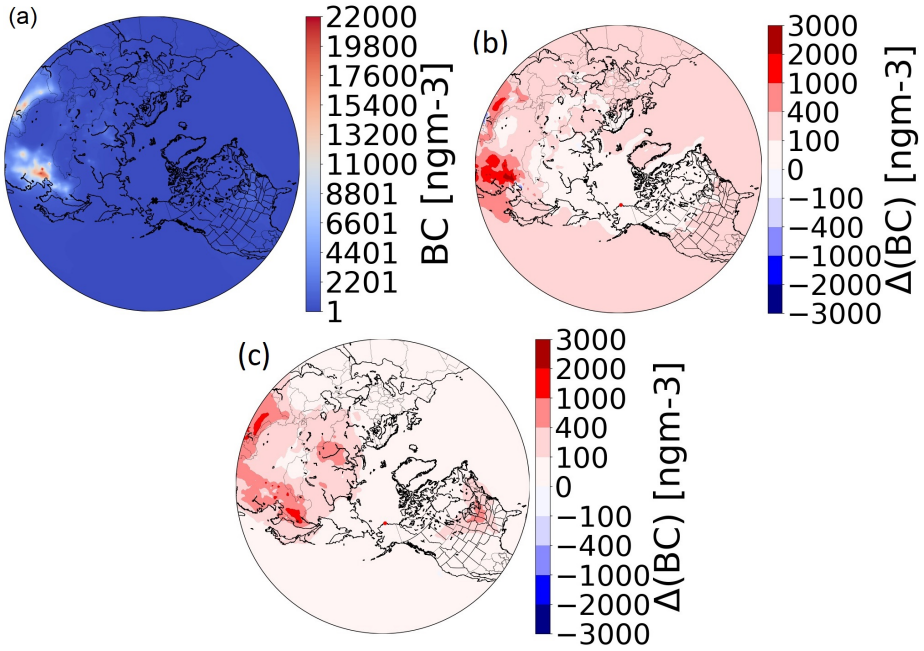

Figure 5.3: *Sub-micron (a) Average modelled BC in ngm^{-3} from CONTROL run, (b) Average differences between WET_DEP_OFF minus CONTROL, (c) Average differences between DRY_DEP_OFF minus CONTROL. All averages are for January and February 2014.*

5.4.2 Role of wet and dry deposition on Arctic BC

It is still uncertain which removal process is more important and how they affect BC at different Arctic locations. To examine the effect of wet removal on Arctic BC during wintertime, a sensitivity simulation is performed, were wet deposition in grid-scale clouds and parameterized cumulus clouds is switched off (WET_DEP_OFF). **Figure 5.3b** shows the average difference between WET_DEP_OFF and CONTROL at the surface. The change in BC due to wet removal is up to 3000 ngm^{-3} over China and India, while the change over continental regions, such as north-west Russia, is smaller, up to 400 ngm^{-3}. The change over the central Arctic Ocean, northern Alaska and Canada is up to 100 ngm^{-3}. **Figure B2** in APPENDIX B.1 shows the same average differences at higher altitudes (2 to 8 km). The change in the Arctic BC varies from 300 ngm^{-3} at 2 km to 100 ngm^{-3} at 8 km. BC at 2 km and 4 km is mostly affected. This illustrates that Arctic BC is also influenced by wet deposition during transport to the Arctic in the free troposphere, as noted in earlier studies *(Stohl, 2006; AMAP, 2015)*.

To examine the effect of dry deposition on BC in the Arctic during wintertime, the model is run with dry deposition and gravitational settling switched off (DRY_DEP_OFF). **Figure 5.3c** shows average differences between DRY_DEP_OFF and CONTROL for January and February 2014. The change in surface BC is up to 3000 ngm^{-3} over sources regions, such

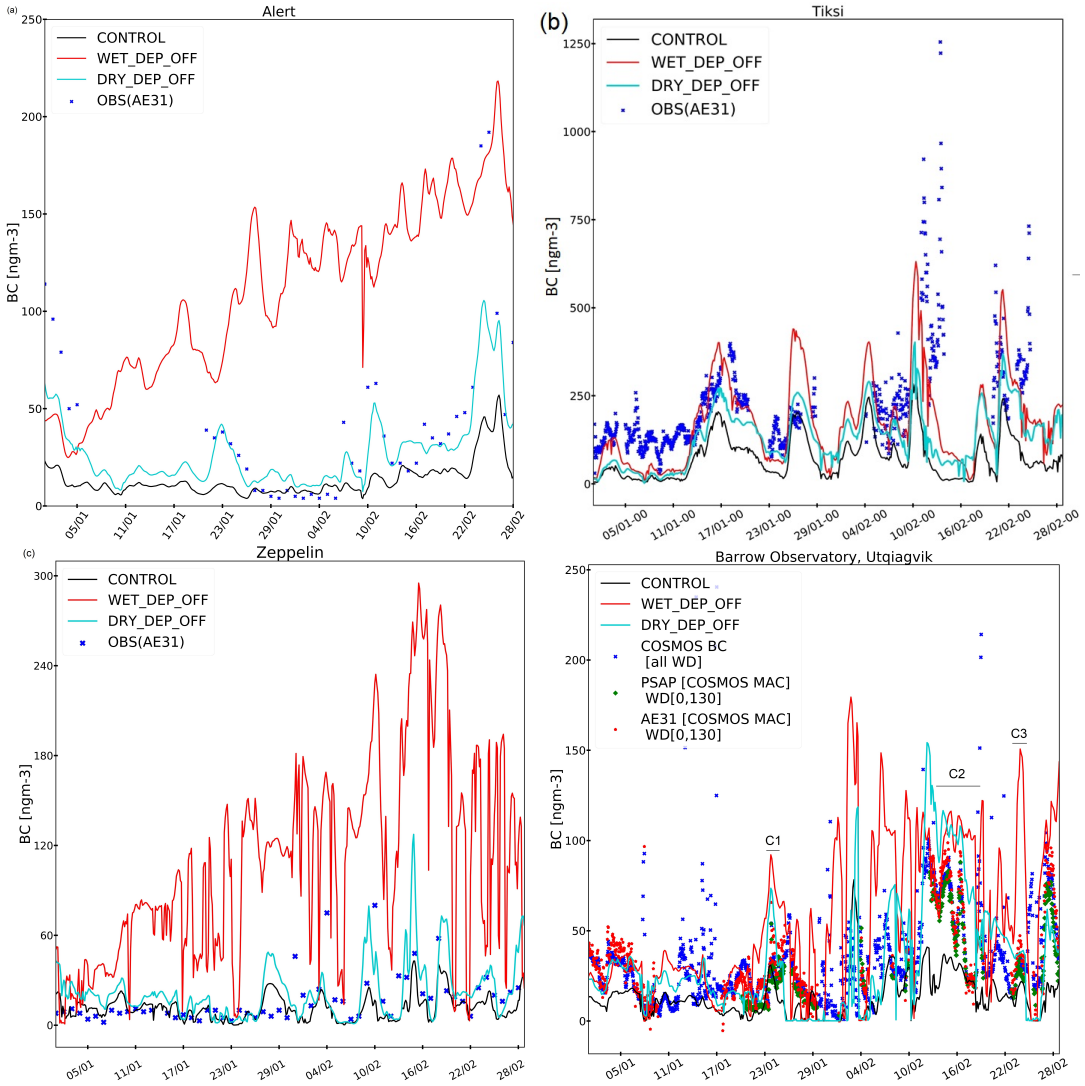

Figure 5.4: *(a) Fine mode EBC at Alert, Canada, (b) total EBC at Tiksi, Russia, (c) sub-micron EBC at Zeppelin, Svalbard, Norway and (d) sub-micron EBC at Barrow, near Utqiaġvik town, Alaska, in UTC during January and February 2014. Black line shows results for CONTROL run, the red line shows WET_DEP_OFF run and dark turquoise line shows DRY_DEP_OFF. Alert, Zeppelin, Tiksi: EBC observations are shown in blue crosses. Barrow: EBC observations are shown in blue crosses (COSMOS) and green triangle (PSAP) in UTC. Note that the scales are different between the four sites. The scales are the same only for Alert and Barrow. See text for details.*

as China and India, and also by up to 1000 ngm^{-3} over Siberia (e.g. south of Kara sea), where Russians emissions are located. BC changes due to dry deposition and gravitational settling are smaller at higher altitudes compared to wet deposition. However, there are insignificant. BC change varies from 250 ngm^{-3} at 2 km to 100 ngm^{-3} at 4 km, especially over source regions, such as China. At 6 km and 8 km the changes on BC are smaller, up to 50 ngm^{-3} and 30 ngm^{-3}, respectively. The BC change at 6 km and 8 km is also shown

over Alaska, due to transport of BC emissions from Asia, but the magnitude is smaller over Alaska, by up to 25 ngm^{-3}, than over China.

The influence of wet and dry deposition on Arctic surface BC is also examined and discussed for all sites. **Figure 5.4(a-d)** shows the time series of observed EBC at four Arctic sites compared to BC from CONTROL and the two sensitivity simulations. At Alert and Zeppelin, the change in modelled BC due to wet deposition is large, up to +150 and +240 ngm^{-3} respectively, compared to the other two sites and shows how wet removal affects BC at remote Arctic sites. These results suggest that excessive wet removal in the model could be contributing to low modelled BC either during long-range transport or in the Arctic, in particular at Alert. At Alert and Zeppelin BC change due to dry deposition (DRY_DEP_OFF) is smaller as shown in **Fig. 5.4**. Interestingly, enhanced EBC in the observations correlates quite well with modelled dry deposition influence. At Tiksi the model results are more sensitive to dry than wet removal. There are sporadic episodes during which wet deposition might be responsible for low modelled BC, such as 22 February 2022. On the other hand, dry deposition might be responsible for low modelled BC for example between 30 January and 2 February 2014. At Barrow modelled BC appears to be more sensitive to wet than to dry deposition. **Figure 5.4d** highlights three cases during which wet, dry or both removal processes could explain low modelled BC. Both sensitivity simulations indicate the sporadic nature of dry and wet removal. For example, between 25 and 26 January (C1) model results show sensitivity to dry deposition (more narrow peak in modelled BC). Between 10 and 16 February (C2) both wet and dry removal are influencing modelled BC, while between 23 and 24 February (C3) modelled BC is more sensitive to wet removal.

5.4.3 Discussion

For winter 2014, the analysis above shows that the model tends to underestimate BC at Arctic sites in agreement with recent multi-model studies *(Eckhardt et al., 2015; Whaley et al., 2022b)*. Even though ECLIPSE v6b includes more gas flaring emissions compared to ECLIPSE v5, as mentioned by *Whaley et al. (2022b)*, the model still cannot capture high observed peaks of BC at the Tiksi observatory probably due to underestimation of regional sources. However, at sites such as Zeppelin, the model captures better the observed variability during January and February 2014, where observed BC concentrations are lower in magnitude than the other sites. As discussed earlier, other processes also contribute to model discrepancies. Here, we focus on the influence of BC removal processes.

Table 5.3 shows average percentage and absolute changes in BC due to wet and dry deposition for January–February 2014. As noted earlier, wet deposition affects more mod-

Table 5.2: *Average BC percentage change (%) and absolute change, in ngm^{-3}, due to wet and dry deposition at four Arctic sites during January and February 2014 at the surface. Percentage change is calculated as* $\frac{(test\_run - CONTROL)}{CONTROL}$ *multiplied by 100.*

	Wet deposition		Dry deposition	
	Change (%)	Absolute change	Change (%)	Absolute change
Alert	+722	+96	+110	+15
Tiksi	+78	+58	+137	+102
Zeppelin	+844	+97	+93	+8.5
Barrow	+317	+42	+151	+20

elled BC at Zeppelin and Alert, and the sensitivity with wet deposition switched off leads to a larger percentage change in modelled BC at these two sites, by up to +844% and +722% respectively. Dry deposition at Zeppelin and Alert leads to a smaller percentage change (6 and 9 times less, respectively) in modelled BC, than wet deposition. At Tiksi, the average percentage change in BC due to dry deposition is almost two times higher than due to wet deposition whereas at Barrow wet deposition affects modelled BC two times more than dry deposition, showing that both removal processes are important at Barrow. In contrast with the work of *Sharma et al. (2013)* and *Mahmood et al. (2016)*, this study, which focuses on wintertime, shows that wet deposition is more important at Alert, Zeppelin and Barrow, while the effect of dry deposition is smaller as shown in **Figure 5.4**. *Mori et al. (2020)* measured EBC and precipitation (snow) and reported that wet removal is not effective during winter and spring at Barrow and wet deposition is maximum during summer, as the precipitation is higher in summer than in winter *(Freud et al., 2017; Mori et al., 2021)*, also in contrast to the results presented here. BC percentage change due to wet deposition at Zeppelin is almost three times more than at Barrow. This is also illustrated in **Figure 5.4** and supports the findings of *Mori et al. (2021)*, who reported that wet deposition fluxes of BC at Zeppelin during winter are higher than at Barrow. This may be because European emissions are more efficiently removed due to wet deposition during low-level transport in winter and spring. Zeppelin is located on Svalbard island, which experiences maximum precipitation during wintertime, in contrast to other regions in the Arctic, where the maximum precipitation occurs during summer *(Freud et al., 2017)*. However, an observation based study at Alert during wintertime suggested that dry deposition may be the dominant removal mechanism of BC and that models may be missing mechanisms linked to dry deposition onto snow in winter *(Macdonald et al., 2017a)*. This is in contrast to the results presented here

At higher altitudes (2-8 km) (see **Table B1 and B2**, APPENDIX B.1), the percentage and absolute change of wet deposition to BC is large at all sites, especially at Tiksi and Alert (2 km) and Zeppelin (2-4 km). At Barrow the effect of wet removal is higher in the

first 4 km, supporting the findings of *Mori et al. (2020)*, using a global model who reported that 90% of BC deposition occurred at altitudes below 4 km. The percentage and absolute changes of dry deposition to BC are also calculated (not shown here). BC change due to dry deposition is smaller compared to BC change due to wet deposition between 2 km and 8 km. At Zeppelin, Tiksi and Alert the BC change due to dry deposition at 2 km is higher than at Barrow, by 10 ngm^{-3}, while the changes on BC at higher altitudes are small at all sites.

In the recent multi-model evaluation *(Whaley et al., 2022b)*, a previous version of WRF-Chem was used, without model improvements and updates described in Chapter 4 (and Chapter 3). *Whaley et al. (2022b)* showed that WRF-Chem underestimates BC at remote Arctic sites, between 50 – 100 % for 2014–2015. This study reported that there is too much BC deposition in the models at mid-latitudes. However, BC deposition measurements are not available in the Arctic at the same sites providing BC observations during winter 2014 which could be used to validate the model results. Such measurements are needed to better constrain the models.

5.5 Regional BC over northern Alaska

The quasi-hemispheric simulations investigated the contribution of wet and dry deposition to BC over the wider Arctic, occurring over mid-latitudes or within Arctic emission regions or during transport. Simulations at higher resolution over northern Alaska are now used to investigate the sensitivity of model results to regional processes at 20km and BC sources over northern Alaska. The model is run from 23 to 28 January 2014 coinciding with *Kirpes et al. (2018)* campaign. The analysis is focused on BC at Barrow investigating the sensitivity of surface local and regional anthropogenic sources, removal processes and boundary layer representation in the model. The influence of horizontal resolution is also examined. As mentioned earlier, the model is also run from 24 to 28 February and the results will discussed briefly here to compare the behaviour of modelled BC during winter and winter-spring transition.

For the regional analysis, COSMOS-BC and PSAP EBC are used to evaluate the model, but also to distinguish regional and local BC contributions at Barrow by using wind direction data. **Figure 5.5** shows EBC observations at Barrow during late January 2014. Observed COSMOS BC concentrations range between 10 and 59 ngm^{-3} during this period. The differences between BC and PSAP EBC are small, by up to 10 ngm^{-3}. As mentioned earlier PSAP EBC is only measured when winds originated from the clean sector (between 0 and 130 degrees, i.e. east of Barrow - North Slope of Alaska), excluding local pollution from

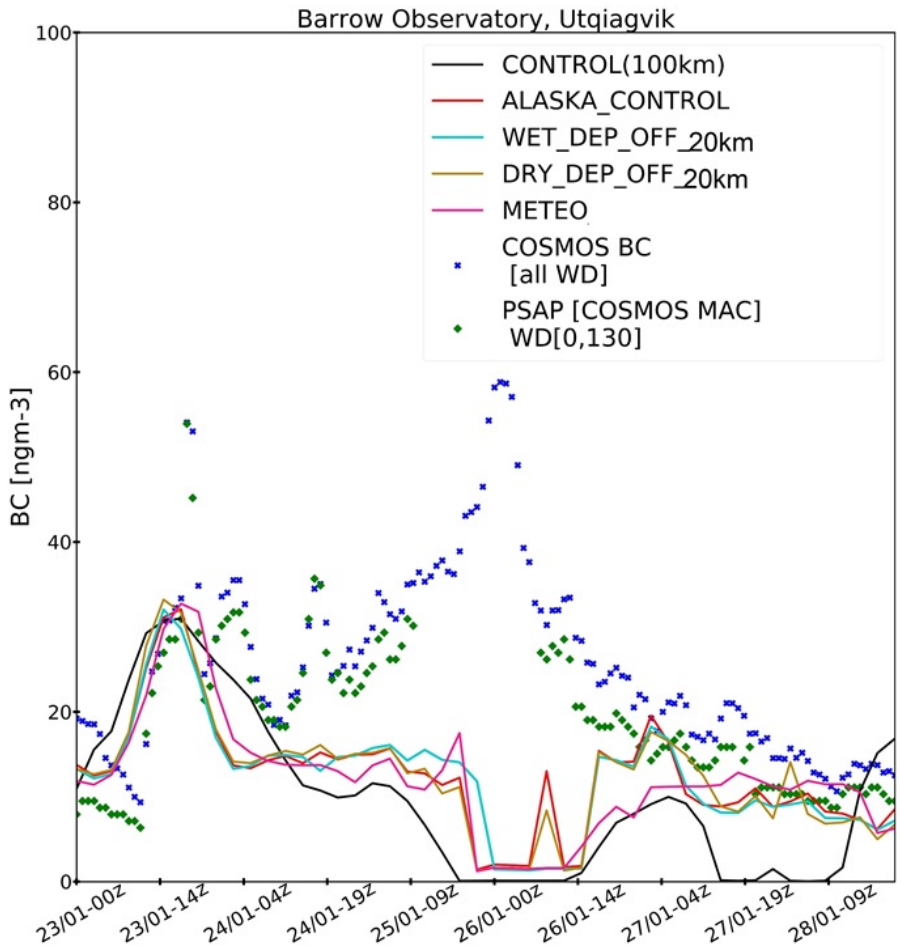

Figure 5.5: *Modelled sub-micron BC, in ngm^{-3}, at Barrow compared to in-situ observations during 23–28 January 2014. Gold line shows BC based on the CONTROL run at 100km. Black line shows ALASKA_CONTROL at 20km. Red line shows BC for the sensitivity simulation METEO. Turquoise line shows the results for the DRY_DEP_OFF run, and pink line shows BC for WET_DEP_OFF. Observations are blue crosses (COSMOS BC) and green triangle (PSAP). Model and observations are in UTC. See text for more details.*

Utqiaġvik town, while no wind criteria are applied to COSMOS measurements. Thus, wind direction observations obtained from Barrow are used to distinguish periods of regional and local influence on EBC observations at this site. During 24–25 and 27–28 January observed EBC may originate from NSA oilfields as winds are easterly (see **Fig. 5.1**). Both COSMOS and PSAP report elevated concentrations, up to 55 ngm^{-3}, at the end of 23 January, when winds are easterly (between 80° and 86°). During 27 and 28 January PSAP EBC and COSMOS BC do not exceed 20 and 30 ngm^{-3}, respectively. On the other hand, from 25 January at 13h (UTC) until 26 January 05h (UTC) the winds were from south-east (131° and 139°), indicating a local contribution from Utqiaġvik region (see **Fig. 5.1**), when PSAP data were excluded. An exception was at 26 January from 01h to 02h (UTC), when the winds

were easterly. During this period COSMOS BC ranged between 36 and 59 ngm^{-3}. During 24–28 February observed BC ranged between 1 and 105 ngm^{-3}, with the elevated observations measured on 27 February and shown at COSMOS and PSAP data, indicating a possible influence from NSA oilfields (not shown here). There were periods with local and Arctic Haze influence, when the winds originated from the south east and west respectively (133° and between 160° and 325°), with BC reaching up to 80 ngm^{-3}.

5.5.1 Horizontal resolution

Ma et al. (2013) showed that using finer horizontal resolution, from 1.9 x 2.5 degrees to the 0.9 x 1.25 degrees, BC biases decreased as resolution increased at least for springtime Arctic BC. **Figure 5.6a** shows the average concentrations of BC at 20km over northern Alaska (ALASKA_CONTROL). The model simulates more BC over source regions, such as Fairbanks, while the magnitude is smaller over the rest of the domain, with up to 60 ngm^{-3} over northern Alaska, due to NSA oilfield emissions included in the ECLIPSE inventory. Compared to quasi-hemispheric simulation (**Fig. 5.3a**) the model at 20 km simulates more BC over central Alaska, and over NSA oilfields, two areas with high regional Alaskan emissions.

Figure 5.5 shows the time series of BC at Barrow for the CONTROL simulation at 100 km compared to the ALASKA_CONTROL run at 20 km and the BC observations. On 23 January observed BC is captured by the model at 100 and 20 km resolution. The model still underestimates BC on 24 and 25 January at 20 km, while on 26 January, during the observed elevated BC, modelled BC at 100 and 20 km is below 5 ngm^{-3}, when observed BC is mainly originates from Utqiaġvik town. The analysis at 100 km shows that there is a washout event on 24 and 25 January, which could explain the low model BC. During 27 and 28 January, low model values are not explained by the results at quasi-hemispheric scale (**Fig. 5.5**), while at 20 km the model simulates more BC, an increase by up to 15-20 ngm^{-3} in better agreement with the observations.

Comparing the two simulations at different resolutions against COSMOS BC, the model at 20 km performs slightly better than at 100 km. More specifically, biases and RMSEs decrease from -15.7 and 21.8 to -13.1 and 18.8 ngm^{-3}, respectively. Though finer resolution leads to a somewhat better representation of BC possible reasons for the remaining discrepancies are investigated in the follow sections.

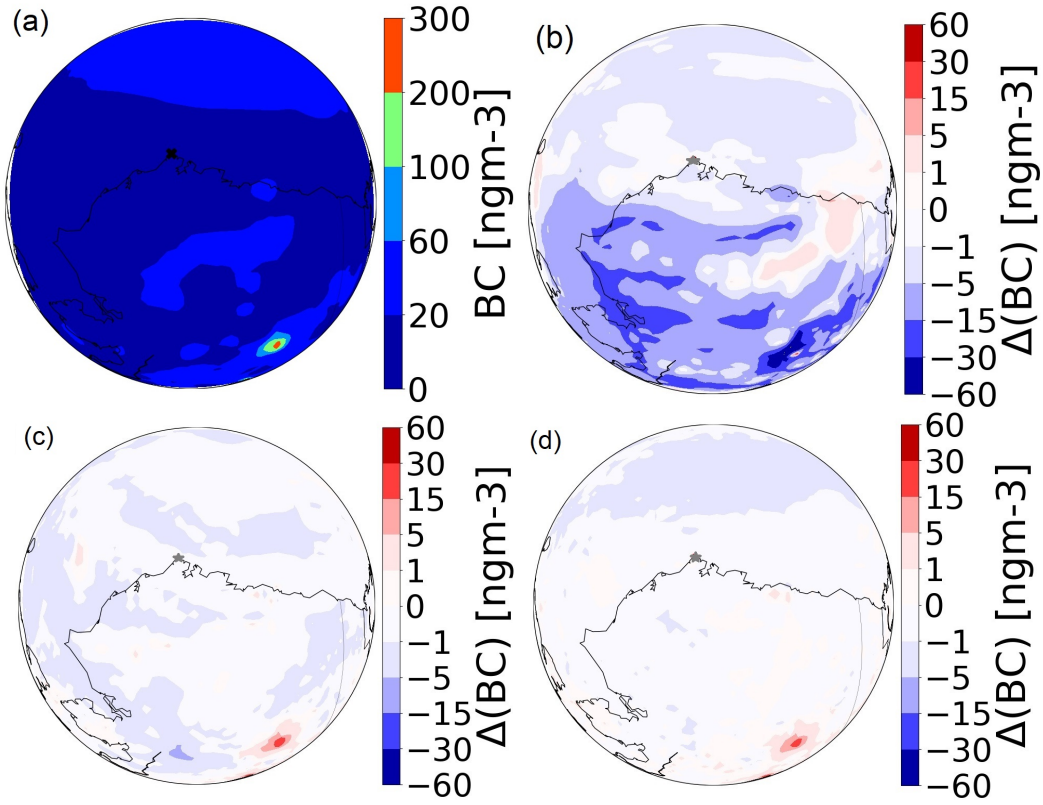

Figure 5.6: *Sub-micron (a) Average modelled BC, in ngm^{-3}, between 23 and 28 January 2014 from ALASKA_CONTROL run. Average differences of BC between (b) METEO, (c) WET_DEP_OFF_20km, (d) DRY_DEP_OFF_20km and ALASKA_CONTROL during January simulation period. Grey and black star indicates Barrow's location. See text for details.*

5.5.2 Boundary layer meteorology

Several studies have showed that meteorological conditions play an important role in the formation, and transport of atmospheric pollutants, during wintertime and the winter-spring transition (e.g. *Tran and Mölders (2011); Bei et al. (2012); Regmi et al. (2019)*). Correct modelling of aerosol dry deposition also depends on the ability of the model to capture the structure of the Arctic boundary layer including vertical temperatures and winds.

This section examines the sensitivity of BC over northern Alaska to the model's ability to capture the boundary layer structure. To achieve this, the MYJ (Mellor–Yamada–Janjic) boundary layer scheme is tested, instead of YSU at 20 km during January. MYJ, a local 1.5 order scheme, with the Eta-similarity surface-layer scheme *(Tastula and Vihma, 2011)*. Briefly, MYJ determines the spatially varying viscosities based on turbulent kinetic energy, local gradients, and a diagnosed length scale. *Sterk et al. (2015, 2016)* used MYJ for WRF simulations over snow-covered surfaces, coupled with the NOAH LSM land surface model, and reported that the model was better able to capture observed winds during late winter

and spring.

Considering the meteorological observations low temperatures were measured from 23 to 24 January at Barrow, with minimum at -21°C. During this period higher winds were measured, up to 14 ms^{-1}, originating from the east. From 25 January to 27 January there was a shift to weaker south-easterly winds ranging between 6 ms^{-1} and 9 ms^{-1} while it was also warmer, with temperatures between -13°C and -18°C. The last two days of the campaign (27–28 January) the temperatures and winds dropped by up to 4°C and 4 ms^{-1}, while winds were easterly. ALASKA_CONTROL captures the general pattern in the temperatures and winds. It is slightly too cold and too windy on 24 January and too warm and windy at the end of the simulation period (27 to 28 January). At the surface the run using MYJ (METEO) is slightly warmer than ALASKA_CONTROL and sometimes better at capturing observed temperature variability, however METEO is more windy and there are larger discrepancies compared to observed wind directions (**Figure B3**, APPENDIX B.3). Overall ALASKA_CONTROL performs better than METEO, based on lower biases and RMSEs for temperature and winds (**Table B3**, APPENDIX B.3). There are also differences between the two simulations and radiosonde observations at Barrow (**Figure B4**, APPENDIX B.2) at higher altitudes. Both simulations are colder in the first 750 m, with METEO capturing better observed temperatures between 250 m and 750 m, while ALASKA_CONTROL performs better below 250 m. Also, both simulations are more windy compared to the observations in the first 150 m, while between 200 m and 400 m METEO performs slightly better than the ALASKA_CONTROL with respect to the observations. Both simulations show discrepancies regarding relative humidity and wind direction at higher altitudes.

Figure 5.6b shows the average differences on modelled surface BC, between METEO and ALASKA_CONTROL over Alaska. Surface BC decreases when switching boundary layer scheme by up to 60 ngm^{-3} especially over source regions, such as the Fairbanks area in central Alaska, while decreases are smaller south of Barrow and over the NSA oilfields (up to 5 and 15 ngm^{-3}, respectively), along to the north coast of Alaska. BC mainly decreases over mountainous areas, such as Brooks Range, located south west of NSA oilfields, due to more precipitation in the METEO simulation (see discussion on APPENDIX B.2). Overall ALASKA_CONTROL captures better BC at Barrow.

These results show that modelled BC is sensitive to boundary layer parametrisations especially over local emission regions. Model discrepancies leading to high winds and temperatures can lead to less stable conditions in the model and as result to less dry deposition. Discrepancies in modelled low levels clouds can affect precipitation and snowfall leading to uncertainties in wet deposition.

5.5.3 Removal processes

The results at quasi-hemispheric scale suggest that wet deposition contributes more to modelled surface BC than dry deposition at Barrow. Here, runs switching off wet and dry removal are used to examine the sensitivity of modelled BC to these processes locally over the 20 km domain. This is in contrast to the simulations at 100 km which also include deposition over source regions (remote and within Arctic) and during transport to northern Alaska.

First, a run with wet removal off (WET_DEP_OFF_20km) is repeated. Surface BC at Barrow does not show significant differences and wet deposition affects BC over the NSA oilfields and Fairbanks area (**Fig. 5.6c**), where BC increases by up to 5 and 30 ngm^{-3}, respectively. At 2 km and 4 km, there is small effect of wet removal to BC over Utqiaġvik region and NSA oilfields (up to 3 ngm^{-3}, not shown here). At higher altitudes (6 to 8 km), the effect of wet removal regionally is insignificant (BC change less than 3 ngm^{-3}). The effect of switching wet deposition at Barrow is mostly notable between 25 January at 09 UTC and 26 January at 01 UTC (**Fig. 5.5**), when modelled BC is below 5 ngm^{-3} and winds are south-easterly (between 120° and 140°), prior to the observed elevated BC episode.

To further understand which removal process affects more model BC over northern Alaska during winter, the model is run also with dry deposition switched off for the same period. In this case, dry deposition affects simulated BC more, with the most significant effect seen in the Fairbanks region where model BC increases by up to 30 ngm^{-3}. Over the NSA oilfields the effect of dry deposition to model BC is small (up to 5 ngm^{-3}, **Fig. 5.6d**). At Barrow modelled BC is influenced by dry deposition mainly during the last two days of the simulation when BC is influenced by NSA oilfields, as discussed in section 5.5.1 (**Fig. 5.5**). Here, dry deposition can change model BC by up to 4 ngm^{-3}.

The results at the regional scale, suggest that wet and dry deposition are equally important during wintertime over northern Alaska with regional variations. More specifically, dry and wet deposition affects BC more over source regions, such as Fairbanks and, to a lesser extent, over the NSA oilfields. Based on the results presented so far, the first elevated BC episode (23–24 January) appears to be due to long range transport (20km results show little sensitivity to removal). At quasi-hemispheric scale (**Fig. 5.4**) the model shows more sensitivity to wet deposition which is not seen at regional scale (**Fig. 5.5**). Between 23–28 January both processes could be removing up to 15-20 ngm^{-3} BC at 20 km, whereas at 100 km wet deposition sporadically removes up to 40-100 ngm^{-3}. In this case, wet deposition during transport to Barrow is also contributing. However, between 25–26 January, the model is more sensitive to dry deposition at 100 km (event C1) whilst at a regional scale, the

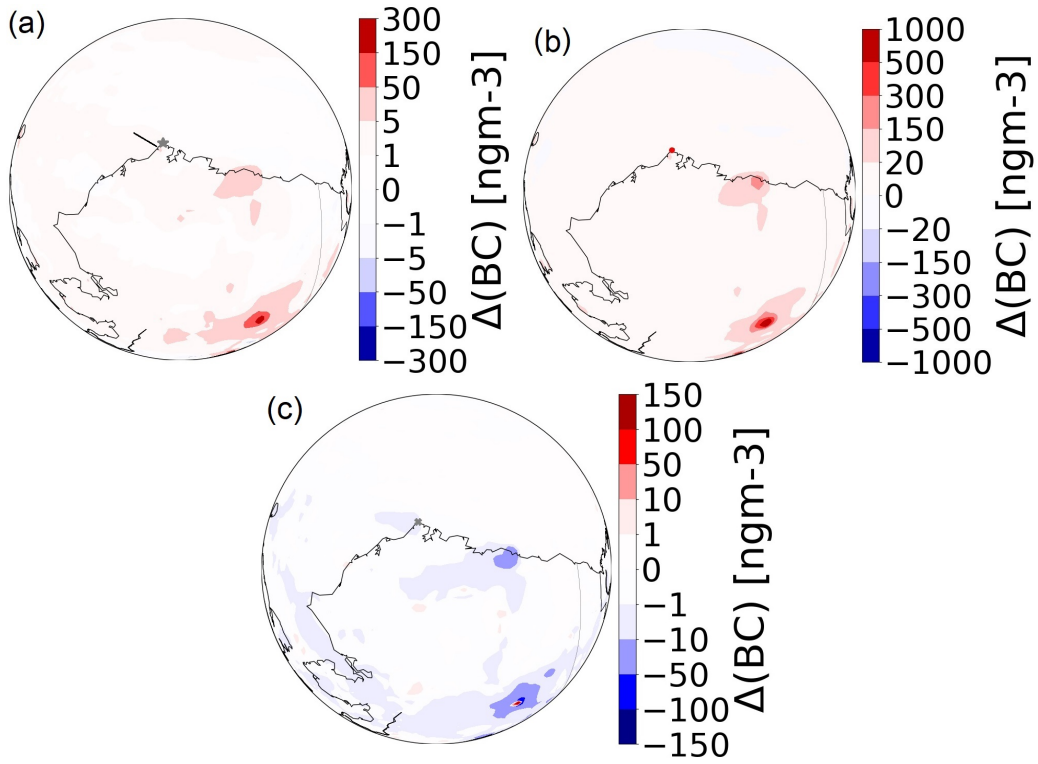

Figure 5.7: *Average differences of sub-micron BC in ngm^{-3}, between (a) ANTHR_OFF, (b) ANTHR_5x, (c) CAMS_ANTHR and ALASKA_CONTROL during January simulation period. Grey star indicates the location of Barrow. See text for more details.*

model is sensitive to both wet and dry deposition. These results illustrate that wet and dry deposition affect BC differently at Arctic-wide and regional scales and suggest that higher resolution simulations are needed to adequately model Arctic BC.

5.5.4 NSA oilfields influence

The sensitivity to regional Alaskan anthropogenic emissions, is examined in order to distinguish the contribution from remote, regional (including NSA oilfields) and local sources to BC at Utqiaġvik. The model is run without Alaskan anthropogenic (ECLIPSE v6b) emissions for the January period. A sensitivity simulation is also performed in which anthropogenic emissions are multiplied by a factor of 5. The aim of this run is to better understand which source regions might be influencing BC at Barrow. The model is also run with CAMS anthropogenic emissions to test the sensitivity to changing emission inventory.

When switching off Alaskan anthropogenic emissions (**Fig. 5.7a**) BC decreases by up to 50 and 300 ngm^{-3} over the NSA oilfields and Fairbanks region, respectively. **Figure 5.7a** shows that south-west of Barrow there is an increase in BC by up to 50 ngm^{-3} (see black line on the map). For example, the ECLIPSE v6b inventory includes BC emissions from domestic,

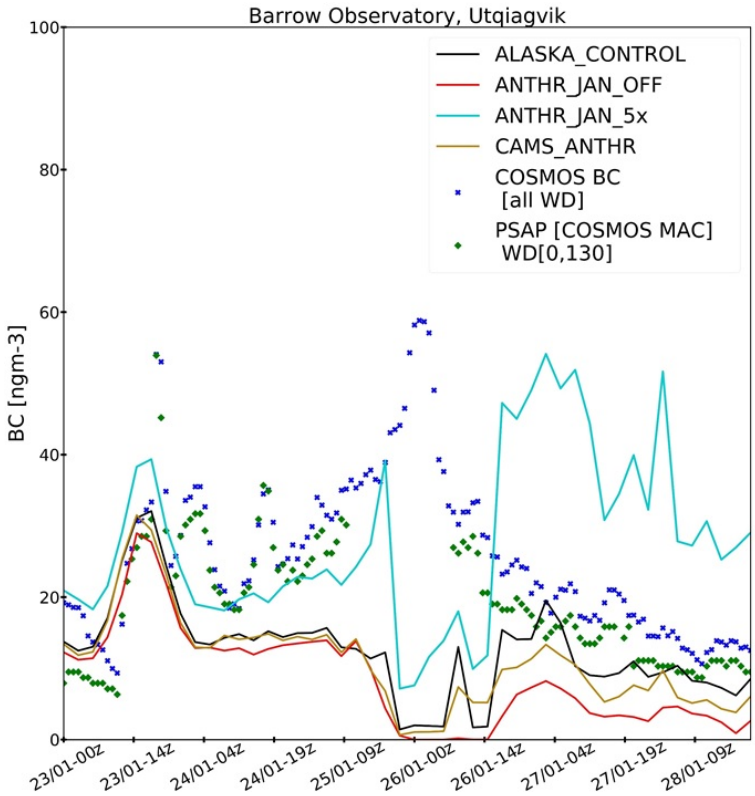

Figure 5.8: *Sub-micron BC, in ngm^{-3}, at Barrow evaluation against in-situ observations during January simulation period. Black line shows ALASKA_CONTROL at 20km. Red line shows BC for the sensitivity simulation ANTHR_OFF. Turquoise line shows the results for the ANTHR_5x run. Gold line shows BC for the CAMS_ANTHR. Observations are in blue crosses (COSMOS BC) and green triangle (PSAP). Model and observations are in UTC. See text for more details.*

transportation, industry and energy sectors at Utqiaġvik (see **Fig. 5.1**), but their magnitude is one to three times smaller compared to gas flaring emissions from the NSA oilfields. This is illustrated by this sensitivity and thus model BC at Barrow may be underestimated. As discussed earlier, COSMOS observed this local pollution on 25-26 January since this data has no filter for wind direction. The extent to which the PSAP EBC data is completely filtering out this "event" requires further investigation since PSAP EBC is elevated just before and after. On average, between 23 and 28 January 2014, NSA oilfield emissions contribute up to 30% of total BC at Barrow (**Figure 5.8**). On the other hand, there is a contribution to model BC, from background sources (remote sources outside the regional domain) between 10 ngm^{-3} (on 27 January) and 30 ngm^{-3} (on 23 January) (**Fig. 5.8**). The model is also run for the campaign period in the last week of February 2014. There is also a strong influence from NSA oilfields on BC at Barrow. When winds were easterly, south-easterly (between 115° and 151°) the contribution of regional emissions to BC at Barrow was more than 50% (not shown).

Running with five times more Alaskan anthropogenic emissions (ANTHR_5x) for January illustrates the sensitivity of modelled BC to local and regional emissions, with large increases in BC of up to 300 ngm^{-3} over the NSA oilfields (**Fig. 5.7b**). This test also illustrates that in the ECLIPSE inventory there are local BC emissions near to Utqiaġvik town, however their magnitude is small and, based on these results the ECLIPSE inventory underestimates these emissions by up to 60%. Higher BC emissions lead to higher BC concentrations at Barrow when air masses originating from the east, namely NSA oilfields (**Fig. 5.8**), suggesting a clear regional influence from this source at Barrow. This confirms the indications discussed earlier based on wind directions.

To further examine the contribution of regional anthropogenic sources to BC at Utqiaġvik town, a higher spatial resolution inventory is used. CAMS emissions are based on Community Emissions Data System version 2 (CEDSv2, *McDuffie et al. (2020)*) and Emissions Database for Global Atmospheric Research version 5 (EDGAR v5) inventories and are prepared originally at a higher spatial resolution, than ECLIPSE v6b (10 km instead of 50 km). The model is run using CAMS version 5.3 instead of ECLIPSE v6b emissions. Figure 8c shows the average differences between CAMS_ANTHR and ALASKA_CONTROL during January 2014. The use of CAMS emissions leads to a significant decrease in BC over NSA oilfields by up to 50 ngm^{-3} and a smaller decrease (up to 10 ngm^{-3}) south west of Utqiaġvik town (**Fig. 5.7c**). The lower BC over northern Alaska could be due to missing (or lower magnitude) oilfield emissions in the CAMS. This inventory includes BC emissions from oil refineries, industry, energy plants, transportation and residential at Utqiaġvik town and NSA region. There is also an increase in BC by up to 150 ngm^{-3} over the Fairbanks area, probably due to more detailed representation of energy, industry and residential sectors in CAMS compared to ECLIPSE. At Barrow, modelled BC decreases when the CAMS emissions are used, by up to 5 ngm^{-3} during the NSA oilfields period of influence (**Fig. 5.8**), otherwise the differences in model BC due to the different emission inventory are very small. The use of ECLIPSE emissions lead to a smaller underestimation in BC at Barrow on 27–28 January (NSA oilfield period of influence - **Fig. 5.8**). It appears that CAMS inventory also misses local emissions at Utqiaġvik town (e.g. 26 January).

5.6 Conclusions

In this study, WRF-Chem is used to evaluate Arctic BC and investigate processes which are affecting BC over the wider Arctic and, in a more focused study, on a regional scale over northern Alaska.

The model is evaluated against EBC observations at four Arctic sites. Whilst the model

underestimates BC, in particular during enhanced episodes at Alert, Tiksi and Barrow, it is able to capture observed variability. The model captures observed EBC variability and magnitudes at Zeppelin. Model biases can be due to various reasons such as the emissions, transport errors or model resolution. Here, the sensitivity of model results to dry and wet deposition is examined. Wet and dry removal do not affect BC in the same way at the four sites presented in this study. During January and February 2014 modelled BC at Tiksi and Barrow is sensitive to both wet, dry or both removal processes which could be contributing to low modelled BC. At Alert and Zeppelin modelled BC is more sensitive to wet removal. During wintertime, surface BC change is larger due to wet deposition at all sites north of 70°N (BC increase between 317% and 844% when wet deposition switched off), except at Tiksi. *Mori et al. (2020)* showed that wet deposition flux is higher at Zeppelin than at Barrow. The results presented here also confirm such regional differences. However, the results at Alert contrast with the findings of *Macdonald et al. (2017a)* who found that dry deposition is more important than wet deposition and suggested that there might be missing mechanisms for dry deposition onto snow in the models. Also, BC sensitivity to wet deposition is greater in the first 4 km, than at higher altitudes at Barrow in agreement with *Mori et al. (2021)*. Modelled BC sensitivity to dry deposition is higher at Tiksi (137%) compared to the other Arctic sites, due to the proximity of important Russian emissions included in the ECLIPSE inventory. This study highlights the sporadic nature of wet and dry removal at remote Arctic sites during wintertime depending on their proximity to local and regional sources (Tiksi, Barrow), and the influence of the air masses arriving at these sites which will vary depending on the transport pathway, for example, transport to Zeppelin at low levels .

A series of sensitivity tests are used to examine processes and sources influencing BC over northern Alaska on a regional scale (compared to the wider Arctic). With respect to horizontal resolution the results indicate that the model performs somewhat better at 20 km than at 100 km. However, the model still cannot capture elevated EBC of local origin at Barrow. To investigate the role of boundary layer dynamics on regional BC during winter conditions, the model is run with a different boundary layer scheme. The initial model setup captures better observed temperatures and winds (lower biases and RSMEs), and the use of a different boundary layer scheme leads to a decrease in modelled BC at the surface, especially over source regions (e.g. NSA oilfields). These results suggest that better simulation of PBL structure is needed, since this can affect model aerosols like BC and, in particular, loss processes like dry deposition in or near to source regions. The results in this study illustrate that wet and dry deposition affect BC differently at Arctic-wide and regional scales. The regional analysis suggests that dry and wet deposition are equally important for BC removal during wintertime over northern Alaska, and especially over source regions

whereas wet deposition is more important in the 100km results. The results at 20 km show less sensitivity compared to the results at 100 km. This may be partly due to the short run at 20 km but nevertheless illustrates differences in removal processes occurring regional and during transport. Further analysis is required to better address potential uncertainties affecting removal treatments. Also, detailed measurements of meteorological fields, wet and dry deposition are needed at different locations, to better constrain the model and help to better understand the model discrepancies at each monitoring site.

A series of sensitivity simulations are also performed to distinguish the contribution of local and regional BC anthropogenic emissions at Barrow and to reveal potential uncertainties in emission inventories. Analysis of wind direction data combined with of COSMOS and PSAP EBC observations at Barrow showed that easterly and south-easterly (NSA oilfields) air masses are influencing BC at Barrow during the latter part of January 2014. On average 30% of BC at Barrow originates from the NSA oilfields during this period, and more than 50% on average at end of February 2014. The sensitivity simulation with 5x regional anthropogenic emissions confirms this regional influence during January and February 2014. These results illustrate the significant contribution of regional NSA emissions to BC at Barrow, which is half of the observed EBC, while the remainder is due to remote, or other Arctic, sources. Local sources close to the site are also influencing measured EBC. It could be useful to apply more sophisticated filters than just wind direction (e.g. trace gas markers) to the Barrow observations in order to distinguish better between air masses influenced by local or remote sources. The local and regional contribution to BC at Barrow could be even higher since ECLIPSE inventory lacks detailed local sources such as those from Utqiaġvik town, and it might be underestimating NSA oilfield emissions. Employing a different inventory (CAMS) with a higher horizontal resolution results in lower BC over source regions, such as NSA, indicating that these, and other local, emissions are underestimated. Emission inventories with more detailed representation of local sources and point sources are needed for regional simulations in the Arctic.

BC is an important short-climate forcer, which contributes to on-going Arctic warming. It is important to further quantify remote, regional and local BC sources within the Arctic in order to improve model simulations of Arctic BC. In that way, we could better communicate to policymakers about the impact of local anthropogenic BC emissions to on-going climate warming and regional pollution.

Chapter 6

Modelling wintertime air pollution: a case study - Fairbanks, Alaska

This Chapter focuses on the pre-ALPACA campaign in Fairbanks, Alaska, in November–December 2019. It describes the measurements obtained during the campaign and analyses meteorological and synoptic conditions over Alaska during this winter. The WRF-Chem model is used to investigate air pollution over Alaska during the campaign. Then, using high-resolution simulations over the Fairbanks area, a series of simulations are performed to investigate the sensitivity of model results to meteorology during a polluted episode and the emissions of aerosols and their precursors. Discrepancies in secondary aerosols could also be explained by missing formation mechanisms in the model. This is not the focus of this first study. For this, more detailed measurements are needed, such as those measured during the main ALPACA campaign in January–February 2022. However, possible secondary aerosol mechanisms are still discussed in light of the results presented here. This study investigates regional pollution using data representative of the background and Fairbanks sites during observed polluted episodes. The objectives of this study are discussed in the following section.

6.1 Motivation

As described previously in this thesis, Arctic Haze is partially caused by elevated concentrations of aerosols (e.g. SO_4^{2-}, BC), originating from mid-latitude source regions during winter and spring *(Barrie, 1986; Quinn et al., 2002a; AMAP, 2015)*. There are also local sources contributing to Arctic air pollution at regional and urban scales in winter *(Nguyen et al., 2013; AMAP, 2015; Winiger et al., 2017; Schmale et al., 2018; Simpson et al., 2019)*. Urban

areas in the Arctic can experience severe air quality problems in winter due to high local emissions for heating and their poor dispersion due to strong wintertime temperature inversions *(Simpson et al., 2019)*. As noted in Chapter 1, Fairbanks is an example of such a city which experiences air quality problems due to high local emissions under stable weather conditions with calm winds and strong temperature inversions, while other Arctic cities also have similar air quality issues during wintertime *(Mölders and Kramm, 2010; Tran and Mölders, 2011; Mölders, 2013; Fochesatto et al., 2015; Mölders and Kramm, 2018)*. As a result, primary and secondary pollutants accumulate in the urban Arctic boundary layer (ABL) *(Mölders and Kramm, 2010; Mölders et al., 2011)*. **Figure 6.1** shows the seasonal variation of $PM_{2.5}$ components, such as EBC, OC, NO_3^-, SO_4^{2-} and NH_4^+ in Fairbanks. More specifically, all $PM_{2.5}$ components peak during January and February, and there is a secondary peak during December. The cold season in Fairbanks usually starts in October and lasts until the end of March, with temperatures lower than -9 °C on average, while the coldest month in Fairbanks is January *(Arguez et al., 2012; Lawrimore et al., 2016)*. Low temperatures lead to extensive heating use and, as a result, severe pollution episodes *(Simpson et al., 2019)*.

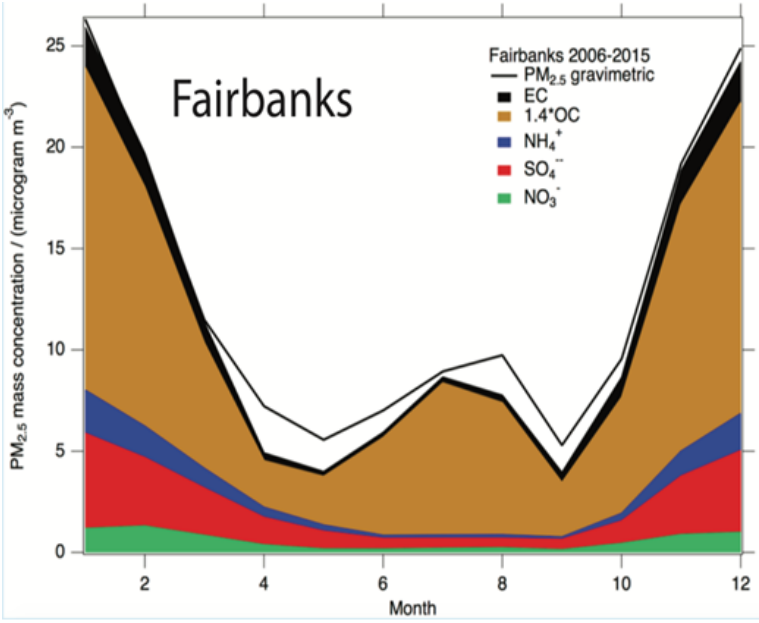

Figure 6.1: *Monthly $PM_{2.5}$ composition averaged over 2006-2015. From William Simpson, UAF.*

The most important emissions in Fairbanks originate from sources such as fuel combustion for residential/commercial purposes, using oil, wood, coal, and gas, transportation, and power plants fuelled by coal and oil *(Ward et al., 2012; Wang et al., 2014; Busby et al., 2016; Ye and Wang, 2020)*. As a result, PM_{10}, CO, SO_2, NO_2 peak during wintertime *(Ye and Wang, 2020)*. Trace gases, such as SO_2, CO, also accumulate in the urban ABL due to lack of sun-

light *(Mölders and Kramm, 2018)*. There are also high NO_x emissions emitted into the stable boundary layer *(Simpson et al., 2019)*. Previous studies showed that OA is the most important contributor to $PM_{2.5}$ due to woodsmoke emissions, while the contribution of inorganics (SO_4^{2-}, NO_3^-, NH_4^+) is larger compared to EC (see **Fig. 6.1**) *(Ward et al., 2012; Wang et al., 2014)*. However, the sources and formation pathways of secondary SO_4^{2-}, NO_3^-, NH_4^+ under dark/cold conditions (non-photo-chemical mechanisms) are unclear, as discussed briefly in Chapters 2 and 4 *(Simpson et al., 2019)*.

As discussed earlier in this thesis, models tend to underestimate wintertime air pollution at remote Arctic sites. The work presented in the previous chapters showed that the model performance is improved with respect to observations of inorganic aerosols compared to the version used in the recent AMAP report *(Whaley et al., 2022b)*. At a regional scale, previous modelling studies *(Mölders and Kramm, 2010; Mölders et al., 2011)* focused on reproducing wintertime inversions and their influence on air pollutants in Fairbanks. *Mölders et al. (2011)* reported that their model could not capture air pollutant concentrations at polluted and remote sites and model errors reproducing temperature gradients leads to errors in simulated $PM_{2.5}$.

Detailed observations of trace gas and aerosols are necessary to gain insights into missing local sources and formation pathways of secondary aerosols under wintertime conditions. Field campaigns can provide further information in regions of interest and fill the missing observations gap. This was the goal of the pre-ALPACA campaign in Fairbanks in November and December 2019. ALPACA and the French pre-ALPACA campaign are discussed in Chapter 3, and the pre-ALPACA measurements and first analyses are summarised below. During winter 2019, detailed measurements of air pollutants were obtained at different locations in Fairbanks (see **Fig. 6.2**) with the aim to identify the origins of high local emissions, e.g. combustion of sulphur-containing fuels, such as fuel oil combustion for residential-commercial purposes *(Simpson et al., 2019)*. The campaign also focused on processes influencing the formation of stable surface conditions, as they trap pollutants close to the ground and lead to high pollution episodes. Thus, detailed meteorological measurements were made at different locations in Fairbanks *(Cesler-Maloney et al., 2022; Maillard et al., 2022)*. During the campaign, two different episodes were identified, including a cold stable episode and a period with possible mixing of air masses from aloft (Roberts et al., in prep.). From now on we will refer to them as the cold period and mixing period.

The main objectives of this study are:

(i) What is the observed aerosol composition at background and regional Alaskan sites during winter 2019? How well does the model reproduce the observations?

(ii) How do meteorological conditions and removal treatments affect modelled aerosols in polluted environments under wintertime stable conditions?

(iii) What are the uncertainties in simulated aerosols due to emissions over the Fairbanks area?

In this study, WRF-Chem is used to perform quasi-hemispheric and regional simulations over the Arctic, focusing on central Alaska and the Fairbanks area during wintertime. To address these objectives, the model is run at a regional scale over the Fairbanks area during the period of the pre-ALPACA campaign. A series of sensitivity simulations are performed during the observed episodes in December 2019 to investigate uncertainties in simulated regional pollution due to removal treatments, meteorology and emissions.

The observed aerosol composition and meteorological fields used to evaluate the model performance are introduced in Section 2. The meteorological conditions during winter 2019–2020 and synoptic conditions that occurred over Alaska during the pre-ALPACA campaign are discussed in Section 6.3. The model setup, including the simulations and emissions, is described in Section 6.4. The results are presented in Sections 6.5 and 6.6. In Section 6.5, background aerosol concentrations over Alaska are discussed and evaluated against the quasi-hemispheric simulation. In section 6.6, the sensitivities to processes and emissions influencing regional air pollution over the Fairbanks area are discussed. Possible contributions from missing or new secondary aerosol mechanisms also are presented. The conclusions are presented in Section 6.7.

6.2 Observations during the pre-ALPACA campaign

This section describes the aerosol, trace gases, and meteorological observations measured at routine monitoring sits and during the pre-ALPACA campaign.

6.2.1 The pre-ALPACA campaign

The French pre-ALPACA campaign took place between 25 November and 13 December 2019 in Fairbanks, Alaska, in collaboration with researchers from the University of Alaska (UAF), Fairbanks, prior to the main ALPACA campaign, which took place in January-February

Figure 6.2: *(a) This map shows the locations where measurements were made in Fairbanks during the pre-ALPACA campaign. This includes the location of the field at Fairbanks University (UAF field), University of Alaska Fairbanks Community and Technical College (CTC) building, the three locations the Tower Trailer was located between November and February 2019 (Trainor Gate, A street and River Road) and NCORE monitoring site, (b) This map shows the location of the monitoring EPA site located in North Pole, which is located south west of Fairbanks. Maps derived from Google Earth.*

2022 as part of the Air Pollution in the Arctic: Climate, Environment and Societies - Alaskan Layered Pollution and Arctic Chemical Analysis (PACES-ALPACA) initiative *(Simpson et al., 2019)*.

Two main locations in downtown Fairbanks were used to install the different instruments: (I) the NCORE site (64.845N,147.727W), located across from a power plant and next to an Environmental Protection Agency (EPA) monitoring site; (II) the University of Alaska Fairbanks Community and Technical College (CTC) building (64.840N, 147.726W). A field at the University of Alaska (UAF field; 64.86N, 147.85W) was also used (**Fig. 6.2**).

Trace gases: High temporal resolution measurements (every 5min) of CO, O_3, NO, NO_2, SO_2 at NCORE were measured using small light-weight AlphaSense Sensors (MICROMEGAS). These measurements have been cross–calibrated with EPA measurements. Observations are in Local Alaskan time (AKST). MICROMEGAS data is provided by Brice Barret (Laboratoire d'Aérologie, Université de Toulouse, CNRS). O_3 was also measured in parts per billion (ppb) and UCT, using a Dasibi 1008-RS O3 analyser, located indoors in a temperature-conditioned room at the top of the CTC building *(Cesler-Maloney et al., 2022)*. SO_2 was measured on a retractable tower attached to a trailer, mentioned as "Trailer Tower"

from now on, at 3m, using a thermo 43C SO_2, and these observations were obtained from Meeta Cesler-Maloney and William Simpson, UAF. Observations are in UTC. During the pre-ALPACA campaign, the trailer tower was located at Trainor gate (see **Fig. 6.2**).

Aerosols: High temporal resolution measurements (every 5min) of EBC at NCORE site were sampled using a Multi-Angle Absorption Photometer (MAAP) instrument. A detailed description of MAAP can be found in *Petzold et al. (2002)* and *Scientific (2007)*. Briefly, MAAP measures b_{abs}, in Mm^{-1}. b_{abs} is converted to mass concentrations of EBC using a constant MAC equal to 6.6 m^2g^{-1}, and no additional correction is applied. However, the MAC value recommended by the manufacture might lead to an overestimation of EBC *(Ohata et al., 2020)*. Early studies, e.g. *Petzold and Schönlinner (2004)*, estimated MAAP b_{abs} uncertainties to be 12%. The absolute uncertainty of MAAP measurements is 0.06 Mm^{-1}, slightly higher compared to particle soot absorption photometer (PSAP) (0.02 Mm^{-1}) for 5-min averages *(Müller et al., 2011)*. EBC MAC-corrected observations are provided by Brice Temime-Roussel (Laboratory of Environmental Chemistry (LCE), Aix-Marseille Université, Marseille, France) and are in AKST.

Meteorology: 2m temperature and winds, turbulent sensible heat fluxes, longwave and shortwave radiative fluxes were measured at the UAF field, and cloud base and cloud optical depth were measured using an aerosol lidar across the CTC building in Fairbanks *(Maillard et al., 2022)*. Four temperature probes were also deployed at 3, 6, 9 and 11 m AGL at the Trailer Tower *(Cesler-Maloney et al., 2022)*.

6.2.2 Aerosol measurements: routine monitoring sites

Surface mass concentration data of OC, NO_3^-, SO_4^{2-}, EBC and PM with $r_d \leq 2.5$ µm, from the EPA is used for model evaluation for sites in the Fairbanks area (**Figure 6.2**). The samples are collected on-site over 24 hours every three days and can be downloaded from the following link: https://aqs.epa.gov/aqsweb/airdata/download_files.html. Also, 2m temperatures data were measured at different stations in Fairbanks (**Fig. 6.2**). Also, detailed (every 5') SO_2 data are also obtained from EPA at NCORE site during the campaign and processed by Meeta Cesler-Maloney (UAF). Data from the IMPROVE database (Malm et al., 1994) for Denali (63.7N, 148.9W), located 195 km southeast of Fairbanks, Toolik Lake Field Station (68.6N, 149.6W), located south of Prudhoe Bay oilfields and 242 km inland from North Slope of Alaska (Toolik from now on) and Simeonof (55.3N, 160.5W) sites in Alaska (see Chapter 4 for details). Following *Malm et al. (1994)*, EC and OC are measured using the thermal optical reflectance (TOR) method *(Chow et al., 1993)*. EBC uncertainty at Simeonof, Toolik and Denali ranges between 8 to 21 ngm^{-3}. The EPA sites report EC estimated using

the TOR method but also based on a thermal/optical transmittance (TOT) method *(Chow et al., 2004)*. EBC and CO data from Poker Flat Research Range (65.1N, -147.3W), located north of Fairbanks (**Fig. 6.5**) provided by Yugo Kanaya (JAMSTEC, Japan) are also used to evaluate the model results. EBC was measured using the COSMOS instrument, with a $PM_{1.0}$ size cut off reported at STP conditions *(Miyazaki et al., 2008; Kondo et al., 2009, 2011; Ohata et al., 2020)*. Observations are in AKST. The COSMOS measurements are described in detail in Chapter 5. For each site, model results are calculated for the same conditions (temperature, pressure) and diameters as the reported observations.

6.3 Weather conditions during winter 2019–2020 and the pre-ALPACA campaign

During winter 2019–2020 (November to end of February), 3m temperatures generally range between 5 and -41 °C at the Trailer Tower, reaching a minimum in the middle of January. The winds were calm, with 10m winds being less than 4 and 7 ms^{-1} at Tower Trailer and NCORE, respectively, as shown in **Fig. 6.3**. During November and December 2019, 3 m temperatures ranged between 5 and -39 °C at the two sites. The Tower Trailer changed location in the middle of January and moved from the Trainor Gate to the River Road on 2 February *(Cesler-Maloney et al., 2022)*.

During the pre-ALPACA campaign, higher temperatures were recorded compared to January and February 2020, with one cold episode at the beginning of December and minimum temperatures around -32°C. Also, higher winds were observed in January and February 2020, unlike the calm winds during pre-ALPACA, not exceeding 3 ms^{-1}. On average, November is usually warmer than December, January and February, December is colder than February, and with January being the coldest month (source: https://en.climate-data.org/north-america/united-states-of-america/alaska/fairbanks-1403/). However, more precipitation generally occurs during November and December than in January and February. During pre-ALPACA, it snowed between 25 and 30 November 2019, with the highest value of 43 mm. There was a second bigger snow event on 2 December, with 51 mm of snow (source: https://www.usclimatedata.com/climate/fairbanks/alaska/united-states/usak0083).

EPA sites around Fairbanks (**Fig. 6.2**), including NCORE, measured similar variations in 2 m temperature (**Fig. 6.3**). More specifically, from the beginning of the campaign until 2 December, the 2 m temperature ranged from 0 to -18 °C. From 3 to 7 December, 2 m temperatures reached -32°C (cold period), before getting warmer at the end of 7 December

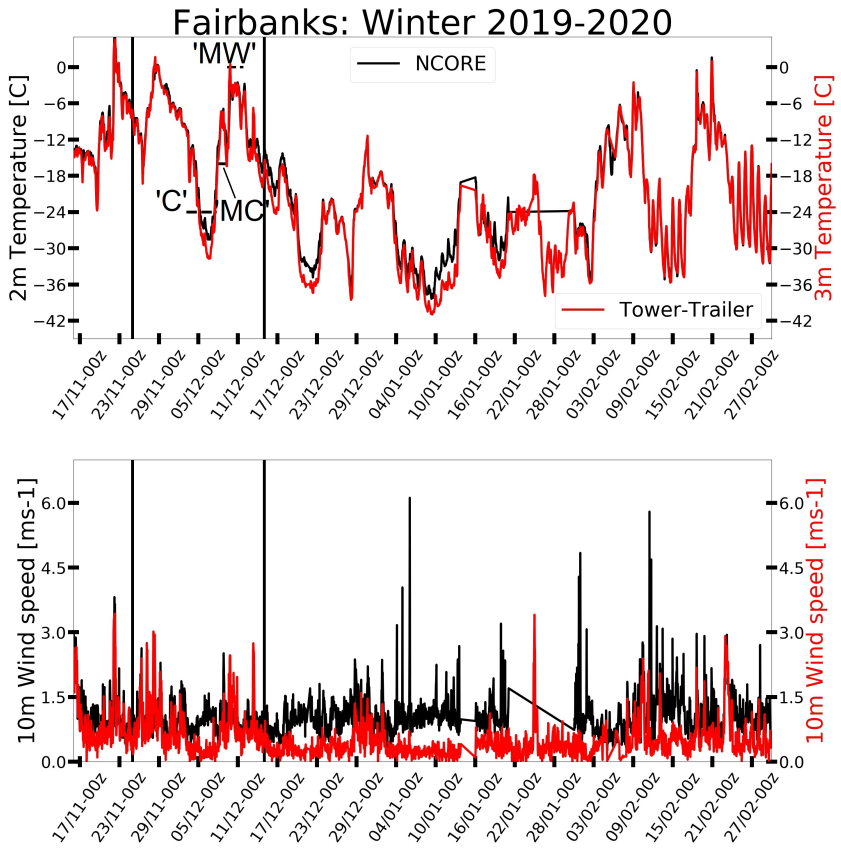

Figure 6.3: *2 and 3 m temperatures and 10m wind speeds at NCORE (black) and the Tower Trailer (red) between 1 November 2019 and 28 February 2020, respectively. The vertical black lines show the period of the pre-ALPACA campaign, while the dashed horizontal lines show the three observed episodes. 'C' stands for the cold period, 'MC' stands for the colder mixing period and 'MW' for the warmer mixing period. Hourly observations are shown when available, in UTC. Observations courtesy of Meeta Cesler-Maloney, UAF.*

and until 12 December (mixing period) *(Maillard et al., 2022)*. Warm air masses originating from south of Alaska brought warm air in Fairbanks, and as result surface temperatures increased which led to the break up of the cold period (see discussion below). Here, the mixing period is examined as two sub-episodes; from 7 to 9 December, when the temperature is still low (cold mixing period), and from 9 to 11 December, when it was getting warmer (warm mixing period) (**Fig. 6.3**). From 2 to 12 December, 10m winds at NCORE and Tower Trailer were below 2.0 ms^{-1}, with sporadic slightly higher wind speeds (2.0 to 2.5 ms^{-1}) on 9 and 10 December (**Fig. 6.3**), during the latter half of the mixing period.

Wintertime synoptic conditions over Alaska are described in Chapter 1. A detailed study by *Maillard et al. (2022)* using ERA5 data, reported that at 0000 UTC on 2 December, a low-pressure system was over the south of Alaska, which gradually weakened as higher pressures moved from the west. The temperature decreased from 4 to 6 December, reaching

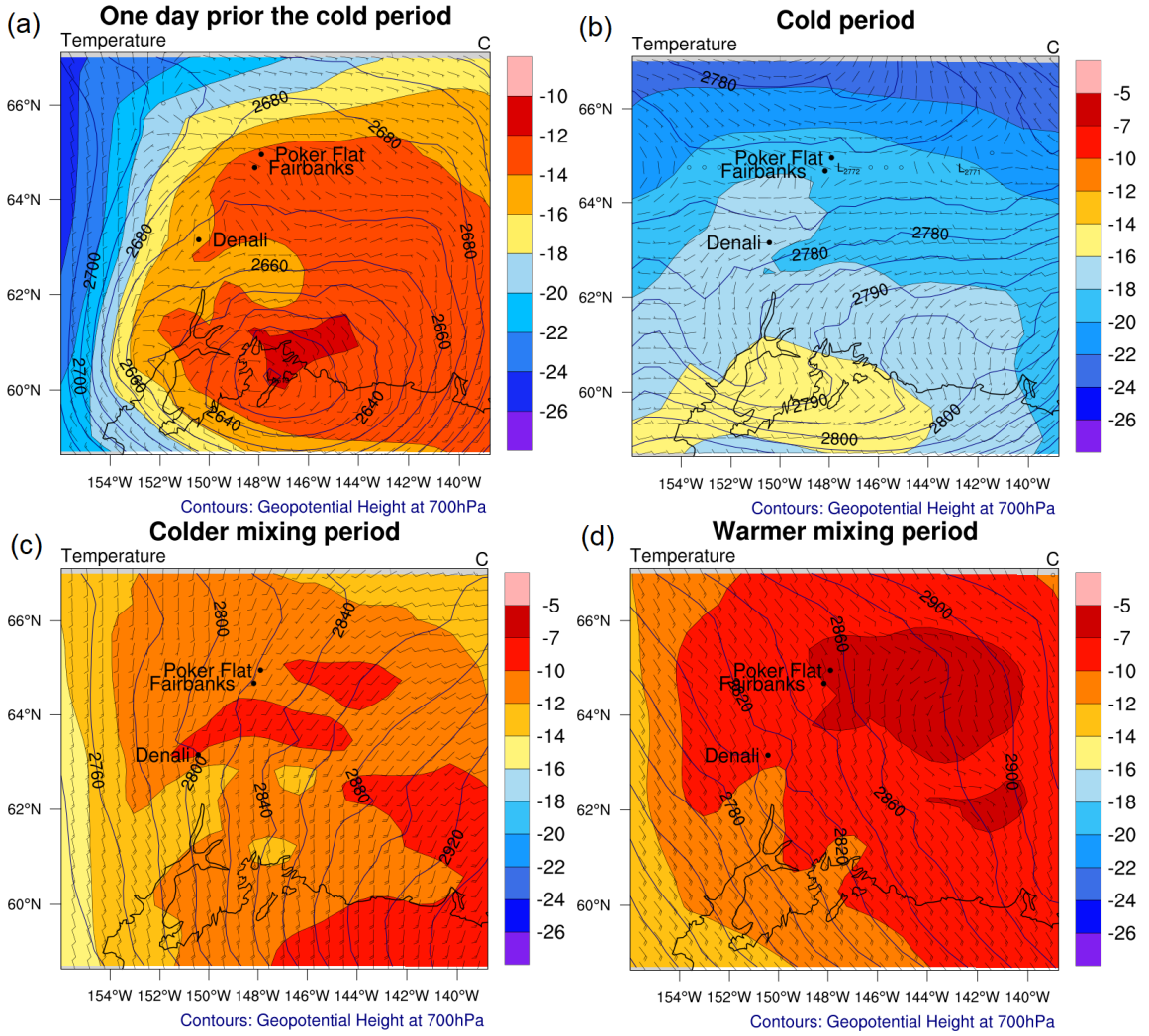

Figure 6.4: *Synoptic conditions at 33km (a) one day prior to the cold period, during (b) the cold period, (c) the mixing period when its colder and (d) when its warmer. The coloured scale shows the temperatures at 700hPa, in ^{o}C. The wind vectors show the strength, in ms^{-1}, and direction at 700hPa, while the contours show the geopotential height at 700hPa hPa. All the model results based on the ALASKA_CONTROL run (see* ***Table 6.1****) and they are averaged over the periods indicated above.*

a minimum of -27°C at the UAF field. From 7 December, low-pressure systems moved northeast into Alaska, and the surface temperature increased by 15°C during this day. These patterns are similar to results presented by *Cassano et al. (2016)* who showed that the large-scale circulation (presence and strength of Aleutian Low and Siberian High) are associated with wintertime warm and cold extremes in southern Alaska.

Using model outputs, this study examines the synoptic conditions at 33 km over the simulation domain covering central Alaska. **Fig. 6.4** shows geopotential height, temperatures and winds at 700 hPa (a) one day prior to the cold period, (b) during the cold period, and during the mixing period when it is (c) colder and (d) warmer. One day prior to the

cold period (**Fig. 6.4a**), a low-pressure system is located south of Alaska with higher temperatures, up to -16°C over the ocean. Over the Fairbanks area, the temperature is lower, reaching up to -14°C and the winds are blowing from the east. During the cold period (**Fig. 6.4b**), the temperature around Fairbanks drops due to clear skies (radiative cooling), varying between -16°C and -20°C. The winds in Fairbanks are calm, while north of Fairbanks the winds are north-easterly. *Maillard et al. (2022)* showed that on 6 December a low pressure system was located on the south west coast of Alaska and cold air remained in central Alaska, while from 7 December several low systems moved north-east into central Alaska. During the colder mixing period (**Fig. 6.4c**), there are strong south/south-westerly winds south of Fairbanks area, which lead to the break up of the pollution episode (cold period), due to advection of warm air from south of Alaska. The temperature increases over the Fairbanks area, ranging between -10°C and -12°C. South of Alaska, there are strong winds, which become more south-easterly during the warmer mixing period (**Fig. 6.4d**) and bring warm and moisture air from the ocean over the Fairbanks area. Due to warm air coming from the southwest (**Fig. 6.4c**), the temperature rises and ranges between -5°C and -7°C around Fairbanks during the latter (warmer) part of the mixing period.

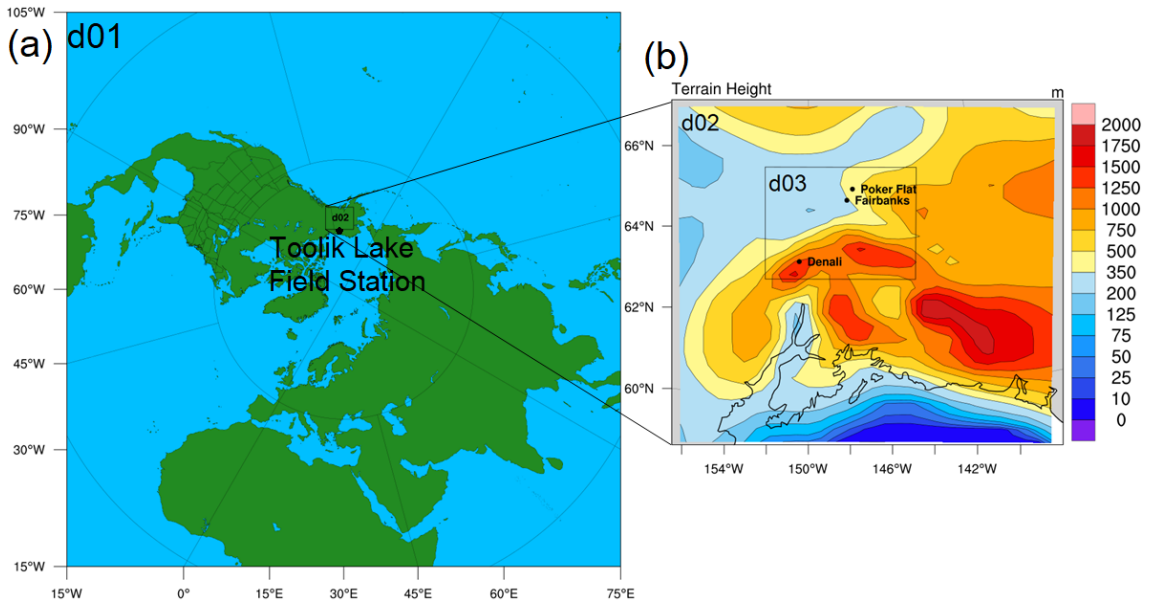

Figure 6.5: *(a,b) WRF-Chem domains at 100 km (d01), 33 km (d02) and 11 km (d03). (a) Black star shows the location of Toolik Lake Field station. (b) The colours show the modelled terrain height, in m, at 33 km and 11 km. d03 also shows the location of Fairbanks, Poker Flat and Denali.*

Table 6.1: *List of WRF-Chem simulations.*

Simulation Name	Description
Quasi- hemispheric simulations (100km)	
CONTROL	Base simulation
Regional simulations - central Alaska (33km)	
ALASKA_CONTROL	Base simulation
Regional simulations - Fairbanks region (11km)	
FAIRB_CONTROL	Base simulation
FAIRB_BL	Sensitivity to boundary layer dynamics
FAIRB_AER_DEP_OFF	Aerosol dry deposition and settling OFF
FAIRB_GAS_DEP_OFF	Trace gas dry deposition OFF
FAIRB_BC	Enhanced BC emissions
FAIRB_SO_2	Enhanced SO_2 emissions
FAIRB_NO	Enhanced NO emissions

6.4 WRF-Chem: Model setup and simulations

The WRF-Chem setup, including meteorological and chemical schemes, is described in detail. Briefly, MYJ (MYJ - boundary layer), Monin-Obukhov (MO (Janjic) - surface layer) and NOAH MP land surface model are used coupled with the MOSAIC aerosol scheme. The other physics and chemistry schemes are the same as described in Chapters 4 and 5.

Three simulation domains (polar stereographic projection) are used in this study, as shown in **Figure 6.5**. The first (parent) domain (d01) covers a large part of the Northern Hemisphere with 100 × 100 km horizontal resolution. The boundary and initial conditions are derived from European Centre for Medium-Range Weather Forecasts (ECMWF) Reanalysis v5 reanalysis data (ERA5 0.3°x0.3°), (*National Centers for Environmental Prediction, National Weather Service, NOAA, U.S. Department of Commerce (2000)* and Community Atmosphere Model with Chemistry (CAM-chem, *Emmons et al. (2020)*) for atmospheric trace gases and aerosols. The first nested domain (d02), run at a horizontal resolution of 33 × 33 km, covers central Alaska (see **Figure 6.5**). The second nested domain (d03) is run at a horizontal resolution of 11 x 11 km over the Fairbanks region. Spectral nudging is used for the 100 and 33 km domains, with the spectral nudging parameters calculated as in *(Hodnebrog et al., 2019)*. 50 vertical levels are used, with 13 being below 2 km, and the first level is at 14 m. WRF-Chem temperatures and winds are nudged at each dynamical step to the reanalysis, which is updated every 6 hours, above the atmospheric boundary layer in d01 and d02 only.

Table 6.1 summarises the simulations performed in this study. For the simulations at 33 and 11 km, the initial and boundary conditions are derived from the 100 km and 33

km control simulations, respectively. The model at 100 km is run from 1 October to 15 December 2019, and one month and 24 days considered as spin-up. The model is run from 12 November to 12 December 2019 at 33 km, and 23 days are considered spin-up. At 11 km, the model is run from 1 to 12 December, focusing on the two different periods reported by *Maillard et al. (2022)* and *Roberts et al. (2022, in prep.)*, and the first day of the simulation is spin-up. In each case, the model output is every 3h.

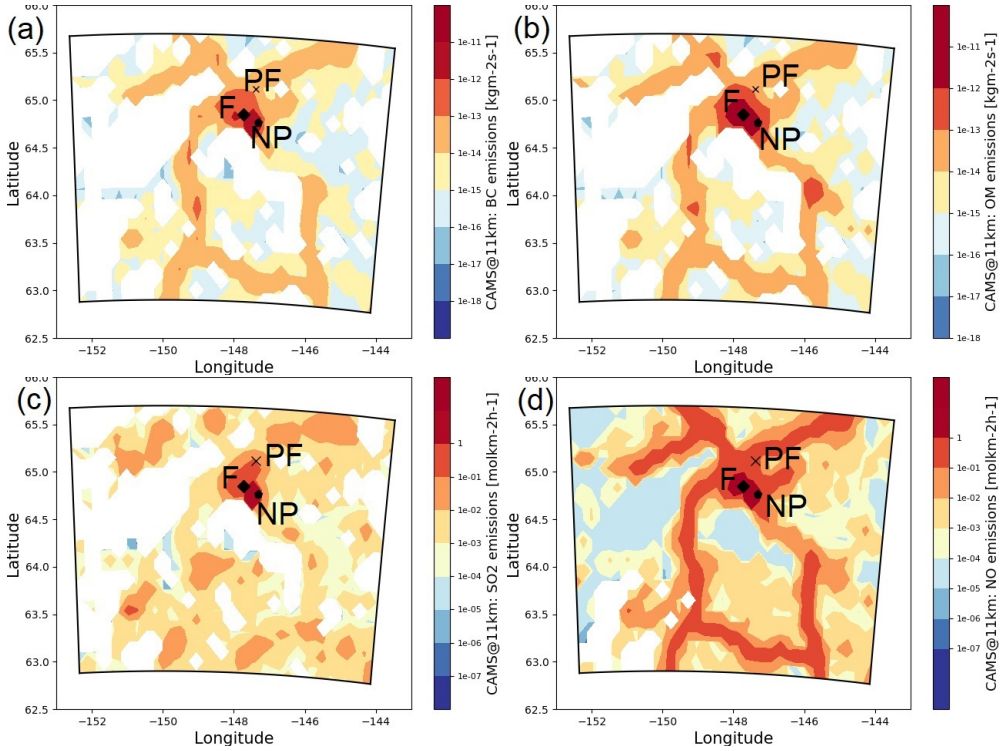

Figure 6.6: *CAMS v5.3 anthropogenic emission fluxes of (a) BC, (b) OM in $kgm^{-2}s^{-1}$, (c) SO_2, (d) NO in $molecskm^{-2}h^{-1}$, interpolated at 11 km WRF grid during December 2019. Black marker x shows the location of Poker Flat (PF), diamond shows the location of NCORE, in Fairbanks (F) and pentagon the location of North Pole (NP).*

Monthly anthropogenic emissions from the Copernicus Atmosphere Monitoring Service version 5.3 (CAMS v5.3) inventory, for 2019 with a resolution of 0.1° x 0.1° *(Granier et al., 2019; Soulie, 2022)* are used in this study. The CAMS anthropogenic emissions inventory is described in detail in Chapter 3. The MOSAIC aerosol scheme requires emissions of organic matter (OM). Thus, OC emissions are multiplied by 1.4. To compare with OC observations, the model output is divided by 1.4. Natural emissions are described in Chapters 3 and 4. **Figure 6.6** shows an example of CAMS emissions for BC, OM, SO_2 and NO on the 11km domain showing two hot spots: Fairbanks and North Pole (to the south-east). In December 2019, the sector that contributes the most is residential and commercial heating for all species shown here. Other sectors which contribute are (i) industrial processes,

(ii) oil refineries and (iii) transportation, especially for NO_x emissions. The energy sector, which includes only power plants in CAMS v5.3, has lower emissions than the above mentioned sectors. Other emissions are low in the Fairbanks area during this period since it is wintertime (snow-covered).

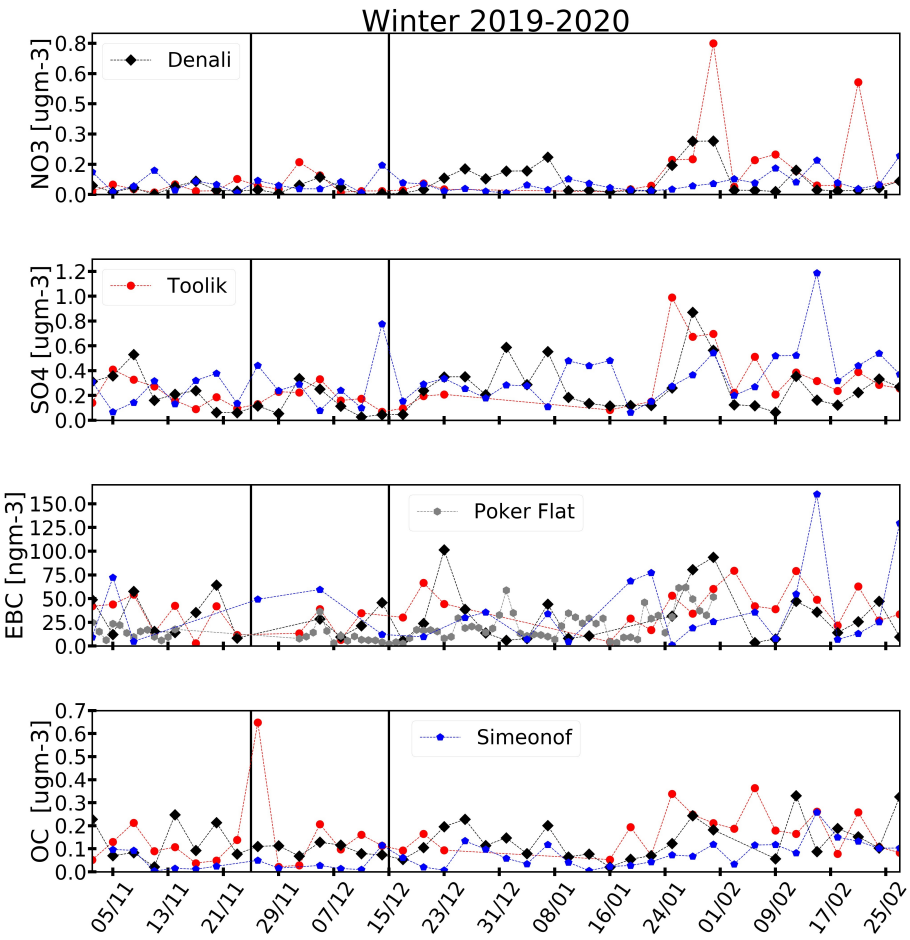

Figure 6.7: *Wintertime NO_3^-, SO_4^{2-}, EBC and OC mass concentrations, in μgm^{-3} ($r_d \leq 2.5\ \mu m$) and AKST, at background Alaskan sites. Black diamonds shows the data at Denali. Red circles shows the data at Toolik. Blue pentagons shows the observations at Simeonof and grey crosses at Poker Flat. Observations are shown where there are available, from 2 November until 27 February 2019.*

6.5 Background contribution to Alaskan air pollution

This section evaluates the contribution of background aerosols during November–December 2019 over Alaska. First, the observations obtained from the monitoring sites are described during winter 2019–2020 and then the model is evaluated at 100 km against the background sites (e.g. Denali, Poker Flat) during the period of the pre-ALPACA campaign.

6.5.1 Alaskan air pollution

First considering the observations during winter 2019–2020, **Figure 6.7** shows observed OC, NO_3^-, SO_4^{2-}, and EBC at four routine monitoring sites: Toolik, Denali, Simeonof and Poker Flat. Enhanced concentrations of NO_3^- are observed at Toolik, reaching up to 0.8 and 0.55 μgm^{-3} at the end of January and February, respectively, indicating Arctic Haze influence. Observed NO_3^- at the other sites is up to 3.0 times less compared to Toolik (**Fig. 6.7**). NO_3^- during pre-ALPACA is lower and does not exceed 0.3 μgm^{-3} at all sites. Total SO_4^{2-} (ss-SO_4^{2-} plus nss-SO_4^{2-}) shows concentrations up to 1.2 μgm^{-3} in the middle of February and also up to 0.9 μgm^{-3} at the end of January. During the pre-ALPACA campaign, an elevated total SO_4^{2-} (0.8 μgm^{-3}) was measured at the end of the campaign. Otherwise, total SO_4^{2-} does not exceed 0.5 μgm^{-3} at all sites discussed here. Alaskan SO_4^{2-} mass concentrations are similar to values measured at remote Arctic sites, such as Zeppelin, Villum, Alert and Barrow Observatory (super-micron), in January and February 2014 (Chapter 4), except for Simeonof, Gates of the Arctic and Barrow Observatory (sub-micron), where higher observations were reported. Observed EBC is higher at Simeonof in the middle of February, reaching up to 150 ngm^{-3}, likely due to transport of pollution from Asia (**Fig. 6.7**). At the other sites, higher EBC concentrations are observed from the end of January. Alaskan observed EBC is lower during January and February 2019, by up to 100 ngm^{-3}, compared to Utqiaġvik, Alert, Zeppelin, and by up to 1100 ngm^{-3} compared to Tiksi during January and February 2014 (see Chapter 5). During the pre-ALPACA campaign, EBC ranges between 2 and 59 ngm^{-3}, with Poker Flat, Denali and Toolik reporting lower EBC by up to 30 ngm^{-3} compared to Simeonof. On 7 December, an event is observed at all sites. It is stronger at Simeonof and likely related to transport by the low pressure system discussed earlier.

Observed OC does not exceed 0.4 μgm^{-3} during winter 2019–2020 and 0.25 μgm^{-3} during the pre-ALPACA campaign, apart from a local episode at Toolik, prior to the cold episode in Fairbanks, at the beginning of December (**Fig. 6.7**). This elevated concentration of OC could be due to a regional influence from NSA oilfields as discussed in Chapter 4 showing, for example, that elevated OC concentrations observed at the Gates of the Arctic in February 2014 did not exceed 0.6 μgm^{-3}. The four sites discussed here are used as an indicator of background Arctic Haze compared to regional/local pollution in Fairbanks.

6.5.2 Model evaluation

Figure 6.8 shows the model evaluation against aerosol composition data at Alaskan background sites during the pre-ALPACA campaign. The model performs well at quasi hemispheric scale (100km). More specifically, at Simeonof (**Fig. 6.8a**), south of Alaska, the model

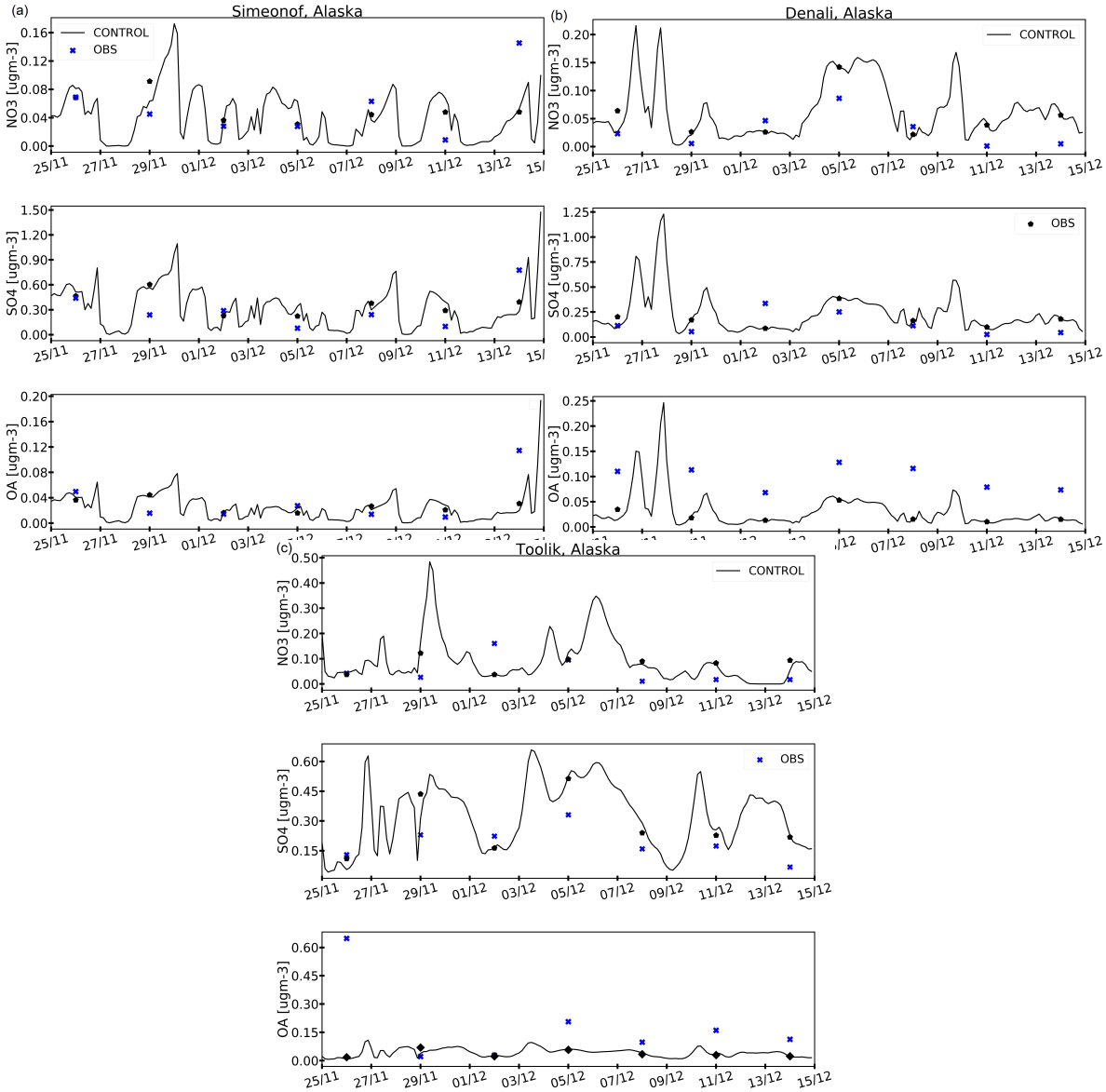

Figure 6.8: *Evaluation of modelled aerosol composition (CONTROL run) against in-situ observations ($r_d \leq 2.5$ μm) at (a) Simeonof, Aleutian Islands, Alaska, (b) Denali, central Alaska and (c) Toolik, northern Alaska, between 25 November and 15 December 2019, in AKST. The black line shows model results from the CONTROL run, while observations are shown as blue crosses. Observations are 24h averages every three days and the corresponding model daily averages are shown as black diamonds for CONTROL. Observations are shown only when they are available. See the text for details about the observations and model run.*

captures observed variability in NO_3^-, OA and SO_4^{2-}, with a small underestimation as indicated by the biases and RMSEs in **Table 6.2** (see Chapter 3 for more details on how biases and RMSEs are calculated). At Denali (**Fig. 6.8b**), central Alaska, the model overestimates NO_3^-, by up to 0.05 μgm^{-3} while the model captures well SO_4^{2-}. On the other hand, the model underestimates OA by up to 0.1 μgm^{-3} possibly due to underestimation of OA emissions or

secondary OA production over Asia. At Toolik, northern Alaska, the model overestimates SO_4^{2-} and NO_3^- by up to 0.15 and 0.1 μgm^{-3}, respectively.

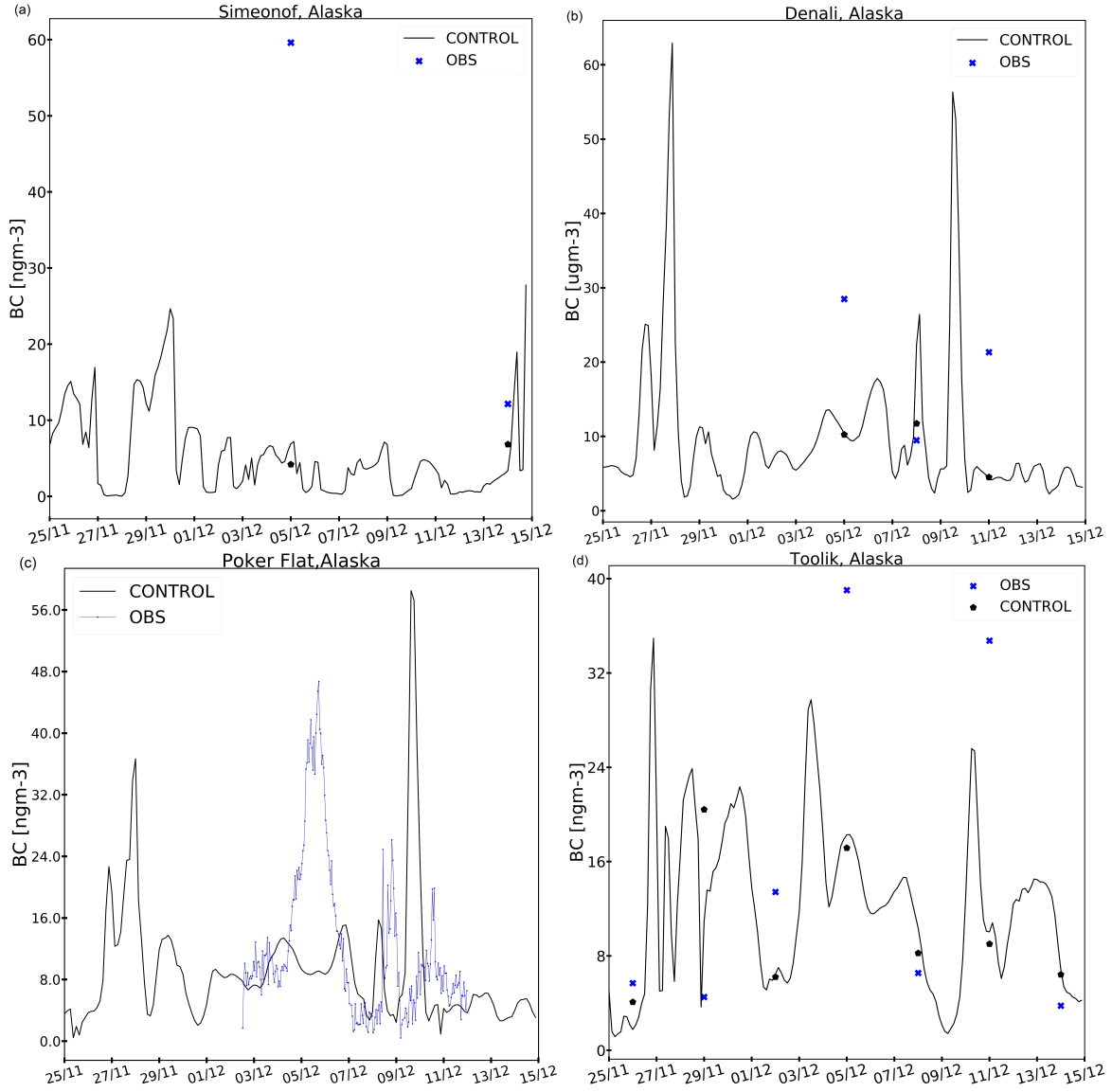

Figure 6.9: *BC in ngm^{-3} at (a) Simeonof, (b) Denali, (c) Poker Flat and (d) Toolik sites in Alaska, with $r_d \leq$ 2.5 μm at Simeonof, Denali and Toolik and $r_d \leq$ 1.0 μm at Poker Flat, , between 25 November and 15 December 2019, and in AKST. Black lines show results for CONTROL, while BC observations are shown as blue crosses, when available. See text for details.*

On the other hand, the model underestimates OA, possibly due to missing regional sources linked to NSA oilfields, as discussed in Chapter 5, or missing regional sources of marine organics (north Alaskan coast) (Chapter 4). The model performs better during November and December 2019 than the results presented in Chapter 4. This could be due to using CAMS anthropogenic emissions, especially for NO_3^- and SO_4^{2-} precursors. The

SSA components, Na^+ and Cl^- (not the scope of this study) are captured well (low biases and RMSES, **Table 6.2**), while the model still underestimates episodic elevated concentrations are measured at Simeonof and Toolik sites (not shown here). This analysis supports the findings presented in Chapter 4 and shows the model's robust performance simulating wintertime Arctic SSA components.

Figure 6.9 shows the model validation against EBC observations at four background sites in Alaska. Overall the model underestimates BC during the simulation period (**Table 6.2**). At Simeonof (**Fig. 6.9a**), only two observations are available. The model cannot capture the elevated EBC concentration ranging between 50 and 60 ngm^{-3}. However, it captures well the lower EBC concentrations, with modelled BC reaching 30 ngm^{-3}. At Denali (**Fig. 6.9b**), the model simulates more BC compared to Simeonof, reaching 80 ngm^{-3}, however it still underestimates observed EBC by up to 40 ngm^{-3}. At Poker Flat (**Fig. 6.9c**), the model captures the observed variability for observations below 20 ngm^{-3} but has difficulties capturing elevated observations reaching 50 ngm^{-3}. At Toolik (**Fig. 6.9d**), the model simulates less BC than at Denali and Poker Flat. It captures the observed EBC variability, however, it underestimates elevated observations by up to 15 ngm^{-3}. Note that EBC observations are reported as 24h averages every three days. There are also uncertainties in the observations, as discussed in Section 2 and Chapter 5, which could be responsible for the high biases reported here.

The analysis here shows that the model performs well over Alaska (**Table 6.2**). However, there are some discrepancies between modelled and observed aerosols. The low modelled aerosols over Alaska, such as OA and BC, could be due to low emissions over source regions in the mid-latitudes or due to excessive deposition in models *(Whaley et al., 2022b)* and Chapter 5 (for BC). To our knowledge, CAMS emissions (v5.3) have not yet been evaluated over source regions in the mid-altitudes (e.g. Siberia, China) as this version was only recently made available. Here, the model results are not evaluated against observations in Asia, as it is not the scope of this study. In this thesis, ECLIPSE and CAMS emissions are used for simulations over different months in winters 2014 and 2019. ECLIPSE and CAMS total annual emissions are compared in Chapter 3 during 2014 for all species. There are differences between the two inventories on the magnitude, for example of BC, OA, NO_x and NH_3 emissions, which is also illustrated by the maps shown in Chapter 3. It is possible that the CAMS inventory includes less, for example, BC and OC emissions over Asia and Siberia compared to ECLIPSE v6b, but a direct comparison is needed for the same year to get clear indications.

Table 6.2: *Biases and RMSEs, in ugm^{-3}, for all available aerosols and in ngm^{-3} for BC, and between model results (CONTROL) and observations at Denali (D), Toolik (T), Poker Flat (PF) and Simeonof (S) sites in Alaska, for simulation at quasi-hemispheric scale.*

	Bias_S	RMSE_S	Bias_D	RMSE_D	Bias_T	RMSE_T	Bias_PF	RMSE_PF
Na	0.21	0.35	0.1	0.2	0.07	0.1	-	-
Cl	-0.01	0.6	0.1	0.2	0.02	0.09	-	-
SO_4^{2-}	-0.06	0.23	0.08	0.1	0.09	0.1	-	-
NO_3^-	-0.003	0.04	0.02	0.04	0.03	0.08	-	-
OA	-0.008	0.03	-0.07	0.08	-0.2	0.3	-	-
BC	-31	39	-20.1	25	-5.2	14.4	-4.0	10.2

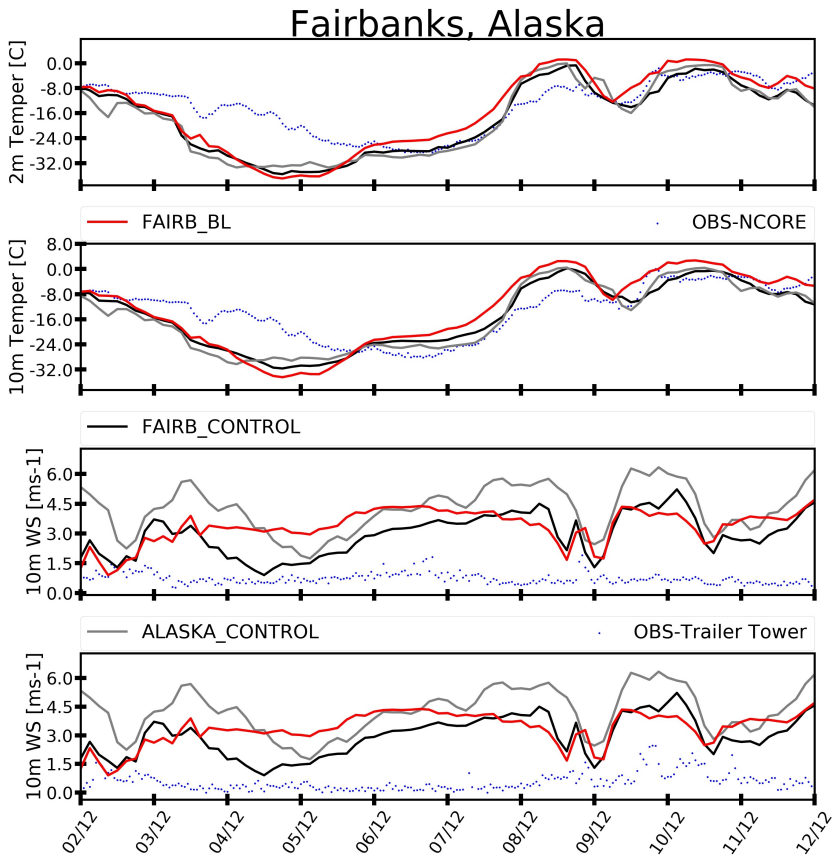

Figure 6.10: *Model comparison between ALASKA_CONTROL (33km), FAIRB_CONTROL (11km) and FAIRB_BL (11km) and evaluation against 2 and 10m temperature observations at NCORE site and 10m winds at NCORE and Tower Trailer, in UTC, between 2 and 12 December 2019. ALASKA_CONTROL is shown in grey, FAIRB_CONTROL in black, FAIRB_BL in red and observations in blue.*

6.6 Air pollution over central Alaska

This section focuses on central Alaska and, more specifically, the Fairbanks area to investigate regional pollution during the pre-ALPACA campaign, particularly during the observed

cold and mixing periods in December 2019. At the regional scale (11 km), a series of sensitivity simulations examining meteorology, removal treatments and emissions are performed. The aim is to investigate if the model can reproduce stable conditions and how the meteorological biases may affect aerosols and trace gases. Also, to what extent CAMS emissions include local sources in the Fairbanks area is examined here.

6.6.1 Meteorology

Model results are evaluated on all domains. Here, only the results at 33 km and 11 km are presented. The model at 100 km is colder during the cold period and during the warmer mixing period compared to 33km and the observations (not shown here). The model at 33km is less windy than at 100 km, but it still overestimates observations. As discussed in previous chapters, running at a higher resolution modelled temperatures and winds are generally improved.

On a regional scale over central Alaska, FAIRB_CONTROL (11 km) captures better than ALASKA_CONTROL (33km) surface temperatures and winds at NCORE and Tower Trailer during December 2019, as shown in **Fig. 6.10**. More specifically, the simulation at 11km is slightly less cold at the beginning of the cold episode and slightly warmer during the mixing from the aloft episode when it is warmer at 2 and 10m compared to the simulation at 33km. At NCORE and Tower Trailer, FAIRB_CONTROL is less windy compared to ALASKA_CONTROL during the whole period of the simulation. However, the model still overestimates observed winds, which during this period did not exceed 1.5 ms^{-1}. The model at 11km also performs better than at 33km at different EPA sites in the Fairbanks area, based on reduced biases (not shown here). Model results are also evaluated against radiosonde data, and here an example is shown during the cold period and colder mixing period for temperatures and winds (**Fig. 6.11**). At higher altitudes, and especially in the first 800 m, ALASKA_CONTROL captures better the observed temperatures during the cold period. Note that the the domain at 33 km is nudged above the boundary layer. During the cold mixing period (**Fig. 6.11a**) ALASKA_CONTROL is colder in the first 400 m and warmer at higher altitudes compared to FAIRB_CONTROL, but both are colder compared to the observations. On the other hand, the model is less windy at 11 km, but too windy compared to the observations (**Fig. 6.11c,d**). During the cold period the resolution slightly improves the meteorology at 11km, but not always and not at all altitudes.

Overall, models show difficulties simulating the boundary layer and surface-based inversions during winter in the Arctic *(Mölders and Kramm, 2010; Kayser et al., 2017; Graham et al., 2017)*. Uncertainties in simulated temperatures and winds at Fairbanks could be due

to errors in stability functions in the model, or the roughness length for vegetation and urban area is low *(Mölders and Kramm, 2010)*. In that study, increased roughness led to lower simulated winds, but the improvement compared to observations was small. These possible discrepancies could be investigated further. Here, the role of nudging and the boundary layer dynamics on modelled aerosols during the wintertime are examined.

In the control simulation (FAIRB_CONTROL), no nudging is applied. In a sensitivity test, spectral nudging is applied at all levels at 11 km (not shown here). When applying spectral nudging, the biases in surface temperatures and winds are decreased compared to no nudging simulation. Also, the simulated temperature profile is better in agreement with the observations. However, high biases remain for surface and higher altitude winds. Previous studies showed that ERA5, used here for nudging, shows high biases in surface temperatures compared to observations could be due to uncertainties in capturing clear sky conditions *(Batrak and Müller, 2019; Krumpen et al., 2021)*. However, with spectral nudging at 11km, aerosols and trace gases did not vary significantly (not shown here).

In a recent study, Maillard et al. (in prep. for GMD, 2022) reported that the calculation of the turbulent diffusion coefficient (C_d) contains a bug when using option 2 in NOAH MP namelist for surface layer drag coefficients calculations (see APPENDIX A for Chapter 4). C_d is too small and does not depend on the wind speed. Thus, the surface temperature was too cold and did not depend on wind speed. To estimate the influence of this bug, the model is run with the corrected version of NOAH MP but leads to insignificant differences in surface temperatures and winds (not more than 0.1 ^{o}C and ms^{-1} - not shown here). At higher altitudes, the model is warmer by up to 1^{o}C during the observed episodes in December 2019, while the changes in winds are small as at the surface. The effect of this bug on aerosols and gases is insignificant (no changes more than 0.05 μgm^{-3} and ppb, respectively). For the sensitivity simulations presented from now on, the corrected version of NOAH MP is used. From now on, we refer to this simulation as FAIRB_CONTROL.

So far in this study, the MYJ boundary layer scheme is used, which is shown to capture better continental stable conditions (e.g. *Sterk et al. (2015)*). To investigate the influence of boundary layer dynamics on aerosol and gases, the YSU boundary layer is used (FAIRB_BL), which performed better than MYJ over northern Alaska (results discussed in Chapter 5). In contrast to the analysis for northern Alaska, YSU over the Fairbanks area is warmer during the colder mixing period (7 to 9 December) and colder during the cold period (**Fig. 6.10**). Also, the use of YSU results in higher winds compared to MYJ. At higher altitudes and during the three observed periods, YSU results in higher winds and lower temperatures compared to MYJ (**Fig. 6.11**). YSU only captures better temperature profiles with respect to the observations over the Fairbanks area during the colder mixing period since YSU simulates

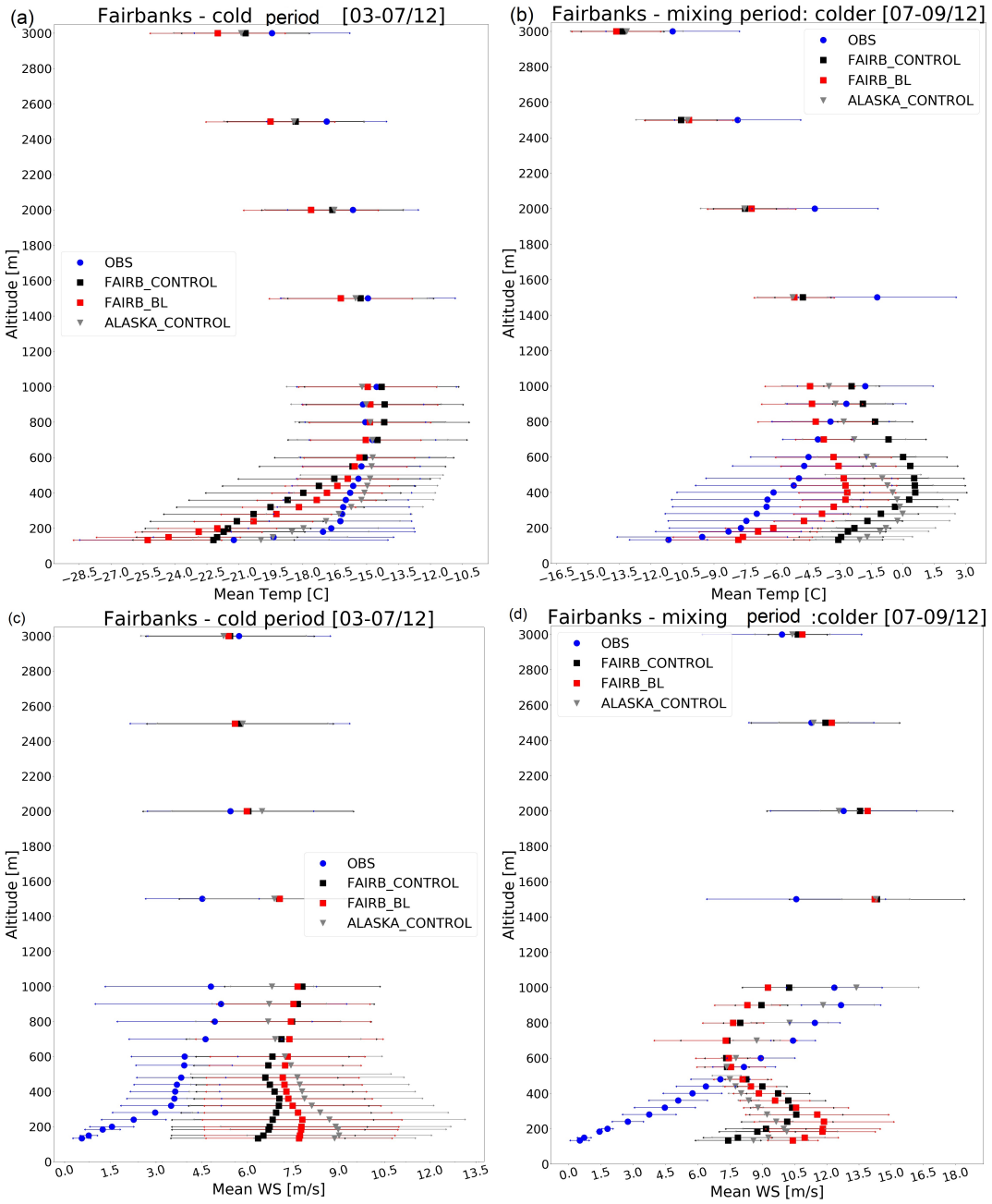

Figure 6.11: *Temperature and wind profiles at Fairbanks airport (in UTC) during the (a,c) cold period and (b,d) colder mixing period. Blue circles shows the observations, black squares shows the FAIRB_CONTROL (11km) simulation, the grey triangles shows the ALASKA_CONTROL (33km) and the red squares shows the FAIRB_BL (11km) run.*

better the vertical mixing, as discussed in Chapter 5. The initial physics parametrisation simulates better the calm conditions observed over the Fairbanks area during December 2019. The influence of YSU in aerosols and traces gases is discussed in section 6.6.3.

6.6.2 Trace gases and aerosols

This section analyses the regional patterns of simulated trace gases and aerosols during the pre-ALPACA campaign first over Alaska. **Figure 6.12** shows average BC, SO_4^{2-}, NO_x, the sum of NO and NO_2, and O_3 at 33km during the pre-ALPACA campaign.

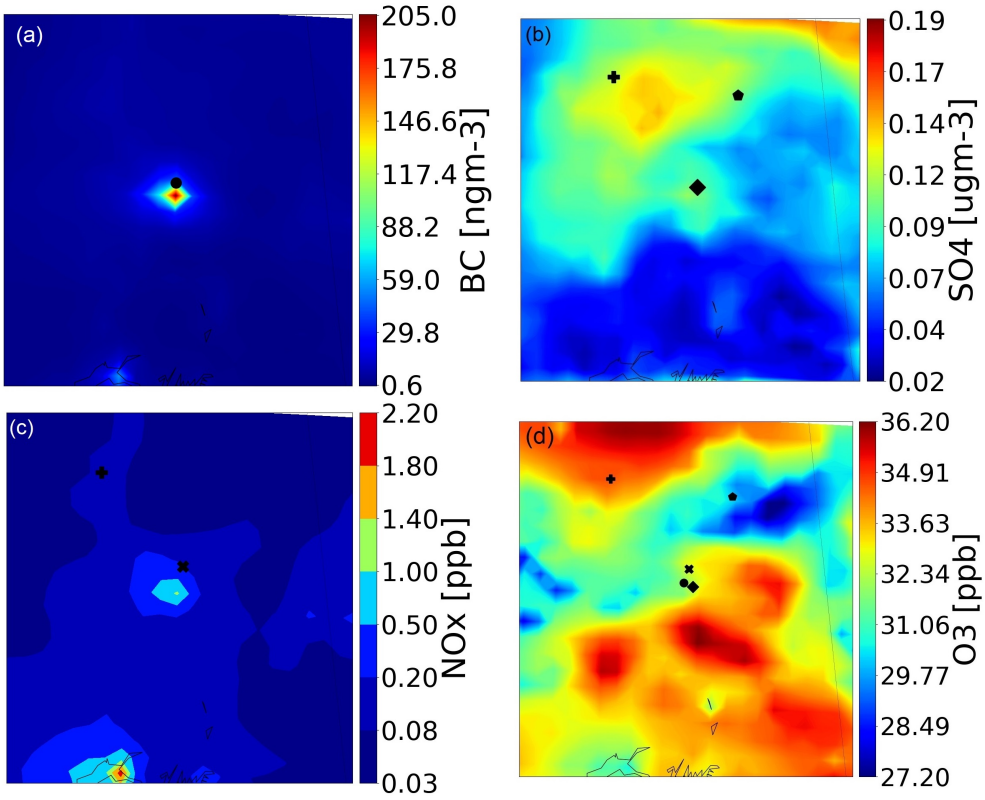

Figure 6.12: *Average values of modelled aerosols and gases at 33km (ALASKA_CONTROL), over central Alaska during the pre-ALPACA campaign (25 November - 15 December) and at the surface. Black circle shows the location of NCORE site in Fairbanks. Black diamond shows the location of North Pole. Black X shows the location of Poker Flat. Black cross shows the location of Gates of the Arctic. Black pentagon shows the location of Yukon Airport.*

Except O_3 and NO_x, BC shows high values over the Fairbanks area, including Fairbanks city and North Pole, due to local emissions including in the inventory, as shown in **Fig. 6.6** and discussed in section 6.4. O_3 shows higher concentrations over background regions than cities. Low concentrations of O_3 east of Fairbanks could be due to higher dry deposition over tundra areas *(Whaley et al., 2022a)*. NO_x shows higher values in the south of Alaska and could be due to local shipping emissions along the coast (ice-free). SO_4^{2-} shows higher values close to the Gates of the Arctic, probably due to local sources and lower NH_4^+ and NO_3^- (not shown here). There is more NH_4^+ and NO_3^- in Fairbanks than at background sites, which could contribute to lower SO_4^{2-}. At background sites, the ALASKA_CONTROL

(33km) simulation captures better observations than the CONTROL run (100km). For example, at Denali the BC bias decreases from -20.1 at 100 km to -17.7 at 33 km and SO_4^{2-} from 0.08 at 100 km to 0.05 at 33 km. The model performs better at 33km than 100km showing the effect of resolution on model results, as already discussed in Chapters 4 and 5.

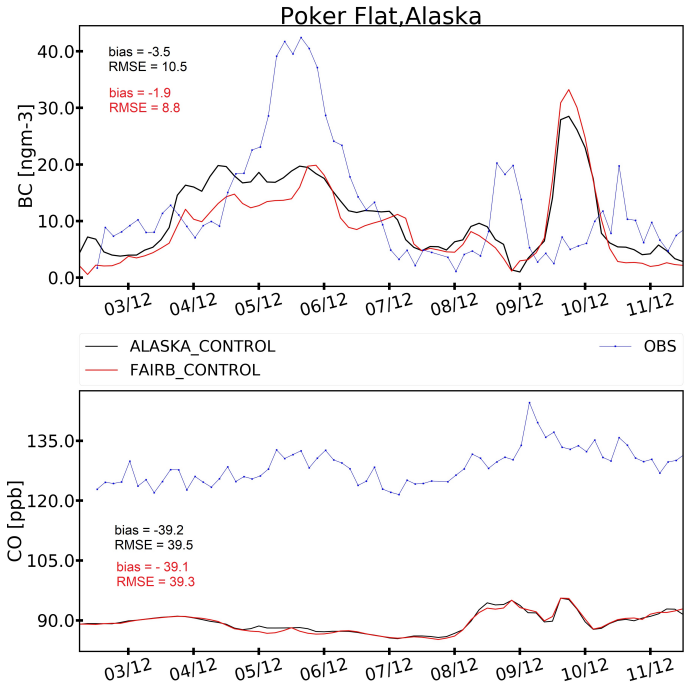

Figure 6.13: *Model comparison against observed BC, in ngm^{-3} ($r_d \leq 1.0\ \mu m$) and CO, in ppb, at Poker Flat, Alaska (AKST), between 2 and 12 December 2019. Black line shows results for ALASKA_CONTROL (33km), red line shows the results for FAIRB_CONTROL (11km), while BC observations, available every hour, are shown in blue dots, when available. See text for details.*

ALASKA_CONTROL (33km) is also compared to FAIRB_CONTROL (11km) and evaluated against available observations of trace gases and aerosols in the Fairbanks area. **Figure 6.13** shows BC and CO validation at Poker Flat, a background site. Both simulations capture observed BC variability with concentrations ranging between 5 and 20 ngm^{-3}. The simulation at 11km (FAIRB_CONTROL) captures observations slightly better, according to bias and RMSE (shown in **Figure 6.13**). However, both simulations underestimate the observed elevated BC during the cold period in Fairbanks. CO at Poker Flat ranges between 120 and 135 ppb during the pollution episode in Fairbanks, with higher concentrations during the mixing period. At Arctic sites, such as Zeppelin and Utqiaġvik, average CO during wintertime varies between 120-150 ppb, similar to that reported at Poker Flat *(Whaley et al., 2022a)*. CO is a good tracer of pollution transport, with only one photochemical sink and a lifetime of around one month *(Duncan and Bey, 2004; Gamnitzer et al., 2006)*. On the other hand, the model simulates background CO at 90 ppb and underestimates observed CO by

up to 40 ppb. Previous studies showed that models tend to underestimate CO (including Alaska), possibly due to an underestimation of CO emissions (such as from combustion over Asia *Pétron et al. (2002)*) and shorter modelled CO lifetime due to an overestimation in OH *(Miyazaki et al., 2012; Quennehen et al., 2016; Whaley et al., 2022b,a)*. The model simulates more CO in Fairbanks (**Fig. 6.14**) compared to Poker Flat. However, it does not exceed 160 ppb. This may be due to underestimations in the CAMS emissions and the fact that the model has only been run at 11 km.

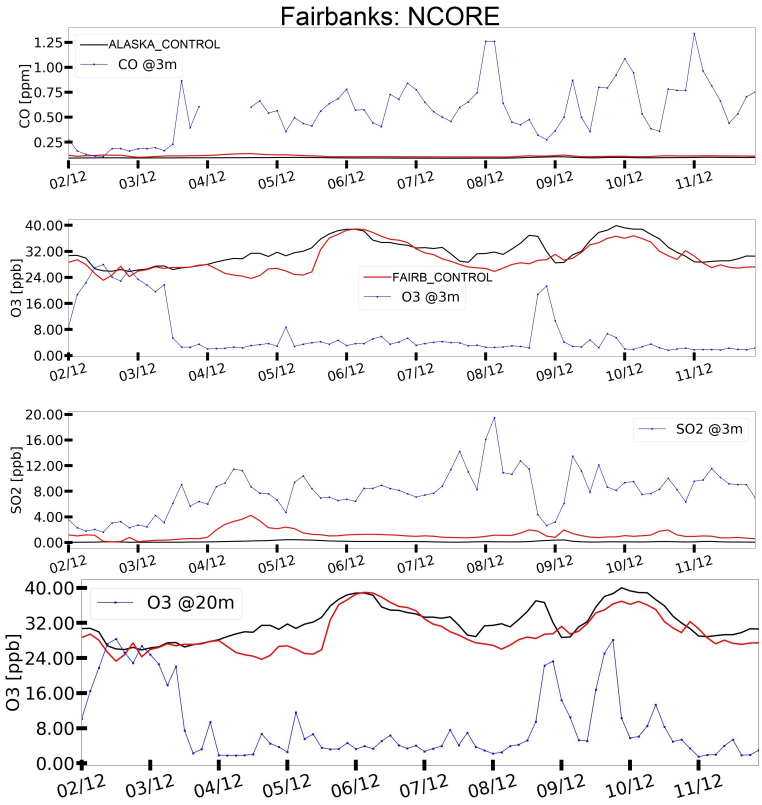

Figure 6.14: *Model evaluation against in-situ observations of CO in parts per million (ppm), O_3 and SO_2 in ppb, at NCORE site in Fairbanks, and O_3 at 20m in the CTC building (in UTC), between 2 and 12 December 2019. The black line shows results for ALASKA_CONTROL (33km), red line shows the results for FAIRB_CONTROL (11km), while observations are shown as blue dots every 3h, when available. See text for details.*

Figure 6.14 shows CO, O_3 and SO_2 observations at NCORE. Compared to Poker Flat, CO at NCORE ranged between 750 and 1250 ppb, with elevated concentrations during the mixing period on 8 and 11 December 2019. CO was also measured at the Trainor Gate (not shown here), near a small residential area just outside of the main Fairbanks city centre. CO ranged between 400 and 1200 ppb, slightly less than the reported measurements at NCORE. The most important CO emissions in Fairbanks are from vehicles and fossil fuel combustion (source EPA). Surface O_3 was higher prior to the cold period, while during

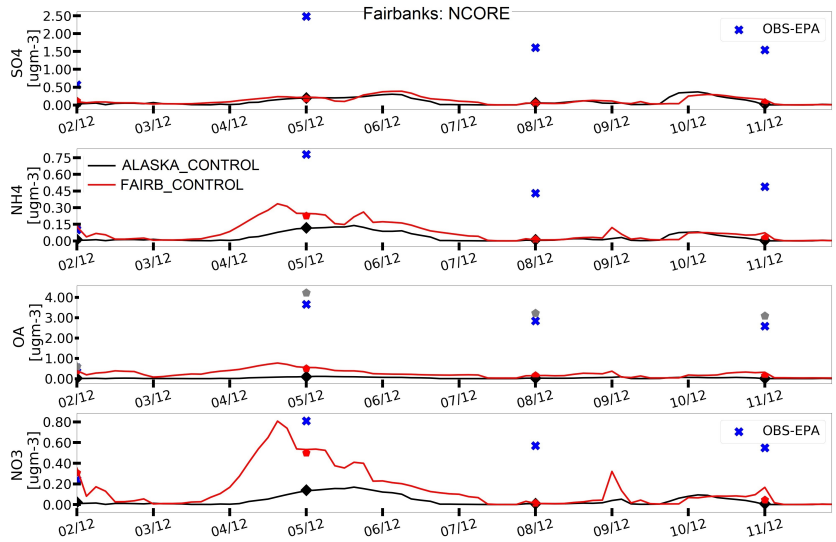

Figure 6.15: *Model evaluation against in-situ observations of NO_3^-, SO_4^{2-}, NH_4^+ and OA aerosol mass concentrations in μgm^{-3} at the NCORE site in Fairbanks ($r_d \leq 2.5$ µm) and in AKST, between 2 and 12 December 2019. The black line shows results for ALASKA_CONTROL (33km), red line shows the results for FAIRB_CONTROL (11km), while observations are shown as blue crosses, when available. Averaged model results are shown as black diamonds (ALASKA_CONTROL) and as red pentagons (FAIRB_CONTROL). See text for details.*

the cold period, O_3 did not exceed 8 ppb and was close to zero (due to complete titration by NO), while during the mixing period, O_3 increased again, up to 24 ppb. During the campaign period, O_3 was also measured at the top of the CTC building (20m), showing the same patterns as at 3m, prior to and during the cold period, while during the mixing period, higher values were observed (see **Figure 6.14**). O_3 is a good tracer of potential mixing from aloft. *Cesler-Maloney et al. (2022)* showed that during SBIs, O_3 is almost zero at 3m, while observed O_3 at 20m is higher due to reduced vertical mixing. NO mixes near the surface, leading to O_3 titration close to the surface and not at the 20m aloft. Background observed O_3 in Fairbanks (not during pollution episodes) is lower than reported values at remote Arctic sites such as Alert, Zeppelin and Utqiaġvik with values around 30-40 ppb during wintertime *(Whaley et al., 2022a)*. High SO_2 is measured between 2 and 11 December. In particular, during the mixing period, up to 20 ppb, possibly due to power plant influence. SO_2 is also measured at Trainor Gate (not shown here), showing elevated concentrations during the mixing period, up to 12 ppb (8 ppb less than at NCORE). During the cold period, SO_2 did not exceed 6 ppb, while at NCORE reached 11 ppb. During winter, major sulphur sources are fuel coal-oil combustion (commercial/residential) for heating purposes, diesel emissions, wood combustion and power plants influencing SO_2 on a regional scale aloft *(Shakya and Peltier, 2013)*. Most sulphur emissions are in the form of SO_2, although SO_4^{2-} could also

be emitted as primary aerosol *(Simpson et al., 2019)*. However, secondary formation is also possible although it is unclear how SO_2 is oxidized to SO_4^{2-} under cold and dark wintertime conditions.

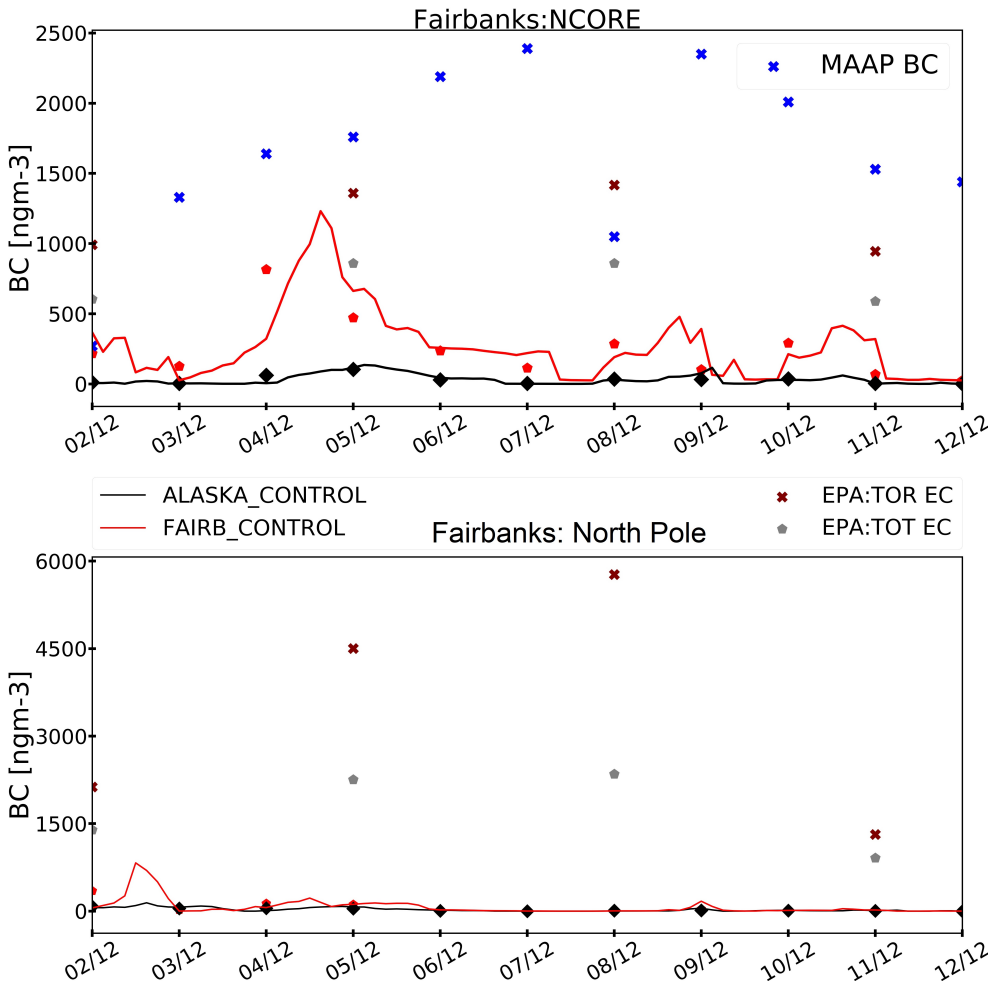

Figure 6.16: *Modelled evaluation of BC, in ngm^{-3}, at two sites in Fairbanks, against MAAP and EPA reported data during December 2019, for $r_d \leq 2.5$ µm and in AKST, between 2 and 12 December 2019. The black line shows ALASKA_CONTROL (33km) and red line shows FAIRB_CONTROL (11km) simulations, and the corresponding symbols are the daily averages every three days to match the observations from EPA. See text for details.*

During the polluted period, high observed SO_4^{2-}, NH_4^+, NO_3^-, OC and EBC are reported (**Figs. 6.15** and **6.16**), with elevated concentrations during the cold period (5 December) and slightly lower values during the mixing period. Prior to the cold period, inorganics, OC, and EBC were very low at NCORE and North Pole, sometimes three to four times lower than the measurements during the cold episode (not shown). **Figure 6.16** also shows EBC at North Pole, with elevated concentrations on 8 December (up to 6000 ngm^{-3}), three times higher than at the NCORE site. Previous studies showed that domestic wood com-

bustion emissions were higher at North Pole than in Fairbanks *(Ward et al., 2012)*. North Pole observations are not shown here, however, OC at North Pole is four times higher than at NCORE, while inorganics such as SO_4^{2-} and NO_3^- are higher at NCORE by up to 0.5 and 0.2 μgm^{-3}, respectively, also reported in previous studies *(Ward et al., 2012; Nattinger, 2016)*. During the campaign period, detailed observations of $PM_{2.5}$ were also measured at different altitudes at Trainor Gate (Tower Trailer), at the CTC building (surface), but also reported at EPA sites over the Fairbanks area (not shown here). Daily averaged surface $PM_{2.5}$ at Trainor Gate was elevated between 10 and 11 December (warmer mixing period), reaching up to 15 μgm^{-3}, while during the cold period, $PM_{2.5}$ did not exceed 9 μgm^{-3}. Daily averaged $PM_{2.5}$ were higher at 9 m and 11 m during the warmer mixing period and the cold period by up to 3 μgm^{-3} and 5 μgm^{-3}, respectively. At the NCORE site, daily averaged $PM_{2.5}$ were higher compared to Trainor Gate during the cold period, with concentrations up to 15 μgm^{-3} and up to 12 μgm^{-3} during the mixing period, as also illustrated in the **Fig. 6.15** and **6.16**, mostly due to high OC and EBC. NCORE is located closer to higher local emissions, such as from vehicles, while the Tower Trailer was located in a residential area. Higher concentrations of $PM_{2.5}$ were measured at the CTC building and at the surface, only at the end of the mixing period (11 December) when $PM_{2.5}$ concentrations reached up to 24 μgm^{-3}. During the cold period daily averaged $PM_{2.5}$ ranged between 6 and 12 μgm^{-3}. At the roof of the CTC building elevated $PM_{2.5}$ measured at the beginning of the colder mixing period and at the end of the warmer mixing period. At the NCORE site, the model overestimates O_3 by up to 25 ppb during the pollution episode (**Fig. 6.14**). However, there is less O_3 at 11km compared to 33km, a decrease of up to 8 ppb. The model overestimation could be due to a lack of NO_x emissions or uncertainties in simulating stable conditions. Finally, the model at 11km simulates more SO_2 compared to 33km, however it still underestimates observed SO_2 by up to 20 ppb, probably due to missing local sources. The implications of these discrepancies, which can in part be due to emissions, are discussed in the following section.

The model is also evaluated against aerosol observations obtained from EPA at the NCORE site (**Fig. 6.15**). Overall, the model at 11km performs better than at 33km, although it still underestimates observed aerosols. More specifically, the model at 11km does not capture elevated SO_4^{2-} and OA concentrations. The analysis in the previous chapters showed that the model lacks OA and underestimates SO_4^{2-} at sites such as Utqiaġvik due to missing local emissions. The model also underestimates NH_4^+ but captures better observed elevated NO_3^- during the cold period (5 December, **Fig. 6.15**), during which the model also simulates slightly more OA and NH_4^+. Similar results are found for North Pole (not shown here), a region with higher combustion emissions than Fairbanks *(Simpson et al., 2019)*. Concerning OA, future work should improve the VBS scheme used in this study (see Chap-

ter 3) and emissions of SVOCS/IVOCS making use of detailed VOC and OA measurements collected in ALPACA 2022. Finally, **Fig. 6.16** shows modelled BC at NCORE and North Pole sites. At 11km, the model simulates more BC (up to 1250 ngm^{-3}) at NCORE, however it still underestimates observed elevated EBC reported by MAAP and EPA. Modelled BC at the North Pole does not capture the high observed EBC due to missing local emissions. Overall, the model results are somewhat improved when using a higher resolution.

6.6.3 Sensitivity to boundary layer dynamics

In section 6.6.1, another boundary layer scheme was tested during the simulation period in December 2019. The analysis showed that when MYJ is used, the model captures better stable conditions, resulting in lower winds compared to YSU. Here the influence of those patterns on aerosols and trace gases is briefly discussed. BC, NO_3^- and SO_2 decrease, by up to 300 ngm^{-3}, 0.2 μgm^{-3} and 1.0 ppb respectively, over source regions (Fairbanks and North Pole, not shown here) when using YSU. However, this leads to an insignificant increase in SO_4^{2-}, which could be due to a shift towards NO_3^-, since NO_3^- and NH_4^+ decrease. Compared to observations at different regional sites (NCORE, CTC, North Pole), the FAIRB_BL leads to an increase in O_3 at 3 and 20m by up to 5 ppb, probably due to a decrease in NO, by up to 0.02 ppb. Modelled NO at 11km (FAIRB_CONTROL) ranges between 0.02 and 0.16 ppb, with elevated observations during the cold period. NO_3^-, OA, NH_4^+ decrease by up to 0.3 μgm^{-3}, as well as SO_2 by up to 2 ppb (not shown here). At background sites, such as Poker Flat, using the YSU boundary layer scheme does not lead to any significant improvements.

6.6.4 Sensitivity to aerosol and trace gas dry deposition

Chapters 4 and 5 showed that dry removal influences aerosols, such as SSA and BC, globally and regionally over source regions. Here, two sensitivity simulations are performed to investigate the effect of dry removal on aerosols and trace gases over the Fairbanks area.

First, the model is run with aerosol deposition, and gravitational settling switched Off. The effect of this sensitivity is shown in **Figure 6.17**, where the average differences between the FAIRB_AER_DEP_OFF and FAIRB_CONTROL simulations are calculated for different species. Overall, dry deposition affects all the species and, in particular over the Fairbanks area where there are high local emissions in the inventory. **Figure 6.25** also shows the FAIRB_AER_DEP_OFF at the NCORE site, and its effect on BC is very small, as also illustrated from the average differences shown in **Fig. 6.17**. On average BC change at NCORE is 3 ngm^{-3} due to dry deposition (**Fig. 6.25**). The small effect of dry deposition during this period could be due to uncertainties in simulating the stable boundary layer.

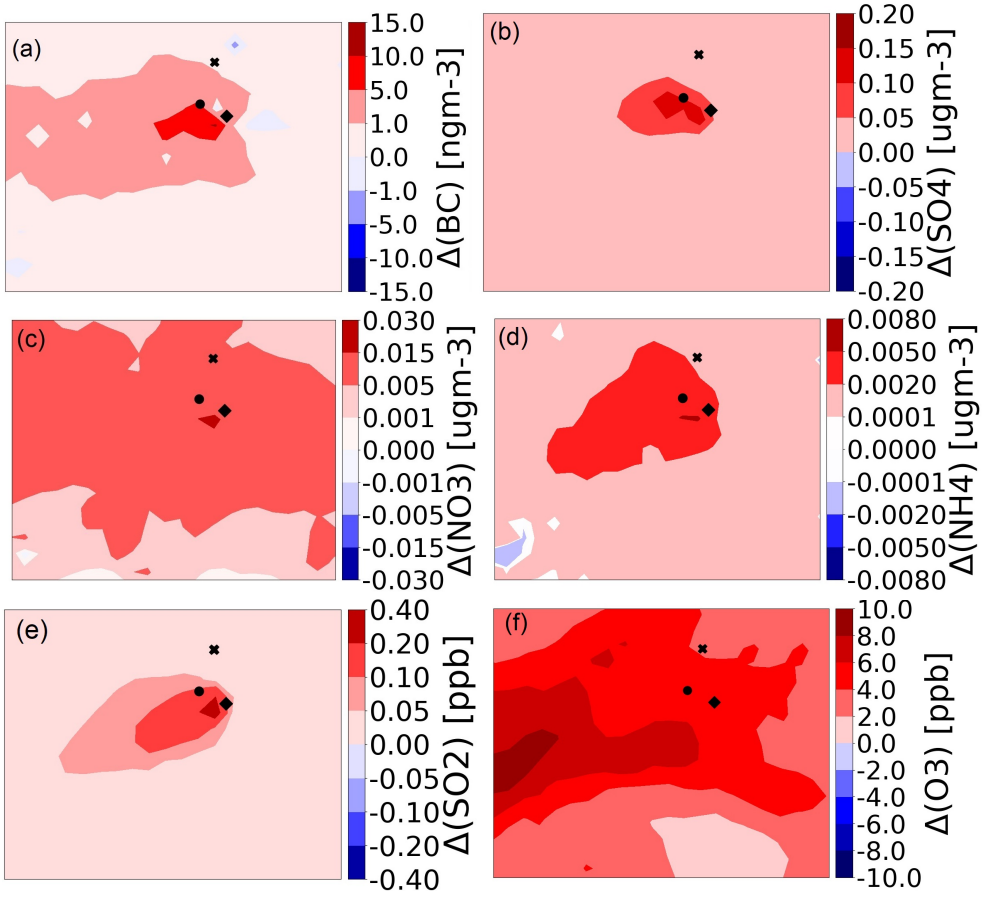

Figure 6.17: *Average differences between FAIRB_AER_DEP_OFF and FAIRB_CONTROL for (a) BC in ngm^{-3}, (b) SO_4^{2-}, (c) NO_3^- and (d) NH_4^+ in μgm^{-3} ($r_d \leq 2.5\ \mu m$). Also, the average differences between FAIRB_GAS_DEP_OFF and FAIRB_CONTROL for (e) SO_2 and (f) O_3 in ppb are shown here. The average differences are calculated during the simulation period at 11km, at the beginning of December (between 2 and 12 December 2019). The black x shows the location of Poker Flat. The black circle shows the location on NCORE site, while the black diamond shows the location of North Pole. Note that the scale is different on these maps.*

Apart from gravitational settling, dry deposition is driven by turbulent diffusion, which is related to the vertical transfer in the ABL. The model evaluation against radiosondes data (**Fig. 6.11**) showed that the model at 11 km is too windy and the temperature gradient at the first 600 m is very small, for example, during the cold period and in contrast during the colder mixing period, thus the ABL is less stable. Dry deposition is usually described using a resistance model that includes gravitational setting and a series of factors to describe the aerodynamic and surface resistances (see Chapters 3 and 4 for more details). Under stable conditions, the aerodynamic resistance term dominates, but under turbulent conditions, the surface resistance term dominates *(Solazzo et al., 2012)*. In this case, due to the model inability to capture stable observed conditions the aerodynamic resistance term might be too

small. However, to justify this assumption further analysis is required where these terms could be increased by a factor of 2 to investigate their effect on dry deposition.

In a second sensitivity test, the model is run with trace gas deposition switched off. **Figure 6.17** shows the average differences during the simulation between 2 and 11 December and between FAIRB_GAS_DEP_OFF and FAIRB_CONTROL for SO_2 and O_3. Gas dry deposition affects SO_2 mostly over the Fairbanks area, where the local sources are. The effect of dry deposition on O_3 is bigger outside towns, such as south-west of Fairbanks, by up to 10 ppb. The smaller increase in Fairbanks could be due to O_3 titration, due to an increase on NO_x.

6.6.5 Sensitivity to regional emissions over the Fairbanks area

Since the model was only run at 11km, it cannot be expected to capture high pollution levels which can be due to local spatial variations in emissions. However, on a regional scale, discrepancies between the model and average regional observations over the Fairbanks area can be used to assess possible discrepancies in the CAMS emissions, provided at 10 km resolution. To accomplish this, observations from regional sites are used to calculate enhancement ratios due to emissions over the Fairbanks area. More specifically, modelled and observed averages of BC, SO_2 and NO are calculated during the simulation period at the beginning of December 2019. The enhancement ratio is defined as the ratio of the modelled to observed average value based on observations and model results from regional sites. The enhancement ratio is calculated for BC, SO_2 and NO. Then, the CAMS emissions are divided by this ratio following the methodology described in *Ikeda et al. (2022)*. For this series of sensitivity runs, the enhancement ratios are calculated using all the available observations for the entire period, and there is no separate analysis per observed cold or mixing period. This is because EPA data, which are used, are reported every three days, and only four observations are available between 2 and 11 December. MAAP EBC and MICROMEGAS NO high-resolution data are also used to calculate the enhancement ratios, from hourly and daily averages to match EPA data temporal resolution. Model results based on the FAIRB_CONTROL simulation are used. This is a first approach, and a more sophisticated approach could be applied in the future. For example, a bias correction to the emissions could be applied using observations from the background and regional sites. However, this approach requires detailed observations which were only available for BC during pre-ALPACA. It could be used during the analysis for the main ALPACA 2022 campaign when detailed observations were also measured at background sites.

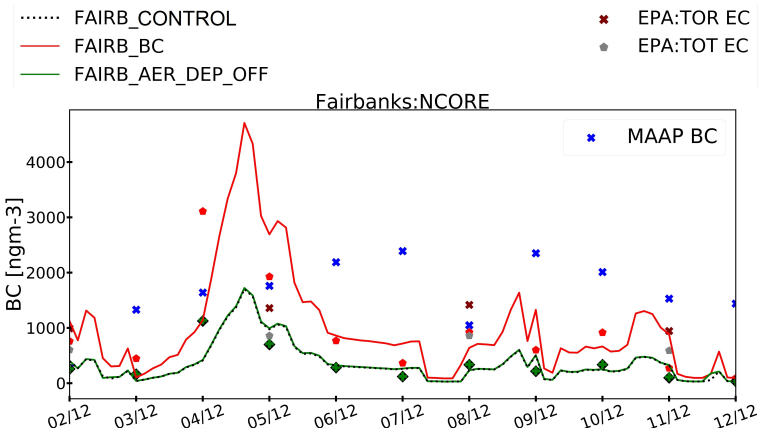

Figure 6.18: *Modelled BC, in ngm^{-3}, between FAIRB_CONTROL(dashed black line), FAIRB_BC (red line) and FAIRB_AER_DEP_OFF (green line) and against observations, between 2 and 12 December 2019, in AKST. The blue crosses show the daily averaged MAAP EBC observations, the brown X's measured EC at NCORE using the method TOR and the grey pentagons show EC measured at NCORE using the method TOT. See text for more details.*

6.6.5.1 BC emissions

The CAMS BC emissions are divided by the enhancement ratio (0.37), leading to an increase in regional BC emissions. The model (FAIRB_BC) is run with these higher emissions leading to an average increase in regional simulated BC by up to 3000 ngm^{-3}. At NCORE (**Fig. 6.25**), the model simulates more BC, capturing some times better observed EBC such as prior to the cold period (2 December), during the cold period (5 December) and the mixing period (8 December). However, the model does not capture enhanced EBC observations at NCORE and North Pole by correcting the emissions. Also, by increasing the emissions, there is a very small effect on background BC (e.g. at Poker Flat and Denali). Other processes, besides meteorology and dry removal, need to be examined, such as BC ageing and lifetime, but also correcting/improving remote (outside of Alaska) BC emissions. The enhancement ratio is also calculated using the model to observations ratio at Poker Flat and Denali, using only measurements available at the same date at both sites, and is found to be 0.99, showing that BC is well represented at background sites between 2 and 11 December.

6.6.5.2 SO_2 emissions

In this sensitivity simulation, CAMS SO_2 emissions are divided by 0.4, which leads to an increase in regional SO_2. As a result, modelled SO_2 and SO_4^{2-} increase over the Fairbanks area by up to 13 ppb and 0.3 µgm^{-3}, respectively (maps not shown here). The increase in SO_4^{2-} leads to a small increase in NH_4^+, by up to 0.06 µgm^{-3} and a decrease of similar magnitude on NO_3^- over the Fairbanks area (not shown here). The model (FAIRB_SO_2) captures

better the observed variability of SO_2, especially at Tower Trailer, however it still cannot capture the elevated observations during the mixing period (not shown here). **Fig. 6.19** shows the model comparison at NCORE against SO_2 and SO_4^{2-}. The model (FAIRB_SO_2) at NCORE also captures observed variability of SO_2 better during the cold than during the mixing period. It suggests that SO_2 emissions should be higher by a factor of 2.5. Elevated power plant emissions also need to be evaluated since they might explain the high SO_2 during the mixing period as noted earlier. However, the influence of this sensitivity on SO_4^{2-} aerosols is small, and the model still underestimates observations. SO_4^{2-} slightly increases at NCORE by up to 0.25 and 0.1 μgm^{-3} on 5 and 9 December, respectively, leading to a small increase in NH_4^+ and an insignificant decrease in NO_3^- during these days. The small increase in SO_4^{2-} aerosols indicates that there are either missing primary emissions of SO_4^{2-} or missing secondary formation mechanisms in the model.

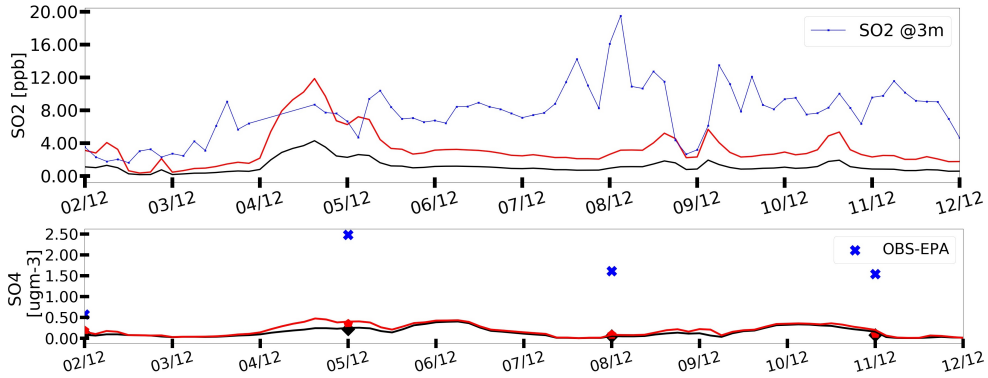

Figure 6.19: *Model comparison between FAIRB_SO_2 and FAIRB_CONTROL and observations of SO_4^{2-} in μgm^{-3} ($r_d \leq 2.5$ µm), and SO_2, in ppb, at NCORE site, between 2 and 12 December 2019. Observations are shown in blue when available, red line shows the sensitivity simulation FAIRB_SO_2 and black line the FAIRB_CONTROL run.*

As discussed briefly in Chapters 2 and 4, this version of WRF-Chem may be missing reactions for the secondary formation of SO_4^{2-}, in particular those which do not require sunlight. The reactions included in the model are described in *Zaveri et al. (2008)*. The following possible mechanisms could be tested in the WRF-Chem version used here. For example, missing reactions could be linked to sulphur oxidation catalysis by transition metals under dark conditions, as previous studies have reported *(Brandt and Van Eldik, 1995; McCabe et al., 2006)*. More recent modelling studies focusing on pollution episodes in China included missing reactions in WRF-Chem, which improved modelled SO_4^{2-} concentrations *(Gao et al., 2016; Li et al., 2018a; Sha et al., 2019)*. More specifically, *Gao et al. (2016)* added heterogeneous oxidation of dissolved SO_2 by NO_2. However, this reaction alone might not be able to explain elevated observed SO_4^{2-} if modelled NH_4^+ is too low, resulting in an aerosol

pH that is too acidic *(Huang et al., 2019)*. In a more recent study by *Sha et al. (2019)*, a simple SO_2 heterogeneous reaction in aerosol water was added into the CBMZ-MOSAIC chemical mechanism, assuming that its irreversible. *Sha et al. (2019)* showed that by including this heterogeneous reaction, SO_4^{2-} increased by 196% during wintertime (January), while other uncertainties linked to SO_4^{2-} production, such as in the gas phase oxidation rate of SO_2 by OH were small, especially during winter. High concentrations of hydroxymethane sulphonate (HMS) have been measured recently during winter and pollution episodes in China *(Moch et al., 2020)*. Modelling studies showed that HMS might explain high sulphur in China during wintertime *(Moch et al., 2018; Song et al., 2021)*. Aqueous-phase formaldehyde (HCHO) and S(IV) in cloud droplets to form a S(IV)-HCHO product could be important for sulphur chemistry in Fairbanks during wintertime. The above proposed mechanisms and others, such as SO_2 oxidation on pre-existing aerosols *(He et al., 2018)*, could be considered to improve modelled SO_4^{2-} concentrations in polluted Arctic environments during wintertime.

6.6.5.3 NO emissions

Here NO emissions are divided by 0.03 to get enhanced/corrected regional emissions and investigate their contribution to NO_3^- aerosols. In this sensitivity, only NO emissions are corrected as in WRF-Chem NO_x emissions are primarily to NO. As a result, modelled NO increased by up to 100 ppb on average over the Fairbanks area during December 2019 (maps not shown here). Also, NO_2 increased by up to 50 ppb. Based on MICROMEGAS data, observed NO at NCORE shows higher values during the mixing period, with measurements up to 110 ppb. Modelled NO levels in the control simulation (FAIRB_CONTROL) are very small, close to zero. When using the enhanced NO emissions, the model simulates more NO by up to 125 ppb, overestimating the observations during the cold period, but capturing observed variability, especially on 10 and 11 December. This sensitivity simulation influences NO_3^-, SO_4^{2-}, NH_4^+, but also O_3. More specifically, NO_3^- increases by up to 1.2 μgm^{-3} at NCORE, Fairbanks during the cold period (5 December) (**Fig. 6.20**), overestimating the observations. O_3 decreases by up to 30 ppb due to higher NO emissions in much better agreement with the observations. Modelled O_3 at 20 m also decreases, especially during the mixing period, in better agreement with the observations. SO_4^{2-} decreases by up to 0.2 μgm^{-3} and NH_4^+ increases by up to 0.08 μgm^{-3}, respectively (not shown here). At North Pole NO_3^- increases, especially during the cold period (5 December), but underestimates observed elevated NO_3^- by 0.3 μgm^{-3} (not shown). During the mixing period, the increase on NO_3^- is quite small, and the model still underestimates observations by up to 0.4 μgm^{-3}.

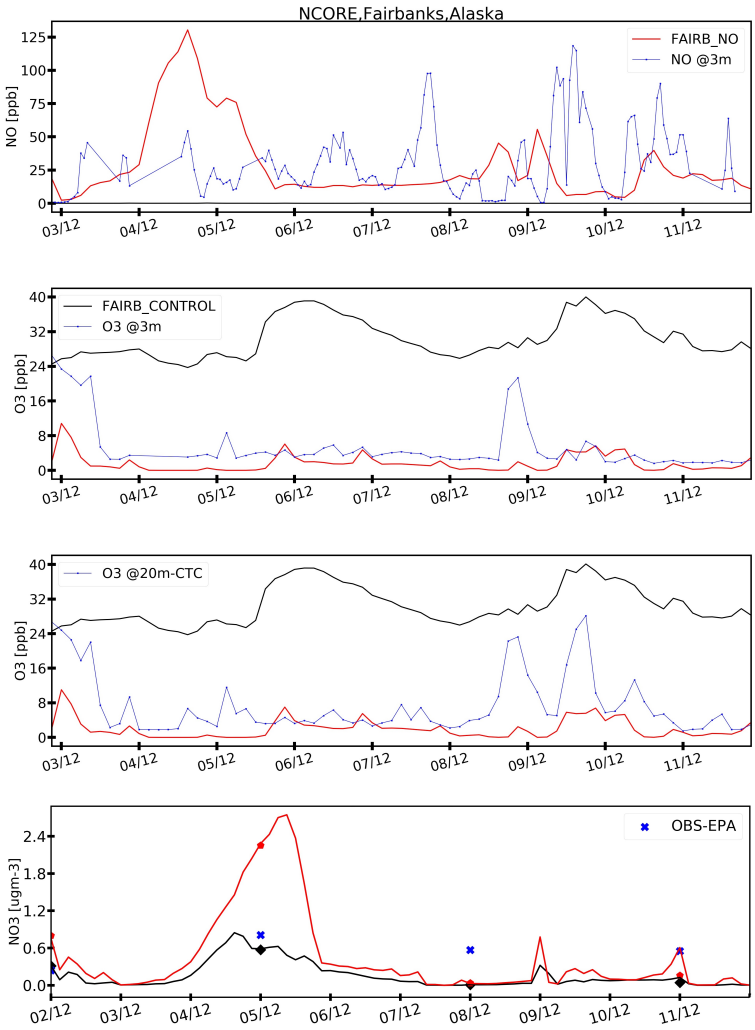

Figure 6.20: *Model comparison between FAIRB_NO and FAIRB_CONTROL and observed NO and O_3 in ppb and NO_3^- in μgm^{-3}, at NCORE site, between 2 and 12 December 2019 . Also the model comparison is shown against observed O_3 at CTC building (20m). Observations are shown in blue when available, red line shows the sensitivity simulation FAIRB_NO and black line the FAIRB_CONTROL. NO and NO_3^- observations are in AKST and O_3 in UTC.*

Unfortunately, there are not available NO observations at North Pole, where the local emissions might be higher and not included in the CAMS inventory. This sensitivity simulation, highlights that the main reason for low modelled NO_3^- aerosols might be the lack of local NO emissions. Higher NO emissions lead to higher NO_3^- concentrations and to O_3 titration, at least at NCORE and CTC (**Fig. 6.20**), showing that the model includes mechanism for the formation of NO_3^- aerosols.

During wintertime in Fairbanks, the duration of sunlight is limited to a few hours (4-5hrs). Thus radical photochemical sources are expected to be weak, and photochemical NO_x oxidation cycles slow (*Simpson et al., 2019*). Heterogeneous reactions of HNO_3 with

Table 6.3: *Averaged ratios of NH_4^+ to SO_4^{2-} during the simulation period in December 2019, based on the observations, and FAIRB_CONTROL, FAIRB_NO simulations.*

	NCORE	North Pole
Observations	0.27	0.26
FAIRB_SF	0.7	0.5
FAIRB_NO	2.2	0.9

NH_3 have been considered an important mechanism of nitrate formation during night-time *(Calvert and Stockwell, 1983; Mentel et al., 1999; Brown and Stutz, 2012)*. However, this requires NH_3 emissions. A recent study by *Lin et al. (2020)* showed that during wintertime polluted conditions in China, NO_3^- formation involving NH_3 occurred under NH_4^+ rich conditions. Previous studies used the ratio of NH_4^+ to SO_4^{2-} equal to 1.5 to determine if an area is NH_4^+ - rich during wintertime *(Pathak et al., 2009; Huang et al., 2011)*. As discussed earlier, between 2 and 11 December, high concentrations of SO_4^{2-} and NO_3^- were measured at NCORE. Also, observed NH_4^+ concentrations were similar to observed NO_3^- concentrations. The control simulation at 11 km (FAIRB_CONTROL) underestimates all three inorganic aerosols. Indeed, by increasing NO emissions there is more NO_3^- on 2, 5 and 11 of December, however despite the increase of NO on 8 December, NO_3^- concentrations did not vary.

To try to understand the low modelled SO_4^{2-} and high NO_3^- and NH_4^+ at NCORE during the FAIRB_NO sensitivity simulation, the same ratio is calculated to estimate if Fairbanks is an NH_4^+ - rich area during the polluted episode in December 2019 (**Table 6.4**). The discussion below also includes North Pole, even the FAIRB_NO sensitivity simulation, slightly increased NO_3^-, while modelled SO_4^{2-} and NH_4^+ did not vary. NCORE and North Pole observations show that these sites are not NH_4^+ - rich. On the contrary, the model at NCORE simulates a higher ratio than the observations, which could be due to low levels of SO_4^{2-}. When increasing NO emissions, there is more NH_4^+ in the model, which also leads to higher NO_3^- concentrations during the cold period. Unfortunately, observations of NH_3 are not available at the sites used in this study, which could help to estimate possible uncertainties on CAMS emissions. Recent studies reported that hot-springs around Fairbanks area are an important source of NH_3 emissions, which can serve as precursors of NH_4^+ and SO_4^{2-} aerosols *(Ye and Wang, 2020; Mölders et al., 2019)*. These regional emissions, and high wintertime local emissions from N-containing fuel from traffic, heating, and power plants *(Pan et al., 2016)*, might be missing from global inventories such as CAMS.

A recent study by *Liu et al. (2020)*, using WRF-Chem, showed the important role of N_2O_5 heterogeneous hydrolysis in the NO_3^- formation during wintertime, which dominates

the nocturnal NO_3^- formation. Homogeneous pathways also contribute to NO_3^- formation. Previous studies have measured NO_3 and N_2O_5 in a nocturnal boundary layer, including Fairbanks *(Ayers and Simpson, 2006; Riedel et al., 2012; Wagner et al., 2013)*. As discussed in Chapter 2, the dark reaction pathway forms NO_3 and N_2O_5 which can react with H_2O and Cl^- to form HNO_3 and NO_3^-. *Joyce et al. (2014)* reported that secondary nitrate formation due to NO_x oxidation in Fairbanks does not contribute to $PM_{2.5}$ due to the slower formation of N_2O_5 and thus NO_3^- and HNO_3 because of O_3 titration. From the beginning of the pre-ALPACA campaign and prior to the cold period, it was cloudy at Fairbanks. During the polluted episode in December 2019, there were periods of clear skies during day and night, such as the night of 5 December and the following morning (6 December), the night of 7 December (during the cold period), while it was mostly cloudy during the mixing period. Cloud formation could lead to N_2O_5 uptake aloft in clouds which will lead to less gas-phase HNO_3 and more NO_3^- aloft *(Joyce et al., 2014)*. However, studies have shown that there are uncertainties in modelling cloud-aerosol interactions, and further investigation is needed to quantify the uncertainties on aerosols *(Toll et al., 2019; Gliß et al., 2021)*.

6.7 Concluding remarks

This chapter focuses on the French pre-ALPACA campaign during November and December 2019. Detailed observations measured during the campaign are used to understand uncertainties in simulated aerosols and trace gases in polluted Arctic environments during wintertime. The WRF-Chem model is used to perform quasi-hemispheric and regional scales simulations, focusing on central Alaska and over the Fairbanks area, coupled with CAMS anthropogenic emissions.

First, the model's ability to capture Alaskan air pollution at background sites is investigated. During the pre-ALPACA campaign, the model performs well, capturing observed concentrations of inorganics and especially SO_4^{2-} and NO_3^-, but also BC and OA (low biases and RMSEs) in background Arctic Haze. The model inability to capture periods with higher BC and OA at background sites could be due to missing regional sources, high modelled deposition in the mid-latitude regions or due to errors in transport patterns. The results presented in this study over Alaska also show that the improved WRF-Chem version, coupled with up-to-date input data and emissions, performs better during winter 2019 compared to winter 2014, at least over Alaska. The sub-Arctic site, Simeonof, which used in both studies, supports the above statement for natural and anthropogenic aerosols. Modelled BC at background Alaskan sites is also well simulated, including Toolik, which is located close to NSA oilfields and may be influenced by regional emissions.

During wintertime, Fairbanks experiences strong temperature inversions due to stable conditions. While the model captures surface temperatures and winds quite well in Fairbanks, there are larger biases at higher altitudes. To address these uncertainties, spectral nudging and another boundary layer scheme are tested at 11 km. Indeed, spectral nudging leads to a better representation of the temperature profile compared to the observations, reducing the temperature biases however high wind speed biases remain. The use of another boundary layer scheme did not improve the model meteorology. Uncertainties in stability functions in WRF boundary layer schemes or in land surface models, such as NOAH MP, linked to, for example, set up of restrictive boundaries on the turbulent diffusion coefficients and stability parameters, as recently shown by Maillard et al. (in prep. for GMD, 2022), might be responsible for weak temperature gradients. Other reasons for these biases could be due to the size of the smallest domain, which might be influenced by the 33km domain or uncertainties linked to the other parameters in the model (e.g. clouds) and reanalysis data (ERA5) or the need to increase model vertical resolution.

Model results at 11km over the Fairbanks area show that the model underestimates aerosols and their precursors. A series of simulations are performed to investigate possible reasons including meteorology, removal treatments, and emissions. The changes in modelled aerosols and trace gases are small due to spectral nudging sensitivity. Also, the use of the YSU scheme leads to lower aerosol concentrations compared to MYJ, since it simulates less stable conditions and enhances vertical mixing. These results show that model results are sensitive to the boundary layer parametrisation that is used since it affects the meteorological conditions, affecting modelled removal treatments and thus simulated aerosols and gases. The effect of dry deposition on aerosols and trace gases is small over the Fairbanks area, despite the fact the model includes regional sources. This could be because the model at 11 km does not simulate the stable conditions accurately leading to biases in the vertical distribution of winds and temperatures (see radiosonde comparison). Wet removal was not examined during this study. A few sporadic measurements in Fairbanks show that precipitation and snow mostly occurred at the beginning of the pre-ALPACA campaign, end of November 2019, before the pollution episode (cold period). Also, it rained and snowed one day before the cold period and towards the end of the mixing period. However, the results presented in Chapter 5 showed that the regional effect of wet removal on BC was small in northern Alaska. The effect of wet removal on aerosols and gases over the Fairbanks area, could be examined in future analysis, over a larger domain, covering the whole Alaska. However, for future simulations, dry and wet deposition measurements of different species are needed to better constrain the model.

Since the model is run only at 11 km it cannot be expected to capture high pollution

episodes. However, possible underestimation in precursor emissions on a regional scale is investigated here. Average ratios of the model to observations at regional sites over Fairbanks are calculated for BC, SO_2 and NO using data measured during the pre-ALPACA campaign and data from EPA. Indeed, by "correcting" the emissions, there is more BC, SO_2 and NO, however the model still underestimates observed elevated aerosols and gases precursor, especially during the mixing period, maybe because there is too much mixing in the model (limitations on model vertical resolution). Low BC could be due to missing higher local emissions. Other uncertainties could be due to BC ageing and lifetime and removal processes regionally and locally. Based on the analysis in this study, CAMS inventory underestimates BC emissions by almost a factor of 3. Using higher-resolution observations, obtained from background and regional sites, will help to better quantify this factor. Note that despite the big increase in SO_2 emissions, by a factor of 3, modelled SO_4^{2-} only increased slightly on 5 December, during the cold period. These results suggest that there are missing mechanisms necessary for secondary formation of SO_4^{2-} or missing primary SO_4^{2-} emissions. However, by only including, missing reactions may not lead to significant improvement inf the model performance, if SO_2 emissions are too low, as in the case of CAMS emissions, and for example during the mixing period. Compared to SO_2 emissions, NO emissions in the CAMS inventory are lower in Fairbanks. An increase in local NO emissions leads to more NO_3^- in the model, in better agreement with the observations compared to SO_4^{2-}, except during the cold period when the model overestimates observations. Compared to the other emission sensitivity simulations, higher NO emissions will further improve modelled NO_3^-. Based on this analysis, CAMS underestimated local NO emissions by a factor of 33. The underestimation might be higher, as the model still underestimates NO_3^- at North Pole. Higher-resolution observations of aerosols and their precursors are needed, at different polluted locations, across Fairbanks region, to better quantify this factor. Higher NO emissions also leads to lower modelled O_3 concentrations, in better much agreement with the observations during the cold and mixing period, at the surface and at 20 m. However, there are sporadic elevated O_3 observations at the beginning of the cold period, during the transition from the colder to the warmer mixing period and during the warmer mixing period, which now are underestimated by the model. Further analysis is needed to quantify whether other uncertainties, such as on dry deposition, might contribute to lower O_3 concentrations in case of high NO emissions.

This analysis shows that one important reason for low modelled aerosols at polluted sites during wintertime might be due the underestimation of local sources, such as NO emissions. Higher BC emissions are also needed for areas with high local sources, such as North Pole. Higher local sources and the inclusion of missing mechanisms, for example, for

the formation of secondary SO_4^{2-} will improve model performance. Further investigation is also needed to quantify, to what extent other emissions over Fairbanks area, such as NH_3, are missing from CAMS. Finally, CAMS inventory could be combined with higher resolution inventories, such as National Emissions Inventory (NEI) from EPA, including point sources, such as power plants.

The pre-ALPACA campaign is a good first step towards understanding wintertime aerosol formation and missing sources in a polluted Arctic city such as Fairbanks. Combined with the main ALPACA campaign, where more detailed observations were obtained might help constrain the models better. Overall, higher spatial and temporal resolution observations are necessary for simulations during a short period. Thus, although detailed BC and trace gases were measured during the pre-ALPACA, detailed aerosol measurements (inorganics and organics) are also needed to investigate local processes and to better constrain the model. EPA provides only daily averages every three days, which might lead to biases. Detailed measurements made during the main ALPACA campaign at different locations in and around the city and altitudes will help to investigate aerosols and gases space evolution, sources, and sinks in more detail. Higher resolution emissions, such as those from NEI-EPA are being prepared at high resolution for the ALPACA 2022 campaign (1.3 km).

Chapter 7

Conclusions

7.1 Summary of scientific findings

The Arctic is warming faster than the rest of the world and this warming is stronger in autumn and winter. Thus, despite the fact that anthropogenic emissions are declining the last 20-30 years in mid-latitudes, there are important local air pollution sources within the Arctic which might increase in the future due to on-going climate warming. This thesis focuses on improving our understanding about local and remote anthropogenic and natural sources, and processes, influencing aerosols in the Arctic during wintertime. To accomplish this, the regional chemical-aerosol transport model WRF-Chem is run on quasi-hemispheric scale and at regional scale over central and northern Alaska, for periods corresponding to two field campaigns. Three main scientific questions are addressed in this thesis as outlined in the Introduction. The main results are discussed below.

(i) *What is the contribution of natural and anthropogenic sources to aerosol composition during the Arctic winter? Can models simulate wintertime aerosol composition in the Arctic?*

WRF-Chem simulations are used to investigate wintertime aerosol composition. Evaluation of aerosol components over the wider Arctic and central/northern Alaska shows that anthropogenic aerosols, and in particular BC and SO_4^{2-} contribute to total aerosol burden, as they have high mass concentrations, especially in regions with high local emissions. Anthropogenic OA are also an important aerosol component at remote Arctic sites during wintertime with elevated concentrations together with natural aerosols.

In this thesis, the contribution of SSA is examined as they are an important component of Arctic Haze during wintertime based on the results of recent observation-based studies

(Chapter 4). Model representation of SSA emissions is improved and used to estimate that SSA contribute between 44% and 85% to fine and coarse mode aerosols, respectively, compared to other inorganic aerosols (SO_4^{2-}, NH_4^+ NO_3^-) at remote coastal Arctic sites during winter 2014. The study presented in Chapter 4 also shows that it is important to include marine OA even during winter where they contribute to total OA at coastal Arctic and sub-Arctic sites. This was motivated by field observations showing significant marine OA associated with SSA and open leads at the coastal Barrow site (Utqiaġvik) in northern Alaska, that are typically missing in models.

One aim of this thesis is to understand possible reasons for model discrepancies compared to observations in Arctic winter. Detailed analysis of model performance over the Arctic during winters 2014 and 2019 is presented. The initial version of WRF-Chem used in this thesis overestimated super-micron and coarse mode SSA, by up to a factor of 3-4 at coastal Arctic sites, while the model underestimated OA and SO_4^{2-}. Improved model treatments of SSA emissions, notably the use of a lower wind speed dependence (based on satellite estimated whitecap fraction), inclusion of an SST dependence and a source of ss-SO_4^{2-}, as well as the activation of a source for marine organics, described in Chapter 4, leads to a better representation of modelled SSA with respect to the observations at remote Arctic sites. This also improved the simulation of other inorganics, such as SO_4^{2-} and NO_3^-. However, the model still underestimates episodes with elevated sub-micron SSA and other inorganics, especially SO_4^{2-} of anthropogenic origin, over northern Alaska, and at coastal sites such as Barrow, Utqiaġvik, which are not fully sea-ice covered during winter. The results suggest that the model lacks local and regional sources. The inclusion of marine organics improved modelled OA at sub-Arctic sites, such as Simeonof and the use of the ratio OC:Na^+ as a proxy for marine OA increased OA along the west and north coast of Alaska, in line with findings of *Kirpes et al. (2018, 2019)*. These improvements could be applied in simulations over the wider Arctic. However, modelled OA are still low compared to the observations over Alaska, possibly due to missing secondary OA formation or underestimation remote or within Arctic anthropogenic emissions.

Wintertime Arctic EBC observations show elevated concentrations at remote Arctic sites due to Arctic Haze influence and the contribution of local and regional sources within the Arctic (Chapters 5 and 6). WRF-Chem underestimates BC on average at remote Arctic sites, such as Tiksi, Utqiaġvik and Alert, but it captures better observed variability at Zeppelin (winter 2014). Reasons for these biases are investigated (see below).

Modelled aerosol composition at background sites influenced by Arctic Haze is improved in simulations for winter 2019, compared to winter 2014, especially over Alaska. More specifically, inorganic aerosols, such as SO_4^{2-} and NO_3^-, and BC, are better simulated

over Alaska during winter 2019 compared to winter 2014. This may be due to the use of a more up-to-date emission inventory (CAMS) for 2019 (Chapter 6).

(ii) *How sensitive are modelled aerosols to removal treatments and physical processes during wintertime?*

Throughout this thesis sensitivity simulations are performed to investigate possible reasons for uncertainties in modelled aerosols during wintertime over the wider Arctic and over Alaska. The focus of the different studies is on the representation of the modelled PBL, sea-ice fraction and wet and dry removal.

The influence of the PBL meteorology is thoroughly investigated in this thesis, since it is important to simulate accurately PBL structure (dynamics), as it affects vertical mixing of aerosols and their precursors, aerosol and gas dry deposition, and can also trap pollution at the ground under stable weather conditions, common in the Arctic during winter. The influence of the PBL is investigated on BC over northern Alaska (Chapter 5). The use of another PBL scheme in the model, namely MYJ, resulted in lower BC concentrations over source regions, such as NSA oilfields and Fairbanks, but also regions with high mountains, such as across the Brooks Range, north of Alaska, probably due to differences in precipitation patterns. For the analysis presented in Chapter 6, first the MYJ PBL scheme since it is often used for modelling stable PBLs in the Arctic and Antarctica. Runs with YSU showed only small differences in aerosols and gases at polluted and background sites. Both PBL schemes have difficulties simulating stable conditions with strong surface temperature inversions. Model winds are too high at the surface and in lower troposphere, and temperature gradients are too low. Such biases affect air pollution regionally over Alaska, but could also lead to high biases on aerosols and gases in the wider Arctic and mid-latitudes. Comprehensive meteorological measurements collected during ALPACA 2022 will help to improve model PBL treatments.

The results presented in Chapter 4 show that SSA along the west and north coast of Alaska are sensitive to sea-ice concentration (fraction). FNL and ERA5 sea-ice products are tested leading to differences in SSA emission fluxes and concentrations. When using ERA5 sea-ice data, SSA emission fluxes mostly increased around the west and east coast of Utqiaġvik and decreased further east. There are also notable differences on the south east coast of Alaska. Both reanalysis data have difficulties representing realistically open leads along the coast of Utqiaġvik during January and February 2014. Other factors, such as using higher wind speed dependence for sub-micron SSA emissions, leads to a significant increase in sub-micron SSA concentrations at the north coast of Alaska. Overall, modelled SSA are more sensitive to sea-ice and wind speed treatments, rather than dry deposition. However,

further analysis is required to include more realistic sea ice concentration in the models (and meteorological reanalyses), for example, based on satellite data in order to reduce model biases, in particular, in sub-micron SSA. This may also improve simulation of marine boundary layer dynamics. The dependence of SSA on SSTs in the Arctic as a function of particle size might also improve model discrepancies during elevated sub-micron SSA episodes. New observations are also needed.

Chapter 5 examines the contribution of removal processes to modelled BC in the Arctic. The analysis show that BC is sensitive to wet and dry removal across the Arctic at the surface and in the free troposphere (mainly wet removal). Results depend on location, with Zeppelin and Alert being more sensitive to wet removal than at Tiksi or Barrow where both wet and dry removal is important (in the model). This study also highlights that BC is sensitive to wet removal during transport to the Arctic and to a lesser extent regionally over northern Alaska. BC is also sensitive to dry removal over the wider Arctic and regionally depending on proximity to local and regional sources. The analysis presented in Chapters 4 and 6 also showed that SSA, other inorganic aerosols and trace gases are sensitive to dry removal regionally over central and northern Alaska during wintertime. Improvements in modelled dry deposition velocities as a function of particle size as well as model PBL dynamics, as noted above, should be investigated. Improvements to modelled aqueous uptake in clouds could, for example, improve modelled wet removal.

(iii) *To what extent are local Arctic anthropogenic sources contributing to wintertime atmospheric composition?*

The focus of this thesis is on regional and local sources over Alaska. The results presented in Chapter 5 show that regional emissions over northern Alaska, especially those from North Slope Alaska (NSA) oilfields are having a significant impact on BC at the Barrow Observatory during winter 2014 with 30—50% of BC coming from this source. This result highlights the impact of local source on wintertime Arctic air pollution. The use of higher resolution inventory (CAMS) resulted to lower BC emissions over the North Slope of Alaska during winter 2014. However, both inventories lack detailed representation of local sources at Utqiaġvik town, also shown to be influencing the BC observations at Barrow. Further analysis using longer model runs is needed for different winters to investigate the influence of NSA oilfield emissions and to determine the uncertainties and limitations in emission inventories.

Model simulations for winter 2019, run with CAMS emissions, are presented in Chapter 6. The results show that regional Alaskan sources may be contributing to background sites in central Alaska, such as Toolik field Lake station. Local emissions are also important in

the Fairbanks area (as also noted in Chapter 5 for BC). However, the model underestimates precursor gases and aerosols over the Fairbanks area. This could be partly due to the resolution of the runs but also that local sources in polluted sites such as Fairbanks are missing or are too low in the CAMS inventory. The analysis presented in Chapter 6 shows that CAMS BC, SO_2 and NO emissions may be underestimated by at least a factor of 2.5 (BC, SO_2) and 33 (NO) over the wider Fairbanks area, including the residential area North Pole. A more sophisticated bias correction on the emissions, using detailed background and regional measurements will help to quantify better this underestimation. This analysis also shows that some of the model biases, for example underestimation of SO_4^{2-} and or BC can be partly explained by lacking emissions. Remaining biases, in the case of SO_4^{2-}, could be explained by additional secondary aerosol formation mechanisms.

During wintertime, local anthropogenic emissions originating from gas flaring, residential and commercial heating, power plants and industry are contributing to regional and local air pollution in the Arctic. However, this contribution might be underestimated due to uncertainties in global emission inventories (Chapters 4,5,6) or lack of detailed documentation on local sources (Chapter 6). Global emission inventories are not updated regularly to take into account changes in emissions due to regulations in countries to decrease their emissions. Also, global inventories are provided at coarse resolution, usually 50 x 50 km or 10 x 10 km and lack detailed representation of local sources. There are small and big (urban) settlements around the wider Arctic, but without detailed observations to help quantify the contribution of local sources it is difficult to assess air pollution levels. This is an important issue because local anthropogenic sources might increase in the future due to on-going climate warming and increased human activity.

7.2 Perspectives and future work

The work undertaken during this thesis improves the performance of the WRF-Chem model at remote Arctic sites during wintertime and provides new insights into how various processes and sources are influencing wintertime Arctic air pollution, and especially Alaskan pollution. Sites such as Barrow, Utqiaġvik or the polluted city of Fairbanks are affected by background, regional and local sources. As such, they could also be representative urban areas of other remote regions in the Arctic for which there are no detailed observations. Arctic composition during winter may change in the future due to changing remote and local sources and as a result of climate warming.

Due to on-going global warming, and especially rapid Arctic warming, less sea-ice will be formed during summer and as a result, thinner ice during winter. Thus, new sources of

marine emissions, including SSA might emerge, which might increase the SSA contribution to aerosol burden, especially at coastal Arctic sites. This could have an impact on the Arctic radiative budget by enhancing cooling in the atmosphere or increasing CCN. To further investigate the effect of SSA on Arctic climate high resolution satellite sea ice concentration data are needed, as discussed earlier. Also, to further understand the interactions between ocean and the lower atmosphere, WRF-Chem could be run coupled with an ocean model.

There are also other important natural sources, such as dust and volcanoes, contributing to the Arctic aerosol burden that were not addressed in this thesis (e.g. *AMAP (2021)*). Especially for dust, there are important natural and anthropogenic sources (e.g. from mining activities) in the Arctic as discussed in Chapter 2, that are not included in the global emission inventories used in this thesis and need to be considered in future studies. Analysis of data from comprehensive field campaigns, such as the ALPACA 2022 campaign, will also help to constrain regional models further and better understand missing aerosol formation pathways under polluted wintertime conditions. Chapter 6 refers to previous modelling studies which have investigated wintertime Arctic Haze conditions in China. These studies have included missing reactions necessary for the secondary formation of SO_4^{2-} and NO_3^-. Such reactions need to be tested in WRF-Chem following ALPACA data analysis. This also includes organic aerosols and their precursor VOCs for which there were detailed measurements during ALPACA 2022. Combined with higher resolution emission inventories, such as EPA-Alaska Department of Environmental Conservation (EPA-ADEC), being produced for winter 2022 at a resolution of 1.3 x 1.3 km, model simulations at higher resolution will help better to investigate chemical and meteorological processes influencing local wintertime Arctic pollution. Related to this, this thesis also highlights that the model lacks anthropogenic organic aerosols. Recent studies have included in models IVOC emissions from mobile sources *(Lu et al., 2018, 2020)*. However, there are still uncertainties regarding non-mobile IVOC emissions due to limited data *(Lu et al., 2020)*. Recent studies also have reported SVOC emissions from mobile sources *(Presto et al., 2012; Zhao and Garrett, 2015; Zhao et al., 2016)*. OA and VOCs measurements collected during the ALPACA 2022 campaign will help to address this limitation in WRF-Chem.

The different studies presented in this thesis showed that aerosols and trace gases are sensitive to dry deposition. Two different modules calculating dry deposition velocities were tested resulting in important differences in aerosol concentrations. However, due to missing observations of dry deposition velocities over different terrains, it is difficult to validate these parametrisations. Modelled BC is also sensitive to wet deposition. Recent studies showed that by improving wet and dry deposition parametrisations, modelled BC in the Arctic might increase by a factor of 50–100 *(Liu and Matsui, 2021)*.

Whaley et al. (2022b) showed uncertainties in modelled dry and wet deposition at mid-latitudes where observations are also limited. It is essential to first address model uncertainties linked to dry and wet deposition at mid-latitudes before focusing on the Arctic, as they influence aerosol concentrations transported in the Arctic as discussed earlier in Chapter 5, and for this, detailed deposition measurements are needed. Last but not least is necessary to further improve land surface models and stability functions at the boundary layer schemes, to limit the uncertainties on aerosols and trace gases due to uncertainties on meteorology. This can be accomplished using detailed measurements of meteorological variables collected at different sites, during field campaigns, such as pre and main ALPACA campaigns. It would also be interesting to investigate possible future changes in, for example, wintertime stability on Arctic air pollution.

In summary, regional models are very useful tools and can be used for detailed case studies to identify important sources and processes influencing Arctic aerosols. The findings can be used to improve global models, which are used to investigate the long-term effects of Arctic air pollution on air quality and climate under different emission scenarios, which is important for policymakers.

Appendix A

Appendix Chapter 4

A.1

Following *Monaghan et al. (2018a)*, NOAH-MP parameter file MPTABLE.TBL has been modified, and it can be used for simulations over Alaska. These modifications improved the model's capability to capture cold surface temperature and meteorological profiles (e.g. wind speed, relative humidity, temperature) over Alaska.

A.2

Fuentes size-resolved sea-spray source flux

$$\frac{dF_{\mathrm{o}}}{dlogD_{\mathrm{po}}} = \frac{dF_{\mathrm{p}}}{dlogD_{\mathrm{po}}} \times \mathrm{W} = \frac{Q}{A_{\mathrm{b}}} \times \frac{dN_{\mathrm{T}}}{dlogD_{\mathrm{po}}} \times \mathrm{W} \tag{A.1}$$

where W(U) is Monahan and O'Muircheartaigh whitecap coverage, $dF_p/dlogD_{p0}$ is the size-resolved particle flux per unit time and water surface covered by bubbles, D_{p0} is the dry diameters, Q is the sweep air flow, A_b is the total surface area covered by bubbles, $dNT/dlogD_{p0}$ is the particle size distribution (the sum of four log-normal modes) and is equal to:

$$\frac{dN_{\mathrm{T}}}{dlogD_{\mathrm{po}}} = \sum_{i=1}^{4} \frac{dN_{\mathrm{T,i}}}{dlogD_{\mathrm{po}}} = \sum_{i=1}^{4} \frac{N_{\mathrm{T,i}}}{\sqrt{2\pi} \times \log\sigma_{\mathrm{i}}} \times exp[-\frac{1}{2} \times (\frac{log\frac{D_{\mathrm{po}}}{D_{\mathrm{pog,i}}}}{log\sigma_{\mathrm{i}}})^2] \tag{A.2}$$

where i is the sub-index for the mode number and N_i, $D_{p0g,i}$ and σ_i are the total particle number, geometric mean and geometric standard deviation for each log-normal mode. $N_{T,i}$

Table A.1: *Land Surface model's (NOAH MP) parametrisation. "Opt_" indicates the namelist option for NOAH MP.*

NOAH MP parametrisation	
Dynamic Vegetation (DVEG)	On
Stomatal Resistance	Ball-Berry *Ball et al. (1987)*, *Collatz et al. (1991)*, *Collatz et al. (1992)*, *Bonan (1996)*, *Sellers et al. (1996)*
Surface layer drag coefficient (opt_sfc)	Original Noah *Chen et al. (1997)*
Soil moisture for stomatal resistance (opt_btr)	Noah (soil moisture)
Runoff (opt_run)	TOPMODEL with groundwater *Niu et al. (2007)*
Supercooled liquid water (opt_frz)	no iteration *Niu and Yang (2004)*
Soil permeability (opt_inf)	linear effects, more permeable *yue Niu and liang Yang (2006)*
Radiative transfer (opt_rad)	modified two-stream (gap = F(solar angle, 3D structure ...)<1-FVEG) *Yang and Friedl (2003)*, *Niu and Yang (2004)*
Ground surface albedo (opt_alb)	BATS *Yang Z.-L. and Vinnikov. (1997)*
Precipitation (snow/rain) partitioning (opt_snf)	*Jordan (1991)*
Soil temperature lower boundary (opt_tbot)	TBOT at ZBOT (8m) read from a file (original Noah)
Soil/snow temperature time scheme (opt_sfc)	semi-implicit; flux top boundary condition
Surface resistance to evaporation/sublimation (opt_rsf)	*Sakaguchi and Zeng (2009)*
Glacier treatment (opt_gla)	include phase change of ice

and $D_{p0g,i}$ are depending on parameters a_i and β_i derived from polynomial and exponential regressions defining the total particle number and geometric mean diameter of the log-normal modes, and can be found in Table 5 *Fuentes et al. (2010)*.

A.3

In this APPENDIX, the biases and RMSEs are calculated for each site, as shown in **Fig. 1**, and are shown in the tables below. Each table corresponds to a site and for the available observed aerosol concentrations, such as Na^+, Cl^-, SO_4^{2-} (total and non-sea component), NO_3^-, NH_4^+ and OC. Bias is calculated as the difference between model simulation and observation.

Table A.2: *Biases and RMSEs, in μ g m^{-3}, are calculated for aerosols at the Alert, Canada, during January and February 2014 and for CONTROL and HEM_NEW simulations at 100km.*

	CONTROL		HEM_NEW	
	Bias	**RMSE**	**Bias**	**RMSE**
$\mathbf{Na^+}$	0.81	0.91	0.12	0.18
$\mathbf{Cl^-}$	1.05	1.2	-0.03	0.19
$\mathbf{NO_3^-}$	0.28	0.30	0.25	0.22
$\mathbf{NH_4^+}$	-0.003	0.01072	0.007	0.01079
$\mathbf{SO_4^{2-}}$	0.06	0.1	0.02	0.11

Table A.3: *Biases and RMSEs, in μ g m^{-3}, are calculated for aerosols at Villum Research station, Greenland, during January and February 2014 and for CONTROL and HEM_NEW simulations at 100km.*

	CONTROL		HEM_NEW	
	Bias	**RMSE**	**Bias**	**RMSE**
$\mathbf{Na^+}$	1.3	1.4	0.25	0.26
$\mathbf{Cl^-}$	1.9	2.1	0.22	0.24
$\mathbf{NO_3^-}$	0.25	0.26	0.17	0.19
$\mathbf{NH_4^+}$	-0.001	0.006	0.01	0.01
$\mathbf{SO_4^{2-}}$	0.05	0.1	0.08	0.1

Table A.4: *Biases and RMSEs, in μ g m^{-3}, are calculated for aerosols at Zeppelin, Norway, during January and February 2014 and for CONTROL and HEM_NEW simulations at 100km.*

	CONTROL		HEM_NEW	
	Bias	**RMSE**	**Bias**	**RMSE**
$\mathbf{Na^+}$	3.31	4.4	0.36	0.78
$\mathbf{Cl^-}$	4.86	6.48	0.22	0.73
$\mathbf{NO_3^-}$	0.13	0.36	0.01	0.29
$\mathbf{NH_4^+}$	-0.03	0.077	-0.02	0.076
$\mathbf{SO_4^{2-}}$	0.16	0.25	0.32	0.45

A.4

Surface observations are used to validate the meteorological conditions that occur over Utqiaġvik and Alaska in wintertime. See also discussion in sub-section 4.5.1 in the main text. The model is validated against the surface (hourly) observations obtained from National Oceanic and Atmospheric Administration / Earth System Research Laboratory / Global Monitoring Division (NOAA/ESRL/GMD) Baseline Observatories. Also, radiosondes data

Table A.5: *Biases and RMSEs, in μ g m^{-3}, are calculated for aerosols at Simeonof, south of Alaska, during January and February 2014 and for CONTROL and HEM_NEW simulations at 100km.*

	CONTROL		HEM_NEW	
	Bias	**RMSE**	**Bias**	**RMSE**
Na^+	1.4	2.5	0.3	0.6
Cl^-	2.0	3.7	0.1	0.7
NO_3^-	0.12	0.23	0.08	0.20
SO_4^{2-}	-0.2	0.25	-0.05	0.26
OA	-0.08	0.1	-0.05	0.08

Table A.6: *Biases and RMSEs, in μ g m^{-3}, are calculated for aerosols at Gates of the Arctic, south of Alaska, during January and February 2014 and for CONTROL and HEM_NEW simulations at 100km.*

	CONTROL		HEM_NEW	
	Bias	**RMSE**	**Bias**	**RMSE**
Na^+	0.6	0.9	0.2	0.3
Cl^-	0.7	1.2	0.1	0.3
NO_3^-	0.3	0.3	0.2	0.2
SO_4^{2-}	-0.04	0.2	-0.1	0.2
OA	-0.24	0.28	-0.21	0.26

are used to evaluate the model's performance at different altitudes. Radiosonde data (every 12h) are derived from Integrated Global Radiosonde Archive version 2 (IGRA 2) (*Durre et al. (2018)*). Site is located at latitude: 71.28 and longitude: -156.78.

Table A.7: *Biases and RMSEs, in μ g m^{-3}, are calculated for super-micron aerosols at Utqiaġvik, north of Alaska, during January and February 2014 and CONTROL and HEM_NEW simulations at 100km.*

	CONTROL		HEM_NEW	
	Bias	**RMSE**	**Bias**	**RMSE**
Na^+	0.3	0.37	-0.07	0.25
Cl^-	0.27	0.48	-0.26	0.51
NO_3^-	0.26	0.3	0.13	0.17
$NH4_4^+$	-0.0004	0.00368	-0.001	0.0037
$SO4_4^{2-}$	0.005	0.005	-0.01	0.06

Table A.8: *Biases and RMSEs, in μ g m^{-3}, are calculated for sub-micron aerosols at Utqiaġvik, north of Alaska, during January and February 2014 and CONTROL and HEM_NEW simulations at 100km.*

	CONTROL		**HEM_NEW**	
	Bias	**RMSE**	**Bias**	**RMSE**
Na^+	-0.485	0.66	-0.489	0.67
Cl^-	-0.116	0.361	-0.124	0.364
NO_3^-	-0.065	0.162	-0.054	0.158
NH_4^+	-0.069	0.106	-0.057	0.100
SO_4^{2-}	-0.621	0.875	-0.591	0.853

Table A.9: *Biases and RMSEs, in μ g m^{-3}, are calculated between ALASKA_NEW_JAN, ALASKA_NEW_FEB and in-situ meteorological parameters derived from NOAA Baseline Observatories during the campaign's periods in January and February 2014. Bias was calculated as the difference between model simulation and observations.*

	January campaign		February campaign	
	Bias	RMSE	Bias	RMSE
2m Temperature	0.1	1.9	-1.0	3.2
10m Temperature	-0.03	1.8	-0.66	2.7
10m Wind speed	0.08	1,4	-0.33	1.7
10m Wind direction	-11.2	13.2	-11.2	39.0

A.5

Here the bias and RMSE are shown between ALASKA_NEW_JAN and ALASKA_NEW_FEB and the observations for Utqiaġvik at 20km.

Table A.10: *Biases and RMSEs, in μ g m^{-3}, are calculated for aerosols at Utqiaġvik, north of Alaska, during January 2014 and for ALASKA_CONTROL_JAN and ALASKA_NEW_JAN simulations at 20km.*

	ALASKA_CONTROL_JAN		**ALASKA_NEW_JAN**	
	Bias	**RMSE**	**Bias**	**RMSE**
Na^+	-0.31	0.38	-0.16	0.26
Cl^-	-0.50	0.59	-0.33	0.43
NO_3^-	-0.040	0.07	0.039	0.09
SO_4^{2-}	-0.396	0.414	-0.398	0.417
NH_4^+	-0.033	0.038	-0.035	0.040

A.6

This APPENDIX shows the comparison for the Gates of the Arctic site at 20 km, for ALASKA_NEW_FEB and

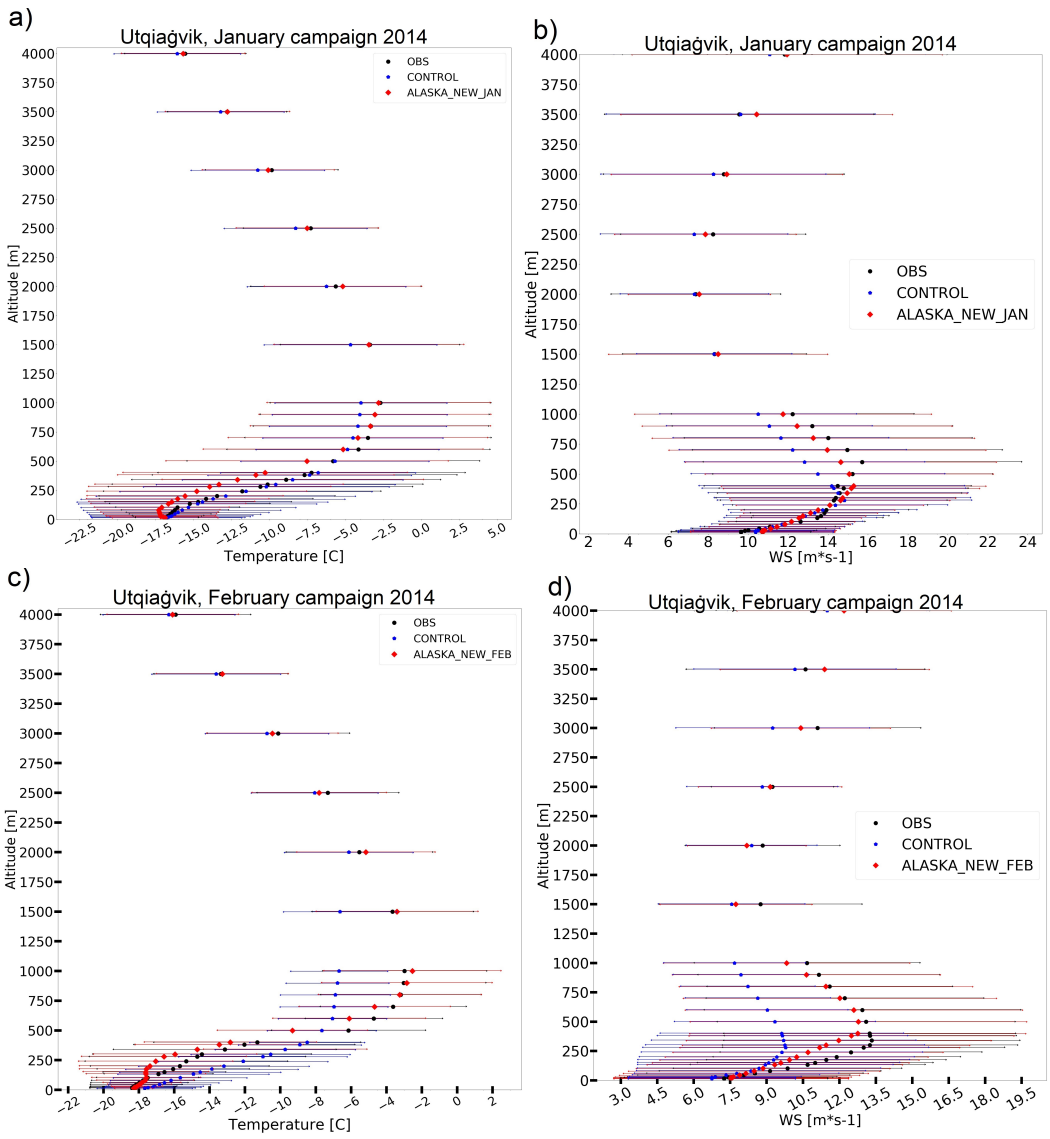

Figure A.1: *Average temperatures, in degrees C, and wind speeds, in ms^{-1}, as a function of altitude (m), up to 4km, during (a,b) January and (c,d) February campaign in 2014, at Utqiaġvik, Alaska. The observations are shown in black (circle). The blue pentagon shows the model results for the CONTROL simulation (at 100km) and the red diamond shows the model results for the NEW_ALASKA_JAN and NEW_ALASKA_FEB simulation. Observations are derived from IGRA2 and are available every 12h (0Z and 12Z, UTC). For the comparison, model output at 0 and 12Z UTC are used. The corresponding horizontal lines show the standard deviation.*

ALASKA_CONTROL_FEB. The observations are only available for the February campaign, daily averaged in local Alaskan time every three days.

Also, the table below shows biases and RMSEs, in μ g m^{-3}, for all available aerosol species at the Gates of the Arctic.

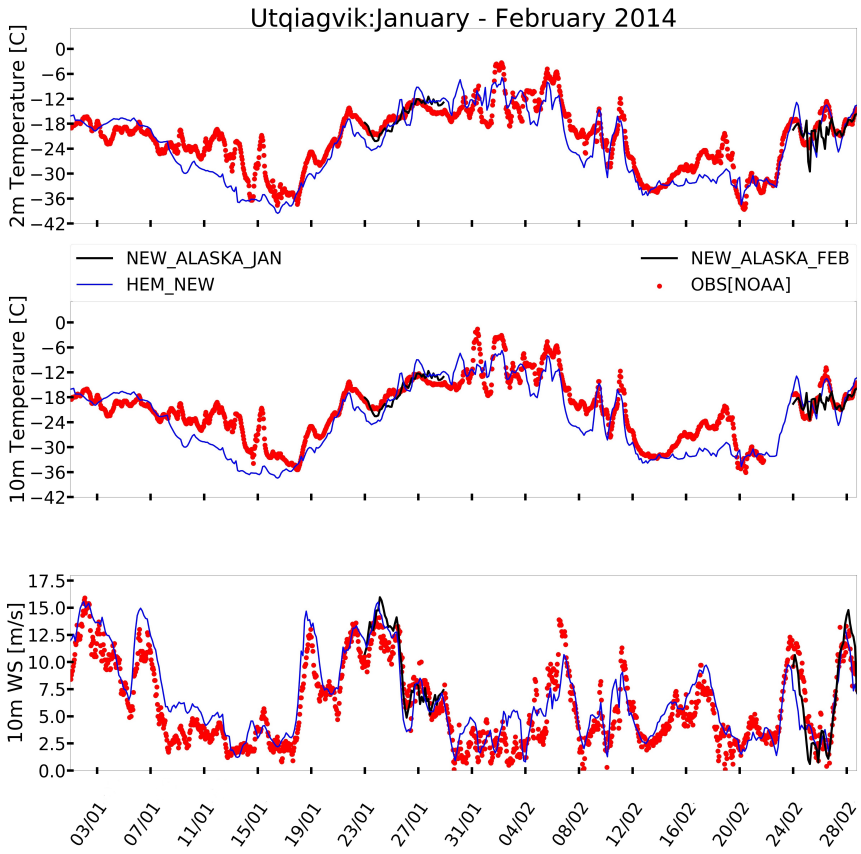

Figure A.2: *Time series of observed and modelled 2m and 10m temperature, and 10m wind speed, at Utqiaġvik, Alaska, in UTC. The observations are shown in red and derived from the NOAA observatory. The blue line shows the results for the HEM_NEW simulation at 100km, while the black line shows the results for ALASKA_NEW_JAN and ALASKA_NEW_FEB simulations at 20km. The observations are hourly, while the model output is every 3h.*

Table A.11: *Biases and RMSEs, in μ g m^{-3}, calculated for aerosols at Utqiaġvik, north of Alaska, during February 2014 and for ALASKA_CONTROL_FEB and ALASKA_NEW_FEB simulations at 20km.*

	ALASKA_CONTROL_FEB		ALASKA_NEW_FEB	
	Bias	**RMSE**	**Bias**	**RMSE**
$\mathbf{Na^+}$	-1.29	1.40	-1.18	1.30
$\mathbf{Cl^-}$	-1.90	1.92	-1.78	1.80
$\mathbf{NO_3^-}$	-0.20	0.40	-0.11	0.38
$\mathbf{SO_4^{2-}}$	-1.019	1.322	-1.020	1.326
$\mathbf{NH_4^+}$	-0.045	0.097	-0.043	0.10

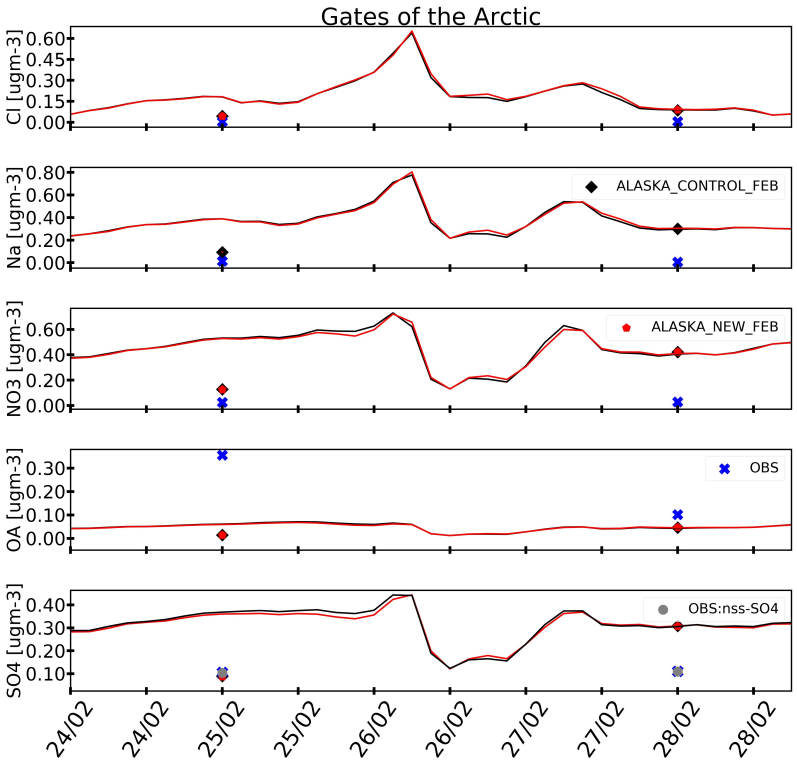

Figure A.3: *Model inter-variability during February campaign. Model simulations are validated against aerosols at the gates of the Arctic site, north of Alaska. The black line shows ALASKA_CONTROL_FEB simulation and the black symbol the daily averaged values. The red line shows ALASKA_NEW_FEB simulation and the red pentagon the daily averaged values. The blue star indicates averaged daily observations. Observations and model are in local Alaskan time. Observed and modelled SO_4^{2-} is total SO_4^{2-}.*

Table A.12: *Biases and RMSEs, in μ g m^{-3}, are calculated for aerosols at Gates of the Arctic, north of Alaska, during February campaign and for ALASKA_CONTROL_FEB and ALASKA_NEW_FEB simulations at 20km.*

	ALASKA_CONTROL_FEB		ALASKA_NEW_FEB	
	Bias	**RMSE**	**Bias**	**RMSE**
Na^+	0.344	0.346	0.342	0.341
Cl^-	0.155	0.1578	0.154	0.1573
NO_3^-	0.47	0.48	0.42	0.47
SO_4^{2-}	0.24	0.24	0.23	0.23
OA	-0.198	0.2446	-0.197	0.2445

Appendix B

Appendix Chapter 5

B.1

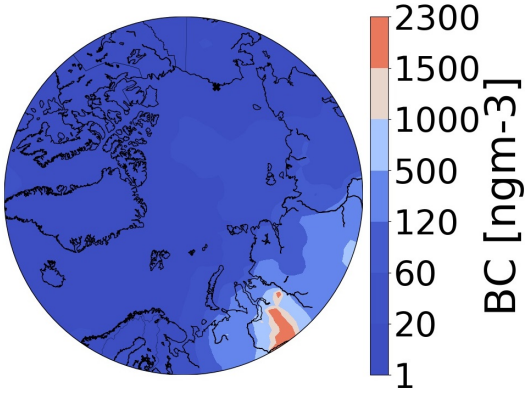

Figure B.1: *Modelled averaged BC, in ngm^{-3}, at the surface and using the CONTROL zooming over the Arctic, during January and February 2014.*

Table B.1: *Average percentage (%) BC change in January - February 2014, due to wet deposition at 2, 4, 6 and 8 km and at four remote Arctic sites. BC change is calculated as in Table 5.3 (see main text).*

	2km	4km	6km	8km
Utqiaġvik	353	353	325	252
Alert	592	449	399	275
Tiksi	456	344	304	230
Zeppelin	769	623	499	367

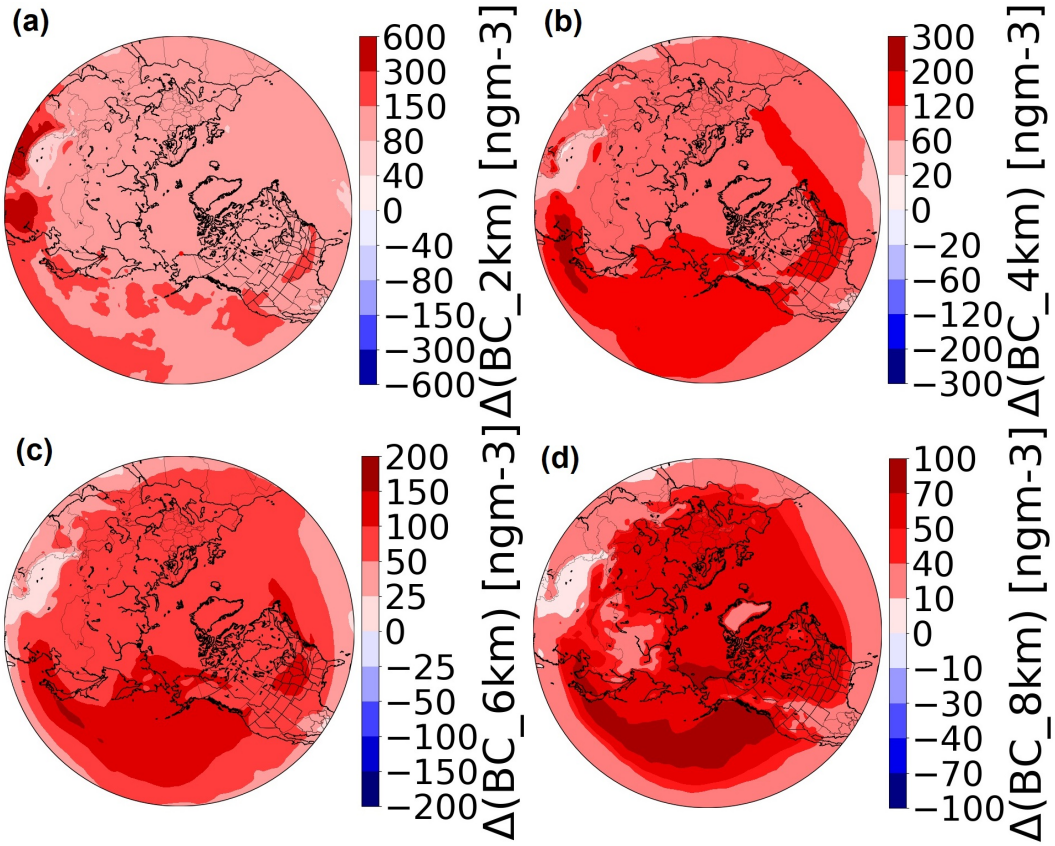

Figure B.2: *Modelled BC averaged differences, in ngm^{-3}, between WET_DEP_OFF and CONTROL at (a) 2km, (b) 4km, (c) 6km and (d) 8km, during January and February 2014.*

Table B.2: *Absolute changes on BC, in ngm^{-3}, in January - February 2014, due to wet deposition at 2, 4, 6 and 8 km and at four remote Arctic sites. Absolute change is calculated as the average differences between the WET_DEP_OFF and CONTROL simulations.*

	2km	4km	6km	8km
Utqiaġvik	138	171	165	151
Alert	113	100	80	52
Tiksi	136	170	185	148
Zeppelin	138	154	163	156

B.2

Evaluation of ALASKA_CONTROL, METEO against in-situ observations and radiosondes at Utqiaġvik, Alaska. The in-situ observations are from National Oceanic and Atmospheric Administration/ Earth System Research Laboratories/ Global Monitoring Laboratory(NOAA/ESRL/GMD) Baseline Observatories Barrow. Radiosonde data is from Integrated Global Radiosonde Archive (IGRA) Version 2 and they are available every 12h. All

the observations are in UTC. Figure B.2 shows the time series of hourly 2 m and 10 m temperatures, 10 m winds speed and winds direction us compared against ALASKA_CONTROL and METEO at 20 km between 23 and 28 January 2014.

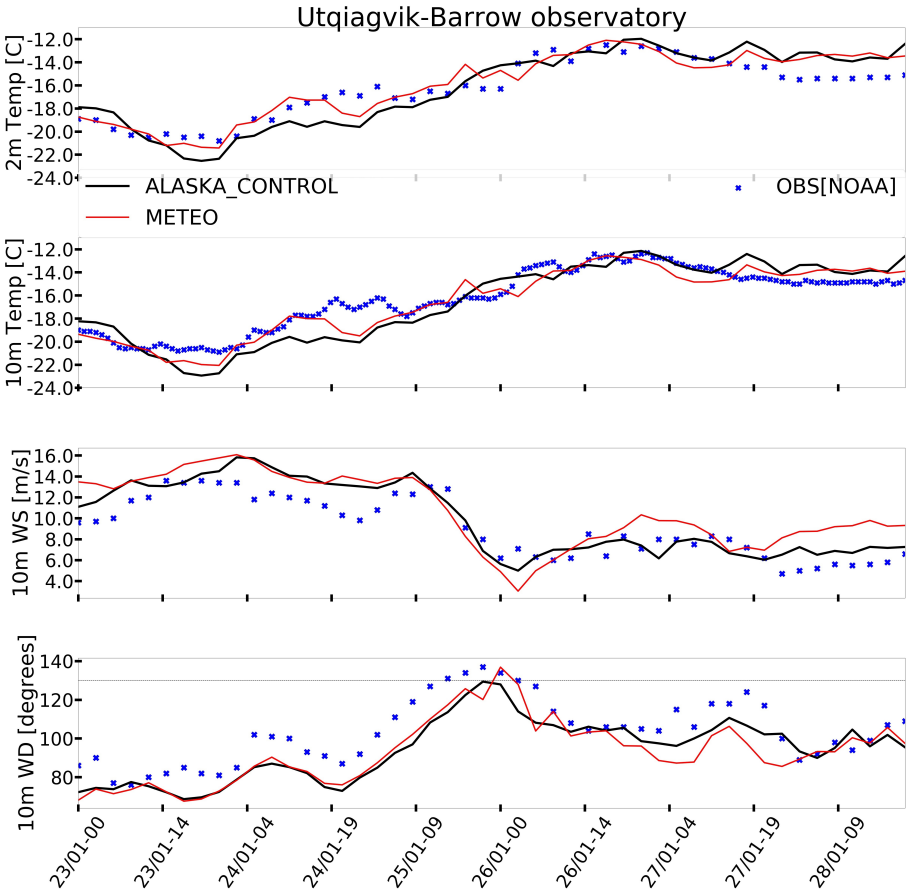

Figure B.3: *Time series of 2m and 10m temperature, 10m wind speed and wind direction during 23-28 January 2014, at Barrow observatory, at Utqiaġvik, Alaska. The black line shows the model results for ALASKA_CONTROL simulation and the red line for METEO. Observations, in blue, are hourly data, while model output is every 3h. Both are in UTC.*

Table B.3: *Statistical analysis between ALASKA_CONTROL, METEO and in-situ meteorological parameters, which derived from NOAA Baseline Observatories, during January simulation. Bias is calculated as the difference between model simulation and observations.*

	ALASKA_CONTROL		METEO	
	Bias	RMSE	Bias	RMSE
2m Temperature	0.05	1.45	0.31	1.1
10m Temperature	-0.26	1.40	-0.25	1.01
10m Wind speed	0.86	1.63	1.6	2.46
10m Wind direction	-9.45	11.91	-10.70	13.32

Precipitation data obtained from Applied Climate Information System, NOAA Regional

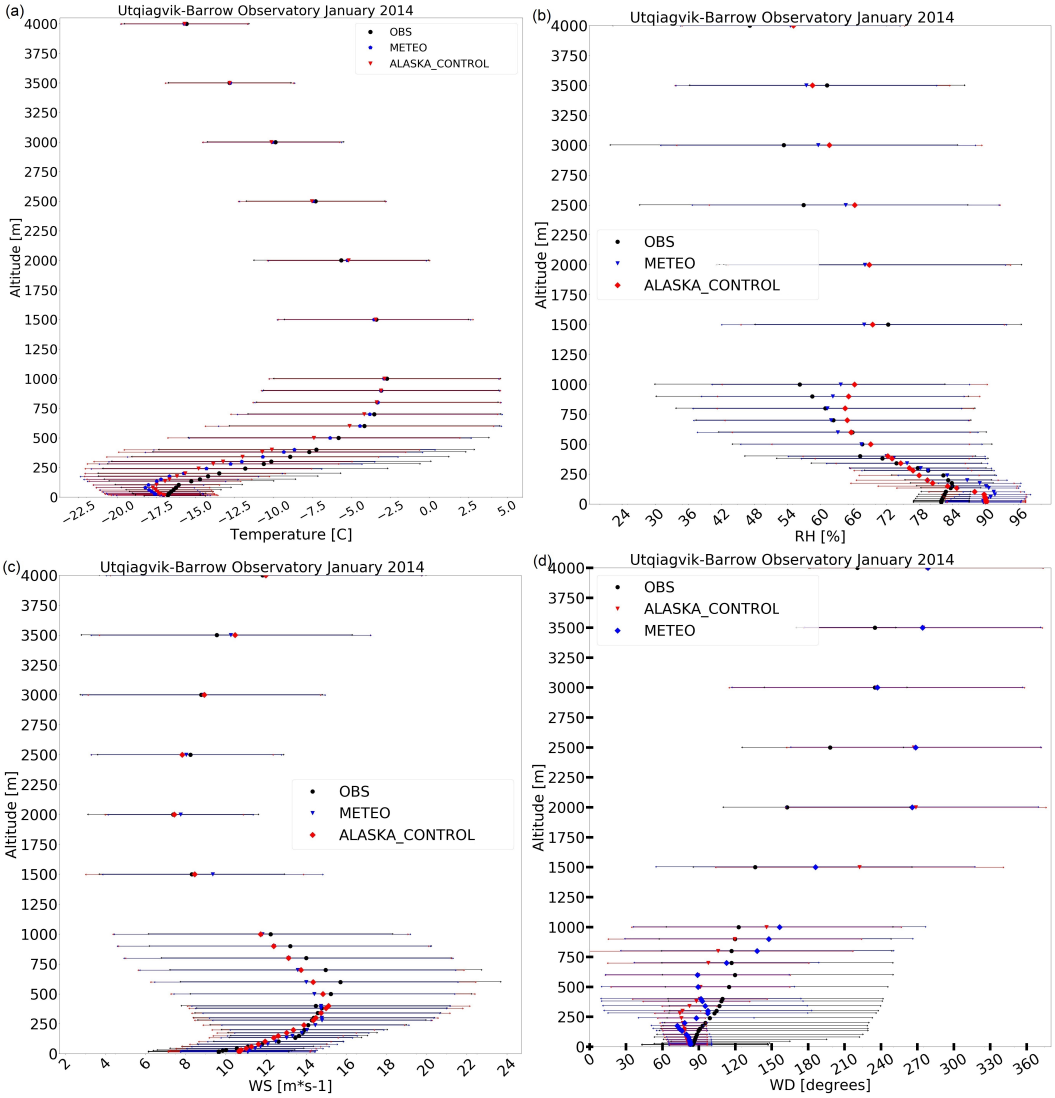

Figure B.4: *Radiosondes for (a) temperature, (b) relative humidity (RH), (c) wind speed and (d) wind direction at Utqiaġvik, Alaska. The red diamond shows the average values for ALASKA_CONTROL simulation and the blue triangle for METEO. Observations are shown in black circle. The corresponding lines show the standard deviation. (b) and (d) show calculated bias, as the mean difference between each simulation and the observations for temperature and RH, respectively at different altitudes.*

Climate Centers and used in this study to validate METEO and ALASKA_CONTROL runs. Three sites across the domain in northern Alaska are used. At Nome (coastal site, west of Alaska) and Fairbanks an event of precipitation and snowfall were observed at 24 January, while a precipitation (snow) even were observed at Barrow at 25 January (in UTC). At all sites, both simulations underestimate observed precipitation and snowfall by up to 2.5 and 20 mm (not shown here). At Barrow both simulations capture quite well observed precipitation peak (0.75 mm), with METEO performing slightly better (more precipitation) than ALASKA_CONTROL (0.1 mm differences).

Résumé long en français

La pollution atmosphérique est un problème qui affecte la santé humaine depuis les premières années de l'histoire de l'humanité *(Fowler et al., 2020)*. Au cours de la révolution industrielle, et en raison de l'utilisation considérable du charbon, des problèmes de qualité de l'air ont commencé à apparaître, comme le Grand Smog de 1952 *(Wang et al., 2016)*. La combustion du charbon était le principal responsable de la pollution atmosphérique et des principaux polluants, tels que le dioxyde de soufre (SO_2) et les oxydes d'azote (NO_x). La pollution atmosphérique touche encore des millions de personnes, en particulier dans les villes, comme Pékin en Chine, où elle dépasse souvent les recommandations de l'OMS en matière de qualité de l'air. L'OMS estime que 8,8 millions de personnes meurent chaque année à cause de la pollution de l'air intérieur et extérieur.

Au cours de la décennie 2011-2020, la température moyenne à la surface du globe a augmenté de 1,09 °C par rapport à la période 1850-1900, et l'on sait désormais que ce réchauffement, qui ne s'est pas produit partout de la même manière, est dû à l'activité humaine *(IPCC, 2021)* en raison des émissions anthropiques telles que le transport, la combustion de combustibles fossiles pour le chauffage et la production d'électricité *(Szopa et al., 2021; Wang et al., 2022)*. L'augmentation des émissions anthropiques a entraîné une augmentation des qui réchauffent l'atmosphère, principalement le CO_2, mais aussi le méthane (CH_4), l'ozone (O_3) et le protoxyde d'azote (N_2O) *(AMAP, 2015; Szopa et al., 2021)*. Par exemple, selon NOAA, IPCC et WMO, le CO les niveaux de CO_4 dans l'atmosphère représentent 149% du niveau préindustriel, tandis que les niveaux de CH_4 représentent environ 156% des niveaux de 1750.

Les polluants atmosphériques agissent également comme des forçeurs climatiques à courte durée de vie (SLCFs) puisqu'ils contribuent au réchauffement de l'atmosphère. Il s'agit notamment des aérosols, en particulier le carbone suie (BC), et des GES, notamment le CH_4 et l'O_3 troposphérique (par exemple *Bindoff et al. (2013)*,*Szopa et al. (2021)*). Les SLCFs n'agissent pas uniformément (refroidissement ou réchauffement) partout. Le BC provoque un forçage radiatif positif (réchauffement) à l'échelle planétaire *(Bond et al., 2013a)*. D'autres aérosols (également des SLCF), et en particulier les sulfates (SO_4^{2-}), ont compensé le réchauffement de la planète car ils réfléchissent le rayonnement solaire et refroidissent le climat *(Horowitz et al., 2020; Masson-Delmotte et al., 2021; Szopa et al., 2021)*.

L'Arctique se réchauffe plus rapidement que toute autre région de la planète, les températures de surface augmentant plus de deux fois par rapport à la moyenne mondiale. En plus du CO, les SLCFs contribuent au réchauffement de l'Arctique, en particulier le BC et le CH_4. *(IPCC, 2021; AMAP, 2021)*. L'ozone troposphérique contribue également au réchauf-

fement de l'Arctique, y compris celui produit par l'oxydation du CH_4 *(AMAP, 2021)*. Les SLCFs contribuent au réchauffement de l'Arctique, soit directement dans l'Arctique, soit à la suite d'un réchauffement plus au sud dû au transport de chaleur. Le BC déposé sur la neige dans l'Arctique entraîne également un réchauffement supplémentaire puisqu'il accélère la fonte de la neige en absorbant le rayonnement solaire *(AMAP, 2015)*. Une augmentation des polluants atmosphériques pourrait également entraîner une augmentation du réchauffement de la surface de l'Arctique par le biais des effets indirects des nuages et des aérosols *(AMAP, 2015)*. Les premiers rapports, comme celui de *Brøgger (1881)*, et les études menées au cours du siècle dernier ont montré que la pollution atmosphérique arctique provenant principalement des régions de latitude moyenne est transportée dans l'Arctique en hiver et au printemps *(Rahn and McCaffrey, 1980; Quinn et al., 2002b)*, un phénomène appelé brume arctique. Cependant, au cours des 20 à 30 dernières années, les émissions des latitudes moyennes ont diminué en raison des réglementations, notamment en Europe et en Amérique du Nord (par exemple *Sharma et al. (2019)*,*Szopa et al. (2021)*). Dans le même temps, il est devenu évident qu'il existe d'importantes sources locales dans l'Arctique, qui pourraient augmenter à l'avenir, en raison du réchauffement futur et de l'augmentation de l'activité humaine *(Schmale et al., 2018)*. Le réchauffement de l'Arctique est le plus important en automne/hiver et les effets radiatifs indirects des aérosols sont plus forts en hiver *(Boisvert and Stroeve, 2015; AMAP, 2015)*. Cependant, la pollution atmosphérique hivernale est moins étudiée que celle des autres saisons, et des incertitudes subsistent quant aux sources locales et à la mesure dans laquelle elles contribuent à la pollution atmosphérique dans l'Arctique et à leur effet sur le réchauffement de l'Arctique *(AMAP, 2015; Schmale et al., 2018)*. Par exemple, en raison des conditions très froides de l'hiver arctique, l'utilisation de combustibles fossiles, par exemple pour le chauffage domestique/commercial et les activités industrielles, est considérable *(Simpson et al., 2019)*. Une nouvelle augmentation de la population de la Terre et d'éventuels mouvements de population vers des latitudes plus élevées en raison du réchauffement climatique en cours pourraient accroître la demande de développement industriel dans l'Arctique, comme l'extraction des ressources *(AMAP, 2021; IPCC, 2021)*. Il est donc essentiel d'améliorer la quantification des émissions locales et des processus influençant la composition de l'atmosphère arctique en hiver afin de mieux communiquer aux décideurs politiques les actions nécessaires pour réduire les impacts locaux sur la qualité de l'air et le climat *(AMAP, 2021)*.

Les modèles sont les outils utilisés pour étudier la pollution atmosphérique et ses impacts. Cependant, les modèles ont encore des difficultés à simuler le cycle saisonnier des gaz à l'état de traces et des aérosols naturels et anthropiques dans l'Arctique, et sous-estiment souvent la composition des aérosols observée pendant l'hiver sur des sites arc-

tiques éloignés *(Eckhardt et al., 2015; Whaley et al., 2022b)*. Par exemple, les modèles ont tendance à manquer de mécanismes essentiels à la production d'aérosols de sel marin (SSA) non seulement pendant l'été, mais aussi pendant l'hiver. D'autres incertitudes dans les modèles sont liées aux traitements de dépôts sec et humide, par exemple *Mahmood et al. (2016)*, *Shen et al. (2017)*. Il est important de mieux quantifier l'effet sur les aérosols dans l'Arctique afin d'améliorer ces processus dans les modèles. En outre, les modèles peuvent ne pas tenir compte de réactions et de voies importantes pour la formation d'aérosols secondaires en hiver. Les incertitudes relatives aux émissions anthropiques ainsi que les processus influençant les émissions naturelles contribuent également aux biais et aux incertitudes des modèles.

Compte tenu du contexte général décrit ci-dessus, l'objectif global de cette thèse est d'améliorer notre compréhension de la pollution atmosphérique locale et lointaine de l'Arctique en hiver. Ces principales questions scientifiques sont abordées dans cette thèse :

(i) Quelle est la contribution des sources naturelles et anthropiques à la composition des aérosols pendant l'hiver arctique ? Les modèles peuvent-ils simuler la composition des aérosols en hiver dans l'Arctique ?

(ii) Quelle est la sensibilité des aérosols modélisés aux traitements de dépôt et aux processus physiques pendant l'hiver ?

(iii) Dans quelle mesure les sources anthropiques locales de l'Arctique contribuent-elles à la composition de l'atmosphère en hiver ?

Dans cette thèse, le modèle de transport régional, couplé à la chimie WRF-Chem est utilisé *(Grell et al., 2005; Fast et al., 2006; Marelle et al., 2017)*. Le modèle est exécuté à l'échelle quasi-hémisphérique et évalué par rapport aux observations sur le grand Arctique pour les hivers 2014 et 2019. Il a également été exécuté pour des périodes plus courtes au-dessus de l'Alaska et évalué par rapport aux données recueillies lors de campagnes de terrain au-dessus du nord de l'Alaska en janvier et février 2014 *(Kirpes et al., 2018)* et du centre de l'Alaska en novembre et décembre 2019 *(Simpson et al., 2019; Maillard et al., 2022)*. Les sensibilités du modèle aux émissions, aux traitements d'élimination et à la dynamique de la couche limite sont examinées, y compris les améliorations apportées aux aérosols SSA, en particulier.

Cette thèse est organisée comme suit. Le chapitre 1 introduit le contexte scientifique et la motivation de cette thèse. Il décrit le réchauffement de l'Arctique et la circulation atmosphérique liée aux principales voies de transport des masses d'air des latitudes moyennes vers l'Arctique, ainsi que les sources éloignées (hors de l'Arctique) et locales dans le cercle

polaire. Le contexte scientifique lié à l'Alaska, objet de cette thèse, est également décrit. Le chapitre 2 présente les aérosols troposphériques, y compris les aérosols anthropiques et naturels, leurs précurseurs et leurs émissions, en se concentrant sur l'Arctique. Ce chapitre décrit également les propriétés et les processus des aérosols. Le chapitre 3 décrit les principaux outils utilisés dans cette thèse, à savoir le modèle, y compris les principaux paramétrages de physique et de chimie, les inventaires d'émissions, ainsi que les observations et les campagnes de terrain. Les chapitres 4, 5 et 6 présentent les principaux résultats de cette thèse.

Le chapitre 4 présente une étude sur la pollution atmosphérique hivernale dans le grand Arctique et au-dessus du nord de l'Alaska, en se concentrant sur la contribution des aérosols inorganiques et, en particulier, des aérosols SSA à la charge aérosol totale de l'Arctique. La capacité du modèle à capturer les aérosols anthropogéniques et naturels de fond dans le grand Arctique, y compris en Alaska, est évaluée. Cette étude se concentre sur les aérosols SSA, et en particulier sur les processus physiques qui influencent leurs émissions dans l'Arctique et dans le nord de l'Alaska en hiver. Ce chapitre a été soumis comme *(Ioannidis et al., 2022)*.

Le chapitre 5 étudie les processus et les sources qui affectent le BC modélisé dans l'Arctique. La sensibilité à l'élimination humide et sèche est examinée sur l'ensemble de l'Arctique ainsi que sur le nord de l'Alaska. L'influence des émissions anthropiques régionales et locales de l'Alaska, telles que celles liées à l'extraction pétrolière dans le nord de l'Alaska, est également examinée (Ioannidis et al. 2022, à soumettre).

Le chapitre 6 présente une étude axée sur la pollution urbaine locale à Fairbanks, au centre de l'Alaska, pendant la campagne préALPACA (hiver 2019). La capacité du modèle à capturer les aérosols de fond sur l'Alaska, et sur Fairbanks, est étudiée. Les incertitudes liées aux traitements d'élimination, à la dynamique de la couche limite et aux émissions de précurseurs d'aérosols sont étudiées. Ces derniers sont utilisés comme indicateur pour examiner dans quelle mesure le modèle peut manquer la formation d'aérosols secondaires en hiver.

Le chapitre 7 résume les principaux résultats de cette étude et discute des perspectives futures.

Conclusions: L'Arctique se réchauffe plus rapidement que le reste du monde et ce réchauffement est plus marqué en automne et en hiver. Ainsi, malgré le fait que les émissions anthropiques sont en baisse depuis 20-30 ans aux latitudes moyennes, il existe d'importantes sources locales de pollution atmosphérique dans l'Arctique qui pourraient augmenter à l'avenir en raison du réchauffement climatique en cours. Cette thèse se concentre sur l'amélioration de notre compréhension des sources anthropiques et naturelles, locales et

éloignées, et des processus qui influencent les aérosols dans l'Arctique pendant l'hiver. Pour ce faire, le modèle régional de transport d'aérosols chimiques WRF-Chem est exécuté à l'échelle quasi-hémisphérique et à l'échelle régionale sur le centre et le nord de l'Alaska, pour des périodes correspondant à deux campagnes de terrain. Trois questions scientifiques principales sont abordées dans cette thèse, comme indiqué dans l'introduction. Les principaux résultats sont discutés ci-dessous.

(i) *Quelle est la contribution des sources naturelles et anthropiques à la composition des aérosols pendant l'hiver arctique ? Les modèles peuvent-ils simuler la composition des aérosols en hiver dans l'Arctique ?*

Les simulations WRF-Chem sont utilisées pour étudier la composition des aérosols en hiver. L'évaluation des composants des aérosols au-dessus du grand Arctique et du centre/nord de l'Alaska montre que les aérosols anthropiques, et en particulier le BC et le SO_4^{2-}, contribuent à la charge totale des aérosols, car ils présentent des concentrations massiques élevées, notamment dans les régions où les émissions locales sont importantes. L'OA anthropique est également un composant aérosol important dans les sites arctiques éloignés pendant l'hiver, avec des concentrations élevées en même temps que les aérosols naturels.

Dans cette thèse, la contribution des SSA est examinée car ils sont une composante importante de la brume arctique pendant l'hiver, sur la base des résultats d'études récentes basées sur l'observation (Chapitre 4). La représentation modélisée des émissions de SSA est améliorée et utilisée pour estimer que les SSA contribuent entre 44% et 85% aux aérosols de mode fin et grossier, respectivement par rapport aux autres aérosols inorganiques (SO_4^{2-}, NH_4^+ NO_3^-) sur des sites côtiers éloignés de l'Arctique pendant l'hiver 2014. L'étude présentée au chapitre 4 montre également qu'il est important d'inclure l'OA marin même pendant l'hiver où il contribue à l'OA total sur les sites côtiers arctiques et subarctiques. Cette étude a été motivée par des observations de terrain montrant des OA marin importants associé aux SSA et des chenaux ouverts sur le site côtier de Barrow (Utqiaġvik) au nord de l'Alaska, qui sont généralement absents des modèles.

Un des objectifs de cette thèse est de comprendre les raisons possibles des divergences entre les modèles et les observations en hiver arctique. Une analyse détaillée des performances des modèles sur l'Arctique pendant les hivers 2014 et 2019 est présentée. La version initiale de WRF-Chem utilisée dans cette thèse a surestimé les SSA en mode supermicronique et grossier, jusqu'à un facteur 3-4 sur les sites côtiers de l'Arctique, tandis que le modèle a sous-estimé l'OA et le SO_4^{2-}. L'amélioration des traitements par le modèle des émissions de SSA, notamment l'utilisation d'une dépendance plus faible de la vitesse du vent (basée sur la fraction de la calotte blanche estimée par satellite), l'inclusion d'une

dépendance de la TSM et d'une source de ss-SO_4^{2-}, ainsi que l'activation d'une source de matières organiques marines, décrite au chapitre 4, conduit à une meilleure représentation des SSA modélisés par rapport aux observations sur les sites arctiques éloignés. Cela a également amélioré la simulation d'autres matières inorganiques, telles que le SO_4^{2-} et le NO_3^-. Cependant, le modèle sous-estime toujours les épisodes avec des concentrations élevées de SSA submicroniques et d'autres matières inorganiques, en particulier le SO_4^{2-} d'origine anthropique, au-dessus du nord de l'Alaska et sur les sites côtiers tels que Barrow, Utqiaġvik, qui ne sont pas entièrement couverts de glace de mer en hiver. Les résultats suggèrent que le modèle manque de sources locales et régionales. L'inclusion des matières organiques marines a amélioré l'OA modélisée sur les sites subarctiques, tels que Simeonof, et l'utilisation du rapport OC:Na^+ comme indicateur de l'OA marin a augmenté l'OA le long de la côte ouest et nord de l'Alaska, conformément aux conclusions de *Kirpes et al. (2018, 2019)*. Ces améliorations pourraient être appliquées dans les simulations sur l'Arctique élargi. Cependant, l'OA modélisée reste faible par rapport aux observations sur l'Alaska, peut-être en raison de l'absence de formation secondaire d'OA ou de la sous-estimation des émissions anthropiques à distance ou au sein de l'Arctique.

Les observations hivernales de l'EBC dans l'Arctique montrent des concentrations élevées sur les sites arctiques éloignés en raison de l'influence de l'Arctic Haze et de la contribution des sources locales et régionales dans l'Arctique (chapitres 5 et 6). Le WRF-Chem sous-estime en moyenne le BC sur sites arctiques éloignés, tels que Tiksi, Utqiaġvik et Alert, mais il capture mieux la variabilité observée à Zeppelin (hiver 2014). Les raisons de ces biais sont étudiées (voir ci-dessous).

La composition modélisée des aérosols aux sites de fond influencés par Arctic Haze est améliorée dans les simulations pour l'hiver 2019, par rapport à l'hiver 2014, en particulier au-dessus de l'Alaska. Plus précisément, les aérosols inorganiques, comme le SO_4^{2-} et le NO_3^-, et le BC, sont mieux simulés au-dessus de l'Alaska pendant l'hiver 2019 par rapport à l'hiver 2014. Cela peut être dû à l'utilisation d'un inventaire des émissions (CAMS) plus à jour pour 2019 (chapitre 6).

(ii) *Quelle est la sensibilité des aérosols modélisés aux traitements d'élimination et aux processus physiques pendant l'hiver ?*

Tout au long de cette thèse, des simulations de sensibilité sont effectuées pour étudier les raisons possibles des incertitudes dans les aérosols modélisés pendant l'hiver sur le grand Arctique et sur l'Alaska. Les différentes études se concentrent sur la représentation de la PBL modélisée, la fraction de glace de mer et l'élimination humide et sèche.

L'influence de la météorologie de la PBL est étudiée en détail dans cette thèse, car il est important de simuler avec précision la structure (dynamique) de la PBL, car elle affecte le mélange vertical des aérosols et de leurs précurseurs, le dépôt sec des aérosols et des gaz, et peut également piéger la pollution au sol dans des conditions météorologiques stables, fréquentes dans l'Arctique en hiver. L'influence de la PBL est étudiée sur la CB au-dessus du nord de l'Alaska (chapitre 5). L'utilisation d'un autre schéma de PBL dans le modèle, à savoir MYJ, a entraîné des concentrations de BC plus faibles au-dessus des régions sources, telles que les champs pétrolifères de la NSA et Fairbanks, mais aussi des régions de hautes montagnes, telles que la chaîne de Brooks, au nord de l'Alaska, probablement en raison de différences dans les schémas de précipitations. Pour l'analyse présentée au chapitre 6, nous avons d'abord utilisé le schéma MYJ PBL car il est souvent utilisé pour modéliser des PBL stables dans l'Arctique et l'Antarctique. Les essais avec le MYJ n'ont montré que de petites différences dans les aérosols et les gaz aux sites pollués et de fond. Les deux schémas PBL ont des difficultés à simuler des conditions stables avec de fortes inversions de température en surface. Les vents du modèle sont trop forts à la surface et dans la basse troposphère, et les gradients de température sont trop faibles. De tels biais affectent la pollution atmosphérique au niveau régional au-dessus de l'Alaska, mais pourraient également entraîner des biais élevés sur les aérosols et les gaz dans l'Arctique et les latitudes moyennes. Les mesures météorologiques complètes recueillies au cours du projet ALPACA 2022 contribueront à améliorer les traitements des PBL des modèles.

Les résultats présentés au chapitre 4 montrent que les SSA le long de la côte ouest et nord de l'Alaska sont sensibles à la concentration de glace de mer (fraction). Les produits de glace de mer FNL et ERA5 sont testés, ce qui entraîne des différences dans les flux d'émission et les concentrations de SSA. En utilisant les données de glace de mer ERA5, les flux d'émission de SSA ont principalement augmenté autour de la côte ouest et est d'Utqiaġvik et ont diminué plus à l'est. On observe également des différences notables sur la côte sud-est de l'Alaska. Les deux données de réanalyse ont des difficultés à représenter de manière réaliste les chenaux ouverts le long de la côte d'Utqiaġvik en janvier et février 2014. D'autres facteurs, comme l'utilisation d'une dépendance plus élevée de la vitesse du vent pour les émissions de SSA submicroniques, conduisent à une augmentation significative des concentrations de SSA submicroniques sur la côte nord de l'Alaska. Dans l'ensemble, les SSA modélisés sont plus sensibles aux traitements de la glace de mer et de la vitesse du vent, plutôt qu'aux dépôts secs. Cependant, une analyse plus approfondie est nécessaire pour inclure une concentration de glace de mer plus réaliste dans les modèles (et les réanalyses météorologiques), par exemple, sur la base de données satellitaires afin de réduire les biais du modèle, en particulier, dans les SSA submicroniques. Cela pourrait

également améliorer la simulation de la dynamique de la couche limite marine. La dépendance du SSA par rapport aux TSM dans l'Arctique en fonction de la taille des particules pourrait également améliorer les divergences entre les modèles pendant les épisodes de SSA submicronique élevé. De nouvelles observations sont également nécessaires.

Le chapitre 5 examine la contribution des processus de dépôt, et à la PBL modélisée dans l'Arctique. L'analyse montre que le BC est sensible au dépôt humide et sèc à travers l'Arctique à la surface et dans la troposphère libre (principalement dépôt humide). Les résultats dépendent de l'emplacement, Zeppelin et Alert étant plus sensibles au dépôt humide qu'à Tiksi ou Barrow où dépôt humide et sec est importante (dans le modèle). Cette étude souligne également que le BC est sensible au dépôt humide pendant le transport vers l'Arctique et, dans une moindre mesure, au niveau régional au-dessus du nord de l'Alaska. Le BC est également sensible au dépôt sec dans l'Arctique et dans la région, selon la proximité des sources locales et régionales. L'analyse présentée aux chapitres 4 et 6 a également montré que le SSA, les autres aérosols inorganiques et les gaz à l'état de traces sont sensibles à l'élimination sèche au niveau régional au-dessus du centre et du nord de l'Alaska pendant l'hiver. Il convient d'étudier les améliorations à apporter aux vitesses de dépôt sec modélisées en fonction de la taille des particules ainsi qu'à la dynamique des PBL modélisées, comme indiqué ci-dessus. L'amélioration de l'absorption aqueuse modélisée dans les nuages pourrait, par exemple, améliorer le dépôt humide modélisée.

(iii) *Dans quelle mesure les sources anthropiques locales de l'Arctique contribuent-elles à la composition de l'atmosphère en hiver ?*

Cette thèse se concentre sur les sources régionales et locales au-dessus de l'Alaska. Les résultats présentés au chapitre 5 montrent que les émissions régionales au-dessus du nord de l'Alaska, en particulier celles des champs pétrolières du North Slope Alaska (NSA), ont un impact significatif sur le BC à l'observatoire de Barrow pendant l'hiver 2014, avec 30 à 50% du BC provenant de cette source. Ce résultat met en évidence l'impact de la source locale sur la pollution atmosphérique hivernale en Arctique. L'utilisation d'un inventaire à plus haute résolution (CAMS) a permis de réduire les émissions de BC sur le versant nord de l'Alaska pendant l'hiver 2014. Cependant, les deux inventaires manquent d'une représentation détaillée des sources locales de la ville d'Utqiaġvik, dont on sait également qu'elles influencent les observations de BC à Barrow. Une analyse plus approfondie utilisant des exécutions de modèle plus longues est nécessaire pour différents hivers afin d'étudier l'influence des émissions des champs pétrolifères NSA et de déterminer les incertitudes et les limites des inventaires d'émissions.

Les simulations du modèle pour l'hiver 2019, effectuées avec les émissions CAMS, sont présentées au chapitre 6. Les résultats montrent que les sources régionales de l'Alaska peuvent contribuer aux sites de fond dans le centre de l'Alaska, comme la station de Toolik field Lake. Les émissions locales sont également importantes dans la région de Fairbanks (comme cela est également indiqué au chapitre 5 pour le BC). Cependant, le modèle sous-estime les gaz précurseurs et les aérosols au-dessus de la région de Fairbanks. Cela pourrait être dû en partie à la résolution des passes mais aussi au fait que les sources locales dans les sites pollués tels que Fairbanks sont absentes ou trop faibles dans l'inventaire du CAMS. L'analyse présentée au chapitre 6 montre que les émissions de BC, SO_2 et de NO du CAMS peuvent être sous-estimées d'un facteur d'au moins 2,5 (BC, SO_2) et 33 (NO) sur l'ensemble de la région de Fairbanks, y compris la zone résidentielle de North Pole. Une correction de biais plus sophistiquée des émissions, utilisant des mesures de fond et régionales détaillées, permettra de mieux quantifier cette sous-estimation. Cette analyse montre également que certains des biais du modèle, par exemple la sous-estimation du SO_4^{2-} ou du BC, peuvent être partiellement expliqués par l'absence d'émissions. Les biais restants, dans le cas du SO_4^{2-}, pourraient être expliqués par des mécanismes supplémentaires de formation d'aérosols secondaires.

En hiver, les émissions anthropiques locales provenant du torchage du gaz, du chauffage résidentiel et commercial, des centrales électriques et de l'industrie contribuent à la pollution atmosphérique régionale et locale dans l'Arctique. Toutefois, cette contribution pourrait être sous-estimée en raison des incertitudes liées aux inventaires des émissions mondiales (chapitres 4, 5 et 6) ou du manque de documentation détaillée sur les sources locales (chapitre 6). Les inventaires mondiaux des émissions ne sont pas mis à jour régulièrement pour prendre en compte les changements dans les émissions dus aux réglementations des pays pour réduire leurs émissions. En outre, les inventaires mondiaux sont fournis à une résolution grossière, généralement 50 x 50 km ou 10 x 10 km, et ne comportent pas de représentation détaillée des sources locales. Il y a de petits et de grands établissements (urbains) dans le Grand Nord, mais sans observations détaillées pour aider à quantifier la contribution des sources locales, il est difficile d'évaluer les niveaux de pollution atmosphérique. Il s'agit d'une question importante car les sources anthropiques locales pourraient augmenter à l'avenir en raison du réchauffement climatique en cours et de l'augmentation de l'activité humaine.

Perspectives et travaux futurs: Les travaux entrepris au cours de cette thèse améliorent les performances du modèle WRF-Chem sur des sites arctiques éloignés pendant l'hiver et fournissent de nouvelles informations sur la manière dont les différents processus et sources influencent la pollution atmosphérique arctique hivernale, et en particulier la pollution en

Alaska. Des sites tels que Barrow, Utqiaġvik ou la ville polluée de Fairbanks sont affectés par des sources de fond, régionales et locales. À ce titre, ils pourraient également être des zones urbaines représentatives d'autres régions éloignées de l'Arctique pour lesquelles il n'existe pas d'observations détaillées. La composition de l'Arctique en hiver pourrait changer à l'avenir en raison de l'évolution des sources éloignées et locales et du réchauffement climatique.

En raison du réchauffement climatique en cours, et en particulier du réchauffement rapide de l'Arctique, il se formera moins de glace de mer en été et, par conséquent, la glace sera plus mince en hiver. Ainsi, de nouvelles sources d'émissions marines, dont les SSA, pourraient apparaître, ce qui pourrait augmenter la contribution des SSA à la charge en aérosols, notamment dans les sites côtiers de l'Arctique. Cela pourrait avoir un impact sur le bilan radiatif de l'Arctique en renforçant le refroidissement de l'atmosphère ou en augmentant des CCN. Pour étudier plus en profondeur l'effet du SSA sur le climat de l'Arctique, des données satellitaires à haute résolution sur la concentration de la glace de mer sont nécessaires, comme nous l'avons vu précédemment. En outre, pour mieux comprendre les interactions entre l'océan et la basse atmosphère, le modèle WRF-Chem pourrait être couplé à un modèle océanique.

Il existe également d'autres sources naturelles importantes, telles que la poussière et les volcans, qui contribuent à la charge en aérosols de l'Arctique et qui n'ont pas été abordées dans cette thèse (par exemple *AMAP (2021)*). En particulier pour la poussière, il existe d'importantes sources naturelles et anthropogéniques (par exemple, les activités minières) dans l'Arctique, comme discuté dans le chapitre 2, qui ne sont pas incluses dans les inventaires d'émissions globales utilisés dans cette thèse et doivent être prises en compte dans les études futures. L'analyse des données provenant de campagnes de terrain complètes, telles que la campagne ALPACA 2022, permettra également de contraindre davantage les modèles régionaux et de mieux comprendre les voies de formation des aérosols manquants dans des conditions hivernales polluées. Le chapitre 6 fait référence à des études de modélisation antérieures qui ont étudié les conditions hivernales de l'Arctic Haze en Chine. Ces études ont inclus les réactions manquantes nécessaires à la formation secondaire de SO_4^{2-} et de NO_3^-. De telles réactions doivent être testées dans WRF-Chem après l'analyse des données ALPACA. Cela inclut également les aérosols organiques et leurs précurseurs, les COV, pour lesquels il y a eu des mesures détaillées pendant ALPACA 2022. Combinées avec des inventaires d'émissions à plus haute résolution, tels que EPA-ADEC, qui sont produits pour l'hiver 2022 à une résolution de 1,3 x 1,3 km, les simulations de modèles à plus haute résolution permettront de mieux étudier les processus chimiques et météorologiques qui influencent la pollution locale de l'Arctique en hiver. Dans le même ordre d'idées, cette

thèse souligne également que le modèle manque d'aérosols organiques anthropiques. Des études récentes ont inclus dans les modèles les émissions d'IVOC provenant de sources mobiles *(Lu et al., 2018, 2020)*. Cependant, des incertitudes subsistent concernant les émissions de IVOCs non mobiles en raison du nombre limité de données *(Lu et al., 2020)*. Des études récentes ont également fait état d'émissions de COVs provenant de sources mobiles *(Presto et al., 2012; Zhao and Garrett, 2015; Zhao et al., 2016)*. Les mesures d'OA et de COV collectées lors de la campagne ALPACA 2022 permettront de remédier à cette limitation dans WRF-Chem.

Les différentes études présentées dans cette thèse ont montré que les aérosols et les gaz traces sont sensibles aux dépôts secs. Deux modules différents calculant les vitesses de dépôt sec ont été testés entraînant des différences importantes dans les concentrations d'aérosols. Cependant, en raison du manque d'observations des vitesses de dépôt sec sur différents terrains, il est difficile de valider ces paramétrisations. La CB modélisée est également sensible aux dépôts humides. Des études récentes ont montré qu'en améliorant les paramétrisations des dépôts humides et secs, la CB modélisée dans l'Arctique pourrait augmenter d'un facteur de 50 à 100 *(Liu and Matsui, 2021)*. *Whaley et al. (2022b)* a montré les incertitudes des dépôts secs et humides modélisés aux latitudes moyennes où les observations sont également limitées. Il est essentiel de s'attaquer d'abord aux incertitudes des modèles liées aux dépôts secs et humides aux latitudes moyennes avant de se concentrer sur l'Arctique, car elles influencent les concentrations d'aérosols transportés dans l'Arctique, comme nous l'avons vu précédemment au chapitre 5, et pour cela, des mesures détaillées des dépôts sont nécessaires. Enfin, il est nécessaire d'améliorer encore les modèles de surface terrestre et les fonctions de stabilité au niveau de la couche limite, afin de limiter les incertitudes sur les aérosols et les gaz à l'état de traces dues aux incertitudes météorologiques. Ceci peut être réalisé en utilisant des mesures détaillées des variables météorologiques collectées sur différents sites, lors de campagnes de terrain, telles que les campagnes pré et principales d'ALPACA. Il serait également intéressant d'étudier les changements futurs possibles, par exemple, la stabilité hivernale de la pollution atmosphérique dans l'Arctique.

En résumé, les modèles régionaux sont des outils très utiles et peuvent être utilisés pour des études de cas détaillées afin d'identifier les sources et processus importants influençant les aérosols arctiques. Les résultats peuvent être utilisés pour améliorer les modèles mondiaux, qui sont utilisés pour étudier les effets à long terme de la pollution atmosphérique arctique sur la qualité de l'air et le climat dans le cadre de différents scénarios d'émission, ce qui est important pour les décideurs.

Bibliography

Aas, W., Eckhardt, S., Fiebig, M., Platt, S. M., Solberg, S., Yttri, K. E., and Zwaaftink, C. G. Monitoring of long-range transported air pollutants in norway. annual report 2020. *NILU rapport*, 2021.

Abbatt, J. and Waschewsky, G. Heterogeneous interactions of hobr, hno3, o3, and no2 with deliquescent nacl aerosols at room temperature. *The Journal of Physical Chemistry A*, 102(21):3719–3725, 1998.

Ackman, R. G., Tocher, C., and McLachlan, J. Occurrence of dimethyl-β-propiothetin in marine phytoplankton. *Journal of the Fisheries Board of Canada*, 23(3):357–364, 1966.

Adams, P. J., Seinfeld, J. H., and Koch, D. M. Global concentrations of tropospheric sulfate, nitrate, and ammonium aerosol simulated in a general circulation model. *Journal of Geophysical Research: Atmospheres*, 104(D11):13791–13823, 1999.

Adefisan, E. and Oghaego, A. Performance evaluation of wrf-chem in simulating harmattan dust over west africa. *J Climatol Weather Forecast*, 6:232, 2018.

Administration, U. E. I. International energy statistics, 2015.

Agency, U. S. E. P. What climate change means for alaska. *Environmental Protection Agency*, 2016.

Aiken, A. C., Decarlo, P. F., Kroll, J. H., Worsnop, D. R., Huffman, J. A., Docherty, K. S., Ulbrich, I. M., Mohr, C., Kimmel, J. R., Sueper, D., et al. O/c and om/oc ratios of primary, secondary, and ambient organic aerosols with high-resolution time-of-flight aerosol mass spectrometry. *Environmental science & technology*, 42 (12):4478–4485, 2008.

Akagi, S., Yokelson, R. J., Wiedinmyer, C., Alvarado, M., Reid, J., Karl, T., Crounse, J., and Wennberg, P. Emission factors for open and domestic biomass burning for use in atmospheric models. *Atmospheric Chemistry and Physics*, 11(9):4039–4072, 2011.

Akperov, M., Mokhov, I., Dembitskaya, M., and Parfenova, M. Tropospheric lapse rate and its changes in the arctic from reanalysis data. In *24th International Symposium on Atmospheric and Ocean Optics: Atmospheric Physics*, volume 10833, pages 1569–1573. SPIE, 2018.

Albergel, C., Dutra, E., Munier, S., Calvet, J.-C., Munoz-Sabater, J., de Rosnay, P., and Balsamo, G. Era-5 and era-interim driven isba land surface model simulations: which one performs better? *Hydrology and Earth System Sciences*, 22(6):3515–3532, 2018.

Alexander, B., Park, R. J., Jacob, D. J., Li, Q., Yantosca, R. M., Savarino, J., Lee, C., and Thiemens, M. Sulfate formation in sea-salt aerosols: Constraints from oxygen isotopes. *Journal of Geophysical Research: Atmospheres*, 110(D10), 2005.

Alexander, B., Park, R. J., Jacob, D. J., and Gong, S. Transition metal-catalyzed oxidation of atmospheric sulfur: Global implications for the sulfur budget. *Journal of Geophysical Research: Atmospheres*, 114(D2), 2009.

Alexander, B., Allman, D., Amos, H., Fairlie, T., Dachs, J., Hegg, D. A., and Sletten, R. S. Isotopic constraints on the formation pathways of sulfate aerosol in the marine boundary layer of the subtropical northeast atlantic ocean. *Journal of Geophysical Research: Atmospheres*, 117(D6), 2012.

Amann, M., Bertok, I., Borken-Kleefeld, J., Cofala, J., Heyes, C., Höglund-Isaksson, L., Klimont, Z., Nguyen, B., Posch, M., Rafaj, P., et al. Cost-effective control of air quality and greenhouse gases in europe: Modeling and policy applications. *Environmental Modelling & Software*, 26(12):1489–1501, 2011.

AMAP. Amap assessment 2015: Black carbon and ozone as arctic climate forcers. 2015.

AMAP. Amap, 2021. arctic climate change update 2021: Key trends and impacts. summary for policy-makers. 2021.

Amosov, P. and Baklanov, A. Assessment of dusting intensity on anof-2 tailing by using a westphal dl dependency. In *X International Symposium on Recycling Technologies and Sustainable Development*, pages 39–43, 2015.

Andreae, M. and Rosenfeld, D. Aerosol–cloud–precipitation interactions. part 1. the nature and sources of cloud-active aerosols. *Earth-Science Reviews*, 89(1-2):13–41, 2008.

Andreas, E. L. Estimation of heat and mass fluxes over arctic leads. *Monthly Weather Review*, 108(12):2057–2063, 1980.

Apodaca, R., Huff, D., and Simpson, W. The role of ice in n 2 o 5 heterogeneous hydrolysis at high latitudes. *Atmospheric Chemistry and Physics*, 8(24):7451–7463, 2008.

Archer-Nicholls, S., Lowe, D., Utembe, S., Allan, J., Zaveri, R. A., Fast, J. D., Hodnebrog, Ø., Denier van der Gon, H., and McFiggans, G. Gaseous chemistry and aerosol mechanism developments for version 3.5.1 of the online regional model, wrf-chem. *Geoscientific Model Development*, 7(6):2557–2579, 2014. doi: 10.5194/gmd-7-2557-2014. URL https://gmd.copernicus.org/articles/7/2557/2014/.

Arguez, A., Durre, I., Applequist, S., Vose, R. S., Squires, M. F., Yin, X., Heim Jr, R. R., and Owen, T. W. Noaa's 1981–2010 us climate normals: an overview. *Bulletin of the American Meteorological Society*, 93(11):1687–1697, 2012.

Arrhenius, S. Xxxi. on the influence of carbonic acid in the air upon the temperature of the ground. *The London, Edinburgh, and Dublin Philosophical Magazine and Journal of Science*, 41(251):237–276, 1896.

Asmi, E., Kondratyev, V., Brus, D., Laurila, T., Lihavainen, H., Backman, J., Vakkari, V., Aurela, M., Hatakka, J., Viisanen, Y., et al. Aerosol size distribution seasonal characteristics measured in tiksi, russian arctic. *Atmospheric Chemistry and Physics*, 16(3):1271–1287, 2016.

Ayers, J. D. and Simpson, W. R. Measurements of n2o5 near fairbanks, alaska. *Journal of Geophysical Research: Atmospheres*, 111(D14), 2006.

Backman, J., Schmeisser, L., Virkkula, A., Ogren, J. A., Asmi, E., Starkweather, S., Sharma, S., Eleftheriadis, K., Uttal, T., Jefferson, A., et al. On aethalometer measurement uncertainties and an instrument correction factor for the arctic. *Atmospheric Measurement Techniques*, 10(12):5039–5062, 2017.

Baklanov, A. A., Penenko, V. V., Mahura, A. G., Vinogradova, A. A., Elansky, N. F., Tsvetova, E. A., Rigina, O. Y., Maksimenkov, L. O., Nuterman, R. B., Pogarskii, F. A., et al. Aspects of atmospheric pollution in siberia. In *Regional environmental changes in Siberia and their global consequences*, pages 303–346. Springer, 2013.

Ball, J. T., Woodrow, I. E., and Berry, J. A. A model predicting stomatal conductance and its contribution to the control of photosynthesis under different environmental conditions. In *Progress in photosynthesis research*, pages 221–224. Springer, 1987.

Ballinger, T., Overland, J., Wang, M., Bhatt, U., Hanna, E., Hanssen-Bauer, I., Kim, S.-J., Thoman, R., and Walsh, J. Arctic report card 2020: Surface air temperature. 2020.

Barnes, E. A. and Polvani, L. M. Cmip5 projections of arctic amplification, of the north american/north atlantic circulation, and of their relationship. *Journal of Climate*, 28(13):5254–5271, 2015.

Barrett, T. and Sheesley, R. Year-round optical properties and source characterization of arctic organic carbon aerosols on the north slope alaska. *Journal of Geophysical Research: Atmospheres*, 122(17):9319–9331, 2017.

Barrett, T., Robinson, E., Usenko, S., and Sheesley, R. Source contributions to wintertime elemental and organic carbon in the western arctic based on radiocarbon and tracer apportionment. *Environmental science & technology*, 49(19):11631–11639, 2015.

Barrie, L. Scavenging ratios: black magic or a useful scientific tool. In *Proc. of 5th Int. Conf. on Precipitation Scavenging and Atmosphere-Surface Exchange Processes, edited by: Schwartz, S. and Slinn, W*, volume 1, pages 403–420, 1992.

Barrie, L. and Barrie, M. Chemical components of lower tropospheric aerosols in the high arctic: Six years of observations. *Journal of Atmospheric Chemistry*, 11(3):211–226, 1990.

Barrie, L. and Hoff, R. The oxidation rate and residence time of sulphur dioxide in the arctic atmosphere. *Atmospheric Environment (1967)*, 18(12):2711–2722, 1984.

Barrie, L., Hoff, R., and Daggupaty, S. The influence of mid-latitudinal pollution sources on haze in the canadian arctic. *Atmospheric Environment (1967)*, 15(8):1407–1419, 1981.

Barrie, L., Bottenheim, J., Schnell, R., Crutzen, P., and Rasmussen, R. Ozone destruction and photochemical reactions at polar sunrise in the lower arctic atmosphere. *Nature*, 334(6178):138–141, 1988.

Barrie, L., Staebler, R., Toom, D., Georgi, B., Den Hartog, G., Landsberger, S., and Wu, D. Arctic aerosol size-segregated chemical observations in relation to ozone depletion during polar sunrise experiment 1992. *Journal of Geophysical Research: Atmospheres*, 99(D12):25439–25451, 1994.

Barrie, L. A. Arctic air pollution: An overview of current knowledge. *Atmospheric Environment (1967)*, 20(4): 643–663, 1986.

Barth, M. C., Wong, J., Bela, M. M., Pickering, K. E., Li, Y., and Cummings, K. A. Simulations of lightning-generated nox for parameterized convection in the wrf-chem model . 2014.

Barthel, S., Tegen, I., and Wolke, R. Do new sea spray aerosol source functions improve the results of a regional aerosol model? *Atmospheric Environment*, 198:265–278, 2019.

Batrak, Y. and Müller, M. On the warm bias in atmospheric reanalyses induced by the missing snow over arctic sea-ice. *Nature communications*, 10(1):1–8, 2019.

Behera, S. N., Sharma, M., Aneja, V. P., and Balasubramanian, R. Ammonia in the atmosphere: a review on emission sources, atmospheric chemistry and deposition on terrestrial bodies. *Environmental Science and Pollution Research*, 20(11):8092–8131, 2013.

Bei, N., Li, G., and Molina, L. Uncertainties in soa simulations due to meteorological uncertainties in mexico city during milagro-2006 field campaign. *Atmospheric Chemistry and Physics*, 12(23):11295–11308, 2012.

Benson, C. S. *Ice fog: Low temperature air pollution*, volume 121. Corps of Engineers, US Army, Cold Regions Research and Engineering Laboratory, 1970.

Berg, L. K., Gustafson, W. I., Kassianov, E. I., and Deng, L. Evaluation of a modified scheme for shallow convection: Implementation of cup and case studies. *Monthly weather review*, 141(1):134–147, 2013.

Berg, L. K., Shrivastava, M., Easter, R. C., Fast, J. D., Chapman, E. G., Liu, Y., and Ferrare, R. A new wrf-chem treatment for studying regional-scale impacts of cloud processes on aerosol and trace gases in parameterized cumuli. *Geoscientific Model Development*, 8(2):409–429, 2015.

Bindoff, N. L., Stott, P. A., AchutaRao, K. M., Allen, M. R., Gillett, N., Gutzler, D., Hansingo, K., Hegerl, G., Hu, Y., Jain, S., et al. Detection and attribution of climate change: from global to regional. 2013.

Binkowski, F. S. and Shankar, U. The regional particulate matter model: 1. model description and preliminary results. *Journal of Geophysical Research: Atmospheres*, 100(D12):26191–26209, 1995.

Bluestein, H. B. *Synoptic-dynamic Meteorology in Midlatitudes: Observations and theory of weather systems*, volume 2. Taylor & Francis, 1992.

Boichu, M., Chiapello, I., Brogniez, C., Péré, J.-C., Thieuleux, F., Torres, B., Blarel, L., Mortier, A., Podvin, T., Goloub, P., et al. Current challenges in modelling far-range air pollution induced by the 2014–2015 bárðarbunga fissure eruption (iceland). *Atmospheric Chemistry and Physics*, 16(17):10831–10845, 2016.

Boisvert, L. and Stroeve, J. C. The arctic is becoming warmer and wetter as revealed by the atmospheric infrared sounder. *Geophysical Research Letters*, 42(11):4439–4446, 2015.

Bonan, G. B. Land surface model (lsm version 1.0) for ecological, hydrological, and atmospheric studies: Technical description and users guide. technical note. Technical report, National Center for Atmospheric Research, Boulder, CO (United States ..., 1996.

Bond, T. C., Anderson, T. L., and Campbell, D. Calibration and intercomparison of filter-based measurements of visible light absorption by aerosols. *Aerosol Science & Technology*, 30(6):582–600, 1999.

Bond, T. C., Doherty, S. J., Fahey, D. W., Forster, P. M., Berntsen, T., DeAngelo, B. J., Flanner, M. G., Ghan, S., Kärcher, B., Koch, D., et al. Bounding the role of black carbon in the climate system: A scientific assessment. *Journal of geophysical research: Atmospheres*, 118(11):5380–5552, 2013a.

Bond, T. C., Doherty, S. J., Fahey, D. W., Forster, P. M., Berntsen, T., DeAngelo, B. J., Flanner, M. G., Ghan, S., Kärcher, B., Koch, D., Kinne, S., Kondo, Y., Quinn, P. K., Sarofim, M. C., Schultz, M. G., Schulz, M., Venkataraman, C., Zhang, H., Zhang, S., Bellouin, N., Guttikunda, S. K., Hopke, P. K., Jacobson, M. Z., Kaiser, J. W., Klimont, Z., Lohmann, U., Schwarz, J. P., Shindell, D., Storelvmo, T., Warren, S. G., and Zender, C. S. Bounding the role of black carbon in the climate system: A scientific assessment. *Journal of Geophysical Research: Atmospheres*, 118(11):5380–5552, 2013b. doi: https://doi.org/10.1002/jgrd.50171. URL https://agupubs.onlinelibrary.wiley.com/doi/abs/10.1002/jgrd.50171.

Böttcher, K., Paunu, V.-V., Kupiainen, K., Zhizhin, M., Matveev, A., Savolahti, M., Klimont, Z., Väätäinen, S., Lamberg, H., and Karvosenoja, N. Black carbon emissions from flaring in russia in the period 2012–2017. *Atmospheric Environment*, 254:118390, 2021.

Boucher, O., Randall, D., Artaxo, P., Bretherton, C., Feingold, G., Forster, P., Kerminen, V.-M., Kondo, Y., Liao, H., Lohmann, U., Rasch, P., Satheesh, S. K., Sherwood, S., Stevens, B., and Zhang, X. Y. *Clouds and aerosols*, pages 571–657. Cambridge University Press, Cambridge, UK, 2013. doi: 10.1017/CBO9781107415324.016.

Bourne, S. M., Bhatt, U. S., Zhang, J., and Thoman, R. Surface-based temperature inversions in alaska from a climate perspective. *Atmospheric Research*, 95(2-3):353–366, 2010.

Bouwman, A., Lee, D., Asman, W., Dentener, F., Van Der Hoek, K., and Olivier, J. A global high-resolution emission inventory for ammonia. *Global biogeochemical cycles*, 11(4):561–587, 1997.

Bowen, H. J. M. et al. *Environmental chemistry of the elements*. Academic Press., 1979.

Bowen, M. and Vincent, R. An assessment of the spatial extent of polar dust using satellite thermal data. *Scientific Reports*, 11(1):1–9, 2021.

Bowling, S. A. Climatology of high-latitude air pollution as illustrated by fairbanks and anchorage, alaska. *Journal of climate and applied meteorology*, 25(1):22–34, 1986.

Bradley, R. S., Keimig, F. T., and Diaz, H. F. Climatology of surface-based inversions in the north american arctic. *Journal of Geophysical Research: Atmospheres*, 97(D14):15699–15712, 1992.

Brandt, C. and Van Eldik, R. Transition metal-catalyzed oxidation of sulfur (iv) oxides. atmospheric-relevant processes and mechanisms. *Chemical Reviews*, 95(1):119–190, 1995.

Brasseur, G. P. and Jacob, D. J. *Modeling of atmospheric chemistry*. Cambridge University Press, 2017.

Brock, C. A., Cozic, J., Bahreini, R., Froyd, K. D., Middlebrook, A. M., McComiskey, A., Brioude, J., Cooper, O., Stohl, A., Aikin, K., et al. Characteristics, sources, and transport of aerosols measured in spring 2008 during the aerosol, radiation, and cloud processes affecting arctic climate (arcpac) project. *Atmospheric Chemistry and Physics*, 11(6):2423–2453, 2011.

Brøgger, W. Note on a contaminated snowfall under the heading mindre meddelelser (short communications). *Naturen*, 5:47, 1881.

Brooks, C. The vertical temperature gradient in the arctic. *Meteor. Mag*, 66:267–268, 1931.

Brown, S. S. and Stutz, J. Nighttime radical observations and chemistry. *Chemical Society Reviews*, 41(19): 6405–6447, 2012.

Browse, J., Carslaw, K. S., Arnold, S. R., Pringle, K., and Boucher, O. The scavenging processes controlling the seasonal cycle in arctic sulphate and black carbon aerosol. *Atmospheric Chemistry and Physics*, 12 (15):6775–6798, 2012. doi: 10.5194/acp-12-6775-2012. URL https://acp.copernicus.org/articles/12/6775/2012/.

Bucaram, C. J. and Bowman, F. M. Wrf-chem modeling of summertime air pollution in the northern great plains: Chemistry and aerosol mechanism intercomparison. *Atmosphere*, 12(9):1121, 2021.

Buchholz, R., Emmons, L., Tilmes, S., and Team, T. Cesm2. 1/cam-chem instantaneous output for boundary conditions. *UCAR/NCAR-Atmospheric Chemistry Observations and Modeling Laboratory. -40 to 90, October - December 2019, 10 Nov 2021*, 2019.

Busby, B. D., Ward, T. J., Turner, J. R., Palmer, C. P., et al. Comparison and evaluation of methods to apportion ambient pm2. 5 to residential wood heating in fairbanks, ak. *Aerosol and Air Quality Research*, 16(3): 492–503, 2016.

Busch, N., Ebel, U., Kraus, H., and Schaller, E. The structure of the subpolar inversion-capped abl. *Archives for meteorology, geophysics, and bioclimatology, Series A*, 31(1):1–18, 1982.

Cai, S., Zhu, L., Wang, S., Wisthaler, A., Li, Q., Jiang, J., and Hao, J. Time-resolved intermediate-volatility and semivolatile organic compound emissions from household coal combustion in northern china. *Environmental Science & Technology*, 53(15):9269–9278, 2019.

Calhoun, J. A., Bates, T. S., and Charlson, R. J. Sulfur isotope measurements of submicrometer sulfate aerosol particles over the pacific ocean. *Geophysical Research Letters*, 18(10):1877–1880, 1991.

Callaghan, A., de Leeuw, G., Cohen, L., and O'Dowd, C. D. Relationship of oceanic whitecap coverage to wind speed and wind history. *Geophysical Research Letters*, 35(23), 2008.

Callaghan, A. H. An improved whitecap timescale for sea spray aerosol production flux modeling using the discrete whitecap method. *Journal of Geophysical Research: Atmospheres*, 118(17):9997–10, 2013.

Callaghan, A. H., Deane, G. B., Stokes, M. D., and Ward, B. Observed variation in the decay time of oceanic whitecap foam. *Journal of Geophysical Research: Oceans*, 117(C9), 2012.

Callaghan, A. H., Stokes, M., and Deane, G. The effect of water temperature on air entrainment, bubble plumes, and surface foam in a laboratory breaking-wave analog. *Journal of Geophysical Research: Oceans*, 119 (11):7463–7482, 2014.

Calvert, J. G. and Stockwell, W. R. Acid generation in the troposphere by gas-phase chemistry. *Environmental science & technology*, 17(9):428A–443A, 1983.

Campbell, S. W., Evans, M. C., and Poor, N. D. Predictions of size-resolved aerosol concentrations of ammonium, chloride and nitrate at a bayside site using equisolv ii. *Atmospheric Environment*, 36(27):4299–4307, 2002.

Carlson, T. N. Speculations on the movement of polluted air to the arctic. *Atmospheric Environment (1967)*, 15(8):1473–1477, 1981.

Carter, W. P. Documentation of the saprc-99 chemical mechanism for voc reactivity assessment. *Contract*, 92 (329):95–308, 2000.

Cassano, J. J., Cassano, E. N., Seefeldt, M. W., Gutowski Jr, W. J., and Glisan, J. M. Synoptic conditions during wintertime temperature extremes in alaska. *Journal of Geophysical Research: Atmospheres*, 121(7):3241–3262, 2016.

Cavalieri, D. J. and Parkinson, C. L. Arctic sea ice variability and trends, 1979–2010. *The Cryosphere*, 6(4): 881–889, 2012.

Cesler-Maloney, M., Simpson, W. R., Miles, T., Mao, J., Law, K. S., and Roberts, T. J. Differences in ozone and particulate matter between ground level and 20 meters aloft are frequent during wintertime surface-based temperature inversions in fairbanks alaska. *Journal of Geophysical Research: Atmospheres*, n/a(n/a):e2021JD036215. doi: https://doi.org/10.1029/2021JD036215. URL https://agupubs.onlinelibrary.wiley.com/doi/abs/10.1029/2021JD036215. e2021JD036215 2021JD036215.

Cesler-Maloney, M., Simpson, W. R., Miles, T., Mao, J., Law, K. S., and Roberts, T. J. Differences in ozone and particulate matter between ground level and 20 meters aloft are frequent during wintertime surface-based temperature inversions in fairbanks alaska. *Journal of Geophysical Research: Atmospheres*, page e2021JD036215, 2022.

Chan, M. A. and Comiso, J. C. Arctic cloud characteristics as derived from modis, calipso, and cloudsat. *Journal of Climate*, 26(10):3285–3306, 2013.

Chang, M., Fan, S., and Wang, X. Impact of refined land-cover data on wrf performance over the pearl river delta region, china. *Huanjing Kexue Xuebao/Acta Scientiae Circumstantiae*, 34(8):1922–1933, 2014.

Chang, W. L., Bhave, P. V., Brown, S. S., Riemer, N., Stutz, J., and Dabdub, D. Heterogeneous atmospheric chemistry, ambient measurements, and model calculations of n2o5: A review. *Aerosol Science and Technology*, 45(6):665–695, 2011.

Chapin, F., Trainor, S., Cochran, P., Huntington, H., Markon, C., McCammon, M., McGuire, A., Serreze, M., Melillo, J., Richmond, T., et al. Alaska. climate change impacts in the united states. *The third national climate assessment*, pages 514–536, 2014.

Chapman, E. G., Gustafson Jr, W., Easter, R. C., Barnard, J. C., Ghan, S. J., Pekour, M. S., and Fast, J. D. Coupling aerosol-cloud-radiative processes in the wrf-chem model: Investigating the radiative impact of elevated point sources. *Atmospheric Chemistry and Physics*, 9(3):945–964, 2009.

Chen, B., Yu, W., Wang, W., Zhang, Z., and Dai, W. A global assessment of precipitable water vapor derived from gnss zenith tropospheric delays with era5, ncep fnl, and ncep gfs products. *Earth and Space Science*, 8(8):e2021EA001796, 2021.

Chen, F. and Dudhia, J. Coupling an advanced land surface–hydrology model with the penn state–ncar mm5 modeling system. part i: Model implementation and sensitivity. *Monthly weather review*, 129(4):569–585, 2001.

Chen, F., Janjić, Z., and Mitchell, K. Impact of atmospheric surface-layer parameterizations in the new land-surface scheme of the ncep mesoscale eta model. *Boundary-Layer Meteorology*, 85(3):391–421, 1997.

Chen, Y., Cheng, Y., Ma, N., Wolke, R., Nordmann, S., Schüttauf, S., Ran, L., Wehner, B., Birmili, W., Gon, H. A., et al. Sea salt emission, transport and influence on size-segregated nitrate simulation: a case study in northwestern europe by wrf-chem. *Atmospheric Chemistry and Physics*, 16(18):12081–12097, 2016.

Chin, M., Ginoux, P., Kinne, S., Torres, O., Holben, B. N., Duncan, B. N., Martin, R. V., Logan, J. A., Higurashi, A., and Nakajima, T. Tropospheric aerosol optical thickness from the gocart model and comparisons with satellite and sun photometer measurements. *Journal of the atmospheric sciences*, 59(3):461–483, 2002.

Chow, J. C., Watson, J. G., Pritchett, L. C., Pierson, W. R., Frazier, C. A., and Purcell, R. G. The dri thermal/optical reflectance carbon analysis system: description, evaluation and applications in us air quality studies. *Atmospheric Environment. Part A. General Topics*, 27(8):1185–1201, 1993.

Chow, J. C., Watson, J. G., Chen, L.-W. A., Arnott, W. P., Moosmüller, H., and Fung, K. Equivalence of elemental carbon by thermal/optical reflectance and transmittance with different temperature protocols. *Environmental science & technology*, 38(16):4414–4422, 2004.

Ciais, P., Sabine, C., Bala, G., Bopp, L., Brovkin, V., Canadell, J., Chhabra, A., DeFries, R., Galloway, J., Heimann, M., et al. Carbon and other biogeochemical cycles. In *Climate change 2013: the physical science basis. Contribution of Working Group I to the Fifth Assessment Report of the Intergovernmental Panel on Climate Change*, pages 465–570. Cambridge University Press, 2014.

Claeys, M., Graham, B., Vas, G., Wang, W., Vermeylen, R., Pashynska, V., Cafmeyer, J., Guyon, P., Andreae, M. O., Artaxo, P., et al. Formation of secondary organic aerosols through photooxidation of isoprene. *Science*, 303(5661):1173–1176, 2004.

Clarke, A. D., Owens, S. R., and Zhou, J. An ultrafine sea-salt flux from breaking waves: Implications for cloud condensation nuclei in the remote marine atmosphere. *Journal of Geophysical Research: Atmospheres*, 111(D6), 2006.

Cohen, A. E., Cavallo, S. M., Coniglio, M. C., and Brooks, H. E. A review of planetary boundary layer parameterization schemes and their sensitivity in simulating southeastern us cold season severe weather environments. *Weather and forecasting*, 30(3):591–612, 2015.

Cohen, A. J., Anderson, H. R., Ostro, B., Pandey, K. D., Krzyzanowski, M., Künzli, N., Gutschmidt, K., Pope III, C. A., Romieu, I., Samet, J. M., et al. Urban air pollution. *Comparative quantification of health risks: global and regional burden of disease attributable to selected major risk factors*, 2:1353–1433, 2004.

Cohen, J., Screen, J. A., Furtado, J. C., Barlow, M., Whittleston, D., Coumou, D., Francis, J., Dethloff, K., Entekhabi, D., Overland, J., et al. Recent arctic amplification and extreme mid-latitude weather. *Nature geoscience*, 7(9):627–637, 2014.

Collatz, G. J., Ball, J. T., Grivet, C., and Berry, J. A. Physiological and environmental regulation of stomatal conductance, photosynthesis and transpiration: a model that includes a laminar boundary layer. *Agricultural and Forest meteorology*, 54(2-4):107–136, 1991.

Collatz, G. J., Ribas-Carbo, M., and Berry, J. Coupled photosynthesis-stomatal conductance model for leaves of c4 plants. *Functional Plant Biology*, 19(5):519–538, 1992.

Croft, B., Wentworth, G. R., Martin, R. V., Leaitch, W. R., Murphy, J. G., Murphy, B. N., Kodros, J. K., Abbatt, J. P., and Pierce, J. R. Contribution of arctic seabird-colony ammonia to atmospheric particles and cloud-albedo radiative effect. *Nature communications*, 7(1):1–10, 2016.

Cross, E., Hunter, J., Carrasquillo, A., Franklin, J., Herndon, S., Jayne, J., Worsnop, D., Miake-Lye, R., and Kroll, J. Online measurements of the emissions of intermediate-volatility and semi-volatile organic compounds from aircraft. *Atmospheric Chemistry and Physics*, 13(15):7845–7858, 2013.

Cross, E. S., Sappok, A. G., Wong, V. W., and Kroll, J. H. Load-dependent emission factors and chemical characteristics of ivocs from a medium-duty diesel engine. *Environmental Science & Technology*, 49(22): 13483–13491, 2015.

Crusius, J., Schroth, A. W., Gassó, S., Moy, C. M., Levy, R. C., and Gatica, M. Glacial flour dust storms in the gulf of alaska: Hydrologic and meteorological controls and their importance as a source of bioavailable iron. *Geophysical Research Letters*, 38(6), 2011.

Csanady, G. Equilibrium theory of the planetary boundary layer with an inversion lid. *Boundary-Layer Meteorology*, 6(1):63–79, 1974.

Curry, J. On the formation of continental polar air. *Journal of Atmospheric Sciences*, 40(9):2278–2292, 1983.

Curry, J. A., Ebert, E., and Herman, G. Mean and turbulence structure of the summertime arctic cloudy boundary layer. *Quarterly journal of the royal meteorological society*, 114(481):715–746, 1988.

Curry, J. A., Schramm, J. L., Rossow, W. B., and Randall, D. Overview of arctic cloud and radiation characteristics. *Journal of Climate*, 9(8):1731–1764, 1996.

Curtis, J., Hartmann, B., and Wendler, G. Climate variability for arctic alaska. In *AMS Proceedings of the Seventh Conference on Polar Meteorology and Oceanography of High Latitude Climate Variations, Hyannis, Mass*, 2003.

Dagsson-Waldhauserova, P., Renard, J.-B., Olafsson, H., Vignelles, D., Berthet, G., Verdier, N., and Duverger, V. Vertical distribution of aerosols in dust storms during the arctic winter. *Scientific reports*, 9(1):1–11, 2019.

Dall'Osto, M., Beddows, D., Tunved, P., Harrison, R. M., Lupi, A., Vitale, V., Becagli, S., Traversi, R., Park, K.-T., Yoon, Y. J., et al. Simultaneous measurements of aerosol size distributions at three sites in the european high arctic. *Atmospheric Chemistry and Physics*, 19(11):7377–7395, 2019.

Dasgupta, P. K., Campbell, S. W., Al-Horr, R. S., Ullah, S. R., Li, J., Amalfitano, C., and Poor, N. D. Conversion of sea salt aerosol to nano3 and the production of hcl: Analysis of temporal behavior of aerosol chloride/nitrate and gaseous hcl/hno3 concentrations with aim. *Atmospheric Environment*, 41(20):4242–4257, 2007.

De Leeuw, G., Neele, F. P., Hill, M., Smith, M. H., and Vignati, E. Production of sea spray aerosol in the surf zone. *Journal of Geophysical Research: Atmospheres*, 105(D24):29397–29409, 2000.

De Leeuw, G., Andreas, E. L., Anguelova, M. D., Fairall, C., Lewis, E. R., O'Dowd, C., Schulz, M., and Schwartz, S. E. Production flux of sea spray aerosol. *Reviews of Geophysics*, 49(2), 2011.

De Meij, A., , and Vinuesa, J. Impact of srtm and corine land cover data on meteorological parameters using wrf. *Atmospheric Research*, 143:351–370, 2014.

Delmas, R., Megie, G., and Peuch, V. Atmosphere physics and chemistry; physique et chimie de l'atmosphere. 2005.

Denby, B. R., Ketzel, M., Ellermann, T., Stojiljkovic, A., Kupiainen, K., Niemi, J., Norman, M., Johansson, C., Gustafsson, M., Blomqvist, G., et al. Road salt emissions: A comparison of measurements and modelling using the nortrip road dust emission model. *Atmospheric environment*, 141:508–522, 2016.

Dentener, F., Williams, J., and Metzger, S. Aqueous phase reaction of hno4: The impact on tropospheric chemistry. *Journal of atmospheric chemistry*, 41(2):109–133, 2002.

Douglas, T. A., Domine, F., Barret, M., Anastasio, C., Beine, H. J., Bottenheim, J., Grannas, A., Houdier, S., Netcheva, S., Rowland, G., et al. Frost flowers growing in the arctic ocean-atmosphere–sea ice–snow interface: 1. chemical composition. *Journal of Geophysical Research: Atmospheres*, 117(D14), 2012.

Drozd, G. T., Zhao, Y., Saliba, G., Frodin, B., Maddox, C., Oliver Chang, M.-C., Maldonado, H., Sardar, S., Weber, R. J., Robinson, A. L., et al. Detailed speciation of intermediate volatility and semivolatile organic compound emissions from gasoline vehicles: Effects of cold-starts and implications for secondary organic aerosol formation. *Environmental science & technology*, 53(3):1706–1714, 2018.

Druckenmiller, M. L., Eicken, H., Johnson, M. A., Pringle, D. J., and Williams, C. C. Toward an integrated coastal sea-ice observatory: System components and a case study at barrow, alaska. *Cold Regions Science and Technology*, 56(2-3):61–72, 2009.

Duncan, B. and Bey, I. A modeling study of the export pathways of pollution from europe: Seasonal and interannual variations (1987–1997). *Journal of Geophysical Research: Atmospheres*, 109(D8), 2004.

Durre, I., Yin, X., Vose, R. S., Applequist, S., and Arnfield, J. Enhancing the data coverage in the integrated global radiosonde archive. *Journal of Atmospheric and Oceanic Technology*, 35(9):1753–1770, 2018.

Easter, R. C., Ghan, S. J., Zhang, Y., Saylor, R. D., Chapman, E. G., Laulainen, N. S., Abdul-Razzak, H., Leung, L. R., Bian, X., and Zaveri, R. A. Mirage: Model description and evaluation of aerosols and trace gases. *Journal of Geophysical Research: Atmospheres*, 109(D20), 2004.

Eckhardt, S., Quennehen, B., Oliviè, D. J. L., Berntsen, T. K., Cherian, R., Christensen, J., Collins, W., Crepinsek, S., Daskalakis, N., Flanner, M., et al. Current model capabilities for simulating black carbon and sulfate concentrations in the arctic atmosphere: a multi-model evaluation using a comprehensive measurement data set. *Atmospheric Chemistry and Physics*, 15(16):9413–9433, 2015.

Eicken, H., Jones, J., Meyer, F., Mahoney, A., Druckenmiller, M. L., Rohith, M., and Kambhamettu, C. Environmental security in arctic ice-covered seas: From strategy to tactics of hazard identification and emergency response. *Marine Technology Society Journal*, 45(3):37–48, 2011.

Eleftheriadis, K., Vratolis, S., and Nyeki, S. Aerosol black carbon in the european arctic: Measurements at zeppelin station, ny-Ålesund, svalbard from 1998–2007. *Geophysical Research Letters*, 36(2), 2009. doi: https://doi.org/10.1029/2008GL035741.

Emmons, L., Arnold, S., Monks, S., Huijnen, V., Tilmes, S., Law, K. S., Thomas, J. L., Raut, J.-C., Bouarar, I., Turquety, S., et al. The polarcat model intercomparison project (polmip): overview and evaluation with observations. *Atmospheric Chemistry and Physics*, 15(12):6721–6744, 2015.

Emmons, L. K., Walters, S., Hess, P. G., Lamarque, J.-F., Pfister, G. G., Fillmore, D., Granier, C., Guenther, A., Kinnison, D., Laepple, T., et al. Description and evaluation of the model for ozone and related chemical tracers, version 4 (mozart-4). *Geoscientific Model Development*, 3(1):43–67, 2010.

Emmons, L. K., Schwantes, R. H., Orlando, J. J., Tyndall, G., Kinnison, D., Lamarque, J.-F., Marsh, D., Mills, M. J., Tilmes, S., Bardeen, C., Buchholz, R. R., Conley, A., Gettelman, A., Garcia, R., Simpson, I., Blake, D. R., Meinardi, S., and Pétron, G. The chemistry mechanism in the community earth system model version 2 (cesm2). *Journal of Advances in Modeling Earth Systems*, 12(4):e2019MS001882, 2020. doi: https://doi.org/10.1029/2019MS001882. URL https://agupubs.onlinelibrary.wiley.com/doi/abs/10.1029/2019MS001882. e2019MS001882 2019MS001882.

Erisman, J. W., Van Pul, A., and Wyers, P. Parametrization of surface resistance for the quantification of atmospheric deposition of acidifying pollutants and ozone. *Atmospheric Environment*, 28(16):2595–2607, 1994.

Esteve, B. J. and Sistach, M. U. Land use influence in wrf model. a high resolution mesoscale modeling over oriental pyrenees.

Evans, M., Kholod, N., Malyshev, V., Tretyakova, S., Gusev, E., Yu, S., and Barinov, A. Black carbon emissions from russian diesel sources: case study of murmansk. *Atmospheric Chemistry and Physics*, 15(14):8349–8359, 2015.

Fahey, K. M. and Pandis, S. N. Optimizing model performance: variable size resolution in cloud chemistry modeling. *Atmospheric Environment*, 35(26):4471–4478, 2001.

Falkovich, A. H., Ganor, E., Levin, Z., Formenti, P., and Rudich, Y. Chemical and mineralogical analysis of individual mineral dust particles. *Journal of Geophysical Research: Atmospheres*, 106(D16):18029–18036, 2001.

Fan, S.-M. and Jacob, D. J. Surface ozone depletion in arctic spring sustained by bromine reactions on aerosols. *Nature*, 359(6395):522–524, 1992.

Fast, J. D., Gustafson Jr, W. I., Easter, R. C., Zaveri, R. A., Barnard, J. C., Chapman, E. G., Grell, G. A., and Peckham, S. E. Evolution of ozone, particulates, and aerosol direct radiative forcing in the vicinity of houston using a fully coupled meteorology-chemistry-aerosol model. *Journal of Geophysical Research: Atmospheres*, 111(D21), 2006.

Fioletov, V. E., McLinden, C. A., Krotkov, N., Li, C., Joiner, J., Theys, N., Carn, S., and Moran, M. D. A global catalogue of large so 2 sources and emissions derived from the ozone monitoring instrument. *Atmospheric Chemistry and Physics*, 16(18):11497–11519, 2016.

Fisher, J. A., Jacob, D. J., Wang, Q., Bahreini, R., Carouge, C. C., Cubison, M. J., Dibb, J. E., Diehl, T., Jimenez, J. L., Leibensperger, E. M., et al. Sources, distribution, and acidity of sulfate–ammonium aerosol in the arctic in winter–spring. *Atmospheric Environment*, 45(39):7301–7318, 2011.

Flanner, M. G. Arctic climate sensitivity to local black carbon. *Journal of Geophysical Research: Atmospheres*, 118(4):1840–1851, 2013.

Flanner, M. G., Zender, C. S., Randerson, J. T., and Rasch, P. J. Present-day climate forcing and response from black carbon in snow. *Journal of Geophysical Research: Atmospheres*, 112(D11), 2007.

Flanner, M. G., Zender, C. S., Hess, P. G., Mahowald, N. M., Painter, T. H., Ramanathan, V., and Rasch, P. Springtime warming and reduced snow cover from carbonaceous particles. *Atmospheric Chemistry and Physics*, 9(7):2481–2497, 2009.

Fochesatto, G. J., Mayfield, J. A., Starkenburg, D. P., Gruber, M. A., and Conner, J. Occurrence of shallow cold flows in the winter atmospheric boundary layer of interior of alaska. *Meteorology and Atmospheric Physics*, 127(4):369–382, 2015.

Foote, E. Art. xxxi.–circumstances affecting the heat of the sun's rays. *American Journal of Science and Arts (1820-1879)*, 22(66):382, 1856.

Fowler, D., Brimblecombe, P., Burrows, J., Heal, M. R., Grennfelt, P., Stevenson, D. S., Jowett, A., Nemitz, E., Coyle, M., Liu, X., et al. A chronology of global air quality. *Philosophical Transactions of the Royal Society A*, 378(2183):20190314, 2020.

Freitas, S. R., Longo, K. M., Chatfield, R., Latham, D., Silva Dias, M., Andreae, M., Prins, E., Santos, J., Gielow, R., and Carvalho Jr, J. Including the sub-grid scale plume rise of vegetation fires in low resolution atmospheric transport models. *Atmospheric Chemistry and Physics*, 7(13):3385–3398, 2007.

Freud, E., Krejci, R., Tunved, P., Leaitch, R., Nguyen, Q. T., Massling, A., Skov, H., and Barrie, L. Pan-arctic aerosol number size distributions: seasonality and transport patterns. *Atmospheric Chemistry and Physics*, 17(13):8101–8128, 2017.

Frey, M. M., Norris, S. J., Brooks, I. M., Anderson, P. S., Nishimura, K., Yang, X., Jones, A. E., Nerentorp Mastromonaco, M. G., Jones, D. H., and Wolff, E. W. First direct observation of sea salt aerosol production from blowing snow above sea ice. *Atmospheric Chemistry and Physics*, 20(4):2549–2578, 2020.

Friedl, M. A., McIver, D. K., Hodges, J. C., Zhang, X. Y., Muchoney, D., Strahler, A. H., Woodcock, C. E., Gopal, S., Schneider, A., Cooper, A., et al. Global land cover mapping from modis: algorithms and early results. *Remote sensing of Environment*, 83(1-2):287–302, 2002.

Frossard, A. A., Shaw, P. M., Russell, L. M., Kroll, J. H., Canagaratna, M. R., Worsnop, D. R., Quinn, P. K., and Bates, T. S. Springtime arctic haze contributions of submicron organic particles from european and asian combustion sources. *Journal of Geophysical Research: Atmospheres*, 116(D5), 2011.

Frossard, A. A., Russell, L. M., Burrows, S. M., Elliott, S. M., Bates, T. S., and Quinn, P. K. Sources and composition of submicron organic mass in marine aerosol particles. *Journal of Geophysical Research: Atmospheres*, 119(22):12,977–13,003, 2014. doi: https://doi.org/10.1002/2014JD021913. URL https://agupubs.onlinelibrary.wiley.com/doi/abs/10.1002/2014JD021913.

Fuchs, N. A., Daisley, R., Fuchs, M., Davies, C., and Straumanis, M. The mechanics of aerosols. *Physics Today*, 18(4):73, 1965.

Fuentes, E., Coe, H., Green, D., Leeuw, G. d., and McFiggans, G. On the impacts of phytoplankton-derived organic matter on the properties of the primary marine aerosol–part 1: Source fluxes. *Atmospheric Chemistry and Physics*, 10(19):9295–9317, 2010.

Fuentes, E., Coe, H., Green, D., and McFiggans, G. On the impacts of phytoplankton-derived organic matter on the properties of the primary marine aerosol–part 2: Composition, hygroscopicity and cloud condensation activity. *Atmospheric Chemistry and Physics*, 11(6):2585–2602, 2011.

Fujiki, T., Matsumoto, K., Honda, M. C., Kawakami, H., and Watanabe, S. Phytoplankton composition in the subarctic north pacific during autumn 2005. *Journal of plankton research*, 31(2):179–191, 2009.

Galle, B., Johansson, M., Rivera, C., Zhang, Y., Kihlman, M., Kern, C., Lehmann, T., Platt, U., Arellano, S., and Hidalgo, S. Network for observation of volcanic and atmospheric change (novac)—a global network for volcanic gas monitoring: Network layout and instrument description. *Journal of Geophysical Research: Atmospheres*, 115(D5), 2010.

Gamnitzer, U., Karstens, U., Kromer, B., Neubert, R. E., Meijer, H. A., Schroeder, H., and Levin, I. Carbon monoxide: A quantitative tracer for fossil fuel co2? *Journal of Geophysical Research: Atmospheres*, 111 (D22), 2006.

Gao, M., Carmichael, G. R., Wang, Y., Ji, D., Liu, Z., and Wang, Z. Improving simulations of sulfate aerosols during winter haze over northern china: the impacts of heterogeneous oxidation by no2. *Frontiers of Environmental Science & Engineering*, 10(5):1–11, 2016.

Gao, Y., Anderson, J. R., and Hua, X. Dust characteristics over the north pacific observed through shipboard measurements during the ace-asia experiment. *Atmospheric Environment*, 41(36):7907–7922, 2007.

Garrett, T. J., Brattström, S., Sharma, S., Worthy, D. E., and Novelli, P. The role of scavenging in the seasonal transport of black carbon and sulfate to the arctic. *Geophysical Research Letters*, 38(16), 2011.

Giorgi, F. Dry deposition velocities of atmospheric aerosols as inferred by applying a particle dry deposition parameterization to a general circulation model. *Tellus B*, 40(1):23–41, 1988.

Gliß, J., Mortier, A., Schulz, M., Andrews, E., Balkanski, Y., Bauer, S. E., Benedictow, A. M., Bian, H., Checa-Garcia, R., Chin, M., et al. Aerocom phase iii multi-model evaluation of the aerosol life cycle and

optical properties using ground-and space-based remote sensing as well as surface in situ observations. *Atmospheric Chemistry and Physics*, 21(1):87–128, 2021.

Goddijn-Murphy, L., Woolf, D., and Callaghan, A. H. Parameterizations and algorithms for oceanic whitecap coverage. *Journal of Physical Oceanography*, 41:742–756, 2011.

Gong, S., Barrie, L., and Blanchet, J.-P. Modeling sea-salt aerosols in the atmosphere: 1. model development. *Journal of Geophysical Research: Atmospheres*, 102(D3):3805–3818, 1997.

Gordon, T. D., Tkacik, D. S., Presto, A. A., Zhang, M., Jathar, S. H., Nguyen, N. T., Massetti, J., Truong, T., Cicero-Fernandez, P., Maddox, C., et al. Primary gas-and particle-phase emissions and secondary organic aerosol production from gasoline and diesel off-road engines. *Environmental science & technology*, 47(24):14137–14146, 2013.

Graf, H.-F., Feichter, J., and Langmann, B. Volcanic sulfur emissions: Estimates of source strength and its contribution to the global sulfate distribution. *Journal of Geophysical Research: Atmospheres*, 102(D9): 10727–10738, 1997.

Graham, R. M., Rinke, A., Cohen, L., Hudson, S. R., Walden, V. P., Granskog, M. A., Dorn, W., Kayser, M., and Maturilli, M. A comparison of the two arctic atmospheric winter states observed during n-ice2015 and sheba. *Journal of Geophysical Research: Atmospheres*, 122(11):5716–5737, 2017.

Graham, R. M., Hudson, S. R., and Maturilli, M. Improved performance of era5 in arctic gateway relative to four global atmospheric reanalyses. *Geophysical Research Letters*, 46(11):6138–6147, 2019.

Granier, C., Bessagnet, B., Bond, T., D'Angiola, A., van Der Gon, H. D., Frost, G. J., Heil, A., Kaiser, J. W., Kinne, S., Klimont, Z., et al. Evolution of anthropogenic and biomass burning emissions of air pollutants at global and regional scales during the 1980–2010 period. *Climatic change*, 109(1):163–190, 2011.

Granier, C., Darras, S., Denier van der Gon, H., Doubalova, J., Elguindi, N., Galle, B., Gauss, M., Guevara, J., Jalkanen, J., Kuenen, C., et al. The copernicus atmosphere monitoring service global and regional emissions. *Reading, United Kingdom: Copernicus Atmosphere Monitoring Service. https://doi.org/10.24380/d0bn-kx16*, 2019.

Grannas, A., Jones, A. E., Dibb, J., Ammann, M., Anastasio, C., Beine, H., Bergin, M., Bottenheim, J., Boxe, C., Carver, G., et al. An overview of snow photochemistry: evidence, mechanisms and impacts. *Atmospheric chemistry and physics*, 7(16):4329–4373, 2007.

Greenaway, K. Experiences with arctic flying weather, royal meteorol. *Soc. Can. Branch, Toronto, Ont., Canada*, page 8, 1950.

Grell, G. A., Dudhia, J., Stauffer, D. R., et al. A description of the fifth-generation penn state/ncar mesoscale model (mm5). 1994.

Grell, G. A., Peckham, S. E., Schmitz, R., McKeen, S. A., Frost, G., Skamarock, W. C., and Eder, B. Fully coupled "online" chemistry within the wrf model. *Atmospheric Environment*, 39(37):6957–6975, 2005.

Grennfelt, P., Engleryd, A., Forsius, M., Hov, Ø., Rodhe, H., and Cowling, E. Acid rain and air pollution: 50 years of progress in environmental science and policy. *Ambio*, 49(4):849–864, 2020.

Groot Zwaaftink, C., Grythe, H., Skov, H., and Stohl, A. Substantial contribution of northern high-latitude sources to mineral dust in the arctic. *Journal of Geophysical Research: Atmospheres*, 121(22):13–678, 2016.

Grythe, H., Ström, J., Krejci, R., Quinn, P., and Stohl, A. A review of sea-spray aerosol source functions using a large global set of sea salt aerosol concentration measurements. *Atmospheric Chemistry and Physics*, 14(3):1277–1297, 2014.

Guenther, A., Karl, T., Harley, P., Wiedinmyer, C., Palmer, P. I., and Geron, C. Estimates of global terrestrial isoprene emissions using megan (model of emissions of gases and aerosols from nature). *Atmospheric Chemistry and Physics*, 6(11):3181–3210, 2006.

Guenther, A., Jiang, X., Heald, C. L., Sakulyanontvittaya, T., Duhl, T., Emmons, L., and Wang, X. The model of emissions of gases and aerosols from nature version 2.1 (megan2. 1): an extended and updated framework for modeling biogenic emissions. *Geoscientific Model Development*, 5(6):1471–1492, 2012.

Hall, A. The role of surface albedo feedback in climate. *Journal of Climate*, 17(7):1550–1568, 2004.

Hancke, K., Lund-Hansen, L. C., Lamare, M. L., Højlund Pedersen, S., King, M. D., Andersen, P., and Sorrell, B. K. Extreme low light requirement for algae growth underneath sea ice: A case study from station nord, ne greenland. *Journal of Geophysical Research: Oceans*, 123(2):985–1000, 2018.

Haque, M. M., Kawamura, K., Deshmukh, D. K., Kunwar, B., and Kim, Y. Biomass burning is an important source of organic aerosols in interior alaska. *Journal of Geophysical Research: Atmospheres*, 126(12): e2021JD034586, 2021.

Hara, K., Osada, K., Matsunaga, K., Iwasaka, Y., Shibata, T., and Furuya, K. Atmospheric inorganic chlorine and bromine species in arctic boundary layer of the winter/spring. *Journal of Geophysical Research: Atmospheres*, 107(D18):AAC–4, 2002.

Hartery, S., Toohey, D., Revell, L., Sellegri, K., Kuma, P., Harvey, M., and McDonald, A. J. Constraining the surface flux of sea spray particles from the southern ocean. *Journal of Geophysical Research: Atmospheres*, 125(4):e2019JD032026, 2020.

Hartmann, B. and Wendler, G. Climatology of the winter surface temperature inversion in fairbanks, alaska. In *8th Conference on Polar Meteorology and Oceanography*, pages 1–7, 2005.

Hatch, L. E., Rivas-Ubach, A., Jen, C. N., Lipton, M., Goldstein, A. H., and Barsanti, K. C. Measurements of i/svocs in biomass-burning smoke using solid-phase extraction disks and two-dimensional gas chromatography. *Atmospheric Chemistry and Physics*, 18(24):17801–17817, 2018.

Haywood, J. and Shine, K. The effect of anthropogenic sulfate and soot aerosol on the clear sky planetary radiation budget. *Geophysical Research Letters*, 22(5):603–606, 1995.

He, L.-Y., Hu, M., Zhang, Y.-H., Huang, X.-F., and Yao, T.-T. Fine particle emissions from on-road vehicles in the zhujiang tunnel, china. *Environmental science & technology*, 42(12):4461–4466, 2008.

He, P., Alexander, B., Geng, L., Chi, X., Fan, S., Zhan, H., Kang, H., Zheng, G., Cheng, Y., Su, H., et al. Isotopic constraints on heterogeneous sulfate production in beijing haze. *Atmospheric Chemistry and Physics*, 18(8):5515–5528, 2018.

Heidam, N., Christensen, J., Skov, H., and Wåhlin, P. Monitoring and modelling of the atmospheric environment in greenland. a review. *Sci Total Environ*, 331(1-3):5–28, 2004.

Hersbach, H. and Dee, D. Era5 reanalysis is in production, ecmwf newsletter, number 147–spring 2016, 2016.

Hinzman, L. D., Deal, C. J., McGuire, A. D., Mernild, S. H., Polyakov, I. V., and Walsh, J. E. Trajectory of the arctic as an integrated system. *Ecological Applications*, 23(8):1837–1868, 2013.

Hirdman, D., Sodemann, H., Eckhardt, S., Burkhart, J. F., Jefferson, A., Mefford, T., Quinn, P. K., Sharma, S., Ström, J., and Stohl, A. Source identification of short-lived air pollutants in the arctic using statistical analysis of measurement data and particle dispersion model output. *Atmospheric Chemistry and Physics*, 10(2):669–693, 2010.

Hirschberg, P. A. and Fritsch, J. M. Tropopause undulations and the development of extratropical cyclones. part ii: Diagnostic analysis and conceptual model. *Monthly weather review*, 119(2):518–550, 1991.

Hodnebrog, Ø., Marelle, L., Alterskjær, K., Wood, R. R., Ludwig, R., Fischer, E. M., Richardson, T., Forster, P., Sillmann, J., and Myhre, G. Intensification of summer precipitation with shorter time-scales in europe. *Environmental Research Letters*, 14(12):124050, 2019.

Hodson, A., Roberts, T. J., Engvall, A.-C., Holmén, K., and Mumford, P. Glacier ecosystem response to episodic nitrogen enrichment in svalbard, european high arctic. *Biogeochemistry*, 98(1):171–184, 2010.

Hodzic, A., Jimenez, J. L., Madronich, S., Canagaratna, M., DeCarlo, P. F., Kleinman, L., and Fast, J. Modeling organic aerosols in a megacity: potential contribution of semi-volatile and intermediate volatility primary organic compounds to secondary organic aerosol formation. *Atmospheric Chemistry and Physics*, 10(12):5491–5514, 2010.

Hoesly, R. M., Smith, S. J., Feng, L., Klimont, Z., Janssens-Maenhout, G., Pitkanen, T., Seibert, J. J., Vu, L., Andres, R. J., Bolt, R. M., et al. Historical (1750–2014) anthropogenic emissions of reactive gases and aerosols from the community emissions data system (ceds). *Geoscientific Model Development*, 11(1): 369–408, 2018.

Hoffman, E. J. and Duce, R. A. Factors influencing the organic carbon content of marine aerosols: A laboratory study. *Journal of Geophysical Research*, 81(21):3667–3670, 1976.

Hofmann, H., Hoffmann, P., and Lieser, K. Transition metals in atmospheric aqueous samples, analytical determination and speciation. *Fresenius' journal of analytical chemistry*, 340(9):591–597, 1991.

Höglund-Isaksson, L., Gómez-Sanabria, A., Klimont, Z., Rafaj, P., and Schöpp, W. Technical potentials and costs for reducing global anthropogenic methane emissions in the 2050 timeframe–results from the gains model. *Environmental Research Communications*, 2(2):025004, 2020.

Holton, J. *The dynamic meteorology of the stratosphere and mesosphere*, volume 15. Springer, 2016.

Hong, S.-Y. A new stable boundary-layer mixing scheme and its impact on the simulated east asian summer monsoon. *Quarterly Journal of the Royal Meteorological Society*, 136(651):1481–1496, 2010.

Hong, S.-Y. and Kim, S.-W. Stable boundary layer mixing in a vertical diffusion scheme. In *18th Symposium on Boundary Layers and Turbulence B*, volume 16, 2008.

Hong, S.-Y., Noh, Y., and Dudhia, J. A new vertical diffusion package with an explicit treatment of entrainment processes. *Monthly weather review*, 134(9):2318–2341, 2006.

Hoppel, W. A., Frick, G. M., and Fitzgerald, J. W. Surface source function for sea-salt aerosol and aerosol dry deposition to the ocean surface. *Journal of Geophysical Research: Atmospheres*, 107(D19):AAC 7–1–AAC 7–17, 2002. doi: https://doi.org/10.1029/2001JD002014. URL https://agupubs.onlinelibrary.wiley.com/doi/abs/10.1029/2001JD002014.

Hordon, R. M. *Siberian (Asiatic) High*, pages 656–657. Springer Netherlands, Dordrecht, 2005. ISBN 978-1-4020-3266-0. doi: 10.1007/1-4020-3266-8_185. URL https://doi.org/10.1007/1-4020-3266-8_185.

Horowitz, H. M., Holmes, C., Wright, A., Sherwen, T., Wang, X., Evans, M., Huang, J., Jaeglé, L., Chen, Q., Zhai, S., and Alexander, B. Effects of sea salt aerosol emissions for marine cloud brightening on atmospheric chemistry: Implications for radiative forcing. *Geophysical Research Letters*, 47(4):e2019GL085838, 2020. doi: https://doi.org/10.1029/2019GL085838. URL https://agupubs.onlinelibrary.wiley.com/doi/abs/10.1029/2019GL085838. e2019GL085838 2019GL085838.

Hu, X.-M., Nielsen-Gammon, J. W., and Zhang, F. Evaluation of three planetary boundary layer schemes in the wrf model. *Journal of Applied Meteorology and Climatology*, 49(9):1831–1844, 2010.

Huang, J. and Jaeglé, L. Wintertime enhancements of sea salt aerosol in polar regions consistent with a sea ice source from blowing snow. *Atmospheric Chemistry and Physics*, 17(5):3699–3712, 2017. doi: 10.5194/acp-17-3699-2017. URL https://acp.copernicus.org/articles/17/3699/2017/.

Huang, J. and Jaeglé, L. Wintertime enhancements of sea salt aerosol in polar regions consistent with a sea ice source from blowing snow. *Atmospheric Chemistry and Physics*, 17(5):3699–3712, 2017.

Huang, L., An, J., Koo, B., Yarwood, G., Yan, R., Wang, Y., Huang, C., and Li, L. Sulfate formation during heavy winter haze events and the potential contribution from heterogeneous so 2+ no 2 reactions in the yangtze river delta region, china. *Atmospheric Chemistry and Physics*, 19(22):14311–14328, 2019.

Huang, X., Qiu, R., Chan, C. K., and Kant, P. R. Evidence of high pm2. 5 strong acidity in ammonia-rich atmosphere of guangzhou, china: transition in pathways of ambient ammonia to form aerosol ammonium at [nh4+]/[so42−]= 1.5. *Atmospheric Research*, 99(3-4):488–495, 2011.

Huang, Z., Huang, J., Hayasaka, T., Wang, S., Zhou, T., and Jin, H. Short-cut transport path for asian dust directly to the arctic: a case study. *Environmental Research Letters*, 10(11):114018, 2015.

Iacono, M. J., D. J. S. M. E. J. S. M. W. C. S. A. and D., C. W. Radiative forcing by long–lived greenhouse gases: Calculations with the aer radiative transfer models. *J. Geophys. Res.*, 113, 2008. doi: doi:10.1029/2008JD009944.

Iacono, M. J. and Nehrkorn, T. R. P3. 7 assessment of radiation options in the advanced research wrf weather forecast model. 2010.

Iacono, M. J., Delamere, J. S., Mlawer, E. J., Shephard, M. W., Clough, S. A., and Collins, W. D. Radiative forcing by long-lived greenhouse gases: Calculations with the aer radiative transfer models. *Journal of Geophysical Research: Atmospheres*, 113(D13), 2008.

Ikeda, K., Tanimoto, H., Sugita, T., Akiyoshi, H., Kanaya, Y., Zhu, C., and Taketani, F. Tagged tracer simulations of black carbon in the arctic: transport, source contributions, and budget. *Atmospheric Chemistry and Physics*, 17(17):10515–10533, 2017a. doi: 10.5194/acp-17-10515-2017. URL https://acp.copernicus.org/articles/17/10515/2017/.

Ikeda, K., Tanimoto, H., Sugita, T., Akiyoshi, H., Kanaya, Y., Zhu, C., and Taketani, F. Tagged tracer simulations of black carbon in the arctic: transport, source contributions, and budget. *Atmospheric Chemistry and Physics*, 17(17):10515–10533, 2017b.

Ikeda, K., Tanimoto, H., Kanaya, Y., and Taketani, F. Evaluation of anthropogenic emissions of black carbon from east asia in six inventories: constraints from model simulations and surface observations on fukue island, japan. *Environmental Science: Atmospheres*, 2(3):416–427, 2022.

Ilyinskaya, E., Schmidt, A., Mather, T. A., Pope, F. D., Witham, C., Baxter, P., Jóhannsson, T., Pfeffer, M., Barsotti, S., Singh, A., et al. Understanding the environmental impacts of large fissure eruptions: Aerosol and gas emissions from the 2014–2015 holuhraun eruption (iceland). *Earth and Planetary Science Letters*, 472:309–322, 2017.

Institute, H. E. State of global air 2019, 2019.

Ioannidis, E., Law, K. S., Raut, J.-C., Marelle, L., Onishi, T., Kirpes, R. M., Upchurch, L., Massling, A., Skov, H., Quinn, P. K., et al. Modelling wintertime arctic haze and sea-spray aerosols. *EGUsphere*, pages 1–56, 2022.

IPCC. Ipcc, 2013: Climate change 2013: The physical science basis. contribution of working group i to the fifth assessment report of the intergovernmental panel on climate change [stocker, t.f., d. qin, g.-k. plattner, m. tignor, s.k. allen, j. boschung, a. nauels, y. xia, v. bex and p.m. midgley (eds.)]. page 1535 pp, 2013.

IPCC. Ipcc, 2021: Summary for policymakers. in: Climate change 2021: The physical science basis. contribution of working group i to the sixth assessment report of the intergovernmental panel on climate change [masson-delmotte, v., p. zhai, a. pirani, s.l. connors, c. péan, s. berger, n. caud, y. chen, l. goldfarb, m.i. gomis, m. huang, k. leitzell, e. lonnoy, j.b.r. matthews, t.k. maycock, t. waterfield, o. yelekçi, r. yu, and b. zhou (eds.)]. page pp. 332, 2021. doi: doi:10.1017/9781009157896.001.

Ishida, Y. 30 years of research on dimethylsulfoniopriopionate. In *Biological and environmental chemistry of DMSP and related sulfonium compounds*, pages 1–12. Springer, 1996.

Iversen, T. On the atmospheric transport of pollution to the arctic. *Geophysical Research Letters*, 11(5):457–460, 1984.

Iversen, T. Atmospheric transport pathways for the arctic. In *Chemical exchange between the atmosphere and polar snow*, pages 71–92. Springer, 1996.

Ives, J. D. and Barry, R. G. *Arctic and alpine environments*, volume 6. Routledge, 2019.

Jacobi, H., Voisin, D., Jaffrezo, J., Cozic, J., and Douglas, T. Chemical composition of the snowpack during the oasis spring campaign 2009 at barrow, alaska. *Journal of Geophysical Research: Atmospheres*, 117(D14), 2012.

Jacobson, M. Z., Turco, R. P., Jensen, E. J., and Toon, O. B. Modeling coagulation among particles of different composition and size. *Atmospheric Environment*, 28(7):1327–1338, 1994.

Jaeglé, L., Quinn, P. K., Bates, T. S., Alexander, B., and Lin, J.-T. Global distribution of sea salt aerosols: new constraints from in situ and remote sensing observations. *Atmospheric Chemistry and Physics*, 11 (7):3137–3157, 2011. doi: 10.5194/acp-11-3137-2011. URL https://acp.copernicus.org/articles/11/3137/2011/.

Janić, Z. I. Nonsingular implementation of the mellor-yamada level 2.5 scheme in the ncep meso model. 2001.

Janjic, Z. The surface layer in the ncep eta model, paper presented at. In *Eleventh Conference on Numerical Weather Prediction, Am. Meteorol. Soc., Norfolk, Va*, 1996.

Janjic, Z. I., Gerrity Jr, J., and Nickovic, S. An alternative approach to nonhydrostatic modeling. *Monthly Weather Review*, 129(5):1164–1178, 2001.

Jiang, J., Stevenson, D. S., Uwizeye, A., Tempio, G., and Sutton, M. A. A climate-dependent global model of ammonia emissions from chicken farming. *Biogeosciences*, 18(1):135–158, 2021.

Jiang, X., Wiedinmyer, C., Chen, F., Yang, Z.-L., and Lo, J. C.-F. Predicted impacts of climate and land use change on surface ozone in the houston, texas, area. *Journal of Geophysical Research: Atmospheres*, 113 (D20), 2008.

Jiménez, P. A., Dudhia, J., González-Rouco, J. F., Navarro, J., Montávez, J. P., and García-Bustamante, E. A revised scheme for the wrf surface layer formulation. *Monthly weather review*, 140(3):898–918, 2012.

Johansson, L., Jalkanen, J.-P., and Kukkonen, J. Global assessment of shipping emissions in 2015 on a high spatial and temporal resolution. *Atmospheric Environment*, 167:403–415, 2017.

Johnson, M. S., Strawbridge, K., Knowland, K. E., Keller, C., and Travis, M. Long-range transport of siberian biomass burning emissions to north america during firex-aq. *Atmospheric Environment*, 252:118241, 2021.

Jordan, R. A one-dimensional temperature model for a snow cover : technical documentation for sntherm.89. 1991.

Joyce, P., Von Glasow, R., and Simpson, W. The fate of no x emissions due to nocturnal oxidation at high latitudes: 1-d simulations and sensitivity experiments. *Atmospheric Chemistry and Physics*, 14(14):7601–7616, 2014.

Jun, S.-Y., Ho, C.-H., Jeong, J.-H., Choi, Y.-S., and Kim, B.-M. Recent changes in winter arctic clouds and their relationships with sea ice and atmospheric conditions. *Tellus A: Dynamic Meteorology and Oceanography*, 68(1):29130, 2016.

Kahl, J. D. Characteristics of the low-level temperature inversion along the alaskan arctic coast. *International Journal of Climatology*, 10(5):537–548, 1990.

Kahl, J. D., Serreze, M. C., and Schnell, R. C. Tropospheric low-level temperature inversions in the canadian arctic. *Atmosphere-Ocean*, 30(4):511–529, 1992.

Kalabin, G. and Moiseenko, T. Ecodynamics of anthropogenic mining provinces: From degradation to rehabilitation. In *Doklady Earth Sciences*, volume 437, pages 432–436. Springer, 2011.

Kanakidou, M., Seinfeld, J., Pandis, S., Barnes, I., Dentener, F. J., Facchini, M. C., Van Dingenen, R., Ervens, B., Nenes, A., Nielsen, C., et al. Organic aerosol and global climate modelling: a review. *Atmospheric Chemistry and Physics*, 5(4):1053–1123, 2005.

Kankanala, P. K. R. *Doppler sodar observations of the winds and structure in the lower atmosphere over Fairbanks, Alaska*. PhD thesis, University of Alaska Fairbanks, 2007.

Kashiwase, H., Ohshima, K. I., Nihashi, S., and Eicken, H. Evidence for ice-ocean albedo feedback in the arctic ocean shifting to a seasonal ice zone. *Scientific reports*, 7(1):1–10, 2017.

Kay, J. E., L'Ecuyer, T., Chepfer, H., Loeb, N., Morrison, A., and Cesana, G. Recent advances in arctic cloud and climate research. *Current Climate Change Reports*, 2(4):159–169, 2016.

Kayser, M., Maturilli, M., Graham, R. M., Hudson, S. R., Rinke, A., Cohen, L., Kim, J.-H., Park, S.-J., Moon, W., and Granskog, M. A. Vertical thermodynamic structure of the troposphere during the norwegian young sea ice expedition (n-ice2015). *Journal of Geophysical Research: Atmospheres*, 122(20):10–855, 2017.

Kellogg, W. W. Climatic feedback mechanisms involving the polar regions. *Climate of the Arctic*, 111:116, 1975.

Kelly, J. T., Bhave, P. V., Nolte, C. G., Shankar, U., and Foley, K. M. Simulating emission and chemical evolution of coarse sea-salt particles in the community multiscale air quality (cmaq) model. *Geoscientific Model Development*, 3(1):257–273, 2010. doi: 10.5194/gmd-3-257-2010. URL https://gmd.copernicus.org/articles/3/257/2010/.

Kenagy, H. S., Sparks, T. L., Ebben, C. J., Wooldrige, P. J., Lopez-Hilfiker, F. D., Lee, B. H., Thornton, J. A., McDuffie, E. E., Fibiger, D. L., Brown, S. S., et al. Nox lifetime and noy partitioning during winter. *Journal of Geophysical Research: Atmospheres*, 123(17):9813–9827, 2018.

Kirpes, R. M., Bondy, A. L., Bonanno, D., Moffet, R. C., Wang, B., Laskin, A., Ault, A. P., and Pratt, K. A. Secondary sulfate is internally mixed with sea spray aerosol and organic aerosol in the winter arctic. *Atmospheric Chemistry and Physics*, 18(6):3937–3949, 2018. doi: 10.5194/acp-18-3937-2018. URL https://acp.copernicus.org/articles/18/3937/2018/.

Kirpes, R. M., Bonanno, D., May, N. W., Fraund, M., Barget, A. J., Moffet, R. C., Ault, A. P., and Pratt, K. A. Wintertime arctic sea spray aerosol composition controlled by sea ice lead microbiology. *ACS Central Science*, 5(11):1760–1767, 2019. doi: 10.1021/acscentsci.9b00541. URL https://doi.org/10.1021/acscentsci.9b00541.

Klimont, Z., Kupiainen, K., Heyes, C., Purohit, P., Cofala, J., Rafaj, P., Borken-Kleefeld, J., and Schöpp, W. Global anthropogenic emissions of particulate matter including black carbon. *Atmospheric Chemistry and Physics*, 17(14):8681–8723, 2017.

Kok, G. L., Gitlin, S. N., and Lazrus, A. L. Kinetics of the formation and decomposition of hydroxymethanesulfonate. *Journal of Geophysical Research: Atmospheres*, 91(D2):2801–2804, 1986.

Kolesar, K. R., Cellini, J., Peterson, P. K., Jefferson, A., Tuch, T., Birmili, W., Wiedensohler, A., and Pratt, K. A. Effect of prudhoe bay emissions on atmospheric aerosol growth events observed in utqiaġvik (barrow), alaska. *Atmospheric Environment*, 152:146–155, 2017. ISSN 1352-2310. doi: https://doi.org/10.1016/j.atmosenv.2016.12.019. URL https://www.sciencedirect.com/science/article/pii/S1352231016309785.

Kondo, Y., Sahu, L., Kuwata, M., Miyazaki, Y., Takegawa, N., Moteki, N., Imaru, J., Han, S., Nakayama, T., Oanh, N. K., et al. Stabilization of the mass absorption cross section of black carbon for filter-based absorption photometry by the use of a heated inlet. *Aerosol Science and Technology*, 43(8):741–756, 2009.

Kondo, Y., Sahu, L., Moteki, N., Khan, F., Takegawa, N., Liu, X., Koike, M., and Miyakawa, T. Consistency and traceability of black carbon measurements made by laser-induced incandescence, thermal-optical transmittance, and filter-based photo-absorption techniques. *Aerosol Science and Technology*, 45(2):295–312, 2011.

Kovacs, K., McIlwaine, R., Gannon, K., Taylor, A., and Scott, S. Complex behavior in the formaldehyde- sulfite reaction. *The Journal of Physical Chemistry A*, 109(1):283–288, 2005.

Krembs, C., Eicken, H., Junge, K., and Deming, J. High concentrations of exopolymeric substances in arctic winter sea ice: implications for the polar ocean carbon cycle and cryoprotection of diatoms. *Deep Sea Research Part I: Oceanographic Research Papers*, 49(12):2163–2181, 2002. ISSN 0967-0637. doi: https://doi.org/10.1016/S0967-0637(02)00122-X. URL https://www.sciencedirect.com/science/article/pii/S096706370200122X.

Krumpen, T., von Albedyll, L., Goessling, H. F., Hendricks, S., Juhls, B., Spreen, G., Willmes, S., Belter, H. J., Dethloff, K., Haas, C., et al. Mosaic drift expedition from october 2019 to july 2020: sea ice conditions from space and comparison with previous years. *The Cryosphere*, 15(8):3897–3920, 2021.

Lack, D. A., Cappa, C. D., Covert, D. S., Baynard, T., Massoli, P., Sierau, B., Bates, T. S., Quinn, P. K., Lovejoy, E. R., and Ravishankara, A. Bias in filter-based aerosol light absorption measurements due to organic aerosol loading: Evidence from ambient measurements. *Aerosol Science and Technology*, 42(12):1033–1041, 2008.

Lana, A., Bell, T., Simó, R., Vallina, S., Ballabrera-Poy, J., Kettle, A., Dachs, J., Bopp, L., Saltzman, E., Stefels, J., et al. An updated climatology of surface dimethlysulfide concentrations and emission fluxes in the global ocean. *Global Biogeochemical Cycles*, 25(1), 2011.

Lange, R., Dall'Osto, M., Skov, H., Nøjgaard, J., Nielsen, I., Beddows, D., Simó, R., Harrison, R. M., and Massling, A. Characterization of distinct arctic aerosol accumulation modes and their sources. *Atmospheric Environment*, 183:1–10, 2018.

Langner, J. and Rodhe, H. A global three-dimensional model of the tropospheric sulfur cycle. *Journal of Atmospheric Chemistry*, 13(3):225–263, 1991.

Laprise, R. The euler equations of motion with hydrostatic pressure as an independent variable. *Monthly weather review*, 120(1):197–207, 1992.

Law, K. S. and Stohl, A. Arctic air pollution: Origins and impacts. *science*, 315(5818):1537–1540, 2007.

Law, K. S., Stohl, A., Quinn, P. K., Brock, C. A., Burkhart, J. F., Paris, J.-D., Ancellet, G., Singh, H. B., Roiger, A., Schlager, H., et al. Arctic air pollution: New insights from polarcat-ipy. *Bulletin of the American Meteorological Society*, 95(12):1873–1895, 2014.

Law, K. S., Roiger, A., Thomas, J. L., Marelle, L., Raut, J.-C., Dalsøren, S., Fuglestvedt, J., Tuccella, P., Weinzierl, B., and Schlager, H. Local arctic air pollution: Sources and impacts. *Ambio*, 46(3):453–463, 2017.

Lawrimore, J., Ray, R., Applequist, S., Korzeniewski, B., and Menne, M. Global summary of the month and year, version 1.0. *NOAA National Centers for Environmental Information*, 2016.

Leaitch, W. R., Russell, L. M., Liu, J., Kolonjari, F., Toom, D., Huang, L., Sharma, S., Chivulescu, A., Veber, D., and Zhang, W. Organic functional groups in the submicron aerosol at 82.5 n, 62.5 w from 2012 to 2014. *Atmospheric Chemistry and Physics*, 18(5):3269–3287, 2018a. doi: 10.5194/acp-18-3269-2018. URL https://acp.copernicus.org/articles/18/3269/2018/.

Leaitch, W. R., Russell, L. M., Liu, J., Kolonjari, F., Toom, D., Huang, L., Sharma, S., Chivulescu, A., Veber, D., and Zhang, W. Organic functional groups in the submicron aerosol at 82.5 n, 62.5 w from 2012 to 2014. *Atmospheric Chemistry and Physics*, 18(5):3269–3287, 2018b.

Leck, C., Norman, M., Bigg, E. K., and Hillamo, R. Chemical composition and sources of the high arctic aerosol relevant for cloud formation. *Journal of Geophysical Research: Atmospheres*, 107(D12): AAC 1–1–AAC 1–17, 2002. doi: https://doi.org/10.1029/2001JD001463. URL https://agupubs.onlinelibrary.wiley.com/doi/abs/10.1029/2001JD001463.

Lee, C., Martin, R. V., van Donkelaar, A., Lee, H., Dickerson, R. R., Hains, J. C., Krotkov, N., Richter, A., Vinnikov, K., and Schwab, J. J. So2 emissions and lifetimes: Estimates from inverse modeling using in situ and global, space-based (sciamachy and omi) observations. *Journal of Geophysical Research: Atmospheres*, 116(D6), 2011.

Lee, C. C.-W. and Thiemens, M. H. The δ17o and δ18o measurements of atmospheric sulfate from a coastal and high alpine region: A mass-independent isotopic anomaly. *Journal of Geophysical Research: Atmospheres*, 106(D15):17359–17373, 2001.

Lee, Y., Lamarque, J.-F., Flanner, M., Jiao, C., Shindell, D., Berntsen, T., Bisiaux, M., Cao, J., Collins, W., Curran, M., et al. Evaluation of preindustrial to present-day black carbon and its albedo forcing from atmospheric chemistry and climate model intercomparison project (accmip). *Atmospheric Chemistry and Physics*, 13 (5):2607–2634, 2013.

Levoni, C., Cervino, M., Guzzi, R., and Torricella, F. Atmospheric aerosol optical properties: a database of radiative characteristics for different components and classes. *Applied optics*, 36(30):8031–8041, 1997.

Li, H., Zhang, H., Mamtimin, A., Fan, S., and Ju, C. A new land-use dataset for the weather research and forecasting (wrf) model. *Atmosphere*, 11(4):350, 2020.

Li, J., Chen, X., Wang, Z., Du, H., Yang, W., Sun, Y., Hu, B., Li, J., Wang, W., Wang, T., et al. Radiative and heterogeneous chemical effects of aerosols on ozone and inorganic aerosols over east asia. *Science of the Total Environment*, 622:1327–1342, 2018a.

Li, L., Ren, L., Ren, H., Yue, S., Xie, Q., Zhao, W., Kang, M., Li, J., Wang, Z., Sun, Y., et al. Molecular characterization and seasonal variation in primary and secondary organic aerosols in beijing, china. *Journal of Geophysical Research: Atmospheres*, 123(21):12–394, 2018b.

Li, M., Song, Y., Huang, X., Li, J., Mao, Y., Zhu, T., Cai, X., and Liu, B. Improving mesoscale modeling using satellite-derived land surface parameters in the pearl river delta region, china. *Journal of Geophysical Research: Atmospheres*, 119(11):6325–6346, 2014.

Li, Q., Fu, X., Peng, X., Wang, W., Badia, A., Fernandez, R. P., Cuevas, C. A., Mu, Y., Chen, J., Jimenez, J. L., et al. Halogens enhance haze pollution in china. *Environmental science & technology*, 55(20):13625–13637, 2021a.

Li, S.-M., Barrie, L., Talbot, R., Harriss, R., Davidson, C., and Jaffrezo, J.-L. Seasonal and geographic variations of methanesulfonic acid in the arctic troposphere. *Atmospheric Environment. Part A. General Topics*, 27 (17-18):3011–3024, 1993.

Li, W., Huang, C., and Zhang, S. Global characteristics of the westward-propagating quasi-16-day wave with zonal wavenumber 1 and the connection with the 2012/2013 ssw revealed by era-interim. *Earth, Planets and Space*, 73(1):1–18, 2021b.

Liang, L., Engling, G., Du, Z., Duan, F., Cheng, Y., Liu, X., and He, K. Contribution of fungal spores to organic carbon in ambient aerosols in beijing, china. *Atmospheric Pollution Research*, 8(2):351–358, 2017.

Liao, H., Adams, P. J., Chung, S. H., Seinfeld, J. H., Mickley, L. J., and Jacob, D. J. Interactions between tropospheric chemistry and aerosols in a unified general circulation model. *Journal of Geophysical Research: Atmospheres*, 108(D1):AAC–1, 2003.

Lin, Y.-C., Zhang, Y.-L., Fan, M.-Y., and Bao, M. Heterogeneous formation of particulate nitrate under ammonium-rich regimes during the high-pm 2.5 events in nanjing, china. *Atmospheric Chemistry and Physics*, 20(6):3999–4011, 2020.

Linell, K. A., Tedrow, J. C., et al. *Soil and permafrost surveys in the arctic.* Oxford University Press, 1981.

Liu, J., Fan, S., Horowitz, L. W., and Levy, H. Evaluation of factors controlling long-range transport of black carbon to the arctic. *Journal of Geophysical Research: Atmospheres*, 116(D4), 2011.

Liu, L., Bei, N., Hu, B., Wu, J., Liu, S., Li, X., Wang, R., Liu, Z., Shen, Z., and Li, G. Wintertime nitrate formation pathways in the north china plain: Importance of n2o5 heterogeneous hydrolysis. *Environmental Pollution*, 266:115287, 2020.

Liu, M. and Matsui, H. Improved simulations of global black carbon distributions by modifying wet scavenging processes in convective and mixed-phase clouds. *Journal of Geophysical Research: Atmospheres*, 126(3): e2020JD033890, 2021.

Liu, P., Tsimpidi, A., Hu, Y., Stone, B., Russell, A., and Nenes, A. Differences between downscaling with spectral and grid nudging using wrf. *Atmospheric Chemistry and Physics*, 12(8):3601–3610, 2012.

Liu, S., Liu, C.-C., Froyd, K. D., Schill, G. P., Murphy, D. M., Bui, T. P., Dean-Day, J. M., Weinzierl, B., Dollner, M., Diskin, G. S., et al. Sea spray aerosol concentration modulated by sea surface temperature. *Proceedings of the National Academy of Sciences*, 118(9), 2021.

Lovejoy C., W. F. Vincent, S. B. S. R. M.-J. M. R. T. M. P. R. M. C. P. Distribution, phylogeny, and growth of cold-adapted picoprasinophytes in arctic seas. *J. Phycol.*, 43:78–89, 2007. doi: https://doi.org/10.1111/j.1529-8817.2006.00310.x.

Lu, Q., Zhao, Y., and Robinson, A. L. Comprehensive organic emission profiles for gasoline, diesel, and gas-turbine engines including intermediate and semi-volatile organic compound emissions. *Atmospheric Chemistry and Physics*, 18(23):17637–17654, 2018.

Lu, Q., Murphy, B. N., Qin, M., Adams, P. J., Zhao, Y., Pye, H. O., Efstathiou, C., Allen, C., and Robinson, A. L. Simulation of organic aerosol formation during the calnex study: updated mobile emissions and secondary organic aerosol parameterization for intermediate-volatility organic compounds. *Atmospheric chemistry and physics*, 20(7):4313–4332, 2020.

Lund, M. T., Samset, B. H., Skeie, R. B., Watson-Parris, D., Katich, J. M., Schwarz, J. P., and Weinzierl, B. Short black carbon lifetime inferred from a global set of aircraft observations. *Npj Climate and Atmospheric Science*, 1(1):1–8, 2018.

Lutsch, E., Strong, K., Jones, D. B., Ortega, I., Hannigan, J. W., Dammers, E., Shephard, M. W., Morris, E., Murphy, K., Evans, M. J., et al. Unprecedented atmospheric ammonia concentrations detected in the high arctic from the 2017 canadian wildfires. *Journal of Geophysical Research: Atmospheres*, 124(14): 8178–8202, 2019.

Ma, P. K., Zhao, Y., Robinson, A. L., Worton, D. R., Goldstein, A. H., Ortega, A. M., Jimenez, J. L., Zotter, P., Prévôt, A. S., Szidat, S., et al. Evaluating the impact of new observational constraints on ps/ivoc emissions, multi-generation oxidation, and chamber wall losses on soa modeling for los angeles, ca. *Atmospheric chemistry and physics*, 17(15):9237–9259, 2017.

Ma, P.-L., Rasch, P. J., Wang, H., Zhang, K., Easter, R. C., Tilmes, S., Fast, J. D., Liu, X., Yoon, J.-H., and Lamarque, J.-F. The role of circulation features on black carbon transport into the arctic in the community atmosphere model version 5 (cam5). *Journal of Geophysical Research: Atmospheres*, 118(10):4657–4669, 2013.

Ma, X., von Salzen, K., and Li, J. Modelling sea salt aerosol and its direct and indirect effects on climate. *Atmospheric Chemistry and Physics*, 8(5):1311–1327, 2008. doi: 10.5194/acp-8-1311-2008. URL https://acp.copernicus.org/articles/8/1311/2008/.

Ma, Y., Yang, Y., Mai, X., Qiu, C., Long, X., and Wang, C. Comparison of analysis and spectral nudging techniques for dynamical downscaling with the wrf model over china. *Advances in Meteorology*, 2016, 2016.

Macdonald, K. M., Sharma, S., Toom, D., Chivulescu, A., Hanna, S., Bertram, A. K., Platt, A., Elsasser, M., Huang, L., Tarasick, D., Chellman, N., McConnell, J. R., Bozem, H., Kunkel, D., Lei, Y. D., Evans, G. J., and Abbatt, J. P. D. Observations of atmospheric chemical deposition to high arctic snow. *Atmospheric Chemistry and Physics*, 17(9):5775–5788, 2017a. doi: 10.5194/acp-17-5775-2017. URL https://acp.copernicus.org/articles/17/5775/2017/.

Macdonald, K. M., Sharma, S., Toom, D., Chivulescu, A., Hanna, S., Bertram, A. K., Platt, A., Elsasser, M., Huang, L., Tarasick, D., et al. Observations of atmospheric chemical deposition to high arctic snow. *Atmospheric Chemistry and Physics*, 17(9):5775–5788, 2017b.

Mahmood, R., von Salzen, K., Flanner, M., Sand, M., Langner, J., Wang, H., and Huang, L. Seasonality of global and arctic black carbon processes in the arctic monitoring and assessment programme models. *Journal of Geophysical Research: Atmospheres*, 121(12):7100–7116, 2016.

Mai, X., Ma, Y., Yang, Y., Li, D., and Qiu, X. Impact of grid nudging parameters on dynamical downscaling during summer over mainland china. *Atmosphere*, 8(10):184, 2017.

Maillard, J., Ravetta, F., Jean-Christophe, R., Fochesatto, G. J., and Law, K. S. Modulation of boundary layer stability and the surface energy budget by a shallow cold flow in central alaska. 2022.

Malm, W. C., Sisler, J. F., Huffman, D., Eldred, R. A., and Cahill, T. A. Spatial and seasonal trends in particle concentration and optical extinction in the united states. *Journal of Geophysical Research: Atmospheres*, 99(D1):1347–1370, 1994. doi: https://doi.org/10.1029/93JD02916. URL https://agupubs.onlinelibrary.wiley.com/doi/abs/10.1029/93JD02916.

Mamane, Y. and Gottlieb, J. Heterogeneous reaction of nitrogen oxides on sea salt and mineral particles—a single particle approach. *Journal of Aerosol Science*, 21:S225–S228, 1990.

Manabe, S., Bryan, K., and Spelman, M. J. Transient response of a global ocean-atmosphere model to a doubling of atmospheric carbon dioxide. *Journal of Physical Oceanography*, 20(5):722–749, 1990.

Marelle, L., Thomas, J. L., Raut, J.-C., Law, K. S., Jalkanen, J.-P., Johansson, L., Roiger, A., Schlager, H., Kim, J., Reiter, A., et al. Air quality and radiative impacts of arctic shipping emissions in the summertime in northern norway: from the local to the regional scale. *Atmospheric Chemistry and Physics*, 16(4): 2359–2379, 2016.

Marelle, L., Raut, J.-C., Law, K. S., Berg, L. K., Fast, J. D., Easter, R. C., Shrivastava, M., and Thomas, J. L. Improvements to the wrf-chem 3.5.1 model for quasi-hemispheric simulations of aerosols and ozone in the arctic. *Geoscientific Model Development*, 10(10):3661–3677, 2017. doi: 10.5194/gmd-10-3661-2017. URL https://gmd.copernicus.org/articles/10/3661/2017/.

Marelle, L., Raut, J.-C., Law, K. S., and Duclaux, O. Current and future arctic aerosols and ozone from remote emissions and emerging local sources—modeled source contributions and radiative effects. *Journal of Geophysical Research: Atmospheres*, 123:12,942–12,963, 2018. doi: https://doi.org/10.1029/2018JD0288637.

Marelle, L., Thomas, J. L., Ahmed, S., Tuite, K., Stutz, J., Dommergue, A., Simpson, W. R., Frey, M. M., and Baladima, F. Implementation and impacts of surface and blowing snow sources of arctic bromine activation within wrf-chem 4.1.1. *Journal of Advances in Modeling Earth Systems*, 13(8):e2020MS002391, 2021. doi: https://doi.org/10.1029/2020MS002391. URL https://agupubs.onlinelibrary.wiley.com/doi/abs/10.1029/2020MS002391. e2020MS002391 2020MS002391.

Mariraj Mohan, S. An overview of particulate dry deposition: measuring methods, deposition velocity and controlling factors. *International journal of environmental science and technology*, 13(1):387–402, 2016.

Massel, S. R. Whitecap coverage of the sea surface. In *Ocean Waves Breaking and Marine Aerosol Fluxes*, pages 183–206. Springer, 2007.

Massling, A., Nielsen, I., Kristensen, D., Christensen, J., Sørensen, L., Jensen, B., Nguyen, Q., Nøjgaard, J., Glasius, M., and Skov, H. Atmospheric black carbon and sulfate concentrations in northeast greenland. *Atmospheric Chemistry and Physics*, 15(16):9681–9692, 2015.

Masson-Delmotte, V., Zhai, P., Pirani, A., Connors, S. L., Péan, C., Berger, S., Caud, N., Chen, Y., Goldfarb, L., Gomis, M., et al. Climate change 2021: the physical science basis. *Contribution of working group I to the sixth assessment report of the intergovernmental panel on climate change*, page 2, 2021.

Matsui, H., Mori, T., Ohata, S., Moteki, N., Oshima, N., Goto-Azuma, K., Koike, M., and Kondo, Y. Contrasting source contributions of arctic black carbon to atmospheric concentrations, deposition flux, and atmospheric and snow radiative effects. *Atmospheric Chemistry and Physics Discussions*, pages 1–31, 2022.

May, N. W., Quinn, P. K., McNamara, S. M., and Pratt, K. A. Multiyear study of the dependence of sea salt aerosol on wind speed and sea ice conditions in the coastal arctic. *Journal of Geophysical Research: Atmospheres*, 121(15):9208–9219, 2016. doi: https://doi.org/10.1002/2016JD025273. URL https://agupubs.onlinelibrary.wiley.com/doi/abs/10.1002/2016JD025273.

Mayfield, J. A. and Fochesatto, G. J. The layered structure of the winter atmospheric boundary layer in the interior of alaska. *Journal of Applied Meteorology and Climatology*, 52(4):953–973, 2013.

McCabe, J. R., Savarino, J., Alexander, B., Gong, S., and Thiemens, M. H. Isotopic constraints on non-photochemical sulfate production in the arctic winter. *Geophysical research letters*, 33(5), 2006.

McCoy, D. T. and Hartmann, D. L. Observations of a substantial cloud-aerosol indirect effect during the 2014–2015 bárðarbunga-veiðivötn fissure eruption in iceland. *Geophysical Research Letters*, 42(23):10–409, 2015.

McDonald, B. C., De Gouw, J. A., Gilman, J. B., Jathar, S. H., Akherati, A., Cappa, C. D., Jimenez, J. L., Lee-Taylor, J., Hayes, P. L., McKeen, S. A., et al. Volatile chemical products emerging as largest petrochemical source of urban organic emissions. *Science*, 359(6377):760–764, 2018.

McDuffie, E. E., Smith, S. J., O'Rourke, P., Tibrewal, K., Venkataraman, C., Marais, E. A., Zheng, B., Crippa, M., Brauer, M., and Martin, R. V. A global anthropogenic emission inventory of atmospheric pollutants from sector-and fuel-specific sources (1970–2017): an application of the community emissions data system (ceds). *Earth System Science Data*, 12(4):3413–3442, 2020.

McNamara, S. M., Kolesar, K. R., Wang, S., Kirpes, R. M., May, N. W., Gunsch, M. J., Cook, R. D., Fuentes, J. D., Hornbrook, R. S., Apel, E. C., et al. Observation of road salt aerosol driving inland wintertime atmospheric chlorine chemistry. *ACS central science*, 6(5):684–694, 2020.

Meinander, O., Dagsson-Waldhauserova, P., Amosov, P., Aseyeva, E., Atkins, C., Baklanov, A., Baldo, C., Barr, S., Barzycka, B., Benning, L., et al. Newly identified climatically and environmentally significant high latitude dust sources. *Atmospheric Chemistry and Physics Discussions*, pages 1–74, 2021.

Mellor, G. L. and Yamada, T. Development of a turbulence closure model for geophysical fluid problems. *Reviews of Geophysics*, 20(4):851–875, 1982.

Mentel, T. F., Sohn, M., and Wahner, A. Nitrate effect in the heterogeneous hydrolysis of dinitrogen pentoxide on aqueous aerosols. *Physical Chemistry Chemical Physics*, 1(24):5451–5457, 1999.

Mernild, S. H. and Liston, G. E. The influence of air temperature inversions on snowmelt and glacier mass balance simulations, ammassalik island, southeast greenland. *Journal of Applied Meteorology and Climatology*, 49(1):47–67, 2010.

Miguez-Macho, G., Stenchikov, G. L., and Robock, A. Spectral nudging to eliminate the effects of domain position and geometry in regional climate model simulations. *Journal of Geophysical Research: Atmospheres*, 109(D13), 2004.

Millero, F. J., Feistel, R., Wright, D. G., and McDougall, T. J. The composition of standard seawater and the definition of the reference-composition salinity scale. *Deep Sea Research Part I: Oceanographic Research Papers*, 55(1):50–72, 2008. ISSN 0967-0637. doi: https://doi.org/10.1016/j.dsr.2007.10.001. URL https://www.sciencedirect.com/science/article/pii/S0967063707002282.

Mitchell, J. Visual range in the polar regions with particular reference to the alaskan arctic. *J. Atmos. Terr. Phys*, 17:195–211, 1957.

Miyazaki, K., Eskes, H., Sudo, K., Takigawa, M., Van Weele, M., and Boersma, K. Simultaneous assimilation of satellite no 2, o 3, co, and hno 3 data for the analysis of tropospheric chemical composition and emissions. *Atmospheric Chemistry and Physics*, 12(20):9545–9579, 2012.

Miyazaki, Y., Kondo, Y., Sahu, L. K., Imaru, J., Fukushima, N., and Kano, M. Performance of a newly designed continuous soot monitoring system (cosmos). *Journal of environmental monitoring*, 10(10):1195–1201, 2008.

Moch, J. M., Dovrou, E., Mickley, L. J., Keutsch, F. N., Cheng, Y., Jacob, D. J., Jiang, J., Li, M., Munger, J. W., Qiao, X., et al. Contribution of hydroxymethane sulfonate to ambient particulate matter: A potential explanation for high particulate sulfur during severe winter haze in beijing. *Geophysical Research Letters*, 45(21):11–969, 2018.

Moch, J. M., Dovrou, E., Mickley, L. J., Keutsch, F. N., Liu, Z., Wang, Y., Dombek, T. L., Kuwata, M., Budisulistiorini, S. H., Yang, L., et al. Global importance of hydroxymethanesulfonate in ambient particulate matter: Implications for air quality. *Journal of Geophysical Research: Atmospheres*, 125(18):e2020JD032706, 2020.

Mölders, N. Investigations on the impact of single direct and indirect, and multiple emission–control measures on cold–season near–surface pm2. 5 concentrations in fairbanks, alaska. *Atmospheric Pollution Research*, 4(1):87–100, 2013.

Mölders, N. and Kramm, G. A case study on wintertime inversions in interior alaska with wrf. *Atmospheric Research*, 95(2-3):314–332, 2010.

Mölders, N. and Kramm, G. Climatology of air quality in arctic cities—inventory and assessment. *Open Journal of Air Pollution*, 7(1):48–93, 2018.

Mölders, N., Tran, H. N., Quinn, P., Sassen, K., Shaw, G. E., and Kramm, G. Assessment of wrf/chem to simulate sub–arctic boundary layer characteristics during low solar irradiation using radiosonde, sodar, and surface data. *Atmospheric Pollution Research*, 2(3):283–299, 2011.

Mölders, N., Fochesatto, G. J., Edwin, S. G., and Kramm, G. Geothermal, oceanic, wildfire, meteorological and anthropogenic impacts on pm2. 5 concentrations in the fairbanks metropolitan area. *Open Journal of Air Pollution*, 8(2):19–68, 2019.

Monaghan, A. J., Clark, M. P., Barlage, M. P., Newman, A. J., Xue, L., Arnold, J. R., and Rasmussen, R. M. High-resolution historical climate simulations over alaska. *Journal of Applied Meteorology and Climatology*, 57(3):709–731, 2018a. ISSN 15588424, 15588432. URL https://www.jstor.org/stable/26501015.

Monaghan, A. J., Clark, M. P., Barlage, M. P., Newman, A. J., Xue, L., Arnold, J. R., and Rasmussen, R. M. High-resolution historical climate simulations over alaska. *Journal of Applied Meteorology and Climatology*, 57(3):709–731, 2018b.

Monahan, E. and Muircheartaigh, I. Optimal power-law description of oceanic whitecap coverage dependence on wind speed. *Journal of Physical Oceanography*, 10:2094–2099, 1980.

Monahan, E., Spiel, D. E., and Davidson, K. A model of marine aerosol generation via whitecaps and wave disruption. 1986a.

Monahan, E. C., Spiel, D. E., and Davidson, K. L. A model of marine aerosol generation via whitecaps and wave disruption. In *Oceanic whitecaps*, pages 167–174. Springer, 1986b.

Monin, A. S. and Obukhov, A. M. Basic laws of turbulent mixing in the surface layer of the atmosphere. *Contrib. Geophys. Inst. Acad. Sci. USSR*, 151(163):e187, 1954.

Monitoring, A. et al. *AMAP assessment report: Arctic pollution issues*. Arctic Monitoring and Assessment Programme (AMAP)„ 1998.

Mori, T., Kondo, Y., Ohata, S., Zhao, Y., Sinha, P., Oshima, N., Matsui, H., Moteki, N., and Koike, M. Seasonal variation of wet deposition of black carbon in arctic alaska. *Journal of Geophysical Research: Atmospheres*, 125(16):e2019JD032240, 2020.

Mori, T., Kondo, Y., Ohata, S., Goto-Azuma, K., Fukuda, K., Ogawa-Tsukagawa, Y., Moteki, N., Yoshida, A., Koike, M., Sinha, P. R., et al. Seasonal variation of wet deposition of black carbon at ny-ålesund, svalbard. *Journal of Geophysical Research: Atmospheres*, page e2020JD034110, 2021.

Morrison, H., De Boer, G., Feingold, G., Harrington, J., Shupe, M. D., and Sulia, K. Resilience of persistent arctic mixed-phase clouds. *Nature Geoscience*, 5(1):11–17, 2012.

Morrison, H., T. G. T. V. Impact of cloud microphysics on the development of trailing stratiform precipitation in a simulated squall line: Comparison of one– and two–moment schemes. *Mon. Wea. Rev.*, 137:991—-1007, 2009. doi: 10.1175/2008MWR2556.1.

Moschos, V., Dzepina, K., Bhattu, D., Lamkaddam, H., Casotto, R., Daellenbach, K. R., Canonaco, F., Rai, P., Aas, W., Becagli, S., et al. Equal abundance of summertime natural and wintertime anthropogenic arctic organic aerosols. *Nature geoscience*, 15(3):196–202, 2022a.

Moschos, V., Schmale, J., Aas, W., Becagli, S., Calzolai, G., Eleftheriadis, K., Moffett, C. E., Schnelle-Kreis, J., Severi, M., Sharma, S., et al. Elucidating the present-day chemical composition, seasonality and source regions of climate-relevant aerosols across the arctic land surface. *Environmental Research Letters*, 17 (3):034032, 2022b.

Müller, T., Henzing, J., De Leeuw, G., Wiedensohler, A., Alastuey, A., Angelov, H., Bizjak, M., Collaud Coen, M., Engström, J., Gruening, C., et al. Characterization and intercomparison of aerosol absorption photometers: result of two intercomparison workshops. *Atmospheric Measurement Techniques*, 4(2):245–268, 2011.

Murray, L. T. Lightning no x and impacts on air quality. *Current Pollution Reports*, 2(2):115–133, 2016.

Naakka, T., Nygård, T., and Vihma, T. Arctic humidity inversions: Climatology and processes. *Journal of Climate*, 31(10):3765–3787, 2018.

National Centers for Environmental Prediction, National Weather Service, NOAA, U.S. Department of Commerce. Ncep fnl operational model global tropospheric analyses, continuing from july 1999, 2000. URL https://doi.org/10.5065/D6M043C6.

Nattinger, K. C. *Temporal and spatial trends of fine particulate matter composition in Fairbanks, Alaska*. University of Alaska Fairbanks, 2016.

Neumann, D., Matthias, V., Bieser, J., Aulinger, A., and Quante, M. Sensitivity of modeled atmospheric nitrogen species and nitrogen deposition to variations in sea salt emissions in the north sea and baltic sea regions. *Atmospheric Chemistry and Physics*, 16(5):2921–2942, 2016. doi: 10.5194/acp-16-2921-2016. URL https://acp.copernicus.org/articles/16/2921/2016/.

Nguyen, L. H., Joshi, D. R., Clay, D. E., and Henebry, G. M. Characterizing land cover/land use from multiple years of landsat and modis time series: A novel approach using land surface phenology modeling and random forest classifier. *Remote Sensing of Environment*, 238:111017, 2020.

Nguyen, Q., Skov, H., Sørensen, L., Jensen, B., Grube, A., Massling, A., Glasius, M., and Nøjgaard, J. Source apportionment of particles at station nord, north east greenland during 2008–2010 using coprem and pmf analysis. *Atmospheric Chemistry and Physics*, 13(1):35–49, 2013.

Nielsen, I. E., Skov, H., Massling, A., Eriksson, A. C., Dall'Osto, M., Junninen, H., Sarnela, N., Lange, R., Collier, S., Zhang, Q., et al. Biogenic and anthropogenic sources of aerosols at the high arctic site villum research station. *Atmospheric Chemistry and Physics*, 19(15):10239–10256, 2019.

Nilsson, E. D. and Rannik, Ü. Turbulent aerosol fluxes over the arctic ocean: 1. dry deposition over sea and pack ice. *Journal of Geophysical Research: Atmospheres*, 106(D23):32125–32137, 2001a.

Nilsson, E. D. and Rannik, Turbulent aerosol fluxes over the arctic ocean: 1. dry deposition over sea and pack ice. *Journal of Geophysical Research: Atmospheres*, 106(D23):32125–32137, 2001b. doi: https://doi.org/10.1029/2000JD900605. URL https://agupubs.onlinelibrary.wiley.com/doi/abs/10.1029/2000JD900605.

Nilsson, E. D., Rannik, , Swietlicki, E., Leck, C., Aalto, P. P., Zhou, J., and Norman, M. Turbulent aerosol fluxes over the arctic ocean: 2. wind-driven sources from the sea. *Journal of Geophysical Research: Atmospheres*, 106(D23):32139–32154, 2001. doi: https://doi.org/10.1029/2000JD900747. URL https://agupubs.onlinelibrary.wiley.com/doi/abs/10.1029/2000JD900747.

Niu, G.-Y. and Yang, Z.-L. Effects of vegetation canopy processes on snow surface energy and mass balances. *Journal of Geophysical Research: Atmospheres*, 109(D23), 2004. doi: https://doi.org/10.1029/2004JD004884. URL https://agupubs.onlinelibrary.wiley.com/doi/abs/10.1029/2004JD004884.

Niu, G.-Y., Yang, Z.-L., Dickinson, R. E., Gulden, L. E., and Su, H. Development of a simple groundwater model for use in climate models and evaluation with gravity recovery and climate experiment data. *Journal of Geophysical Research: Atmospheres*, 112(D7), 2007. doi: https://doi.org/10.1029/2006JD007522. URL https://agupubs.onlinelibrary.wiley.com/doi/abs/10.1029/2006JD007522.

Niu, G.-Y., Yang, Z.-L., Mitchell, K. E., Chen, F., Ek, M. B., Barlage, M., Kumar, A., Manning, K., Niyogi, D., Rosero, E., Tewari, M., and Xia, Y. The community noah land surface model with multiparameterization options (noah-mp): 1. model description and evaluation with local-scale measurements. *Journal of Geophysical Research: Atmospheres*, 116(D12), 2011a. doi: https://doi.org/10.1029/2010JD015139. URL https://agupubs.onlinelibrary.wiley.com/doi/abs/10.1029/2010JD015139.

Niu, G.-Y., Yang, Z.-L., Mitchell, K. E., Chen, F., Ek, M. B., Barlage, M., Kumar, A., Manning, K., Niyogi, D., Rosero, E., et al. The community noah land surface model with multiparameterization options (noah-mp): 1. model description and evaluation with local-scale measurements. *Journal of Geophysical Research: Atmospheres*, 116(D12), 2011b.

Notz, D. How well must climate models agree with observations? *Philosophical Transactions of the Royal Society A: Mathematical, Physical and Engineering Sciences*, 373(2052):20140164, 2015.

Notz, D. and Stroeve, J. Observed arctic sea-ice loss directly follows anthropogenic co2 emission. *Science*, 354 (6313):747–750, 2016.

O'Dowd, C. D., Smith, M. H., Consterdine, I. E., and Lowe, J. A. Marine aerosol, sea-salt, and the marine sulphur cycle: a short review. *Atmospheric Environment*, 31(1):73–80, 1997. ISSN 1352-2310. doi: https://doi.org/10.1016/S1352-2310(96)00106-9. URL https://www.sciencedirect.com/science/article/pii/S1352231096001069.

Ogren, J. A. Comment on "calibration and intercomparison of filter-based measurements of visible light absorption by aerosols". *Aerosol Science and Technology*, 44(8):589–591, 2010.

Ohata, S., Kondo, Y., Moteki, N., Mori, T., Yoshida, A., Sinha, P. R., and Koike, M. Accuracy of black carbon measurements by a filter-based absorption photometer with a heated inlet. *Aerosol Science and Technology*, 53(9):1079–1091, 2019.

Ohata, S., Mori, T., Kondo, Y., Sharma, S., Hyvärinen, A., Andrews, E., Tunved, P., Asmi, E., Backman, J., Servomaa, H., et al. Estimates of mass absorption cross sections of black carbon for filter-based absorption photometers in the arctic. *Atmospheric Chemistry and Physics Discussions*, pages 1–38, 2020.

Ohtake, T. Alaskan ice fog i:(a progress report of ice fog research). *Physics of Snow and Ice: proceedings*, 1(1): 105–118, 1967.

Omrani, H., Drobinski, P., and Dubos, T. Using nudging to improve global-regional dynamic consistency in limited-area climate modeling: What should we nudge? *Climate Dynamics*, 44(5):1627–1644, 2015.

Pan, Y., Tian, S., Liu, D., Fang, Y., Zhu, X., Zhang, Q., Zheng, B., Michalski, G., and Wang, Y. Fossil fuel combustion-related emissions dominate atmospheric ammonia sources during severe haze episodes: evidence from 15n-stable isotope in size-resolved aerosol ammonium. *Environmental science & technology*, 50(15):8049–8056, 2016.

Panno, S., Hackley, K. C., Hwang, H., Greenberg, S., Krapac, I., Landsberger, S., and O'kelly, D. Characterization and identification of na-cl sources in ground water. *Groundwater*, 44(2):176–187, 2006.

Papineau, J. M. Wintertime temperature anomalies in alaska correlated with enso and pdo. *International Journal of Climatology: A Journal of the Royal Meteorological Society*, 21(13):1577–1592, 2001.

Pathak, R. K., Wu, W. S., and Wang, T. Summertime pm 2.5 ionic species in four major cities of china: nitrate formation in an ammonia-deficient atmosphere. *Atmospheric Chemistry and Physics*, 9(5):1711–1722, 2009.

Pattantyus, A. K., Businger, S., and Howell, S. G. Review of sulfur dioxide to sulfate aerosol chemistry at kīlauea volcano, hawai 'i. *Atmospheric Environment*, 185:262–271, 2018.

Pavelsky, T. M., Boé, J., Hall, A., and Fetzer, E. J. Atmospheric inversion strength over polar oceans in winter regulated by sea ice. *Climate Dynamics*, 36(5):945–955, 2011.

Penner, J. E., Andreae, M., Annegarn, H., Barrie, L., Feichter, J., Hegg, D., Jayaraman, A., Leaitch, R., Murphy, D., Nganga, J., et al. Aerosols, their direct and indirect effects. In *Climate change 2001: the scientific basis. Contribution of working group I to the third assessment report of the intergovernmental panel on climate change*, pages 289–348. Cambridge University Press, 2001.

Peters, G., Nilssen, T., Lindholt, L., Eide, M., Glomsrød, S., Eide, L., and Fuglestvedt, J. Future emissions from shipping and petroleum activities in the arctic. *Atmospheric Chemistry and Physics*, 11(11):5305–5320, 2011.

Peterson, P. K., Pöhler, D., Sihler, H., Zielcke, J., General, S., Frieß, U., Platt, U., Simpson, W. R., Nghiem, S. V., Shepson, P. B., et al. Observations of bromine monoxide transport in the arctic sustained on aerosol particles. *Atmospheric Chemistry and Physics*, 17(12):7567–7579, 2017.

Pétron, G., Granier, C., Khattatov, B., Lamarque, J.-F., Yudin, V., Müller, J.-F., and Gille, J. Inverse modeling of carbon monoxide surface emissions using climate monitoring and diagnostics laboratory network observations. *Journal of Geophysical Research: Atmospheres*, 107(D24):ACH–10, 2002.

Petters, M. D., Prenni, A. J., Kreidenweis, S. M., DeMott, P. J., Matsunaga, A., Lim, Y. B., and Ziemann, P. J. Chemical aging and the hydrophobic-to-hydrophilic conversion of carbonaceous aerosol. *Geophysical research letters*, 33(24), 2006.

Petzold, A. and Schönlinner, M. Multi-angle absorption photometry—a new method for the measurement of aerosol light absorption and atmospheric black carbon. *Journal of Aerosol Science*, 35(4):421–441, 2004.

Petzold, A., Kramer, H., and Schönlinner, M. Continuous measurement of atmospheric black carbon using a multi-angle absorption photometer. *Environ. Sci. Pollut. Res*, 4(Special Issue):78–82, 2002.

Petzold, A., Ogren, J. A., Fiebig, M., Laj, P., Li, S.-M., Baltensperger, U., Holzer-Popp, T., Kinne, S., Pappalardo, G., Sugimoto, N., et al. Recommendations for reporting" black carbon" measurements. *Atmospheric Chemistry and Physics*, 13(16):8365–8379, 2013.

Pilson, M. E. Q. *An Introduction to the Chemistry of the Sea*. Cambridge University Press, 2 edition, 2012. doi: 10.1017/CBO9781139047203.

Pohl, B. and Crétat, J. On the use of nudging techniques for regional climate modeling: application for tropical convection. *Climate dynamics*, 43(5):1693–1714, 2014.

Polissar, A., Hopke, P., Paatero, P., Kaufmann, Y., Hall, D., Bodhaine, B., Dutton, E., and Harris, J. The aerosol at barrow, alaska: long-term trends and source locations. *Atmospheric Environment*, 33(16):2441–2458, 1999.

Polissar, A. V., Hopke, P. K., and Harris, J. M. Source regions for atmospheric aerosol measured at barrow, alaska. *Environmental science & technology*, 35(21):4214–4226, 2001.

Polyakov, I. V., Beszczynska, A., Carmack, E. C., Dmitrenko, I. A., Fahrbach, E., Frolov, I. E., Gerdes, R., Hansen, E., Holfort, J., Ivanov, V. V., et al. One more step toward a warmer arctic. *Geophysical Research Letters*, 32(17), 2005.

Popovicheva, O., Diapouli, E., Makshtas, A., Shonija, N., Manousakas, M., Saraga, D., Uttal, T., and Eleftheriadis, K. East siberian arctic background and black carbon polluted aerosols at hmo tiksi. *Science of the Total Environment*, 655:924–938, 2019.

Popovicheva, O. B., Evangeliou, N., Kobelev, V. O., Chichaeva, M. A., Eleftheriadis, K., Gregorič, A., and Kasimov, N. S. Siberian arctic black carbon: gas flaring and wildfire impact. *Atmospheric Chemistry and Physics*, 22(9):5983–6000, 2022.

Pósfai, M., Li, J., Anderson, J. R., and Buseck, P. R. Aerosol bacteria over the southern ocean during ace-1. *Atmospheric Research*, 66(4):231–240, 2003.

Presto, A. A., Hennigan, C. J., Nguyen, N. T., and Robinson, A. L. Determination of volatility distributions of primary organic aerosol emissions from internal combustion engines using thermal desorption gas chromatography mass spectrometry. *Aerosol Science and Technology*, 46(10):1129–1139, 2012.

Prospero, J. M. Long-range transport of mineral dust in the global atmosphere: Impact of african dust on the environment of the southeastern united states. *Proceedings of the National Academy of Sciences*, 96(7): 3396–3403, 1999.

Qi, L., Li, Q., Henze, D. K., Tseng, H.-L., and He, C. Sources of springtime surface black carbon in the arctic: an adjoint analysis for april 2008. *Atmospheric Chemistry and Physics*, 17(15):9697–9716, 2017. doi: 10.5194/acp-17-9697-2017. URL https://acp.copernicus.org/articles/17/9697/2017/.

Qi, L., Liu, H., Shen, X., Fu, M., Huang, F., Man, H., Deng, F., Shaikh, A. A., Wang, X., Dong, R., et al. Intermediate-volatility organic compound emissions from nonroad construction machinery under different operation modes. *Environmental Science & Technology*, 53(23):13832–13840, 2019.

Quality, I. A. Organic pollutants. *EURO Reports and Studies*, 111, 1989.

Quennehen, B., Raut, J.-C., Law, K. S., Daskalakis, N., Ancellet, G., Clerbaux, C., Kim, S.-W., Lund, M., Myhre, G., Olivié, D., et al. Multi-model evaluation of short-lived pollutant distributions over east asia during summer 2008. *Atmospheric Chemistry and Physics*, 16(17):10765–10792, 2016.

Quinn, P., Miller, T., Bates, T., Ogren, J., Andrews, E., and Shaw, G. A 3-year record of simultaneously measured aerosol chemical and optical properties at barrow, alaska. *Journal of Geophysical Research: Atmospheres*, 107(D11):AAC–8, 2002a.

Quinn, P., Shaw, G., Andrews, E., Dutton, E., Ruoho-Airola, T., and Gong, S. Arctic haze: current trends and knowledge gaps. *Tellus B: Chemical and Physical Meteorology*, 59(1):99–114, 2007a.

Quinn, P., Bates, T., Baum, E., Doubleday, N., Fiore, A., Flanner, M., Fridlind, A., Garrett, T., Koch, D., Menon, S., et al. Short-lived pollutants in the arctic: their climate impact and possible mitigation strategies. *Atmospheric Chemistry and Physics*, 8(6):1723–1735, 2008.

Quinn, P., Bates, T., Schulz, K., and Shaw, G. Decadal trends in aerosol chemical composition at barrow, alaska: 1976–2008. *Atmospheric Chemistry and Physics*, 9(22):8883–8888, 2009.

Quinn, P., Stohl, A., Arneth, A., Berntsen, T., Burkhart, J., Christensen, J., Flanner, M., Kupiainen, K., Lihavainen, H., Shepherd, M., et al. Amap: The impact of black carbon on arctic climate (2011). *Arctic Monitoring and Assessment Programme (AMAP): Tromso, Norway*, 2011.

Quinn, P., Coffman, D., Johnson, J., Upchurch, L., and Bates, T. Small fraction of marine cloud condensation nuclei made up of sea spray aerosol. *Nature Geoscience*, 10(9):674–679, 2017.

Quinn, P. K. and Bates, T. S. Regional aerosol properties: Comparisons of boundary layer measurements from ace 1, ace 2, aerosols99, indoex, ace asia, tarfox, and neaqs. *Journal of Geophysical Research: Atmospheres*, 110(D14), 2005.

Quinn, P. K., Coffman, D. J., Kapustin, V. N., Bates, T. S., and Covert, D. S. Aerosol optical properties in the marine boundary layer during the first aerosol characterization experiment (ace 1) and the underlying chemical and physical aerosol properties. *Journal of Geophysical Research: Atmospheres*, 103(D13):16547–16563, 1998. doi: https://doi.org/10.1029/97JD02345. URL https://agupubs.onlinelibrary.wiley.com/doi/abs/10.1029/97JD02345.

Quinn, P. K., Miller, T. L., Bates, T. S., Ogren, J. A., Andrews, E., and Shaw, G. E. A 3-year record of simultaneously measured aerosol chemical and optical properties at barrow, alaska. *Journal of Geophysical Research: Atmospheres*, 107(D11):AAC 8–1–AAC 8–15, 2002b. doi: https://doi.org/10.1029/2001JD001248. URL https://agupubs.onlinelibrary.wiley.com/doi/abs/10.1029/2001JD001248.

Quinn, P. K., SHAW, G., ANDREWS, E., DUTTON, E. G., RUOHO-AIROLA, T., and GONG, S. L. Arctic haze: current trends and knowledge gaps. *Tellus B*, 59(1):99–114, 2007b. doi: https://doi.org/10.1111/j.1600-0889.2006.00238.x. URL https://onlinelibrary.wiley.com/doi/abs/10.1111/j.1600-0889.2006.00238.x.

Rahn, K. A. Relative importances of north america and eurasia as sources of arctic aerosol. *Atmospheric Environment (1967)*, 15(8):1447–1455, 1981.

Rahn, K. A. and McCaffrey, R. J. On the origin and transport of the winter arctic aerosol. *Annals of the New York Academy of Sciences*, 338(1):486–503, 1980.

Rahn, K. A., Borys, R. D., and Shaw, G. E. The asian source of arctic haze bands. *Nature*, 268(5622):713–715, 1977.

Ramachandran, S. and Srivastava, R. Mixing states of aerosols over four environmentally distinct atmospheric regimes in asia: coastal, urban, and industrial locations influenced by dust. *Environmental Science and Pollution Research*, 23(11):11109–11128, 2016.

RANDERSON, J., VAN DER WERF, G., GIGLIO, L., COLLATZ, G., and KASIBHATLA, P. Global fire emissions database, version 4.1 (gfedv4), 2017. URL https://daac.ornl.gov/cgi-bin/dsviewer.pl?ds_id=1293.

Raut, J.-C., Marelle, L., Fast, J. D., Thomas, J. L., Weinzierl, B., Law, K. S., Berg, L. K., Roiger, A., Easter, R. C., Heimerl, K., et al. Cross-polar transport and scavenging of siberian aerosols containing black carbon during the 2012 access summer campaign. *Atmospheric Chemistry and Physics*, 17(18):10969–10995, 2017.

Regmi, R. P., Kitada, T., Maharjan, S., Shrestha, S., Shrestha, S., and Regmi, G. Wintertime boundary layer evolution and air pollution potential over the kathmandu valley, nepal. *Journal of Geophysical Research: Atmospheres*, 124(8):4299–4325, 2019.

Ren, L., Yang, Y., Wang, H., Zhang, R., Wang, P., and Liao, H. Source attribution of arctic black carbon and sulfate aerosols and associated arctic surface warming during 1980–2018. *Atmospheric Chemistry and Physics*, 20(14):9067–9085, 2020.

Revell, L. E., Kremser, S., Hartery, S., Harvey, M., Mulcahy, J. P., Williams, J., Morgenstern, O., McDonald, A. J., Varma, V., Bird, L., and Schuddeboom, A. The sensitivity of southern ocean aerosols and cloud microphysics to sea spray and sulfate aerosol production in the hadgem3-ga7.1 chemistry–climate model. *Atmospheric Chemistry and Physics*, 19(24):15447–15466, 2019. doi: 10.5194/acp-19-15447-2019. URL https://acp.copernicus.org/articles/19/15447/2019/.

Rhodes, R. H., Yang, X., Wolff, E. W., McConnell, J. R., and Frey, M. M. Sea ice as a source of sea salt aerosol to greenland ice cores: a model-based study. *Atmospheric Chemistry and Physics*, 17(15):9417–9433, 2017. doi: 10.5194/acp-17-9417-2017. URL https://acp.copernicus.org/articles/17/9417/2017/.

Riddick, S., Dragosits, U., Blackall, T., Daunt, F., Wanless, S., and Sutton, M. The global distribution of ammonia emissions from seabird colonies. *Atmospheric Environment*, 55:319–327, 2012.

Riedel, T., Bertram, T., Ryder, O., Liu, S., Day, D., Russell, L., Gaston, C., Prather, K., and Thornton, J. Direct n 2 o 5 reactivity measurements at a polluted coastal site. *Atmospheric Chemistry and Physics*, 12(6): 2959–2968, 2012.

Riemer, N., Vogel, H., and Vogel, B. Soot aging time scales in polluted regions during day and night. *Atmospheric Chemistry and Physics*, 4(7):1885–1893, 2004.

Robinson, A. L., Donahue, N. M., Shrivastava, M. K., Weitkamp, E. A., Sage, A. M., Grieshop, A. P., Lane, T. E., Pierce, J. R., and Pandis, S. N. Rethinking organic aerosols: Semivolatile emissions and photochemical aging. *Science*, 315(5816):1259–1262, 2007.

Roe, S. M., Spivey, M. D., Lindquist, H. C., Thesing, K. B., and Strait, R. P. Estimating ammonia emissions from anthropogenic nonagricultural sources-draft final report. *Emission Inventory Improvement Program, US Environmental Protection Agency*, 2004.

Roiger, A., Thomas, J.-L., Schlager, H., Law, K. S., Kim, J., Schäfler, A., Weinzierl, B., Dahlkötter, F., Krisch, I., Marelle, L., et al. Quantifying emerging local anthropogenic emissions in the arctic region: The access aircraft campaign experiment. *Bulletin of the American Meteorological Society*, 96(3):441–460, 2015.

Roscoe, H. K., Brooks, B., Jackson, A., Smith, M., Walker, S., Obbard, R. W., and Wolff, E. W. Frost flowers in the laboratory: Growth, characteristics, aerosol, and the underlying sea ice. *Journal of Geophysical Research: Atmospheres*, 116(D12), 2011.

Rudich, Y. Laboratory perspectives on the chemical transformations of organic matter in atmospheric particles. *Chemical Reviews*, 103(12):5097–5124, 2003.

Russell, L. M., Hawkins, L. N., Frossard, A. A., Quinn, P. K., and Bates, T. S. Carbohydrate-like composition of submicron atmospheric particles and their production from ocean bubble bursting. *Proceedings of the National Academy of Sciences*, 107(15):6652–6657, 2010. ISSN 0027-8424. doi: 10.1073/pnas.0908905107. URL https://www.pnas.org/content/107/15/6652.

Sakaguchi, K. and Zeng, X. Effects of soil wetness, plant litter, and under-canopy atmospheric stability on ground evaporation in the community land model (clm3.5). *Journal of Geophysical Research: Atmospheres*, 114(D1), 2009. doi: https://doi.org/10.1029/2008JD010834. URL https://agupubs.onlinelibrary.wiley.com/doi/abs/10.1029/2008JD010834.

Saliba, G., Chen, C.-L., Lewis, S., Russell, L. M., Rivellini, L.-H., Lee, A. K. Y., Quinn, P. K., Bates, T. S., Haëntjens, N., Boss, E. S., Karp-Boss, L., Baetge, N., Carlson, C. A., and Behrenfeld, M. J. Factors driving the seasonal and hourly variability of sea-spray aerosol number in the north atlantic. *Proceedings of the National Academy of Sciences*, 116(41):20309–20314, 2019. ISSN 0027-8424. doi: 10.1073/pnas.1907574116. URL https://www.pnas.org/content/116/41/20309.

Salisbury, D. J., Anguelova, M. D., and Brooks, I. M. On the variability of whitecap fraction using satellite-based observations. *Journal of Geophysical Research: Oceans*, 118(11):6201–6222, 2013. doi: https://doi.org/10.1002/2013JC008797. URL https://agupubs.onlinelibrary.wiley.com/doi/abs/10.1002/2013JC008797.

Salisbury, D. J., Anguelova, M. D., and Brooks, I. M. Global distribution and seasonal dependence of satellite-based whitecap fraction. *Geophysical Research Letters*, 41(5):1616–1623, 2014. doi: https://doi.org/10.1002/2014GL059246. URL https://agupubs.onlinelibrary.wiley.com/doi/abs/10.1002/2014GL059246.

Salter, M. E., Nilsson, E. D., Butcher, A., and Bilde, M. On the seawater temperature dependence of the sea spray aerosol generated by a continuous plunging jet. *Journal of Geophysical Research: Atmospheres*, 119(14):9052–9072, 2014.

Salter, M. E., Zieger, P., Acosta Navarro, J. C., Grythe, H., Kirkevåg, A., Rosati, B., Riipinen, I., and Nilsson, E. D. An empirically derived inorganic sea spray source function incorporating sea surface temperature. *Atmospheric Chemistry and Physics*, 15(19):11047–11066, 2015. doi: 10.5194/acp-15-11047-2015. URL https://acp.copernicus.org/articles/15/11047/2015/.

Samset, B., Myhre, G., Herber, A., Kondo, Y., Li, S.-M., Moteki, N., Koike, M., Oshima, N., Schwarz, J. P., Balkanski, Y., et al. Modelled black carbon radiative forcing and atmospheric lifetime in aerocom phase ii constrained by aircraft observations. *Atmospheric Chemistry and Physics*, 14(22):12465–12477, 2014.

Samset, B. H., Myhre, G., Schulz, M., Balkanski, Y., Bauer, S., Berntsen, T. K., Bian, H., Bellouin, N., Diehl, T., Easter, R. C., et al. Black carbon vertical profiles strongly affect its radiative forcing uncertainty. *Atmospheric Chemistry and Physics*, 13(5):2423–2434, 2013.

Sandu, A., Verwer, J., Blom, J., Spee, E., Carmichael, G., and Potra, F. Benchmarking stiff ode solvers for atmospheric chemistry problems ii: Rosenbrock solvers. *Atmospheric environment*, 31(20):3459–3472, 1997.

Sato, Y., Miura, H., Yashiro, H., Goto, D., Takemura, T., Tomita, H., and Nakajima, T. Unrealistically pristine air in the arctic produced by current global scale models. *Scientific Reports*, 6, 2016. ISSN 2045-2322. doi: 10.1038/srep26561.

Schicker, I., Arnold Arias, D., and Seibert, P. Influences of updated land-use datasets on wrf simulations for two austrian regions. *Meteorology and Atmospheric Physics*, 128(3):279–301, 2016.

Schmale, J., Schneider, J., Ancellet, G., Quennehen, B., Stohl, A., Sodemann, H., Burkhart, J. F., Hamburger, T., Arnold, S. R., Schwarzenboeck, A., et al. Source identification and airborne chemical characterisation of aerosol pollution from long-range transport over greenland during polarcat summer campaign 2008. *Atmospheric Chemistry and Physics*, 11(19):10097–10123, 2011.

Schmale, J., Arnold, S., Law, K. S., Thorp, T., Anenberg, S., Simpson, W., Mao, J., and Pratt, K. Local arctic air pollution: A neglected but serious problem. *Earth's Future*, 6(10):1385–1412, 2018.

Schmale, J., Sharma, S., Decesari, S., Pernov, J., Massling, A., Hansson, H.-C., von Salzen, K., Skov, H., Andrews, E., Quinn, P. K., et al. Pan-arctic seasonal cycles and long-term trends of aerosol properties from 10 observatories. *Atmospheric Chemistry and Physics*, 22(5):3067–3096, 2022.

Schroeder, W. H., Anlauf, K., Barrie, L., Lu, J., Steffen, A., Schneeberger, D., and Berg, T. Arctic springtime depletion of mercury. *Nature*, 394(6691):331–332, 1998.

Schumann, T., Zinder, B., and Waldvogel, A. Aerosol and hydrometeor concentrations and their chemical composition during winter precipitation along a mountain slope—i. temporal evolution of the aerosol, microphysical and meteorological conditions. *Atmospheric Environment (1967)*, 22(7):1443–1459, 1988.

Schwarz, J. P., Weinzierl, B., Samset, B. H., Dollner, M., Heimerl, K., Markovic, M. Z., Perring, A. E., and Ziemba, L. Aircraft measurements of black carbon vertical profiles show upper tropospheric variability and stability. *Geophysical Research Letters*, 44(2):1132–1140, 2017. doi: https://doi.org/10.1002/2016GL071241. URL https://agupubs.onlinelibrary.wiley.com/doi/abs/10.1002/2016GL071241.

Scientific, T. Model 5012 instruction manual multi angle absorption photometer (maap). *Thermo Fisher Scientific: Madison, WI, USA*, 2007.

Screen, J. A. and Simmonds, I. Increasing fall-winter energy loss from the arctic ocean and its role in arctic temperature amplification. *Geophysical Research Letters*, 37(16), 2010.

Seidel, D. J., Ao, C. O., and Li, K. Estimating climatological planetary boundary layer heights from radiosonde observations: Comparison of methods and uncertainty analysis. *Journal of Geophysical Research: Atmospheres*, 115(D16), 2010.

Seinfeld, J. and Pandis, S. *Atmospheric Chemistry and Physics: From Air Pollution to Climate Change*. 1998.

Seinfeld, J. and Pandis, S. Atmospheric chemistry and physics 2nd edn (hoboken, nj, 2006.

Seinfeld, J. H. Atmospheric chemistry and physics of air polution. *California, California Institute of Technology Pasadena*, 1986.

Seinfeld, J. H. and Pandis, S. N. *Atmospheric Chemistry and Physics: From Air Pollution to Climate Change*. MTM, 2013.

Sellers, P., Randall, D., Collatz, G., Berry, J., Field, C., Dazlich, D., Zhang, C., Collelo, G., and Bounoua, L. A revised land surface parameterization (sib2) for atmospheric gcms. part i: Model formulation. *Journal of Climate*, 9:676–705, 04 1996. doi: 10.1175/1520-0442(1996)009<0676:ARLSPF>2.0.CO;2.

Serreze, M. C. and Barrett, A. P. The summer cyclone maximum over the central arctic ocean. *Journal of Climate*, 21(5):1048–1065, 2008.

Serreze, M. C. and Francis, J. A. The arctic amplification debate. *Climatic change*, 76(3):241–264, 2006.

Serreze, M. C., Kahl, J. D., and Schnell, R. C. Low-level temperature inversions of the eurasian arctic and comparisons with soviet drifting station data. *Journal of Climate*, 5(6):615–629, 1992.

Serreze, M. C., Barrett, A. P., and Stroeve, J. Recent changes in tropospheric water vapor over the arctic as assessed from radiosondes and atmospheric reanalyses. *Journal of Geophysical Research: Atmospheres*, 117(D10), 2012.

Sessions, W., Fuelberg, H., Kahn, R., and Winker, D. An investigation of methods for injecting emissions from boreal wildfires using wrf-chem during arctas. *Atmospheric Chemistry and Physics*, 11(12):5719–5744, 2011.

Sha, T., Ma, X., Jia, H., Tian, R., Chang, Y., Cao, F., and Zhang, Y. Aerosol chemical component: Simulations with wrf-chem and comparison with observations in nanjing. *Atmospheric Environment*, 218:116982, 2019.

Shakya, K. M. and Peltier, R. E. Investigating missing sources of sulfur at fairbanks, alaska. *Environmental science & technology*, 47(16):9332–9338, 2013.

Sharma, S., Andrews, E., Barrie, L., Ogren, J., and Lavoué, D. Variations and sources of the equivalent black carbon in the high arctic revealed by long-term observations at alert and barrow: 1989–2003. *Journal of Geophysical Research: Atmospheres*, 111(D14), 2006.

Sharma, S., Ishizawa, M., Chan, D., Lavoué, D., Andrews, E., Eleftheriadis, K., and Maksyutov, S. 16-year simulation of arctic black carbon: Transport, source contribution, and sensitivity analysis on deposition. *Journal of Geophysical Research: Atmospheres*, 118(2):943–964, 2013.

Sharma, S., Leaitch, W. R., Huang, L., Veber, D., Kolonjari, F., Zhang, W., Hanna, S. J., Bertram, A. K., and Ogren, J. A. An evaluation of three methods for measuring black carbon in alert, canada. *Atmospheric Chemistry and Physics*, 17(24):15225–15243, 2017.

Sharma, S., Barrie, L. A., Magnusson, E., Brattström, G., Leaitch, W., Steffen, A., and Landsberger, S. A factor and trends analysis of multidecadal lower tropospheric observations of arctic aerosol composition, black carbon, ozone, and mercury at alert, canada. *Journal of Geophysical Research: Atmospheres*, 124(24): 14133–14161, 2019.

Shaw, P. M., Russell, L. M., Jefferson, A., and Quinn, P. K. Arctic organic aerosol measurements show particles from mixed combustion in spring haze and from frost flowers in winter. *Geophysical Research Letters*, 37(10), 2010. doi: https://doi.org/10.1029/2010GL042831. URL https://agupubs.onlinelibrary.wiley.com/doi/abs/10.1029/2010GL042831.

Shen, Z., Ming, Y., Horowitz, L. W., Ramaswamy, V., and Lin, M. On the seasonality of arctic black carbon. *Journal of Climate*, 30(12):4429–4441, 2017.

Shindell, D., Chin, M., Dentener, F., Doherty, R., Faluvegi, G., Fiore, A., Hess, P., Koch, D., MacKenzie, I., Sanderson, M., et al. A multi-model assessment of pollution transport to the arctic. *Atmospheric Chemistry and Physics*, 8(17):5353–5372, 2008.

Shrivastava, M., Fast, J., Easter, R., Gustafson Jr, W., Zaveri, R. A., Jimenez, J. L., Saide, P., and Hodzic, A. Modeling organic aerosols in a megacity: comparison of simple and complex representations of the volatility basis set approach. *Atmospheric Chemistry and Physics*, 11(13):6639–6662, 2011a.

Shrivastava, M., Fast, J., Easter, R., Gustafson Jr., W. I., Zaveri, R. A., Jimenez, J. L., Saide, P., and Hodzic, A. Modeling organic aerosols in a megacity: comparison of simple and complex representations of the volatility basis set approach. *Atmospheric Chemistry and Physics*, 11(13):6639–6662, 2011b. doi: 10.5194/acp-11-6639-2011. URL https://acp.copernicus.org/articles/11/6639/2011/.

Shrivastava, M., Easter, R. C., Liu, X., Zelenyuk, A., Singh, B., Zhang, K., Ma, P.-L., Chand, D., Ghan, S., Jimenez, J. L., et al. Global transformation and fate of soa: Implications of low-volatility soa and gas-phase fragmentation reactions. *Journal of Geophysical Research: Atmospheres*, 120(9):4169–4195, 2015.

Sievering, H., Boatman, J., Galloway, J., Keene, W., Kim, Y., Luria, M., and Ray, J. Heterogeneous sulfur conversion in sea-salt aerosol particles: the role of aerosol water content and size distribution. *Atmospheric Environment. Part A. General Topics*, 25(8):1479–1487, 1991.

Simpson, W., Carlson, D., Hönninger, G., Douglas, T., Sturm, M., Perovich, D., and Platt, U. First-year sea-ice contact predicts bromine monoxide (bro) levels at barrow, alaska better than potential frost flower contact. *Atmospheric Chemistry and Physics*, 7(3):621–627, 2007.

Simpson, W., Law, K., Schmale, J., Pratt, K., Arnold, S., Mao, J., Alexander, B., Anenberg, S., Baklanov, A., Bell, D., et al. Alaskan layered pollution and chemical analysis (alpaca) white paper, 84, 2019.

Skamarock, W., Klemp, J., Dudhia, J., Gill, D. O., Barker, D. M., Duda, M. G., Huang, X.-Y., Wang, W., and Powers, J. G. A description of the advanced research wrf version 3, mesoscale and microscale meteorology division. *National Center for Atmospheric Research, Boulder, Colorado, USA*, 88:7–25, 2008a.

Skamarock, W. C., Klemp, J. B., Dudhia, J., Gill, D. O., Barker, D. M., Wang, W., and Powers, J. G. A description of the advanced research wrf version 3. ncar technical note -475+str, 2008b.

Slinn, W. Predictions for particle deposition to vegetative canopies. *Atmospheric Environment (1967)*, 16 (7):1785–1794, 1982. ISSN 0004-6981. doi: https://doi.org/10.1016/0004-6981(82)90271-2. URL https://www.sciencedirect.com/science/article/pii/0004698182902712. Precipitation chemistry.

Sobhani, N., Kulkarni, S., and Carmichael, G. R. Source sector and region contributions to black carbon and pm 2.5 in the arctic. *Atmospheric Chemistry and Physics*, 18(24):18123–18148, 2018.

Sofiev, M., Soares, J., Prank, M., de Leeuw, G., and Kukkonen, J. A regional-to-global model of emission and transport of sea salt particles in the atmosphere. *Journal of Geophysical Research: Atmospheres*, 116(D21), 2011. doi: https://doi.org/10.1029/2010JD014713. URL https://agupubs.onlinelibrary.wiley.com/doi/abs/10.1029/2010JD014713.

Solazzo, E., Bianconi, R., Pirovano, G., Matthias, V., Vautard, R., Moran, M. D., Appel, K. W., Bessagnet, B., Brandt, J., Christensen, J. H., et al. Operational model evaluation for particulate matter in europe and north america in the context of aqmeii. *Atmospheric Environment*, 53:75–92, 2012.

Solberg, S., Dye, C., Schmidbauer, N., Herzog, A., and Gehrig, R. Carbonyls and nonmethane hydrocarbons at rural european sites from the mediterranean to the arctic. *Journal of Atmospheric Chemistry*, 25(1): 33–66, 1996.

Song, C. H. and Carmichael, G. R. The aging process of naturally emitted aerosol (sea-salt and mineral aerosol) during long range transport. *Atmospheric Environment*, 33(14):2203–2218, 1999.

Song, S., Ma, T., Zhang, Y., Shen, L., Liu, P., Li, K., Zhai, S., Zheng, H., Gao, M., Moch, J. M., et al. Global modeling of heterogeneous hydroxymethanesulfonate chemistry. *Atmospheric Chemistry and Physics*, 21(1):457–481, 2021.

Soulie. in preparation. 2022.

Spada, M., Jorba, O., Pérez García-Pando, C., Janjic, Z., and Baldasano, J. M. Modeling and evaluation of the global sea-salt aerosol distribution: sensitivity to size-resolved and sea-surface temperature dependent emission schemes. *Atmospheric Chemistry and Physics*, 13(23):11735–11755, 2013. doi: 10.5194/acp-13-11735-2013. URL https://acp.copernicus.org/articles/13/11735/2013/.

Spracklen, D., Jimenez, J., Carslaw, K., Worsnop, D., Evans, M., Mann, G., Zhang, Q., Canagaratna, M., Allan, J., Coe, H., et al. Aerosol mass spectrometer constraint on the global secondary organic aerosol budget. *Atmospheric Chemistry and Physics*, 11(23):12109–12136, 2011.

Stafford, J., Wendler, G., and Curtis, J. Temperature and precipitation of alaska: 50 year trend analysis. *Theoretical and Applied Climatology*, 67(1):33–44, 2000.

Stauffer, D. R. and Seaman, N. L. Use of four-dimensional data assimilation in a limited-area mesoscale model. part i: Experiments with synoptic-scale data. *Monthly Weather Review*, 118(6):1250–1277, 1990.

Steinfeld, J. I. Atmospheric chemistry and physics: from air pollution to climate change. *Environment: Science and Policy for Sustainable Development*, 40(7):26–26, 1998.

Sterk, H., Steeneveld, G., Vihma, T., Anderson, P., Bosveld, F., and Holtslag, A. Clear-sky stable boundary layers with low winds over snow-covered surfaces. part 1: Wrf model evaluation. *Quarterly Journal of the Royal Meteorological Society*, 141(691):2165–2184, 2015.

Sterk, H., Steeneveld, G., Bosveld, F., Vihma, T., Anderson, P., and Holtslag, A. Clear-sky stable boundary layers with low winds over snow-covered surfaces. part 2: Process sensitivity. *Quarterly Journal of the Royal Meteorological Society*, 142(695):821–835, 2016.

Stjern, C. W., Lund, M. T., Samset, B. H., Myhre, G., Forster, P. M., Andrews, T., Boucher, O., Faluvegi, G., Fläschner, D., Iversen, T., et al. Arctic amplification response to individual climate drivers. *Journal of Geophysical Research: Atmospheres*, 124(13):6698–6717, 2019.

Stohl, A. Characteristics of atmospheric transport into the arctic troposphere. *Journal of Geophysical Research: Atmospheres*, 111(D11), 2006.

Stohl, A., Klimont, Z., Eckhardt, S., Kupiainen, K., Shevchenko, V. P., Kopeikin, V., and Novigatsky, A. Black carbon in the arctic: the underestimated role of gas flaring and residential combustion emissions. *Atmospheric Chemistry and Physics*, 13(17):8833–8855, 2013a.

Stohl, A., Klimont, Z., Eckhardt, S., Kupiainen, K., Shevchenko, V. P., Kopeikin, V. M., and Novigatsky, A. N. Black carbon in the arctic: the underestimated role of gas flaring and residential combustion emissions. *Atmospheric Chemistry and Physics*, 13(17):8833–8855, 2013b. doi: 10.5194/acp-13-8833-2013. URL https://acp.copernicus.org/articles/13/8833/2013/.

Stohl, A., Aamaas, B., Amann, M., Baker, L. H., Bellouin, N., Berntsen, T. K., Boucher, O., Cherian, R., Collins, W., Daskalakis, N., Dusinska, M., Eckhardt, S., Fuglestvedt, J. S., Harju, M., Heyes, C., Hodnebrog, Ø., Hao, J., Im, U., Kanakidou, M., Klimont, Z., Kupiainen, K., Law, K. S., Lund, M. T., Maas, R., MacIntosh, C. R., Myhre, G., Myriokefalitakis, S., Olivié, D., Quaas, J., Quennehen, B., Raut, J.-C., Rumbold, S. T., Samset, B. H., Schulz, M., Seland, Ø., Shine, K. P., Skeie, R. B., Wang, S., Yttri, K. E., and Zhu, T. Evaluating the climate and air quality impacts of short-lived pollutants. *Atmospheric Chemistry and Physics*, 15(18): 10529–10566, 2015a. doi: 10.5194/acp-15-10529-2015. URL https://acp.copernicus.org/articles/15/10529/2015/.

Stohl, A., Aamaas, B., Amann, M., Baker, L. H., Bellouin, N., Berntsen, T. K., Boucher, O., Cherian, R., Collins, W., Daskalakis, N., et al. Evaluating the climate and air quality impacts of short-lived pollutants. *Atmospheric Chemistry and Physics*, 15(18):10529–10566, 2015b.

Stone, R. S., Sharma, S., Herber, A., Eleftheriadis, K., Nelson, D. W., Helmig, D., and Bottenheim, J. W. A characterization of arctic aerosols on the basis of aerosol optical depth and black carbon measurementsa characterization of arctic aerosols. *Elementa: Science of the Anthropocene*, 2, 2014.

Stroeve, J. and Notz, D. Changing state of arctic sea ice across all seasons. *Environmental Research Letters*, 13 (10):103001, 2018.

Stroeve, J., Serreze, M., Holland, M., Kay, J., Malanik, J., and Barrett, A. The Arctic's rapidly shrinking sea ice cover: a research synthesis. *Climatic Change*, 110(3):1005–1027, February 2012a. doi: 10.1007/s10584-011-0101-1. URL https://ideas.repec.org/a/spr/climat/v110y2012i3p1005-1027.html.

Stroeve, J. C., Serreze, M. C., Holland, M. M., Kay, J. E., Malanik, J., and Barrett, A. P. The arctic's rapidly shrinking sea ice cover: a research synthesis. *Climatic change*, 110(3):1005–1027, 2012b.

Stull, R. B. *An introduction to boundary layer meteorology*, volume 13. Springer Science & Business Media, 1988.

Sulikowska, A., Walawender, J. P., and Walawender, E. Temperature extremes in alaska: temporal variability and circulation background. *Theoretical and Applied Climatology*, 136(3):955–970, 2019.

Szopa, S., Naik, V., Adhikary, B., Artaxo, P., Berntsen, T., Collins, W., Fuzzi, S., Gallardo, L., Kiendler-Scharr, A., Klimont, Z., H. Liao, a. U., and Zanis, P. Short-lived climate forcers. in climate change 2021: The physical science basis. contribution of working group i to the sixth assessment report of the intergovernmental panel on climate change, [masson-delmotte, v., p. zhai, a. pirani, s.l. connors, c. péan, s. berger, n. caud, y. chen, l. goldfarb, m.i. gomis, m. huang, k. leitzell, e. lonnoy, j.b.r. matthews, t.k. maycock, t. waterfield, o. yelekçi, r. yu, and b. zhou (eds.)]. page pp. 817–922, 2021. doi: 10.1017/9781009157896.008.

Takemura, T., Egashira, M., Matsuzawa, K., Ichijo, H., O'ishi, R., and Abe-Ouchi, A. A simulation of the global distribution and radiative forcing of soil dust aerosols at the last glacial maximum. *Atmospheric Chemistry and Physics*, 9(9):3061–3073, 2009.

Tastula, E.-M. and Vihma, T. Wrf model experiments on the antarctic atmosphere in winter. *Monthly Weather Review*, 139(4):1279–1291, 2011.

Thishan Dharshana, K., Kravtsov, S., and Kahl, J. D. Relationship between synoptic weather disturbances and particulate matter air pollution over the united states. *Journal of Geophysical Research: Atmospheres*, 115(D24), 2010.

Thoman, R. and Walsh, J. E. *Alaska's changing environment: Documenting Alaska's physical and biological changes through observations*. International Arctic Research Center, University of Alaska Fairbanks, 2019.

Tissari, J., Hytönen, K., Lyyränen, J., and Jokiniemi, J. A novel field measurement method for determining fine particle and gas emissions from residential wood combustion. *Atmospheric Environment*, 41(37): 8330–8344, 2007.

Toll, V., Christensen, M., Quaas, J., and Bellouin, N. Weak average liquid-cloud-water response to anthropogenic aerosols. *Nature*, 572(7767):51–55, 2019.

Tran, H. N. and Mölders, N. Investigations on meteorological conditions for elevated pm2. 5 in fairbanks, alaska. *Atmospheric Research*, 99(1):39–49, 2011.

Trochkine, D., Iwasaka, Y., Matsuki, A., Yamada, M., Kim, Y.-S., Nagatani, T., Zhang, D., Shi, G.-Y., and Shen, Z. Mineral aerosol particles collected in dunhuang, china, and their comparison with chemically modified particles collected over japan. *Journal of Geophysical Research: Atmospheres*, 108(D23), 2003.

Tsigaridis, K., Krol, M., Dentener, F., Balkanski, Y., Lathiere, J., Metzger, S., Hauglustaine, D., and Kanakidou, M. Change in global aerosol composition since preindustrial times. *Atmospheric Chemistry and Physics*, 6(12):5143–5162, 2006.

Udisti, R., Traversi, R., Becagli, S., Tomasi, C., Mazzola, M., Lupi, A., and Quinn, P. K. Arctic aerosols. In *Physics and Chemistry of the Arctic Atmosphere*, pages 209–329. Springer, 2020.

Van Marle, M. J., Kloster, S., Magi, B. I., Marlon, J. R., Daniau, A.-L., Field, R. D., Arneth, A., Forrest, M., Hantson, S., Kehrwald, N. M., et al. Historic global biomass burning emissions for cmip6 (bb4cmip) based on merging satellite observations with proxies and fire models (1750–2015). *Geoscientific Model Development*, 10(9):3329–3357, 2017.

von Storch, H., Langenberg, H., and Feser, F. A spectral nudging technique for dynamical downscaling purposes. *Monthly weather review*, 128(10):3664–3673, 2000.

Wagner, N., Riedel, T., Young, C. J., Bahreini, R., Brock, C. A., Dubé, W., Kim, S., Middlebrook, A., Öztürk, F., Roberts, J., et al. N2o5 uptake coefficients and nocturnal no2 removal rates determined from ambient wintertime measurements. *Journal of Geophysical Research: Atmospheres*, 118(16):9331–9350, 2013.

Waldron, K. M., Paegle, J., and Horel, J. D. Sensitivity of a spectrally filtered and nudged limited-area model to outer model options. *Monthly weather review*, 124(3):529–547, 1996.

Wang, G., Zhang, R., Gomez, M. E., Yang, L., Zamora, M. L., Hu, M., Lin, Y., Peng, J., Guo, S., Meng, J., et al. Persistent sulfate formation from london fog to chinese haze. *Proceedings of the National Academy of Sciences*, 113(48):13630–13635, 2016.

Wang, H., Skamarock, W. C., and Feingold, G. Evaluation of scalar advection schemes in the advanced research wrf model using large-eddy simulations of aerosol–cloud interactions. *Monthly Weather Review*, 137(8): 2547 – 2558, 2009. doi: 10.1175/2009MWR2820.1. URL https://journals.ametsoc.org/view/journals/mwre/137/8/2009mwr2820.1.xml.

Wang, H., Easter, R. C., Rasch, P. J., Wang, M., Liu, X., Ghan, S. J., Qian, Y., Yoon, J.-H., Ma, P.-L., and Vinoj, V. Sensitivity of remote aerosol distributions to representation of cloud–aerosol interactions in a global climate model. *Geoscientific Model Development*, 6(3):765–782, 2013.

Wang, Q., Jacob, D. J., Fisher, J. A., Mao, J., Leibensperger, E., Carouge, C., Le Sager, P., Kondo, Y., Jimenez, J., Cubison, M., et al. Sources of carbonaceous aerosols and deposited black carbon in the arctic in winter-spring: implications for radiative forcing. *Atmospheric Chemistry and Physics*, 11(23):12453–12473, 2011.

Wang, S., McNamara, S. M., Moore, C. W., Obrist, D., Steffen, A., Shepson, P. B., Staebler, R. M., Raso, A. R., and Pratt, K. A. Direct detection of atmospheric atomic bromine leading to mercury and ozone depletion. *Proceedings of the National Academy of Sciences*, 116(29):14479–14484, 2019a.

Wang, X., Jacob, D. J., Eastham, S. D., Sulprizio, M. P., Zhu, L., Chen, Q., Alexander, B., Sherwen, T., Evans, M. J., Lee, B. H., et al. The role of chlorine in global tropospheric chemistry. *Atmospheric Chemistry and Physics*, 19(6):3981–4003, 2019b.

Wang, Y., Hopke, P. K., et al. Is alaska truly the great escape from air pollution?-long term source apportionment of fine particulate matter in fairbanks, alaska. *Aerosol and Air Quality Research*, 14(7):1875–1882, 2014.

Wang, Y., Duan, X., Liang, T., Wang, L., and Wang, L. Analysis of spatio-temporal distribution characteristics and socioeconomic drivers of urban air quality in china. *Chemosphere*, 291:132799, 2022.

Ward, T., Trost, B., Conner, J., Flanagan, J., Jayanty, R., et al. Source apportionment of pm2. 5 in a subarctic airshed-fairbanks, alaska. *Aerosol and Air Quality Research*, 12(4):536–543, 2012.

Warneke, C., Bahreini, R., Brioude, J., Brock, C., De Gouw, J., Fahey, D., Froyd, K., Holloway, J., Middlebrook, A., Miller, L., et al. Biomass burning in siberia and kazakhstan as an important source for haze over the alaskan arctic in april 2008. *Geophysical Research Letters*, 36(2), 2009.

Warneke, C., Froyd, K., Brioude, J., Bahreini, R., Brock, C., Cozic, J., De Gouw, J., Fahey, D., Ferrare, R., Holloway, J., et al. An important contribution to springtime arctic aerosol from biomass burning in russia. *Geophysical Research Letters*, 37(1), 2010.

Warren, S. G. and Wiscombe, W. J. A model for the spectral albedo of snow. ii: Snow containing atmospheric aerosols. *Journal of the Atmospheric Sciences*, 37(12):2734–2745, 1980.

Wendler, G. Heat balance studies during an ice-fog period in fairbanks, alaska. *Monthly Weather Review*, 97 (7):512–520, 1969.

Wendler, G. and Nicpon, P. Low-level temperature inversions in fairbanks, central alaska. *Monthly Weather Review*, 103(1):34–44, 1975.

Wendler, G. and Shulski, M. A century of climate change for fairbanks, alaska. *Arctic*, pages 295–300, 2009.

Wesely, M. Parameterization of surface resistances to gaseous dry deposition in regional-scale numerical models. *Atmospheric Environment (1967)*, 23(6):1293–1304, 1989. ISSN 0004-6981. doi: https://doi.org/10.1016/0004-6981(89)90153-4. URL https://www.sciencedirect.com/science/article/pii/0004698189901534.

Wexler, A. S., Lurmann, F. W., and Seinfeld, J. H. Modelling urban and regional aerosols—i. model development. *Atmospheric Environment*, 28(3):531–546, 1994.

Wexler, H. Cooling in the lower atmosphere and the structure of polar continental air. *Monthly Weather Review*, 64(4):122–136, 1936.

Wexler, H. *Observations of Nocturnal Radiation at Fairbanks, Alaska, and Fargo, N. Dak: Investigations Conducted by the Weather Bureau Under Bankhead-Jones Special Research Fund*. US Government Printing Office, 1941.

Whaley, C. H., Makar, P. A., Shephard, M. W., Zhang, L., Zhang, J., Zheng, Q., Akingunola, A., Wentworth, G. R., Murphy, J. G., Kharol, S. K., et al. Contributions of natural and anthropogenic sources to ambient ammonia in the athabasca oil sands and north-western canada. *Atmospheric Chemistry and Physics*, 18 (3):2011–2034, 2018.

Whaley, C. H., Law, K. S., Hjorth, J. L., Skov, H., Arnold, S. R., Langner, J., Pernov, J. B., Chien, R.-Y., Christensen, J. H., Deushi, M., et al. Arctic tropospheric ozone: assessment of current knowledge and model performance. *Atmospheric Chemistry and Physics Discussions*, pages 1–34, 2022a.

Whaley, C. H., Mahmood, R., von Salzen, K., Winter, B., Eckhardt, S., Arnold, S., Beagley, S., Becagli, S., Chien, R.-Y., Christensen, J., et al. Model evaluation of short-lived climate forcers for the arctic monitoring and assessment programme: a multi-species, multi-model study. *Atmospheric Chemistry and Physics*, 22(9): 5775–5828, 2022b.

Whitby, K. T. The physical characteristics of sulfur aerosols. In *Sulfur in the Atmosphere*, pages 135–159. Elsevier, 1978.

Wild, O., Zhu, X., and Prather, M. Fast-j: Accurate simulation of in- and below-cloud photolysis in tropospheric chemical models. *Journal of Atmospheric Chemistry*, 37:245–282, 2000.

Williams, J., De Reus, M., Krejci, R., Fischer, H., and Ström, J. Application of the variability-size relationship to atmospheric aerosol studies: estimating aerosol lifetimes and ages. *Atmospheric Chemistry and Physics*, 2(2):133–145, 2002.

Winiger, P., Andersson, A., Eckhardt, S., Stohl, A., and Gustafsson, Ö. The sources of atmospheric black carbon at a european gateway to the arctic. *Nature Communications*, 7(1):1–8, 2016.

Winiger, P., Andersson, A., Eckhardt, S., Stohl, A., Semiletov, I. P., Dudarev, O. V., Charkin, A., Shakhova, N., Klimont, Z., Heyes, C., et al. Siberian arctic black carbon sources constrained by model and observation. *Proceedings of the National Academy of Sciences*, 114(7):E1054–E1061, 2017.

Winiger, P., Barrett, T., Sheesley, R., Huang, L., Sharma, S., Barrie, L. A., Yttri, K. E., Evangeliou, N., Eckhardt, S., Stohl, A., et al. Source apportionment of circum-arctic atmospheric black carbon from isotopes and modeling. *Science advances*, 5(2):eaau8052, 2019.

Winiwarter, W., Bauer, H., Caseiro, A., and Puxbaum, H. Quantifying emissions of primary biological aerosol particle mass in europe. *Atmospheric Environment*, 43(7):1403–1409, 2009.

Witek, M. L., Flatau, P. J., Quinn, P. K., and Westphal, D. L. Global sea-salt modeling: Results and validation against multicampaign shipboard measurements. *Journal of Geophysical Research:Atmospheres*, 112(D8), 2007.

Xu, J., Wang, Q., Deng, C., McNeill, V. F., Fankhauser, A., Wang, F., Zheng, X., Shen, J., Huang, K., and Zhuang, G. Insights into the characteristics and sources of primary and secondary organic carbon: High time resolution observation in urban shanghai. *Environmental Pollution*, 233:1177–1187, 2018.

Xu, J., Zhang, J., Liu, J., Yi, K., Xiang, S., Hu, X., Wang, Y., Tao, S., and Ban-Weiss, G. Influence of cloud microphysical processes on black carbon wet removal, global distributions, and radiative forcing. *Atmospheric Chemistry and Physics*, 19(3):1587–1603, 2019.

Xu, J.-W., Martin, R. V., Morrow, A., Sharma, S., Huang, L., Leaitch, W. R., Burkart, J., Schulz, H., Zanatta, M., Willis, M. D., Henze, D. K., Lee, C. J., Herber, A. B., and Abbatt, J. P. D. Source attribution of arctic black carbon constrained by aircraft and surface measurements. *Atmospheric Chemistry and Physics*, 17(19): 11971–11989, 2017. doi: 10.5194/acp-17-11971-2017. URL https://acp.copernicus.org/articles/17/11971/2017/.

Xu, L., Russell, L. M., Somerville, R. C. J., and Quinn, P. K. Frost flower aerosol effects on arctic wintertime longwave cloud radiative forcing. *Journal of Geophysical Research: Atmospheres*, 118(23):13,282–13,291, 2013. doi: https://doi.org/10.1002/2013JD020554. URL https://agupubs.onlinelibrary.wiley.com/doi/abs/10.1002/2013JD020554.

Xu, L., Russell, L. M., and Burrows, S. M. Potential sea salt aerosol sources from frost flowers in the pan-arctic region. *Journal of Geophysical Research: Atmospheres*, 121(18):10,840–10,856, 2016. doi: https://doi.org/10.1002/2015JD024713. URL https://agupubs.onlinelibrary.wiley.com/doi/abs/10.1002/2015JD024713.

Yang, R. and Friedl, M. A. Modeling the effects of three-dimensional vegetation structure on surface radiation and energy balance in boreal forests. *Journal of Geophysical Research: Atmospheres*, 108(D16), 2003. doi: https://doi.org/10.1029/2002JD003109. URL https://agupubs.onlinelibrary.wiley.com/doi/abs/10.1029/2002JD003109.

Yang, Y., Wang, H., Smith, S. J., Easter, R. C., and Rasch, P. J. Sulfate aerosol in the arctic: Source attribution and radiative forcing. *Journal of Geophysical Research: Atmospheres*, 123(3):1899–1918, 2018.

Yang, Z.-L., Niu, G.-Y., Mitchell, K. E., Chen, F., Ek, M. B., Barlage, M., Longuevergne, L., Manning, K., Niyogi, D., Tewari, M., et al. The community noah land surface model with multiparameterization options (noah-mp): 2. evaluation over global river basins. *Journal of Geophysical Research: Atmospheres*, 116 (D12), 2011.

Yang Z.-L., R. E. Dickinson, A. R. and Vinnikov., K. Y. Validation of the snow sub-model of the biosphere-atmosphere transfer scheme with russian snow cover and meteorological observational data. *J. Clim.*, 10:353—-373, 1997. doi: 10.1175/1520-0442(1997)010<0353:VOTSSO>2.0.CO;2.

Ye, L. and Wang, Y. Long-term air quality study in fairbanks, alaska: Air pollutant temporal variations, correlations, and pm2. 5 source apportionment. *Atmosphere*, 11(11):1203, 2020.

yue Niu, G. and liang Yang, Z. Effects of frozen soil on snowmelt runoff and soil water storage at a continental scale. *J. Hydrometeorol*, pages 937–952, 2006.

Yun, Y., Penner, J., and Popovicheva, O. The effects of hygroscopicity on ice nucleation of fossil fuel combustion aerosols in mixed-phase clouds. *Atmospheric Chemistry and Physics*, 13(8):4339–4348, 2013.

Zaveri, R. A. and Peters, L. K. A new lumped structure photochemical mechanism for large-scale applications. *Journal of Geophysical Research: Atmospheres*, 104(D23):30387–30415, 1999.

Zaveri, R. A., Easter, R. C., Fast, J. D., and Peters, L. K. Model for simulating aerosol interactions and chemistry (mosaic). *Journal of Geophysical Research: Atmospheres*, 113(D13), 2008. doi: https://doi.org/10.1029/2007JD008782. URL https://agupubs.onlinelibrary.wiley.com/doi/abs/10.1029/2007JD008782.

Zeng, Y., Wang, M., Zhao, C., Chen, S., Liu, Z., Huang, X., and Gao, Y. Wrf-chem v3. 9 simulations of the east asian dust storm in may 2017: modeling sensitivities to dust emission and dry deposition schemes. *Geoscientific Model Development*, 13(4):2125–2147, 2020.

Zhang, L., Gong, S., Padro, J., and Barrie, L. A size-segregated particle dry deposition scheme for an atmospheric aerosol module. *Atmospheric Environment*, 35(3):549–560, 2001. ISSN 1352-2310. doi: https://doi.org/10.1016/S1352-2310(00)00326-5. URL https://www.sciencedirect.com/science/article/pii/S1352231000003265.

Zhang, Y., Seidel, D. J., Golaz, J.-C., Deser, C., and Tomas, R. A. Climatological characteristics of arctic and antarctic surface-based inversions. *Journal of Climate*, 24(19):5167–5186, 2011.

Zhao, C. and Garrett, T. J. Effects of arctic haze on surface cloud radiative forcing. *Geophysical Research Letters*, 42(2):557–564, 2015.

Zhao, Y., Nguyen, N. T., Presto, A. A., Hennigan, C. J., May, A. A., and Robinson, A. L. Intermediate volatility organic compound emissions from on-road gasoline vehicles and small off-road gasoline engines. *Environmental science & technology*, 50(8):4554–4563, 2016.

Zhu, C., Kanaya, Y., Takigawa, M., Ikeda, K., Tanimoto, H., Taketani, F., Miyakawa, T., Kobayashi, H., and Pisso, I. Flexpart v10. 1 simulation of source contributions to arctic black carbon. *Atmospheric Chemistry and Physics*, 20(3):1641–1656, 2020.

Zhuang, H., Chan, C. K., Fang, M., and Wexler, A. S. Formation of nitrate and non-sea-salt sulfate on coarse particles. *Atmospheric Environment*, 33(26):4223–4233, 1999.

Zinder, B., Schumann, T., and Waldvogel, A. Aerosol and hydrometeor concentrations and their chemical composition during winter precipitation along a mountain slope—ii. enhancement of below-cloud scavenging in a stably stratified atmosphere. *Atmospheric Environment (1967)*, 22(12):2741–2750, 1988.

Zwaaftink, C. G., Grythe, H., Skov, H., and Stohl, A. Substantial contribution of northern high-latitude sources to mineral dust in the arctic. *Journal of Geophysical Research: Atmospheres*, 121(22):13–678, 2016.